

FACULTY
OF MATHEMATICS
AND PHYSICS
Charles University

DOCTORAL THESIS

Narendra Prabhakar Arasu

Electronic, mechanical and transport properties of molecular junctions

Department of Condensed Matter Physics

Supervisor of the doctoral thesis: Dr. Héctor Vázquez

Study programme: Doctoral, full-time

Study branch: Physics of Condensed Matter and Materials Research (P4F3)

Prague 2021

I declare that I carried out this doctoral thesis independently, and only with the cited sources, literature and other professional sources. It has not been used to obtain another or the same degree.

I understand that my work relates to the rights and obligations under the Act No. 121/2000 Sb., the Copyright Act, as amended, in particular the fact that the Charles University has the right to conclude a license agreement on the use of this work as a school work pursuant to Section 60 subsection 1 of the Copyright Act.

In ..... date ....

Author's signature

I dedicate this thesis to my mom Mrs. Valarmathy Arasu who is the pillar of support in every aspect of my life. I want to thank my friends Gautham, Hugo, and Muthu, to name a few, who have helped me stay composed throughout and have instilled confidence in myself whenever needed.

I also extend my gratitude to all of my colleagues at Fyzikální ústav for their contribution in participating in valuable discussions and consultations during my doctoral stay. I would also like to thank our collaborators for their impetus to deliver high quality scientific outcomes. Finally, I am immensely grateful to my supervisor Héctor Vázquez, for guiding me to learn and grow, both personally and professionally.

Title: Electronic, mechanical and transport properties of molecular junctions

Author: Narendra Prabhakar Arasu

Department: Department of Condensed Matter Physics

Supervisor: Dr. Héctor Vázquez, Institute of Physics of the Czech Academy of Sciences, Department of surfaces and molecular structures, Molecular Transport Group

Abstract: Research and development in the single-molecule circuit are interesting from a fundamental perspective and have a great potential impact on electronics, catalysis, and organic energy cells. In this thesis, I present my contributions to molecular junctions through theory and simulations. Chapter 1 starts with a basic overview of fundamental concepts in the electronic structure of molecules and molecular electronics. Starting from simple models, I introduce the main ideas governing electron transmission through molecular structures, such as confinement and quantization of energy levels, tunneling through a potential barrier, or transmission through a single electronic level. I then present the fundamentals of electronic structure and Green's function methods. The concepts and simulation methods outlined here are the theoretical background for the works presented in this thesis. I also briefly discuss a few widely used experimental techniques studying molecular circuits.

Chapters 2 and 3 describe the behavior of novel individual molecules adsorbed on a metallic substrate. Using theory and simulations, we study the electronic properties of molecular systems in collaboration with experimentalists. I worked on two systems. The first is a donor-bridge-acceptor molecule studied on a Pt surface. We investigate the preservation of donor-acceptor properties of the molecule upon adsorption on a highly reactive substrate. The second work is a surface study of a class of molecules called carbene. We study the geometrical and adsorption properties of a novel carbene molecule on the Au surface. Chapter 4 acts as a bridge between molecular surface science and molecular electronics. We propose a new bipodal molecular platform that is mechanically robust, as it forms two covalent bonds to the Au substrate. We then contact the molecule from the top with a tip and study the electron transport properties. Our study provides a guideline for designing molecular platforms on Au.

Finally, chapter 5 focuses on conductance and antiaromaticity. Aromaticity is a key concept in chemistry, describing the stability of conjugated molecules, which play a central role in molecular electronic studies. Antiaromatic compounds were long predicted to have remarkable conducting properties but not previously tested. Our study, carried in close collaboration with synthetic and experimental partners, was the first to study the conductance of genuinely antiaromatic molecules. Calculations revealed the origin of this increased conductance. In a subsequent article, we generalized our previous work to reveal the relationship between (anti)aromaticity, molecular connectivity, and quantum interference.

Keywords: Molecular electronics, Molecular transport, Density functional theory-DFT, Donor-acceptor molecule, Carbenes, Aromaticity, Antiaromaticity

Contents

1 Introduction **2**
- 1.1 Molecular electronics . . . 2
- 1.2 Room-temperature STM-BJ experiments . . . 3
- 1.3 STM LT-UHV experiments . . . 5
- 1.4 Theoretical background . . . 6
  - 1.4.1 Particle in a 1D box . . . 7
  - 1.4.2 Particle in a 2D box . . . 9
  - 1.4.3 Electron tunneling . . . 10
  - 1.4.4 Electron transmission through a double barrier . . . 12
- 1.5 Green's functions . . . 15
- 1.6 Tunneling: single level model . . . 18
- 1.7 Transmission calculations . . . 19
- 1.8 Electronic structure calculations . . . 20
- 1.9 Tight binding model . . . 20
  - 1.9.1 Benzene: molecular orbitals . . . 21
  - 1.9.2 Benzene: transmission spectra . . . 22
- 1.10 DFT based calculations . . . 25
  - 1.10.1 An example: DFT-based transmission through naphthalene 29
- 1.11 Summary of following chapters . . . 32

2 Donor-acceptor molecule on the Pt surface **33**
- 2.1 Introduction . . . 33
- 2.2 My contribution to the article . . . 37

3 Adsorption of a novel carbene molecule on the Au surface **59**
- 3.1 Introduction . . . 59
- 3.2 My contribution to the article . . . 61

4 Proposal for a biphenylene based molecular junction **83**
- 4.1 Introduction . . . 83
- 4.2 My contribution to the article . . . 86

5 Conductance of aromatic and antiaromatic molecules **103**
- 5.1 Introduction . . . 103
- 5.2 My contribution to article 1 . . . 106
- 5.3 My contribution to article 2 . . . 107

Conclusion **140**

Bibliography **142**

List of Figures **152**

List of Abbreviations **155**

1. Introduction

1.1 Molecular electronics

Molecular electronics is the field that describes the study and use of various organic molecules as active (transistors, molecular switches, etc.) and passive (rectifier, energy cell, etc.) electronic components. The versatility of molecules provides a variety of electrical, mechanical, and optical properties. Researchers in the field of molecular electronics is working towards condensing electronics functionalities into organic molecules by chemical design [1]. However, before molecular devices are fabricated, the single-molecule component must be characterized to understand their electronic properties. Single-molecule electronics expand the fundamental understanding of electron transfer mechanisms in organic molecules, which has significant consequences in chemistry and biology. Therefore, development in the field of molecular electronics is vital for fundamental scientific advancements.

A single-molecule junction consists of an organic molecule embedded between two electrodes. Early predictions by Aviram and Ratner suggested that such junctions assist the one-way flow of current (rectification) mediated by the molecule [2]. Their 1974 article "Molecular rectifiers" theoretically proposed that molecular devices made of a single organic molecule exhibit excellent rectification and demonstrated the potential of single-molecules in enabling electronic functionalities. Early experiments showed that while attempting to form single-molecule junctions, the problem of direct electrode contact formation was difficult to overcome. Later on, the employment of scanning tunneling microscopy (STM) in molecular electronics paved the way for the first single-molecule junction.

STM was first invented by physicists Gerd Binning and Heinrich Roher from the IBM research division[3, 4]. They demonstrated for the first time that the atomic-scale resolution of the surface could be obtained using tunneling through a vacuum nanogap. In STM, an atomically sharp tip (probe) is controlled by a material that expands and contracts reversibly with applied voltage (piezoelectric). The piezoelectric tip probing over a surface resolves images at atomic-scale precision. For this achievement, Gerd Binning and Heinrich Roher shared the Nobel Prize for physics with Ernst Ruska (for his contribution to electron microscopy) in 1986. Initially, STM was used in surface science to explore the properties of metal and semiconductor surfaces. In 1996, Bumm et al. used the tip of an STM to form a single-molecule junction consisting of a biphenyl-based molecule contacted by Au electrodes on either side [5]. The STM study by Bumm et al. is the first measurement of electronic characteristics of a single-molecule junction. They used the STM tip to measure the conductivity of the molecule by modulating the position of the STM tip and observing the change in current with respect to the tip position. Their result suggested that single-molecule could show current rectification, proving predictions by Aviram and Ratner that single-molecule electronics are feasible. In the beginning, the charge transport through saturated hydrocarbon chains such as fatty acids was puzzling as they were thought to be insulating. A breakthrough measurement of single-molecule transport came from Mark Reed's group at Yale University in collaboration with James Tour's group

at the University of South Carolina [6]. Their articles in the late 1990s and early 2000s advanced our understanding of single-molecule transport measurements and provided insights into the charge transport properties of various molecules [7–10]. Since then, significant advancements have been made in the field of single-molecule junctions [11–20]. Several chemical functionalizations called anchoring groups were studied and showed that many principles from chemistry could be utilized to control physics at molecular scale junctions [17]. Electronic components such as resistive wires and reversible switches were constructed using single-molecule circuits [21–24]. Beyond electronics, single-molecule junctions were also used to study mechanical, optical, and thermoelectric properties at molecular scale [25–28].

To understand single-molecule junctions, we must be familiarized with how a molecule conducts when placed between the electrodes. In this work, we will derive the transmission of electrons by resonant tunneling mechanism and, through that, the electron transport theory behind single-molecule junctions.

The content of this chapter is majorly inspired by "Molecular Electronics" by Juan Carlos Cuevas and Elke Scheer and "Quantum Transport: Atom to Transistor" by Supriyo Datta [29, 30].

Although the work I performed during my Ph.D. is theoretical, there are mentions of experimental studies of single-molecule junctions performed by our collaborators. We will present a brief overview of the most common experimental techniques in the following section.

1.2 Room-temperature STM-BJ experiments

In molecular electronics two main types of experiments employed are room-temperature experiments [5, 31–33] and low temperature experiments [6, 34–36]. Rather different scientific communities develop the two techniques. Chemists often practice room-temperature experiments investigating molecular properties under solution, and low-temperature experiments are performed mostly by physicists because of the tradition of surface science. We discuss both methods briefly in the following sections.

A molecular junction is formed by contacting the molecule by source and drain electrodes comprising a closed circuit. In air or solution, it is challenging to gain precise control over molecular contact at room-temperature. Therefore, a gap between electrodes is opened and closed repeatedly. In the presence of molecules, during some instances, the molecule bridges the gap. Such techniques are called break junction experiments as a large amount of data is collected. Statistical analysis is necessary to analyze the results obtained from break junction experiments. In electrochemical break junctions, the electrode gap is formed by passing a high current opening a pathway by electromigration [37]. The drawback of such a technique is that the possibility of residual nanocluster left in the gap disrupts the measurement. The commonly used break junction technique is the mechanically controlled break junction (MCBJ) technique, in which a nanogap is opened by a mechanically controlled pushing rod as shown in [38]. The MCBJ method is highly efficient in forming stable molecular junctions without any nanocluster formation.

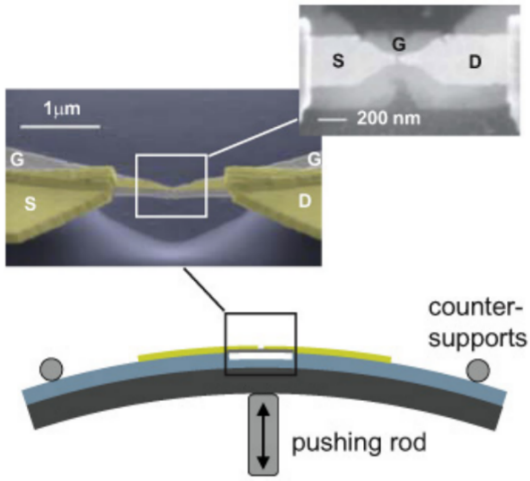

Figure 1.1: Mechanical break junction experiment (taken from Ref. [38]). The inset shows the sourse (S) and drain (D) of the electronic device, molecule can be tunned by gate electrode (G) in the background. The nanometer gap is controlled by mechanical motion through piezoelectric material (pushing rod).

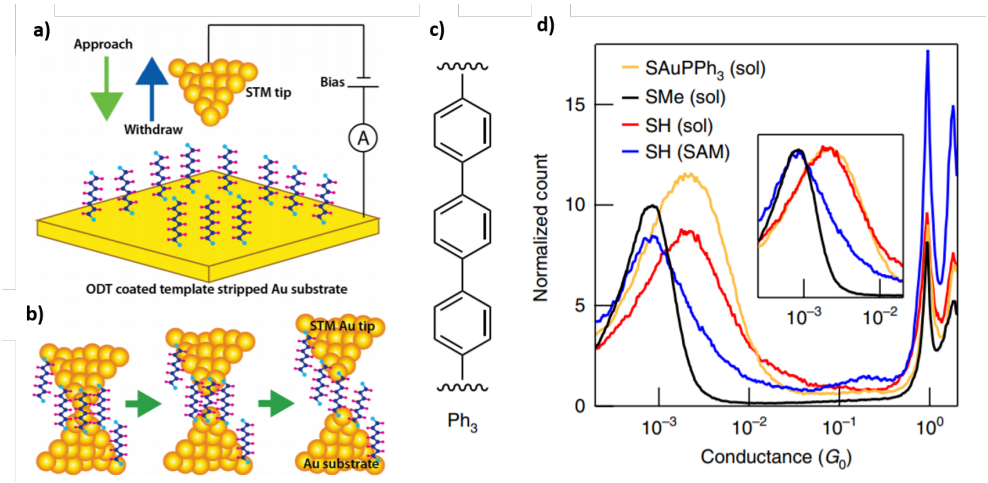

Figure 1.2: a) STM break junction experiment (taken from Ref. [39]) STM tip is pushed and pulled against a substrate containing molecules in solution while measuring current with respect to voltage. b) Graphics of a molecule filling the gap between electrodes during tip retraction c) chemical structure of a triphenyl molecule for which conductance histogram is shown in d). Histograms corresponds to change in chemical groups at metal-molecule interface. Figure c) and d) are adapted from Ref.[40]

In 2003, the break junction technique with scanning probe tip (STM-BJ) inside a solution of the target molecule was first reported [41]. The molecular junction is formed dynamically by crashing a Au tip is crashed on a Au surface, forming a Au-Au contact. The tip is retracted, and in certain instances, a molecule closes the gap. At every crashing and retracting cycle, the conductance is measured with respect to the tip distance, as shown in figure 1.2 a). During pulling, the gap formed between the electrodes is bridged by a molecule at certain instances, giving rise to a plateau in conductance instead of exponential conductance decay with increasing tip distance when there is no molecule in the gap. The experiment is repeated thousands of times, and conductance is plotted as a histogram. The histogram of conductance shows a peak corresponding to the conductance taking place through the molecule, as shown graphically in figure 1.2b). The maximum of the peak is the statistically most likely conductance value, which is interrupted as the conductance of the molecule at equilibrium. The broadness of the peaks corresponds to the change in molecular configuration during pulling and subsequent breaking of the molecule electrode contact. I-V characteristics of the junction can be recorded by repeating the experiment with different voltages.

In break junction experiments at room temperature, the molecular geometry cannot be controlled, but the presence of the molecule can be established by analyzing the statistical measurements and through inelastic tunneling spectroscopy (IETS) or shot-noise. Break junction techniques are powerful for building single-molecule junctions at room-temperature, but it is not straightforward to extract information about the structural and electronic properties of the junction. On the contrary, using low-temperature experiments, it is possible to obtain atomically precise geometry at the expense of a highly complex experimental setup.

1.3 STM LT-UHV experiments

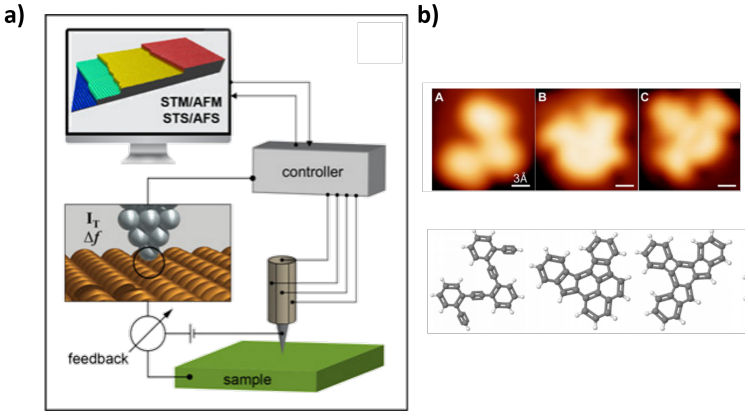

Figure 1.3: a) Experimental setup of STM (figure is taken from Ref.[42]). b) STM images of molecules (above) and chemical structure (below) (figure adapted from Ref.[43]).

Atomic resolution STM experiments are carried out at low temperatures, typically few K but could reach as low as few millikelvin (LT) and at ultra-high vacuum (UHV). The molecules are evaporated into the UHV chamber, often forming molecular films over the substrate, which act as the first electrode. The STM tip (or sample) is directly mounted over the surface on a piezoelectric element that controls the lateral position of the tip at nanometer precision. LT-STM operates in two basic modes, constant height, and constant current. In constant height mode, the height of the tip is fixed at a certain distance, and the change in current is measured along the plane of the sample. At constant current mode, an electronic feedback loop keeps the current constant by modulating the tip position vertically (Ref.1.3).

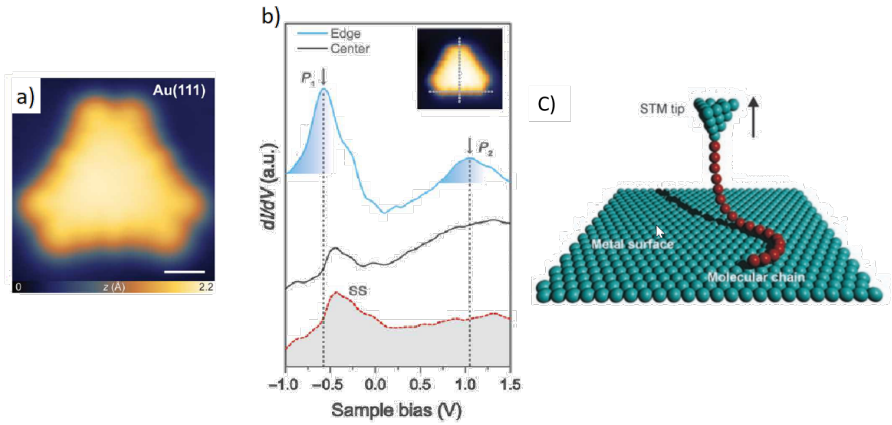

Figure 1.4: (a) STM images of a single triangulene on Au(111) surface. (b) dI/dV spectra measured over different sites of the triangulene molecule on the Au(111) substrate. dI/dV curves taken at the edge (blue) and at the center (black) of triangulene and measurment taken on the clean Au(111) surface (red) are shown. The figure is taken from [44]. c) A single molecule chain is lifted by a STM tip, the figure is taken from [36].

Using the STM setup, once the contact is established between the molecule on the surface and the tip electrode, the change in current with respect to the voltage (I-V) can be recorded. The first derivative current with respect to voltage gives the differential conductance of the single-molecule junction (dI/dV). It is the measurement of the energy of an electron tunneling through the molecule due to applied bias. The dI/dV spectrum is an approximate measurement of the density of the states (DOS) of the molecule, dI/dV measurements taken over the triangulene molecule are shown in 1.4 b). The low bias dI/dV measurements also give the conductance estimate of the molecule. In some cases, molecules can be contacted and sometimes lifted by the tip, thus creating a junction where the molecule is positioned vertically, bonded to both tip and sample [36]

1.4 Theoretical background

Quantum tunneling is the phenomenon in which a particle penetrates a potential energy barrier higher than the particle's energy. In a single-molecule junction,

conductance is mediated by electrons tunneling between two electrodes, where the molecule acts as a bridge. The height of the energy barrier is determined by the work function of the electrode and the chemistry of electrode molecule contact. Before we derive an expression for the energy of the incident electron and electron tunneling through a molecular bridge, we should first understand how an electron behaves inside the molecule. A particle in a box is a fundamental quantum mechanical approximation that describes an electron confined in a closed system. First, we will see how a quantum particle acts when confined in a 1D box, and then we will extend the derivation to the 2D case. These simple examples allow us to understand the energy levels of individual molecules fundamentally.

1.4.1 Particle in a 1D box

Let us consider a particle inside an infinitely deep 1D potential well of length L. The particle is represented by a wavefunction $\psi(x)$. By solving the Schrödinger equation, we obtained the values for ψ and allowed energies E. The modulus squared of the wavefunction ($|\psi(x)|^2$) gives the probability of locating the particle at a certain position within the box at a given position. Thus $\psi(x)$ is the probability amplitude and $|\psi(x)|^2$ is the probability distribution.

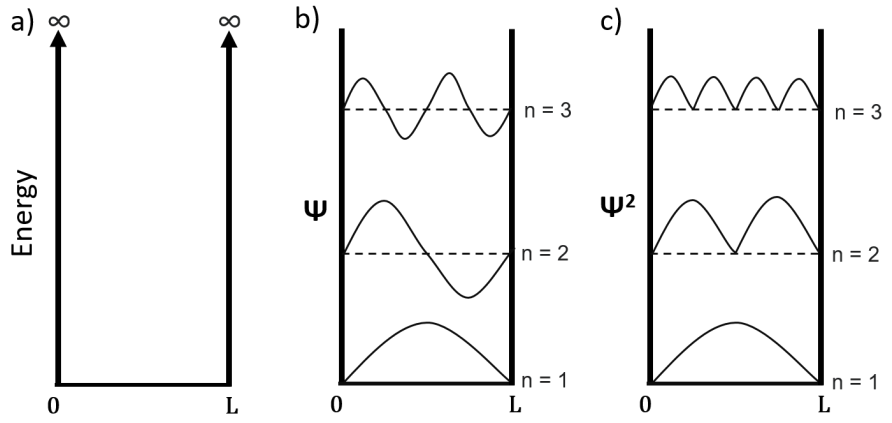

Figure 1.5: a) Quantum particle in a 1D box with potential energy walls of infinite height. b) Wavefunctions (ψ) at energies corresponding to first three (n = 1,2 3) principal quantum numbers. c) Probability density ψ^2 of the wavefunctions shown in b).

The time-independent Schrödinger equation for a free particle in a potential well is given as,

$$-\frac{\hbar^2}{2m}\frac{d^2\psi(x)}{dx^2} = E\psi(x), \tag{1.1}$$

where $\hbar$ is the reduced Planck constant ($\hbar = h/2\pi$). This equation has been well studied and gives a general solution,

$$\psi(x) = Asin(kx) + Bcos(kx), \tag{1.2}$$

where A, B and k are constants. Our boundary conditions are obtained from the fact that the probability of finding the particle at positions x = 0 and x = L is

zero. If we apply the value of x at the boundaries to the equation 1.2, we see that, when x = 0 the first term sin(0) = 0 and second term cos(0) = 1. Therefore, B = 0 is necessary to satisfy of boundary condition. Hence, equation 1.2 becomes,

$$\psi(x) = Asin(kx) \tag{1.3}$$

Differentiating the above equation twice with respect to x we get,

$$\frac{d^2\psi(x)}{dx^2} = -k^2 Asin(kx) \tag{1.4}$$

Substituting equation 1.3 to 1.4 we get,

$$\frac{d^2\psi(x)}{dx^2} = -k^2\psi(x) \tag{1.5}$$

Substituting to 1.1 and rearranging for k we get,

$$k = \left(\frac{8\pi^2 mE}{h^2}\right)^{1/2} \tag{1.6}$$

By plugging k to 1.3 we get the following equation for the wavefunction,

$$\psi(x) = Asin\left[\left(\frac{8\pi^2 mE}{h^2}\right)^{1/2} x\right] \tag{1.7}$$

To further simplify, we recall the boundary condition of $\psi = 0$ when x = L. Applying the condition to 1.7 we get,

$$0 = Asin\left[\left(\frac{8\pi^2 mE}{h^2}\right)^{1/2} L\right] \tag{1.8}$$

The above equation is true only when,

$$\left(\frac{8\pi^2 mE}{h^2}\right)^{1/2} L = n\pi, \tag{1.9}$$

where principal quantum number (n) is any positive (n = 1,2,3...) integer. The number n labels the allowed energies of the box. Substituting 1.9 to 1.7 the wavefunction becomes,

$$\psi_n(x) = Asin\left(\frac{n\pi}{L}x\right) \tag{1.10}$$

Solving equation 1.9 for E we get,

$$E_n = \frac{n^2 h^2}{8mL^2} \quad \text{for} \quad n = 1, 2, 3.. \tag{1.11}$$

Equations 1.10 and 1.11 are the solutions for wavefunction and energies of a particle confined in a 1D box. The wavefunction is determined by the principal quantum number and the length of the molecule. The normalization condition of the wavefunction defines A. We can see that the particle has discrete energy levels increasing along with the term n, also known as quantization of energy

levels. The lowest energy of the particle is non-zero, showing that the particle always has finite kinetic energy.

The wavefunctions ψ_n of the particle for n = 1,2 and 3 energy levels and the probability density ψ^2 are shown in figure1.5 b) and c). The number of nodes (intersections) in the wavefunction increases with increasing n. Next, we expand the derivation to 2D potential energy well.

1.4.2 Particle in a 2D box

Let us consider a particle confined in a 2D infinite potential well. The length and width of the well are given as L_x and L_y. The time-independent Schrödinger equation of the particle is,

$$-\frac{\hbar^2}{2m}\left(\frac{\partial^2\psi(x,y)}{\partial x^2}+\frac{\partial^2\psi(x,y)}{\partial y^2}\right)=E\psi \tag{1.12}$$

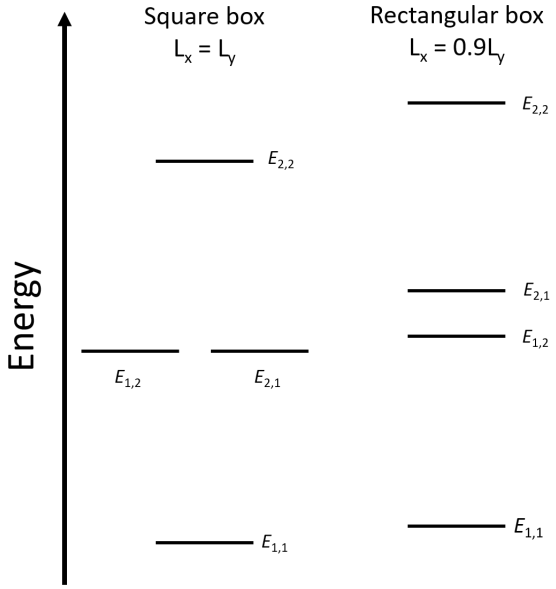

Figure 1.6: Energies plotted using equation 1.18 for 2D symmetric (square) box and asymmetric (rectangular) box. We can see that the symmetry gives rise to degeneracy of states i.e., there are two states at the same energy ($E_{1,2}$ and $E_{2,1}$).

The left side of the above equation is the sum of two independent terms. For equations of this form, according to separation of variables approach, the solution to the 2D term is the product of two 1D terms. Therefore, 2D wavefunction can be written as,

$$\psi(x,y)=\psi(x)\psi(y) \tag{1.13}$$

Similar to equation 1.2 the general solution to the time-independent Schrödinger equation for a particle in 2D potential well,

$$\psi(x)=A_x sin(k_x x)+B_x cos(k_x x) \tag{1.14}$$

$$\psi(y)=A_y sin(k_y y)+B_y cos(k_y y) \tag{1.15}$$

Like the boundary conditions of 1D box, the probability of finding the particle at boundaries is zero for 2D box too. Hence, B_X and B_y become zero. Then, we substitute equation 1.14 1.15 to 1.17 the wavefunction in 2D is,

$$\psi(x,y) = Nsin(k_x x)sin(k_y y), \tag{1.16}$$

where N is a constant, which will be set by the normalization condition. Slightly modifying and adapting equations 1.10 and 1.11 to 2D case we get the following expressions for wavefunction and energy of a 2D particle,

$$\psi(x,y) = Nsin\left(\frac{n_x \pi x}{L_x}\right) sin\left(\frac{n_y \pi y}{L_y}\right) \tag{1.17}$$

$$E_{nx,ny} = \frac{h^2}{8m}\left(\frac{n_x^2}{L_x} + \frac{n_y^2}{L_y}\right) \tag{1.18}$$

For symmetric 2D box of length $L_x = L_y =$ L, from equations 1.17 and 1.18 we can see that the wavefunction depends only on two variables n_x and n_y. In the ground state when $n_x = n_y = 1$ there is only one solution to the wavefunction. In fact, for all the energies when $n_x = n_y$ there can be only one wavefunction. But when $n_x \neq n_y$ there can be two wavefunctions with the same energy, this phenomenon is known as degeneracy. According to equation 1.18 the values $n_x = 1$, $n_y = 2$ and $n_x = 2$, $n_y = 1$ have the same energy,

$$E_{1,2} = E_{2,1} = \frac{5h^2}{8mL^2} \tag{1.19}$$

But the two wavefunctions corresponding to the energies are not the same $\psi(2,1)\psi(1,2)$. The degeneracy of the wavefunction occurs in the symmetric system, such as the square box we have considered. If the length of the 2D box is rectangular, the symmetry is broken, and there will be no degeneracy. In natural systems such as molecules, there can be multiple degenerate states depending on the degree of symmetry. The simple quantum-mechanical problem we just solved provides an insight into molecules' chemistry and electronic structure.

We have shown the behavior of a quantum particle (electron) inside a confined system (box). The following section will derive an expression for tunneling the particle (electron) through a barrier, the fundamental principle of single-molecule conductance.

1.4.3 Electron tunneling

To illustrate quantum tunneling, consider an electron incident on a potential barrier from the left side as shown in figure 1.8. Let E be the energy of the electron with mass m. The potential energy barrier has a height U and width a. At the boundaries of the potential energy wall, the electron wave is partly transmitted and partly reflected. The solution to the electron wave vector at regions 1, 2, and 3 as shown in figure 1.8 is,

$$\begin{aligned} \psi_1 &= A_+ e^{i\beta x} + A_- e^{-i\beta x} \\ \psi_2 &= B_+ e^{-\alpha x} + B_- e^{\alpha x} \\ \psi_3 &= C_+ e^{i\beta x} \end{aligned} \tag{1.20}$$

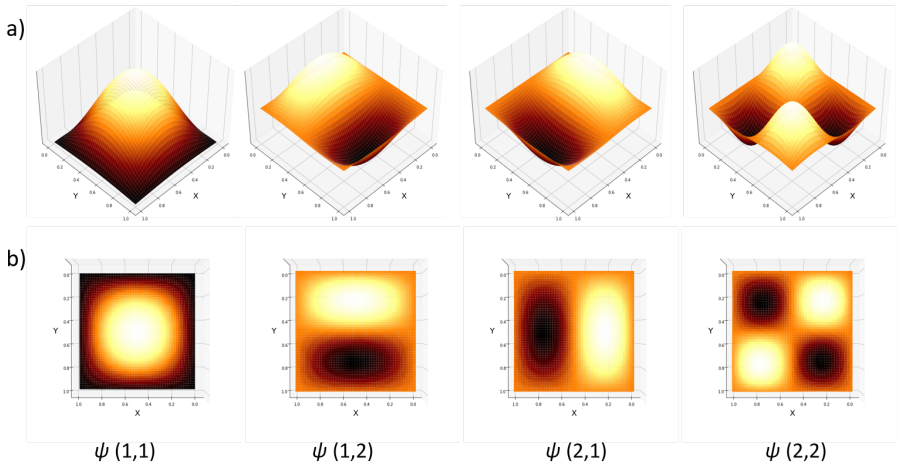

Figure 1.7: Wavefunction of the first four states of a particle in a symmetric 2D box plotted with equation 1.17. a) 3D plot with z axis showing the energy. x and y directions are the box dimension, b) projection of panel a) over x and y planes. We can see the increase in number of nodes with increasing n. States $\psi(1,2)$ and $\psi(2,1)$ are degenerate, rotated with respect to each other by 90°.

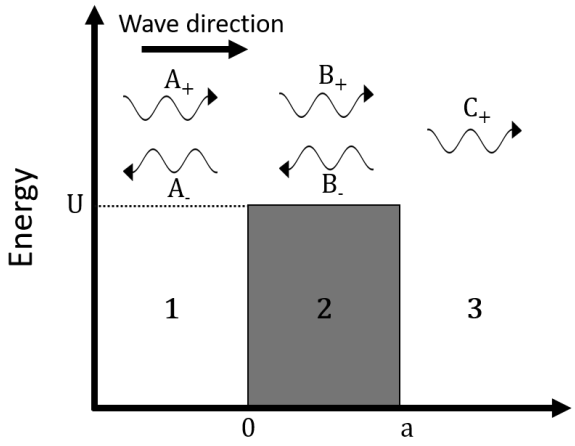

Figure 1.8: Illustration of an electron passing a rectangular potential barrier of height U and width a. A, B and C are the coefficients of the electron wave vector. + and - indicate incoming and outgoing waves respectively.

α and β are a wave number and the complex exponent denotes oscillations. There is no reflection in region 3 because the electron is travelling from left to right. Using the relation that the wavefunction and its derivative are continuous at the boundaries of the barriers we can write the boundary conditions as,

$$\begin{aligned} &A_+ + A_- = B_+ + B_- \\ &-i\beta(A_+ - A_-) = \alpha(B_+ - B_-) \\ &B_+ e^{-i\alpha a} + B_- e^{i\alpha a} = C_+ e^{i\beta a} \\ &\alpha(B_- e^{\alpha a} - B_+ e^{-\alpha a}) = i\beta C_+ e^{\alpha a} \end{aligned} \tag{1.21}$$

We substitute reflection (r) and transmission (t) coefficients explicitly to the above conditions, we get, $A_+ = 1$, $C_+ =$ t and $A_- =$ r. Rearranging 1.21 we obtain the following expressions for transmission (t) and reflection (r),

$$t = \frac{4\alpha\beta e^{ia(\beta-\alpha)}}{(\alpha+\beta)^2 - e^{2ia\alpha}(\beta-\alpha)^2} \tag{1.22}$$

$$r = \frac{(\beta^2 - \alpha^2)\ sin(a\alpha)}{2i\beta\alpha\ cos(a\alpha) + (\alpha^2+\beta^2)\ sin(a\alpha)} \tag{1.23}$$

$$\alpha = \sqrt{\frac{\pm 2m(E-U)}{\hbar^2}},\ \beta = \sqrt{\frac{2mE}{\hbar^2}}, \tag{1.24}$$

Substituting equation 1.28 in 1.22 we get the transmission coefficient T as a function of energy (E) of the particle. For particle energy lower that the barrier (E < U) T is,

$$T(E) = |t|^2 = \frac{4E(U-E)}{4E(U-E) + U^2\ sinh^2(\alpha a)}, E < U \tag{1.25}$$

Similarly the transmission coefficient for E > U is,

$$T(E) = |t|^2 = \frac{4E(E-U)}{4E(E-U) + U^2\ sin^2(\alpha a)}, E > U \tag{1.26}$$

The length and energy dependence of the transmission of this potential energy barrier is shown in fig 1.9. The important feature is that $T > 0$ for E < U increases exponentially. This decay is given by T $\propto$ exp(-αa), i.e., slopes in figure 1.9 b) are mainly determined by the square root of the difference between the electron energy and the barrier height. Since transmission determines a device's conductivity, this model explains exponential decay of conductance with the distance between the electrodes in a tunnel junction. The model also explains the importance of the barrier height, which is the difference between the conducting frontier orbitals at the junction and the Fermi energy of the electrode for single-molecule junctions.

1.4.4 Electron transmission through a double barrier

In the previous section, we derived an expression for the transmission of an electron passing through a barrier. Nevertheless, in a molecular device, as we will see

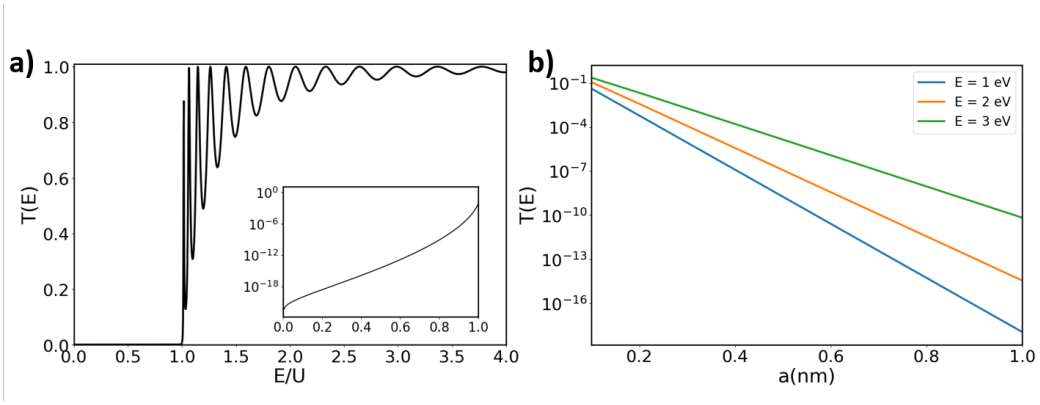

Figure 1.9: a) Transmission probability as a function of energy plotted using equations 1.26 and 1.25. When E < U (inset) transmission increases exponentially with with the energy of the particle. b) Transmission is plotted as a function of the length of the potential barrier showing exponential decay with length. The height of potential energy barrier U is fixed at 4 eV (i.e., E < U).

the barrier is the link between a molecule and the electrode, usually the molecule trapped between two electrodes leading to two barriers. This scenario is similar to an electron passing through two potential barriers. An illustration of an electron incident from the left to the right side of a double potential barrier is shown in 1.10. Similar to equation 1.20 of single barrier, the wave vector has five different solutions at five regions described as,

$$\begin{aligned}
\psi_1 &= A_+ e^{i\beta x} + A_- e^{-i\beta x} \\
\psi_2 &= B_+ e^{-\alpha x} + B_- e^{\alpha x} \\
\psi_3 &= C_+ e^{i\beta x} + C_- e^{-i\beta x} \\
\psi_4 &= D_+ e^{-\alpha x} + D_- e^{\alpha x} \\
\psi_5 &= E_+ e^{i\beta x}
\end{aligned} \tag{1.27}$$

$$\alpha = \sqrt{\frac{\pm 2m(E-U)}{\hbar^2}},\ \beta = \sqrt{\frac{2mE}{\hbar^2}}, \tag{1.28}$$

where α and β are wavenumbers. Both potential energy barriers have a height U and width a. L is the distance between the barriers as shown in figure 1.10. We solve the transmission coefficient with respect to the energy of the electron using equations 1.20, 1.28, and the boundary conditions. The transmission coefficient for the electron with E < U through a double potential barrier is,

$$T(E) = |t|^2 = \frac{1}{(2G^2-1)^2 + 4S^2\,G^2} \tag{1.29}$$

$$G = cosh(\beta a)\ cos(\alpha L) - \zeta\ sinh(\beta a)\ sin(\alpha L) \tag{1.30}$$

$$S = cosh(\beta a)\ sin(\alpha L) + \zeta\ sinh(\beta a)\ cos(\alpha L) \tag{1.31}$$

$$and\ \zeta = \frac{\alpha^2 - \beta^2}{2\alpha\beta} \tag{1.32}$$

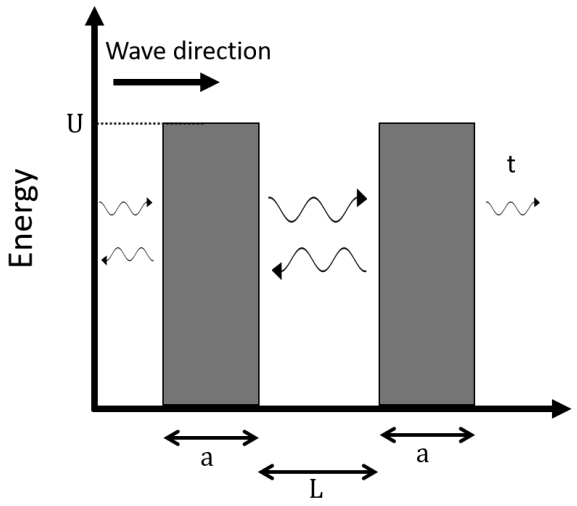

Figure 1.10: Illustration of an electron passing two symmetric potential barriers of height U and width a. The distance between the two barriers is L.

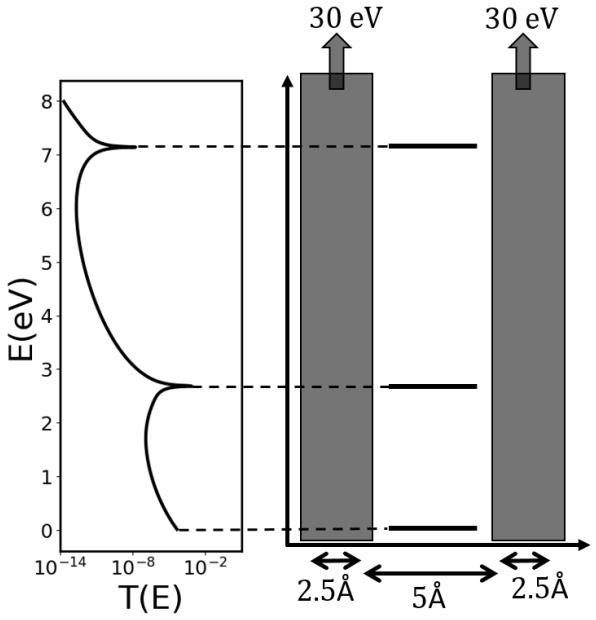

Figure 1.11: Transmission probability vs energy plotted using equations 1.29, showing enhanced tunneling coefficients at specific energies, the energy axis is in log scale. The corresponding states between the double potential barrier are also shown.

The transmission coefficient with respect to the energy of an incident electron is plotted using equation 1.11. The parameters used are U = 30 eV and a = 2.5 Å, and L = 5 Å. From figure 1.11 we see enhanced transmission at energies 0 eV, 2.6 eV and 7.1 eV. Similar energies can be obtained from equation 1.11 which gives energies for infinite potential well, proving its resemblance to the double potential barrier. We see that the peaks in transmission match these energies. The main finding is that when the incident electron's energy matches the energies of the allowed states in the well, transmission is enhanced $T \approx 1$. This is known as resonant transport. When the energy does not match these states, a condition known as non-resonant tunneling occurs where transmission is substantially lowered. As we will see, this behavior is seen in molecular conductance.

1.5 Green's functions

It is challenging to calculate the transmission of real systems such as molecular junctions where there are many electrons and energy levels. Green's functions are mathematical techniques used to obtain many physical properties of a system. In the context of the thesis, we use Green's functions to calculate the transmission spectra and electrical current in a single-molecule junction. Following Schrodinger's equation, Green's function G can be written as,

$$(E - H)G(E) = I \tag{1.33}$$

The Hamiltonian (H) of a single-molecule junction consists of device region (H_d), left electrode (H_L) and right electrode (H_R). The off diagonal terms which define the interaction of the device region to the left and right electrodes are t_L and t_R respectively († represents complex conjugate). Then 1.33 can be expanded as [45],

$$\begin{pmatrix} E - H_L & -t_L & 0 \\ -t_L^\dagger & E - H_d & -t_R^\dagger \\ 0 & -t_R & E - H_R \end{pmatrix} \begin{pmatrix} G_{LL} & G_{Ld} & G_{LR} \\ G_{Ld} & G_d & G_{Rd} \\ G_{RL} & G_{Rd} & G_{RR} \end{pmatrix} = \begin{pmatrix} 1 & 0 & 0 \\ 0 & 1 & 0 \\ 0 & 0 & 1 \end{pmatrix} \tag{1.34}$$

As there is no interaction between left and right electrodes by construction, the terms G_{LR} and G_{RL} are zero. The three linear equation from the middle column of the Green's function matrix are,

$$\begin{aligned} &(E - H_L)G_{Ld} - t_L G_d = 0 \\ &-t_L^\dagger G_{Ld} + (E - H_d)G_d - t_R^\dagger G_{Rd} = 1 \\ &-t_R G_d + (E - H_R)G_{Rd} = 0 \end{aligned} \tag{1.35}$$

Substituting the first and third equations into the second one,

$$\frac{-t_L^\dagger t_L}{E - H_L} G_d + (E - H_d)G_d - \frac{t_R^\dagger t_R}{E - H_R} G_d = 1 \tag{1.36}$$

According to the definition of Green's function, $(E - H_L)g_L = I$ and $(E - H_R)g_R = I$ are the Green's function of the isolated contacts. Substituting g_L and g_R to equation 1.36 we get,

$$-t_L^\dagger g_L t_L G_d + (E - H_d)G_d - t_R^\dagger g_R t_R G_d = 1 \tag{1.37}$$

The term G_d above is the retarded Green's function of the junction which corresponds to the incoming wave, which can also be written as G_d^r. The complex conjugate of the $G_d^\dagger$ is called advanced Green's function G_d^a which corresponds to the outgoing wave. Substituting $\Sigma_L(E) = -t_L^\dagger g_L t_L$ and $\Sigma_R(E) = t_R^\dagger g_R t_R$ to the equation 1.37 we get,

$$G_d = (E - H_d - \Sigma_L(E) - \Sigma_R(E))^{-1} \tag{1.38}$$

The above equation allows us to calculate many physical properties of a system. Using Green's functions, we can calculate the density of states, transmission, and electrical current of the single-molecule junction. We should be careful in calculating the terms Σ_L and Σ_R, which are called the self-energies of the electrodes. They are independent of the device region and can be calculated with the periodicity of the electrode. They mimic the effect of coupling to semi-infinite electrodes when in fact finite slabs are used.

We will discuss the calculation of electrical current with Green's function in the following section.

Electrical current

Let an external perturbation $|v\rangle$ be applied to the system [45]. The Green's function gives the linear response to the applied perturbation to Schrodinger's equation.

$$(E - H)\,|\psi\rangle = E\,|\psi\rangle + |v\rangle \tag{1.39}$$

$$|\psi\rangle = -G(E)\,|v\rangle \tag{1.40}$$

In case of single-molecule circuit, the bias difference between the two electrodes can inject electrons into the device, it is a non-equilibrium problem. To solve this we first calculate the wavefunction $|\psi_L\rangle$ of the incoming wave from the left electrode. Using relation 1.40, the device wave $|\psi_d\rangle$ function can be written in terms of the incoming wave $|\psi_L\rangle$ is,

$$|\psi_d\rangle = -G_d t_L^\dagger\,|\psi_L\rangle\,, \tag{1.41}$$

where $t_L^\dagger$ is the coupling term of the left electrode to the device. Similarly, the wave entering from device to the right electrode is given by,

$$|\psi_R\rangle = g_R t_R^\dagger\,|\psi_d\rangle \tag{1.42}$$

To get the wavefunction of the left electrode we need to add the incoming wave the the relation. Then $|\psi_L\rangle$ becomes,

$$|\psi_L\rangle = |\psi_L\rangle + g_L t_L\,|\psi_d\rangle \tag{1.43}$$

Substituting equation 1.41 to 1.42 and 1.43 we get,

$$|\psi_R\rangle = -g_R t_R^\dagger G_d t_L^\dagger\,|\psi_L\rangle \tag{1.44}$$

$$|\psi_L\rangle = \left(1 + g_L t_L G_d t_L^\dagger\right) |\psi_L\rangle \tag{1.45}$$

Before deriving the current, we need an expression for the spectral function in terms of the Green's function. It is given as,

$$A = i(G - G^\dagger) \tag{1.46}$$

Expanding the spectral function in an eigenbasis leads to the following,

$$A = 2\pi \sum_k \delta(E - \epsilon_k) \left|k\right\rangle \left\langle k\right|, \tag{1.47}$$

where ϵ_k are the eigenvectors, $|k\rangle$ are the corresponding eigenvalues of Hamiltonian, and δ is the delta function.

For any arbitrary contact j, the electrical current is given as,

$$i_j = -\frac{ie}{\hbar} \left(\left\langle \psi_j \right| t_j \left|\psi_d\right\rangle - \left\langle \psi_d | \psi_j \right\rangle\right) \tag{1.48}$$

The above equation generalizes the electric current as a product of charge and the probability current. Extending the idea to the single-molecule junction, the current flowing from contact L to R is given by, substituting 1.41, 1.45 and 1.44 to equation 1.48.

$$i_R = -\frac{ie}{\hbar} \left(\left\langle \psi_R \right| t_j \left|\psi_d\right\rangle - \left\langle \psi_d | \psi_R \right\rangle\right) \tag{1.49}$$

$$= -\frac{ie}{\hbar} \left(\left\langle \psi_L \right| t_L G_d^\dagger t_R^\dagger (g_R^\dagger - g_R) t_R G_d t_L^\dagger \left|\psi_L\right\rangle\right) \tag{1.50}$$

We introduce a new term $\Gamma_R = t_R^\dagger (g_R^\dagger - g_R) t_R = t_R^\dagger (a_R) t_R$, where a_R is the spectral function of the right electrode. Γ_R gives the coupling of right contact to the device.

$$i_R = -\frac{ie}{\hbar} \left(\left\langle \psi_L \right| t_L G_d^\dagger \Gamma_R G_d t_L^\dagger \left|\psi_L\right\rangle\right) \tag{1.51}$$

Integrating i_R over the whole energy range gives the total current (I). The incoming wave ψ_L has several modes in the contact; hence the summation over all principal quantum numbers n is required.

$$I = \frac{2e}{\hbar} \int_{E=-\infty}^{\infty} dE \sum_n \delta(E - E_n) \left(\left\langle \psi_{L,n} \right| t_L G_d^\dagger \Gamma_R G_d t_L^\dagger \left|\psi_{L,n}\right\rangle\right) \tag{1.52}$$

$$= \frac{2e}{\hbar} \int_{E=-\infty}^{\infty} dE f(E, \mu_1) \sum_{m,n} \delta(E - E_n) \left(\left\langle \psi_{L,n} \right| t_L \left|m\right\rangle \left\langle m\right| G_d^\dagger \Gamma_R G_d t_L^\dagger \left|\psi_{L,n}\right\rangle\right) \tag{1.53}$$

$$= \frac{2e}{\hbar} \int_{E=-\infty}^{\infty} dE f(E, \mu_1) \sum_m \left(\left\langle m \right| G_d^\dagger \Gamma_R G_d (t_L \frac{a_L}{2\pi} t_L^\dagger) \left|m\right\rangle\right), \tag{1.54}$$

where a_L is the spectral function of left contact described as,

$$a_L = 2\pi \sum_n \delta(E - E_n) \langle \psi_{L,n} | \psi_{L,n} \rangle$$

Substituting $\Gamma_L = t_L^\dagger (g_L^\dagger - g_L) t_L = t_L^\dagger (a_L) t_L$ into equation 1.54 we get,

$$I = \frac{2e}{\hbar} \int_{-\infty}^{\infty} dE f(E, \mu_1) \sum_m \left(\langle m | G_d^\dagger \Gamma_R G_d \Gamma_L) | m \rangle \right) \tag{1.55}$$

Subtracting the incoming wave from the right contact to 1.55 we get,

$$I = \frac{e}{\pi\hbar} \int_{-\infty}^{\infty} dE \left[f(E, \mu_L) - f(E, \mu_R) \right] Tr(G_d^\dagger \Gamma_R G_d \Gamma_L) \tag{1.56}$$

The above equation is the Landauer equation for current. It describes the total current through a molecular junction as the sum of all the transmission probabilities of an electron between occupied and empty states given by the Fermi function of the electrodes. Using Green's function and coupling to the electrode terms, the transmission as a function of energy can be calculated as,

$$T(E) = Tr(G_d^\dagger(E) \Gamma_R(E) G_d(E) \Gamma_L(E)) \tag{1.57}$$

Dependence on voltage (V) is implicit in all the terms. Landauer pioneered the theory of electronic transport as a framework for understanding electrical conductance. He emphasized the fundamental connection as "Conductance is transmission." The Fermi distribution function of left and right electrode become step function at 0K. Then the conductance G = I/V at the Fermi energy is derived from equation 1.56 as,

$$G = \frac{2e^2}{h} T(E_F) \tag{1.58}$$

The above expression shows that for a tunnel junction such as a single-molecule circuit, the maximum conductance of a single transmission eigenchannel is $G = 2e^2/h$. The value $G = 2e^2/h$ is a constant also known as the conductance quantum G_0. Another feature is that the tunnel junction will always have a finite resistance ($1/G_0 = h/2e^2$) even when transmission is maximal ($T(E_F) = 1$). The relationship between transmission and Green's function is the foundation of several ab-initio based molecular transport calculations. In this work, we use SIESTA Density Functional Theory (DFT) software coupled with the TranSIESTA transport code to calculate the transmission spectra and the related properties [46, 47].

1.6 Tunneling: single level model

In single-molecule junctions, the gap between barriers is bridged by an organic molecule. Now, looking at figure 1.12 (b), an electron incident from one of the electrodes is transmitted non-resonantly through a frontier molecular level.

Transmission with respect to energy is similar to the one we derived for transmission to a barrier in equation 1.25. The energy of the conducting molecular resonance measured from the Fermi level ($E_F = 0$) is ϵ_0. The Γ_L and Γ_R are the

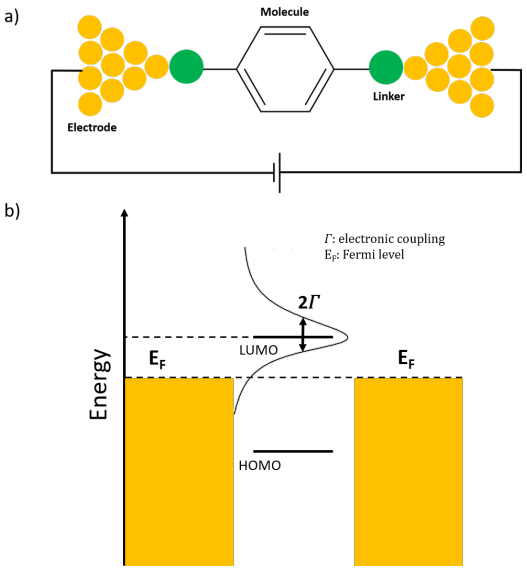

Figure 1.12: a) A prototypical single-molecule circuit. b) Illustration of molecular discrete energy state coupling to the metal Fermi level.

scattering rates of the molecule to the left and right electrodes, respectively. The transmission as a function of energy is given by,

$$T(E,V) = \frac{4\Gamma_L\Gamma_R}{(E-\epsilon_0(V))^2 + (\Gamma_L+\Gamma_R)^2} \tag{1.59}$$

The above equation 1.59 is called the Breit-Wigner formula. Transmission is a Lorentian where $\epsilon_0(V)$ gives the peak position, and width is determined by coupling to the electrodes Γ_L and Γ_R, usually, transmission is calculated at zero bias (V = 0).

1.7 Transmission calculations

The single-level model is a simple case where the electron transmission is happening through a single energy level. In real systems such as molecular junctions, there are many energy levels, and the transmission spectrum is calculated from Green's function and coupling to the electrodes as given in equation 1.57. The Green's function is calculated in terms of the device Hamiltonian (H_d) and self-energies (Σ_L and Σ_R) as shown in equation 1.38. The device Hamiltonian includes the geometry of the molecule and surface layers. The self-energies represent the electrodes as semi-infinite contacts, which is a simplification used to calculate the transport of molecular junctions. The simplification is called wide-band approximation, which assumes that the detailed description of the electronic structure of the leads is not vital for the transport calculations, which simplifies the computation.

1.8 Electronic structure calculations

In the previous section, we outlined the methods to calculate the electron transport properties of the single-molecule junction. We need to describe the electronic structure of the single-molecule junction to determine the Hamiltonians and subsequently Green's function. There are various methods to calculate the electronic structure. First, we will discuss the tight-binding method, which is an approximate but easily accessible and intuitive method to understand the physics behind the molecule's electronic structure connected to the electrode. To develop a more accurate description of the electronic structure, we need DFT. We will see the DFT in the section after the tight-binding method.

1.9 Tight binding model

In a tight-binding model, electrons are represented by localized orbitals, where the electrons are confined around the atomic centers (nuclei). The main advantage of the tight-binding model is the simplicity of the model, and for example, a meaningful physical picture can be obtained from a simple model in which we consider only one π electron per atom. The Linear Combination of Atomic Orbital (LCAO) is a popular localized orbital method in quantum chemistry to calculate molecular electronic structure. In this method, the Hamiltonian $\mathbf{H}$ of a system is constructed with the atoms given by their positions $\mathbf{R_i}$. The diagonal elements of $\mathbf{H}$ are the onsite energy of the orbitals, and off-diagonal terms constitute the hopping term or interaction energy between the orbitals. The elements of $\mathbf{H}$ can be obtained either from many approximations such as fitting experimental data or other theoretical calculations.

We consider free electron model, ie., there is no electron-electron interaction. In the LCAO approach the single particle Hamiltonian using the tight-binding $\mathbf{H}$ approach takes the following form,

$$\mathbf{H} = \sum_{ij,\alpha\beta} H_{i\alpha,j\beta} \left|i\alpha\right\rangle \left\langle j\beta\right|, \tag{1.60}$$

where $|i\alpha\rangle$ is the localised orbital α. The localized atomic orbital around site $\mathbf{R_i}$ is, $\phi_{i\alpha}(\vec{r}) = \phi_\alpha(\mathbf{r} - \mathbf{R_i})$. For an isolated molecule, the wavefunction in a tight-binding representation can be determined as a combination of atomic orbitals.

$$\Psi(\vec{r}) = \sum_{j\beta} c_{i\alpha,j\beta}\phi_{j\beta}(\vec{r}), \tag{1.61}$$

where $c_{i\alpha,j\beta}$ is the wavefunction coefficient. Subsequently, we get the following equation to determine the coefficients,

$$\sum_{j\beta} \left[H_{i\alpha,j\beta} - ES_{i\alpha,j\beta}\right] c_{i\alpha,j\beta} = 0, \tag{1.62}$$

where E is the energy, and S is the overlap matrix between the states $|i\alpha\rangle$ and $|j\beta\rangle$. The eigenvalue and eigenvectors of equation 1.62 give us the energies of molecular state and wavefunction coefficients of atomic orbitals at the corresponding states. The solution of the equation can be obtained with the following matrix determinant form,

$$det(\mathbf{H} - E\mathbf{S}) = 0 \tag{1.63}$$

In any electronic structure calculation, the matrix dimension equals the number of orbitals we consider to represent in the system. The electronic structure of a small molecule can be analytically solved using the tight-binding model. We will consider a benzene molecule with six carbon atoms in the following example. We use a simplified basis set of one π electron per orbital.

1.9.1 Benzene: molecular orbitals

Let us assume a benzene molecule as a hexagon with each vertex representing a carbon atom with energy ϵ_0 as shown in figure 1.13 a). We consider one π orbital per carbon site, a carbon site is interacting only with the two neighboring carbon atoms via a hopping term t. The off-diagonal neighbor interaction H_{ij} is a bonding term which is negative, therefore, use $t > 0$ and we write $H_{ij} = -t$. We consider an orthonormal basis i.e, $S_{ij} = \delta_{ij}$. Following equation 1.62 the molecular states and molecular orbitals are obtained by solving the following secular determinant,

$$\begin{vmatrix} \epsilon_0 - E & -t & 0 & 0 & 0 & -t \\ -t & \epsilon_0 - E & -t & 0 & 0 & 0 \\ 0 & -t & \epsilon_0 - E & -t & 0 & 0 \\ 0 & 0 & -t & \epsilon_0 - E & -t & 0 \\ 0 & 0 & 0 & -t & \epsilon_0 - E & -t \\ -t & 0 & 0 & 0 & -t & \epsilon_0 - E \end{vmatrix} = 0 \tag{1.64}$$

Solving 1.64 the eigenvalues of the molecule are,

$$\begin{aligned} E_1 &= \epsilon_0 - 2t \\ E_2 &= E_3 = \epsilon_0 - t \\ E_4 &= E_5 = \epsilon_0 + t \\ E_6 &= \epsilon_0 + 2t \end{aligned} \tag{1.65}$$

The molecular orbitals or the eigenvectors of the corresponding states are,

$$\begin{aligned} \phi_1 &= \frac{1}{\sqrt{6}}(|1\rangle + |2\rangle + |3\rangle + |4\rangle + |5\rangle + |6\rangle) \\ \phi_2 &= \frac{1}{\sqrt{4}}(|2\rangle + |3\rangle - |5\rangle - |6\rangle) \\ \phi_3 &= \frac{1}{\sqrt{12}}(2\,|1\rangle + |2\rangle + |3\rangle - 2\,|4\rangle - |5\rangle - |6\rangle) \\ \phi_4 &= \frac{1}{\sqrt{4}}(|2\rangle - |3\rangle + |5\rangle - |6\rangle) \\ \phi_5 &= \frac{1}{\sqrt{12}}(2\,|1\rangle - |2\rangle - |3\rangle + 2\,|4\rangle - |5\rangle - |6\rangle) \\ \phi_6 &= \frac{1}{\sqrt{6}}(|1\rangle - |2\rangle + |3\rangle - |4\rangle + |5\rangle - |6\rangle) \end{aligned} \tag{1.66}$$

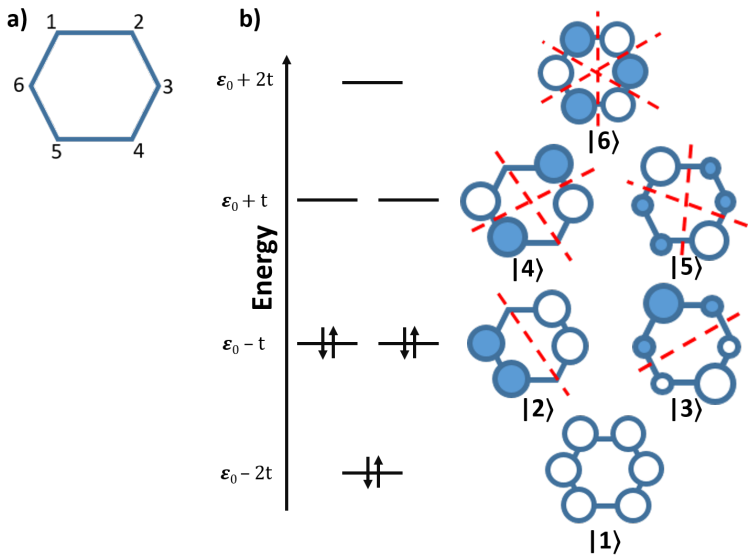

Figure 1.13: a) Benzene molecule represented as a hexagon, each corner is a carbon site b) Molecular orbitals and energy level diagram of benzene obtained with onsite energy $\epsilon_0 = 0$ and hopping energy $t = 1$. The solid circles on the hexagon are positive, and the hollow circles are the negative amplitude of the wavefunction. Red dashed lines show nodal planes.

Even this simple tight-binding model gives us an insight into many valuable features of the electronic structure. We can see from 1.13 b) that the confinement is similar to what we saw in the example of a particle in a box. The red dotted line denotes the nodal planes of the molecular orbitals. State $|1\rangle$ has zero nodal planes. The highest occupied molecular orbital $|2\rangle$ $|3\rangle$ (HOMO) and lowest unoccupied molecular orbital $|4\rangle$ $|5\rangle$ (LUMO) are both doubly degenerate in benzene. HOMO states have one nodal plane, and LUMO states have two nodal planes. The highest energy state $|6\rangle$ has three nodal planes.

From the analytical solution of the benzene molecule, we can see that tight-binding is a valuable tool for understanding the molecular electronic structure with simple approximations. However, we use DFT for a more accurate description, where all the parameters are calculated from the first principles.

1.9.2 Benzene: transmission spectra

Electronic structure calculated from a simple tight-binding model can be used to understand many physical properties. We will mention one such property in this section. Several quantum phenomena appear due to the quantum nature of the electrons. An example is a quantum interference (QI). We illustrate it here by changing the attachment points of benzene. In cyclic molecules, we can see the suppression of transmission at certain energies. This phenomenon is known as quantum interference. We calculated the destructive quantum interference (DQI) feature by theoretically changing the connectivity of a molecule to the electrode. We calculated transmission spectra for benzene molecule with equation 1.57, we used the simple tight-binding Hamiltonian similar to equation 1.64. We calculate the retarded Green's function by following the equation 1.38 as,

$$G_d(E) = \begin{bmatrix} E-\epsilon_0+i\frac{\Gamma_L}{2} & -t & 0 & 0 & 0 & -t \\ -t & E-\epsilon_0 & -t & 0 & 0 & 0 \\ 0 & -t & E-\epsilon_0 & -t & 0 & 0 \\ 0 & 0 & -t & E-\epsilon_0+i\frac{\Gamma_R}{2} & -t & 0 \\ 0 & 0 & 0 & -t & E-\epsilon_0 & -t \\ -t & 0 & 0 & 0 & -t & E-\epsilon_0 \end{bmatrix}^{-1}, \quad (1.67)$$

where ϵ_0 and t are the onsite energy and hopping term respectively. In the simplest approximation, the self-energies of left and right electrodes are described by a constant imaginary term $\Sigma_{L,R} = -i\frac{\Gamma_{L,R}}{2}$ added to the onsite energy of contact atoms. In equation 1.14 the Green's function for benzene molecule with linkers at para position is shown, the self-energy term is added to the carbon atoms at 1,4 position of the molecule. Similarly, the Green's functions of ortho and meta connections are calculated by adding the self-energy terms to the respective contacts.

Using the equations 1.67 and 1.57 we calculated the transmission spectra for ortho, meta, and para configurations of the benzene molecule. The interaction with the neighboring atoms is set as t = 1 eV, and the onsite energy of the atoms was set to zero (ϵ_0=0). Same coupling parameter was use for left and right electrodes ($\Gamma_{L,R}$ = 0.5 eV). The three possible connectives of a benzene molecule to two electrodes are meta, para, and ortho configurations. The transmission spectrum of the molecule connected at the meta position shows DQI at E = 0 as shown in figure 1.14.

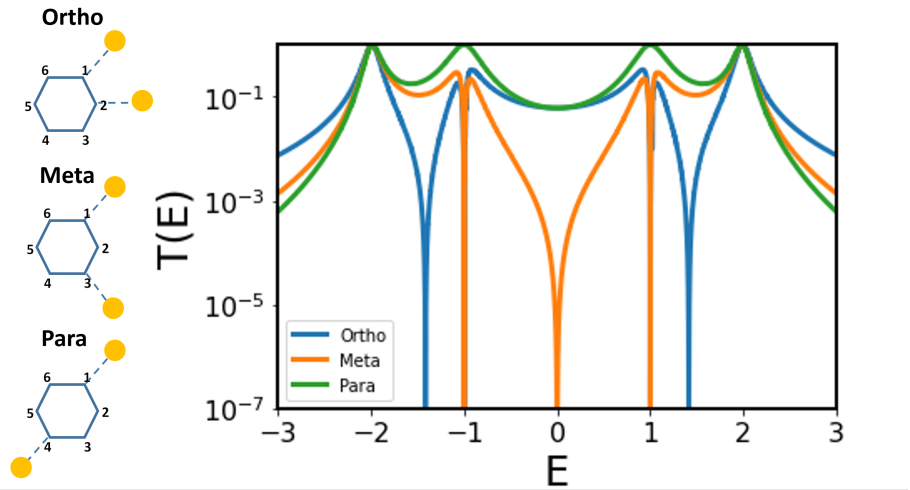

Figure 1.14: Transmission spectra plotted using equation 1.57. Hamiltonian of the molecule is from the tight-binding model show in equation 1.64. The molecule is connected to the electrodes via meta, para and ortho positions.

The tight-binding approach is computationally efficient. However, the accuracy of these calculations depends on the quality of the parameters we use in the calculation. The parameters can be obtained from experiments or ab-initio theory calculations such as DFT.

Destructive quantum interference (DQI)

The presence/absence of DQI features in the transmission spectra of the conjugated systems is widely studied in the literature. Several guidelines based on graphical rules [48], connectivity [49] and phase of wavefunction coefficient at contact point have been proposed to predict the DQI features. The graphical rule of Markussen et al. [48] predicts where DQI features can be expected. In the Markussen et al. graphical rule, the contact points are connected by a continuous path and the remaining sites are paired. If a connection or paring is not possible for a particular site, the DQI feature appears. In figure 1.15 we see that in molecules CC1 and CC2, there is an isolated site marked by a green spot leading to quantum interference. For molecule CC3, all the sites can be either connected or paired; therefore, no DQI feature appears. Those findings are supported by DFT calculations. Since then, the graphical rule was tested and proved in various systems, notably in thiophene molecule [50–53]. The molecular orbital rule predicts the presence/absence of DQI feature with the relative phase of HOMO-LUMO orbitals [54, 55]. The molecular orbital rule and its implications are discussed in detail in chapter 5 of this thesis.

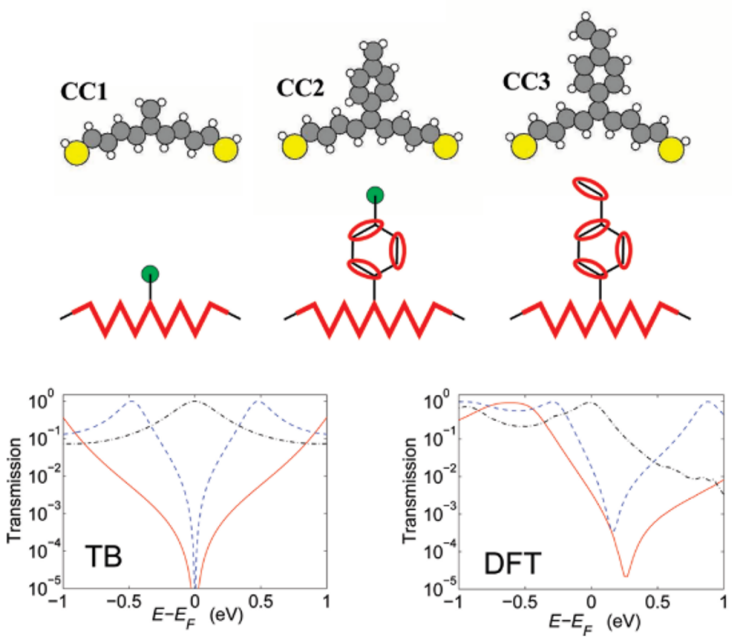

Figure 1.15: Molecular structures (top), graphical rules applied to the molecules (middle), and transmission plotted as a function of energy by tight-binding and DFT calculations (bottom)/ Color code of the transmission functions, CC1 (red), CC2 (dotted blue) and CC3 (dotted black). According to the graphical rule the green circle denotes the unpaired atom which results in DQI feature. The graphical rules correctly predicts DQI feature in CC1 CC2 and no DQI in CC3. The figure is taken from [48].

1.10 DFT based calculations

Though the tight-binding model gives us valuable information, the parameters for the method are obtained from fitting the experimental results or other theoretical approaches. Through DFT, we will see an ab-initio method to calculate the electronic structure.

Before we arrive to the formalism of the DFT, we should first briefly summarize the approximations led to the development of DFT. The mass of nuclei in an atom is much higher than the mass of the electrons. As a result, the ions are static in the time scale relevant for electrons. This assumption is called the Born-Oppenheimer approximation. Applying the Born-Oppenheimer approximation the solution to Schrödinger equation of a free electron gas becomes,

$$\begin{aligned}\mathbf{H}\Psi = &\sum_{i=1}^{N}\left(-\frac{\hbar^2}{2m}\Delta_i^2\Psi - e^2\sum_{I=1}^{M}\frac{Z_I}{|r_i - R_I|}\Psi\right) \\ &+ \sum_{I=1}^{M}\sum_{J>I}^{M}\frac{Z_I Z_J}{R_{IJ}}\Psi + \frac{1}{2}\sum_{i}^{N}\sum_{j>i}^{N}\frac{e^2}{r_{ij}}\Psi = \mathbf{E}\Psi,\end{aligned} \tag{1.68}$$

where r, R are the electrons and nuclei, respectively, and their total number is denoted as N and M. In 1.68, the first term is the kinetic energy of the electrons T, and the second term accounts for the attractive electrostatic potential $\hat{U}_{eN}(\vec{r})$ due to nuclei. The third term is the nuclear repulsion $\hat{U}_{Ncl}$. The last term is the electron-electron interaction $\hat{U}_{ee}(\vec{r})$. The method to obtain the exact value of this term for any realistic system is unknown until now. The solution to this equation is only possible for a few atoms. Hence, there are several approximations proposed based on physical ideas to solve realistic systems with several atoms.

We can simplify the problem by assuming that an electron is placed between averaged distributions of the other electrons. This reasonable approximation leads to a physically meaningful and computationally viable solution. For an electron r, the interaction with the density of other electrons ρ is given by the potential term,

$$\hat{U}_{el}(\vec{r}) = -e\int dr'\rho(\vec{r'})\frac{1}{|\vec{r} - \vec{r'}|} \tag{1.69}$$

where the total electronic charge density ρ is obtained by summing the wavefunction probability over all the occupied states. It is given as,

$$\rho(\vec{r}) = -e\sum_{i}|\psi_i(\vec{r})|^2 \tag{1.70}$$

Substituting 1.69 into 1.68 we get a set of equations of the following formn,

$$\mathbf{H}\Psi = \hat{T}(\vec{r})\Psi + \hat{U}_{eN}(\vec{r})\Psi + \hat{U}_{Ncl}(\vec{r})\Psi + \hat{U}_{el}[\rho]\Psi = E\Psi \tag{1.71}$$

Total energy for the N electron system (we will not state the term $\hat{U}_{Ncl}$ from hereon) is written commonly as,

$$E = T(\vec{r}) + E_{eN}(\vec{r}) + E_{el}(\vec{r}) \tag{1.72}$$

The set of equations 1.71 is called the Hartree equations. The Hartree equations are solved in an iterative method. An initial form for the potential term $\hat{U}_{el}$ is guessed to obtain the wavefunctions $\psi_i(\vec{r})$. From the calculated wavefunctions $\psi_i(\vec{r})$ a new $\hat{U}_{el}$ is calculated, the procedure is repeated until two consecutive iterations do not change the potential significantly.

The variational principle provides the lowest energy solution of the equation1.68. It states that the energy computed from guessed wavefunctions are upper bound to the real ground state solution E_0. The true ground state Ψ_0 of the initial wavefunction Ψ is found by minimizing the expectation value of the energy,

$$E[\Psi] = \frac{\langle \Psi | \, H \, | \psi \rangle}{\langle \Psi | \psi \rangle} \tag{1.73}$$

$$\langle \Psi | \, H \, | \psi \rangle = \int \Psi^* H \Psi dx$$

$$E_0 = \min_{\Psi \to N} E[\Psi] \tag{1.74}$$

N is the number of electron wavefunctions, and the variational principle provides a method to calculate the ground state energy as a function of wavefunctions. Other properties, such as ground state wavefunction Ψ_0, electrostatic potential, etc., can be extracted from the ground state energy configuration.

Hartree equations are numerically complex to solve. DFT uses the electronic density ρ to calculate all the terms of the electronic Hamiltonian.

Density Functional Theory

The electron density $\rho(\vec{r})$ gives the probability of finding an electron around the region $(\vec{r})$. It has the following properties a) the likelihood of finding an electron at infinity is zero b) the integral over the entire volume gives the total number of electrons. Electron density is a measurable quantity in experiments such as STM, diffraction experiments, etc., The solution to the N-electron wavefunction is complex to solve with equation 1.72. The idea of calculating the total energy only with the electron density marked the beginning of DFT. The Kohn-Sham equation assumes that the exact ground state density can be obtained from the ground state density of non-interacting particles. This gives us a set of numerically solvable independent equations. The ground state energy of a N electron system can be written as,

$$\mathbf{H}\Psi = \hat{T}(\rho) + \hat{U}_{eN}(\rho) + \hat{U}_{el}(\rho) \tag{1.75}$$

The contributions to the total energy is written as,

$$E_0 = T[\rho] + E_{eN}[\rho] + E_{el}[\rho] \tag{1.76}$$

The second term of equation 1.76 is the potential felt by the electron due to the attraction from the nucleus, which is simpler to calculate. It is given as,

$$E_{eN}[\rho] = \sum_{I=1}^{M} \frac{Z_I \rho(\vec{r})}{|r - R_I|} \tag{1.77}$$

Furthermore, Kohn and Sham suggested that the kinetic energy of the fully interacting particle can be calculated from the density of a non-interacting system. Thus T_S is,

$$T_S[\rho] = \sum_{i=1}^{N} \langle \psi_i | -\frac{1}{2}\Delta^2 | \psi_i \rangle \tag{1.78}$$

$$\rho(\vec{r}) = \sum_{i=1}^{N} |\psi_i(\vec{r})|^2,$$

where ψ_i is the non-interacting particle wavefunction. The third term E_{el} (electron-electron interaction) can be split into its classical Coulomb $J[\rho]$ and quantum $E_{ee}[\rho]$ contributions.

$$E_{el}[\rho] = J[\rho] + E_{ee}[\rho] \tag{1.79}$$

The Coulomb term $J[\rho]$ is straightforward to calculate. Whereas the exact solution for quantum electron-electron interaction E_{el} is not known for realistic systems. Several approximations are proposed to account for the E_{el} and another unknown term; we will discuss these approximations briefly in this section. All the unknown terms are refereed commonly as exchange-correlation energy E_{XC}. Now the final Kohn-Sham equation is,

$$E_{KS}[\rho] = T_S[\rho] + E_{eN}[\rho] + J[\rho] + E_{XC}[\rho] \tag{1.80}$$

$$E_{XC}[\rho] = T[\rho] - T_S[\rho] + E_{ee}[\rho] - J[\rho] \tag{1.81}$$

Finally, in Kohn-Sham DFT, the system's ground state energy is calculated using the variation principle.

$$E_0 = \min_{\rho \to N} \left(T_S[\rho] + E_{eN}[\rho] + J[\rho] + E_{XC}[\rho] \right) \tag{1.82}$$

The exact solution for the exchange-correlation energy E_{XC} is not known. We will briefly discuss some commonly used functional used to approximate exchange-correlation energy.

LDA

The local density approximation (LDA) is the basis of all approximations to the exchange-correlation (E_{XC}) term. The LDA is based on the uniform electron gas, which assumes that the electrons move on a positive background charge such that the total ensemble is zero. In LDA, the (E_{XC}) can be written as

$$E_{XC} = \int \rho(\vec{r}) \epsilon_{XC}(\rho(\vec{r})) d\vec{r}$$

ϵ_{XC} is the exchange-correlation energy of a uniform electron gas of density $\rho(\vec{r})$. The quantity ϵ_{XC} can be split into exchange and correlation contributions,

$$\epsilon_{XC}(\rho(\vec{r})) = \epsilon_X(\rho(\vec{r})) + \epsilon_C(\rho(\vec{r}))$$

The exchange part ϵ_X, is the exchange energy of an electron in a uniform electron gas of a particular density, was originally derived in 1920's by Bloch and Dirac. It is given by,

$$\epsilon_X = -\frac{3}{4}\left(\frac{3\rho(\vec{r})}{\pi}\right)^{1/3}$$

The explicit solution for the correlation part ϵ_C is not known. However, numerically accurate quantum Monte-Carlo simulations of the homogeneous electron gas are available. Various authors have presented analytical expressions of correlation terms based on sophisticated interpolation schemes.

Let us briefly mention the accuracy of LDA. Bond lengths calculated with LDA are accurate. However, the ionization energies and adsorption energies calculated with LDA are less accurate. The accuracy of LDA is insufficient for physical chemistry systems such as single-molecule junctions. The molecule electrode interactions calculated by LDA are often imprecise. The first step beyond the local approximation is a functional based on the gradient of the density ($\nabla\rho(\vec{r})$) called generalized gradient approximation (GGA).

GGA

The most commonly used exchange-correlation functional in DFT is GGA. Using GGA and bond lengths, the adsorption and dissociation energies are calculated with much better accuracy than LDA. In GGA, the gradient of the electron density is also used to calculate the exchange-correlation energy, and the functional modifies the behavior at large gradients such that the desired properties are preserved. The GGA functional is the workhorse of current DFT, and they can be written as,

$$E_{XC}^{GGA}[\rho] = \int f(\rho, \nabla\rho)d\vec{r}, \tag{1.83}$$

where $\nabla\rho$ represents the gradient of the density. In GGA E_{XC} is divided into its exchange E_X and correlation E_C term during implementation. The exchange part can be written as,

$$E_X^{GGA} = E_X^{LDA} + \sum_{\sigma=\uparrow,\downarrow}\int F(s_\sigma)\rho_\sigma^{4/3}(\vec{r})d\vec{r} \tag{1.84}$$

The argument of the function F is the reduced density gradient for spin,

$$s_\sigma = \frac{|\nabla\rho_\sigma(\vec{r})|}{\rho_\sigma^{4/3}} \tag{1.85}$$

There are several implementations of GGA available. Perdew, Burke, and Ernzerhof propose the one we use in this work, also known as GGA-PBE functional [56].

In general, GGA based functional proved to reproduce various physical properties such as electron density, periodic distribution to a reasonable accuracy. Additionally, GGA functional is faster compared to advanced hybrid functionals. Hence, GGA is used in this work for most systems.

Hybrid functionals

The exchange contributions are usually larger than the correlation effects. An accurate expression for exchange terms is more vital to obtain meaningful DFT results. Therefore, it is important to know that the exchange energy of a Slater determinant can be calculated precisely within the Hartree-Fock (HF) approximation. Hybrid functionals use a combination of orbital-dependent Hartree-Fock and an explicit density functional to calculate the electronic structure. Hybrid functional are the most accurate functional to calculate energies and are the method of choice for quantum chemical simulations.

To get closer to the exact E_{XC} values, the calculation of the exact exchange term is necessary as it is usually much higher than the correlation term. A hybrid functional calculates the exchange term with the orbital-dependent Hartree-Fock method, and correlation energy is calculated using density methods such as GGA. The energy of hybrid functional can be written as E_{XC}^{Hy},

$$E_{XC}^{Hy} = \frac{1}{2}(E_{XC}^{DFT} + E_{X}^{HF}) \tag{1.86}$$

Hybrid functionals provide many physical properties more accurately than semi-local functionals such as GGA. Some of the features we calculate using hybrid functionals are binding energies, molecular ring current, and potential surface. The parameters for hybrid potentials are obtained by fitting experimental results. However, the Hartree-Fock term of the exchange is inadequate in computing free-electron gas. Hence, the usage of hybrid potential is limited to isolated molecules.

In this work, we used B3LYP hybrid functional for the calculation of several isolated molecules and metal complexes. B3LYP includes a combination of LDA, exact exchange, and the correlation functional of Lee, Yang and Parr. Their mixing weight was obtained by fitting to a set of atomization and ionization energies, proton affinities, and total atomic energies.

1.10.1 An example: DFT-based transmission through naphthalene

In the previous chapters, we briefly introduced several concepts related to quantum tunneling. Through the example of a particle in a box, we illustrated discrete energy levels of quantum particles, the degeneracy of wavefunctions, and the nodal pattern of wavefunctions. Subsequently, we illustrated the tunneling of an electron through a potential energy barrier showing exponential decay in transmission for a barrier with a height greater than the particle's energy. The double barrier derivation showed that the transmission of electrons is enhanced greatly when the incident electron's energy is in resonance with the molecular energy level.

We connect the basic concepts previously introduced with DFT-NEGF methods, discuss transmission through a naphthalene molecule. We calculated the electronic and transport properties of a naphthalene molecule. Naphthalene is a molecule with two aromatic rings shown in figure 1.16a). The electronic energy levels of the electrons inside the naphthalene molecule were calculated using DFT with GGA. The energy levels of the naphthalene molecule and the corresponding

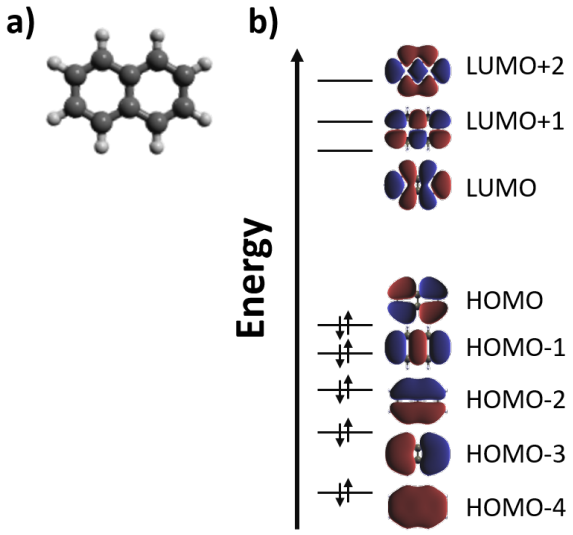

Figure 1.16: a) Atomic structure of naphthalene molecule. b) Energies and wavefunctions of five occupied and three unoccupied π molecular orbitals.

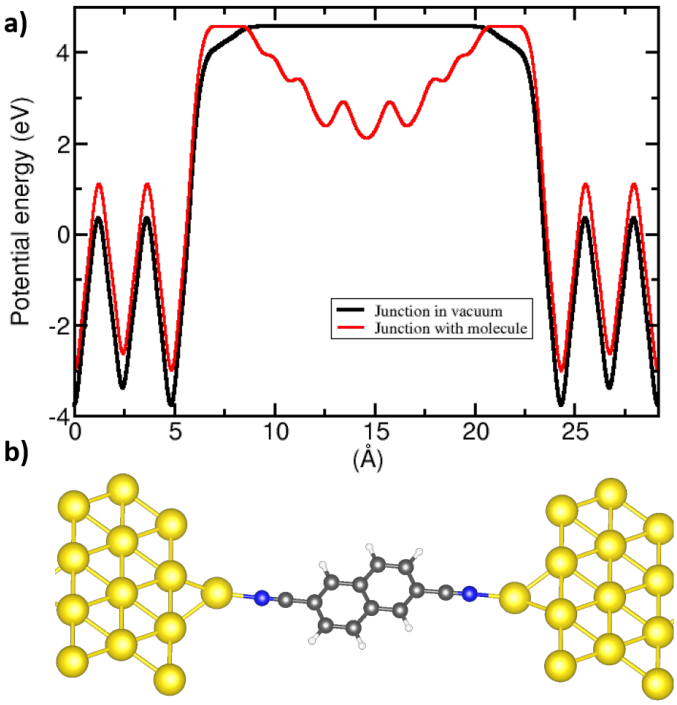

Figure 1.17: a) Potential energy along the z-direction of a junction with naphthalene molecule (red) and without molecule i.e, a vacuum gap (black). The Fermi energy is set at the origin. b) Atomic structure of a naphthalene molecule pinned between Au electrodes, the geometry is aligned with the horizontal axis of a). The potential energy barrier created by the molecular region is similar to the potential barriers in section 1.4.3

wavefunctions are shown in figure 1.16. This section focuses on the wavefunctions with π symmetry as these determine transport characteristics. The number of nodes of the wavefunctions increases with the increasing energy. The HOMO and LUMO are the two important wavefunctions as the low-bias transmission will happen non-resonantly via one of those orbitals.

The molecule, when coupled between the electrodes, will act as a potential barrier. To visualize this, we have embedded the naphthalene molecule between two gold electrodes through -CN (nitrile) linker groups on either side. Using DFT, we calculated the potential energy of the single-molecule junction. We have plotted the potential energy along the z-direction (red) along with the potential energy of the junction without the molecule (black) as shown in figure 1.17. The calculated potential energy and the corresponding atomic structure show that in the region at which the Au electrode terminates, the potential energy is much higher than the electrode's Fermi energy (set to zero). In the case in which the naphthalene molecule bridges the gap, potential energy drops significantly when compared to the vacuum gap between the tips. In this respect, the molecule acts as a potential energy barrier to electron transport though it is less insulating than the vacuum tunneling barrier. We use NEGF calculations to simulate the transmission through the single-molecule junction.

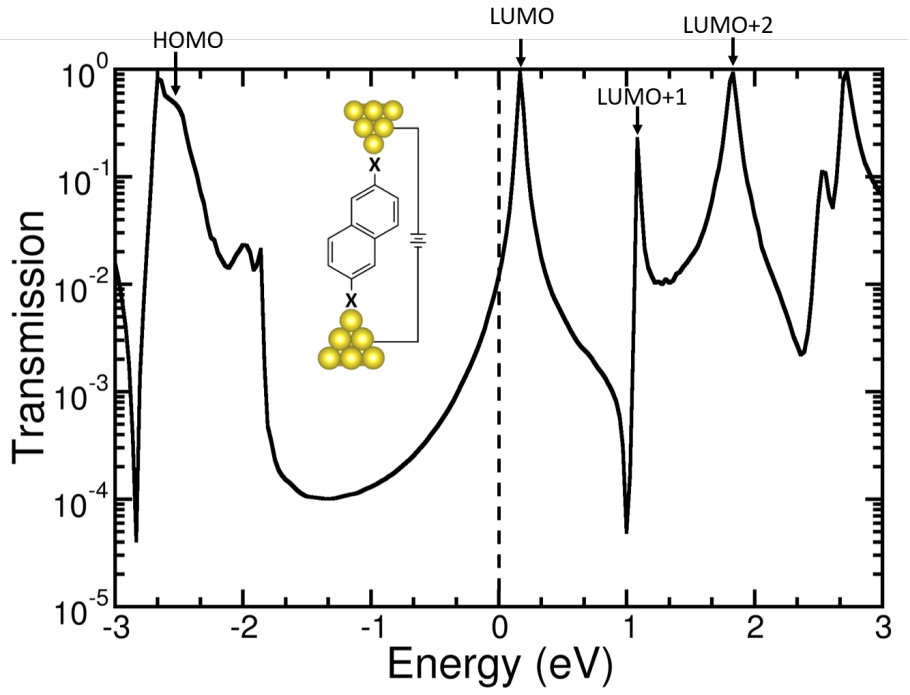

Figure 1.18: Transmission spectra of the naphthalene molecule (inset) contacted by two electrodes on either side. The arrows point to peaks corresponding to relevant frontier molecular orbitals. This naphthalene junction shows LUMO derived conductance.

The NEGF transmission spectrum for the naphthalene-based single-molecule junction is shown in figure 1.18. We can see that the molecular orbitals in figure 1.16 b) broaden to transmission peaks in figure 1.18, the width of the peak corresponds to the metal-molecule electronic coupling at the given energy. The low-bias transmission of the molecule shows that the conductance is derived from

the tail of the LUMO resonance of the molecule. The figure is similar to the transmission calculated between the double potential barrier in figure 1.11.

The naphthalene example illustrates how conductance can be simulated from the DFT-NEGF approximation. The molecule placed between electrodes showed that the analytical solutions we derived throughout the chapter are related to DFT results. DFT-NEGF has become the standard methodology to calculate the transport properties of single-molecule junctions. We will see several interesting studies of single-molecule junctions using our simulations and our collaborations with experimentalists.

1.11 Summary of following chapters

We have introduced basic theoretical concepts and some experimental setups of single-molecule junctions. We also outlined the methods for electronic structure calculations, which are helpful to simulate various properties of the single-molecule junction. In the following chapters, we present in detail the different systems we studied using the theoretical background we established.

Chapter 2 shows our study of a novel donor-bridge-acceptor molecule adsorbed on a Pt surface. Using theory and simulations, we reveal that the molecule preserves its donor-acceptor properties even on a Pt surface, which has a high affinity for electrons. Our study shows the potential of donor-bridge-acceptor molecules as a good candidate for solar energy applications.

A study of the electronic structure of the smallest carbene molecule on a Au surface is shown in chapter 3. The novel molecule demonstrates stronger adsorption than previously known carbene molecules. Ours is the first study of this new carbene, which shows strong tilted adsorption to Au surface and thereby a valuable addition to surface science studies.

Our comparison of mechanical and transport properties of different linker groups for single-molecule junctions is shown in chapter 4. We used a biphenylene (antiaromatic) based platform to study the mechanical stability and transmission properties of five linker groups representing five different chemical groups. We also establish a relationship between mechanical and transport properties based on the reactivity and conductance of linker groups. Our work proposes a novel bipodal platform for single-molecule conductance as a design guide for modeling single-molecule junctions.

Chapter 5 describes our work on the conductance of aromatic-antiaromatic molecules. We performed the electronic structure and transport characterization properties of the first stable antiaromatic molecule. Our results show antiaromatic molecule to be an order of magnitude more conducting than its aromatic counterpart. Our work is the first proof of the long speculated theory that antiaromaticity enhances conductance, thus, opening a doorway to following studies on a new class of conjugated molecules based on antiaromaticity. Subsequently, we present our work, which generalizes the electronic, and transport properties of several aromatic-antiaromatic pairs of molecules. We show that antiaromaticity effectively double p-dopes the aromatic electronic structure. The rules we developed help to predict the transport properties of antiaromatic (aromatic) pairs of molecules.

2. Donor-acceptor molecule on the Pt surface

2.1 Introduction

Organic solar energy harvesting is enabled by photoinduced energy transfer between molecules. The three processes involved in organic solar cells are as follows: i) a photosensitive layer absorbs light and generates excitons upon photoexcitation, ii) an interface separates charge, and iii) the separated charge is moved through the metal electrode to the external circuitry. A heterojunction consisting of two organic semiconductors with offset energy levels, the donor-acceptor is effective at separating the tightly bound exciton. For the charge to separate, an electron must be transferred into the LUMO of the acceptor and leaves a hole in the donor's HOMO. The charge separation intermediated by donor and acceptor unit leads to photoinduced charge generation. If donor and acceptor units are spatially close to each other, they might electronically hybridize. In addition, HOMO and LUMO being localized on different parts of the molecule aid this initial separation between electron and hole. In an efficient solar energy harvesting device, the donor-acceptor molecule must have excellent charge delocalization, photoinduced charge transfer, and long charge lifetime properties [57–61]. Several studies have shown that introducing a bridging unit connecting the donor and acceptor units breaks the conjugation between them and provides long-lived charge-separated states [62, 63].

To build an organic solar cell, a donor-acceptor molecule must be deposited on a surface that acts as an electrode for carrying the generated charge. Most studies on donor-acceptor molecules are performed in solution due to difficulty preserving charge transfer properties on the surface. Usually, when adsorbed on a surface, the donor and acceptor units hybridize with the metal or with each other, or the electronic structure is otherwise modified. The few successful STM studies of donor-acceptor dyads preserving charge transfer properties on the surface were performed on insulating salt layers[64, 65]. However, an insulating electrode is not capable of transferring the generated charge to the storage unit. To efficiently collect the generated charge, the donor-acceptor dyad must be deposited on a metal substrate. In particular, the metal surface must be conducive to the donor-acceptor molecule's favorable mechanical and electronic properties. The high reactivity of Pt substrate leads to a mechanically robust metal-donor-acceptor interface. In the literature, Pt has been used as a substrate because of high malleability, inertness under biological solution, and durability, which are highly desirable in an organic electronic device [66].

We studied a donor-acceptor dyad on Pt substrate in collaboration with the chemists and experimentalists from Germany. The donor-acceptor dyad was synthesized by Dr. Lisa Bensch from the group of Thomas J. J. Müller, University of Münster. The molecule was deposited and measured with STM by Dr. René Ebeling from the group of Dr. Silvia Karthauser, Forschungszentrum Jülich GmbH. We performed DFT calculations of the donor-acceptor molecule on the Pt(111) surface. We studied the adsorbed molecule by calculating adsorption configura-

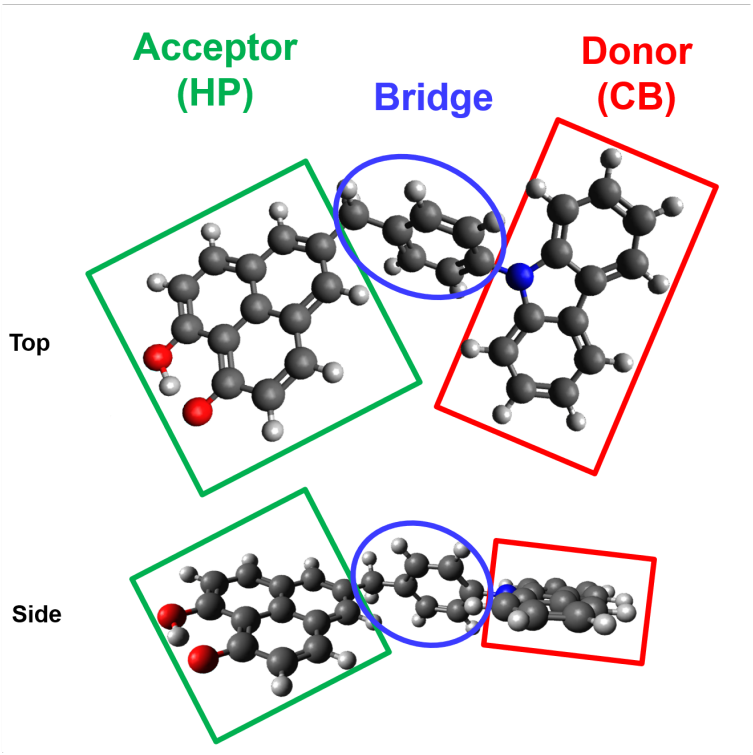

Figure 2.1: Top and side vies of carbazole donor (CB), a phenalenone (HP) acceptor, and an aliphatic methylene bridge of CBHP donor-acceptor molecule. Upon deposition to Pt(111) substrate the -OH group of the acceptor unit dissociates and the molecule forms an O-Pt bond with a Pt adatom.

tions, electronic structures, and charge transfer properties. Our study is the first report of a non-planar donor-acceptor dyad on a metal surface.

The donor-acceptor dyad (CBHP) is made of a carbazole donor (CB), a phenalenone (HP) acceptor, and an aliphatic methylene bridge, as shown in figure 2.1. The molecule at the gas phase is extremely flexible, and the donor-acceptor units are electronically well separated without any conjugation between them. During adsorption, the flexibility of the methylene bridge helps break conjugation between donor and acceptor units, despite the molecule being mostly flat on the Pt(111) surface.

In our calculations, we adsorbed the CBHP molecule on Pt(111) surface. Since Pt(111) is a new surface, different from Au(111), we first benchmarked the electronic properties of Pt.

We calculated the lattice constant and electronic structure of bulk Pt with pseudopotential provided by Rivero et al. [67]. In their work, the pseudopotential was validated with all-electron DFT calculations. We initially considered the default SIESTA pseudopotential for Pt and found that it did not properly reproduce the low energy band structure. Additionally, the SIESTA default pseudopotential resulted in a lattice constant of 4.22 Å, which was significantly higher than the Pt lattice of 3.92 Å reported in the literature [68]. Using the Rivero et al., pseudopotential we found an improved lattice parameter (4.01 Å). By comparing the band structures from both pseudopotentials, we found that the Rivero et al. pseudopotential significantly improves the electronic dispersion, as shown in figure 2.2.

Bulk Pt has an onset of d-band around Fermi energy as shown by the density of states in figure 2.2. The d-band plays a vital role during the adsorption of molecules on the Pt surface. Therefore, it is important to describe this well because the high density of states around Fermi energy indicates high reactivity of the Pt surface. Consequently, the CBHP molecule forms a strong electronic hybridization to the Pt(111) surface.

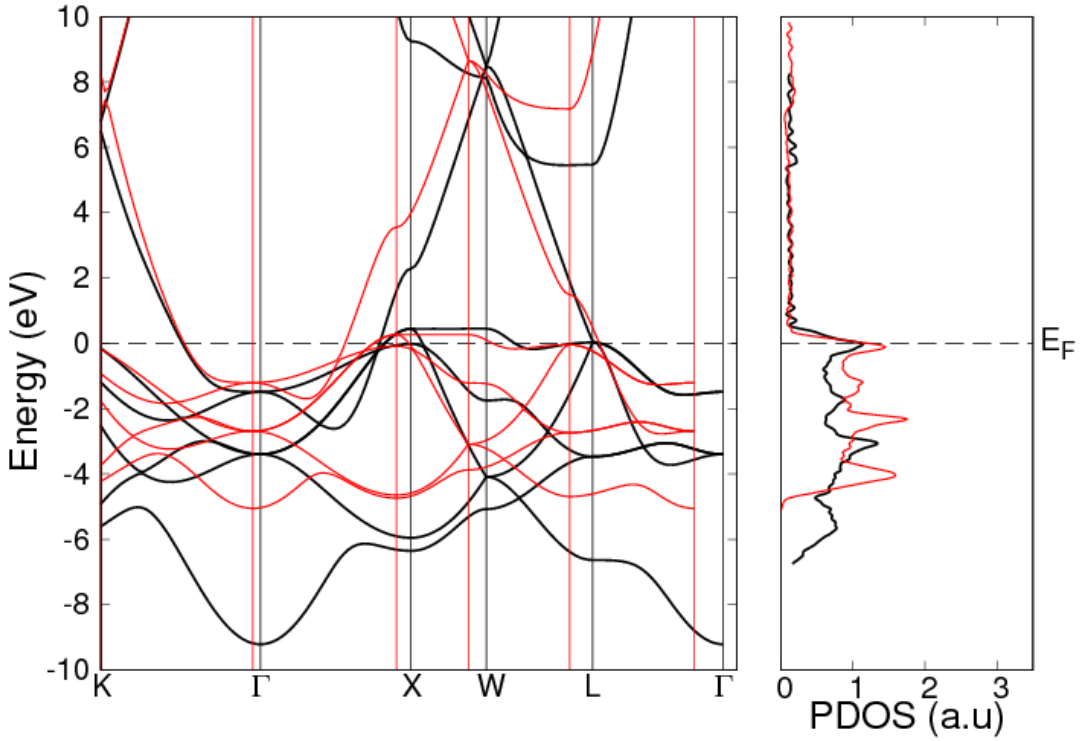

Figure 2.2: Band structure (left) and projected density of states (right) plots of bulk Pt calculated using the SIESTA default pseudopotential (red) and the pseudopotential obtained from Rivero et al., [67] (black). Rivero et al., pseudopotential provides an improvement on the electronic dispersion.

Having properly described the Pt electronic structure, we then studied the CBHP molecule's adsorption on the Pt(111) surface. The acceptor unit of the molecule has two oxygen atoms, and a hydrogen atom saturates one of the oxygens to form a hydroxyl group as seen in 2.1. The HP acceptor unit is known to form multiple stable complex structures with metal atoms [69]. In STM experiments by our collaborators, a pronounced blob-like feature was observed on the side of the acceptor unit. We hypothesize that the feature comes from the -OH group dissociating and forming an O-Pt bond on Pt(111) surface. We term the CBHP molecule bonded to the Pt adatom as CBHP-Pt complex. In our calculations, we examined the geometry of the adsorbed molecule and found that the CBHP-Pt complex formation hypothesis was accurate.

The flexibility of the CBHP molecule might lead to several adsorption configurations on the surface. Using DFT, we optimized the CBHP-Pt complex with 50 different initial configurations on the surface to explore the possible configurations. We use vdW-DF exchange-correlation functional, which features an accurate description of vdW dispersion interaction. We found several possible,

stable adsorption geometries for the CBHP-Pt complex. From their relative energies and by comparing the STM experiments, we identified two configurations. ConA is marked with a blue arrow and ConB with a red arrow in figure 2.3. Both ConA and ConB are the two most energetically favorable configurations, ConA being slightly more favorable than ConB. However, kinetic trapping during the deposition process makes both ConA and ConB appear significantly on the surface.

We simulate the constant current images of ConA and ConB from the local density of states (LDOS) within the Tersoff–Hamann approximation [70]. In both ConA and ConB, the acceptor and donor units are closer to the surface due to strong covalent bonds to the substrate and appear dark in simulated images. In contrast, the bridge unit is mechanically and electronically decoupled from the surface and appears brighter. The bride unit in ConB is brighter than in ConA. The features from our simulated STM images are in good agreement with experiments.

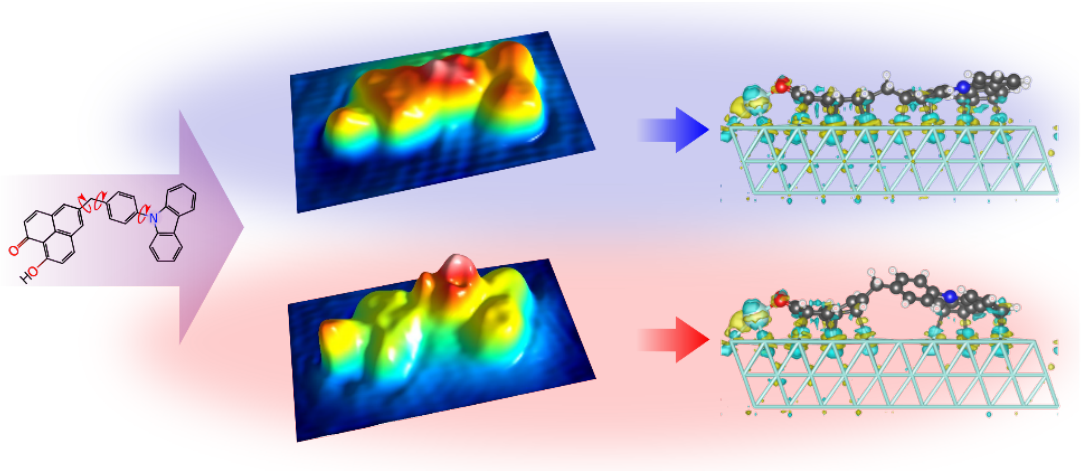

Figure 2.3: CBHP molecule consisting of carbazole donor and phenalenone acceptor units seperated by a methylene unit. When deposited on a Pt(111) substrate the CBHP molecule forms two distinct configurations, ConA (top) and ConB (bottom). The figure was taken from the TOC figure from the article [71].

Our study investigates the evolution of molecular states from the gas phase to the substrate through PDOS and LDOS plots. The spectral features of the adsorbed CBHP-Pt complex are significantly broadened and shifted in energy, indicating high electronic hybridization with the Pt substrate. From PDOS and LDOS plots, we concluded that the donor-acceptor character of the CBHP dyad is modified on the Pt(111) substrate as expected. We examined the electrostatic potential and charge density difference to evaluate the change in the donor-acceptor character of the CBHP dyad. This analysis showed that the conformational difference between ConA and ConB does not influence the electrostatic potential distribution. Furthermore, the electrostatic potential of the molecule scales down but was identified on the surface. The analysis revealed that both donor and acceptor units donate electrons to the substrate through strong covalent bonds. However, the donor-acceptor character is (although reduced) still preserved upon surface adsorption.

Our results suggest that the CBHP molecule adsorbed on a Pt(111) metal substrate retains many donor-acceptor characters. Our study demonstrates that a carbazole and a phenalenone derived donor-acceptor dyad separated by a methylene bridge on a Pt(111) surface is an exciting candidate for organic energy harvesting devices.

2.2 My contribution to the article

I performed the theory and simulations related to this work. The geometries were optimized in DFT calculation using vdW-DF functional [72]. I developed a Python script to broaden the simulated images to account for the experimental broadening due to the STM tip. A moderate Gaussian width of 0.25 $\mathring{A}$ was used in the script. The article's figures were produced in collaboration with René Ebeling (experiments).

Nanoscale Advances

ROYAL SOCIETY OF CHEMISTRY

PAPER

View Article Online
View Journal | View Issue

Check for updates

Cite this: *Nanoscale Adv.*, 2021, **3**, 538

Preservation of the donor–acceptor character of a carbazole–phenalenone dyad upon adsorption on Pt(111)†

René Ebeling,[ab] Narendra P. Arasu,[cd] Lisa Bensch,[e] Bertram Schulze Lammers,[a] Bernhard Mayer,[e] Thomas J. J. Müller,[e] Héctor Vázquez *[c] and Silvia Karthäuser *[a]

Donor–acceptor molecules are a subject of great attention due to their immense potential in molecular electronics and photovoltaics. Despite numerous extensive studies demonstrating their functionality in solution, the donor–acceptor character is usually lost upon adsorption on a conducting substrate. Here the concept of breaking the conjugation between the donor and acceptor unit by insertion of a bridge is used. Furthermore, the bridge introduces a kink into the dyad and thus, reduces the possibility of hybridization with the substrate. A donor–bridge–acceptor dyad composed of carbazole and phenalenone units joined through a flexible bridge is synthesized and deposited on a Pt(111) surface. Its electronic properties are investigated with a combination of low temperature scanning tunneling microscope measurements and density functional theory simulations. Two preferential adsorption configurations are identified, in which individual molecules form strong bonds to the substrate and to a Pt adatom. Differential conductance measurements and atomistic simulations evidence the preservation of a reduced donor–acceptor character upon adsorption of the molecule, where this reduction is ascribed to the strong molecule-metal hybridization. Our results highlight the changes in donor–acceptor character of the dyad induced by the substrate and provide guidelines for the use of donor–bridge–acceptor molecules as functional units in solid-state devices.

Received 4th November 2020
Accepted 29th November 2020

DOI: 10.1039/d0na00925c

rsc.li/nanoscale-advances

Open Access Article. Published on 08 December 2020. Downloaded on 10/10/2021 7:52:07 PM.
This article is licensed under a Creative Commons Attribution-NonCommercial 3.0 Unported Licence.

1. Introduction

An increased interest and manifold activities in the research field of donor–acceptor dyads are motivated by their electronic and optoelectronic properties which render possible to use them as memory devices, sensors, organic solar cells[1] or organic light emitting diodes.[2] Donor–acceptor dyads enable intramolecular electron transfer induced by thermal, electrical or optical stimulation and often show fluorescence or solvatochromism.[3–7] However, the application of donor–acceptor dyads in advanced devices requires a careful molecular design regarding the efficiency of electron transfer and the lifetime of the charge separated state. Several factors have been suggested to enhance the quantum yields and lifetimes in the charge separated states, such as spin restriction rules, conformational gating, and orientation effects. These concepts have successfully been applied to develop highly efficient dyads with long-lived charge separated states showing that the bridge mediating the charge transfer in donor–bridge–acceptor systems has a pronounced effect upon the charge transfer kinetics.[6–9] However, usually these studies are performed on molecules in solution.

To date, only a few studies exist which characterize groups or single donor–acceptor dyads deposited on solid surfaces by scanning probe methods that have the potential to reveal the intrinsic molecular properties with sub-nanometer resolution. It was found, that the theoretically predicted spatial localization of the frontier orbitals in donor–acceptor dyads, based on *ab initio* modeling of isolated molecules, could be observed experimentally if the dyads were electronically decoupled from the metallic substrate by an insulating layer.[10,11] On the other hand, the direct adsorption on metallic substrates or the formation of chemical contacts to metal atoms, which is a fundamental requirement for the application in functional devices, is expected to change the intrinsic molecular properties.[12,13] Therefore the preservation of the donor–acceptor

[a]*Peter Grünberg Institut (PGI-7), JARA-FIT, Forschungszentrum Jülich GmbH, 52425 Jülich, Germany. E-mail: s.karthaeuser@fz-juelich.de*

[b]*Faculty 1 – Mathematics, Computer Science and Natural Science, RWTH Aachen University, 52056 Aachen, Germany*

[c]*Institute of Physics, Academy of Sciences of the Czech Republic, CZ-162 00 Prague 6, Czech Republic. E-mail: vazquez@fzu.cz*

[d]*Department of Condensed Matter Physics, Faculty of Mathematics and Physics, Charles University, CZ-12116 Prague 2, Czech Republic*

[e]*Institut für Organische Chemie und Makromolekulare Chemie, Heinrich-Heine Universität Düsseldorf, Universitätsstrasse 1, 40225 Düsseldorf, Germany*

† Electronic supplementary information (ESI) available. See DOI: 10.1039/d0na00925c

© 2021 The Author(s). Published by the Royal Society of Chemistry

Open Access Article. Published on 08 December 2020. Downloaded on 10/10/2021 7:52:07 PM.
This article is licensed under a Creative Commons Attribution-NonCommercial 3.0 Unported Licence.

character after adsorption of a dyad and forming a chemical contact to a metallic electrode remains a challenge.

Recently, we studied a non-planar naphthalene diimide (NDI) derivative in contact with a Pt(111) electrode using low-temperature ultra-high vacuum scanning tunneling microscopy (LT-UHV-STM) at the single molecule level.[14] Here, a phenyl group is forced to adopt an out-of-plane coordination by a methylene bridge, which links it to the NDI acceptor. Thus, the phenyl group is decoupled from the substrate as well as from the NDI acceptor. However, the inspection of dyads composed of donors and acceptors, both with an extended π-electron system, indicates that larger donor groups cannot easily be forced to exhibit an out-of-plane coordination. Therefore, in this work, we investigate an especially designed non-planar donor–acceptor dyad with a bridging unit. The employed dyad is composed of a carbazole and a phenalenone derivative used as donor and acceptor, respectively. Hereby, the 9-hydroxy-1*H*-phenalen-1-one (HP) acceptor shows attractive opportunities like the formation of a stable radical anion, interesting photophysical characteristics and it is employed as a ligand in multiple stable metal complexes.[15,16] Recently 5-(hetero) aryl substituted conjugated 9-HP dyads were successfully synthesized in a modular fashion and their ensemble electronic ground and excited state properties were studied in detail.[17] However, here the delocalized donor and acceptor π-systems of the studied 5-[4-(9*H*-carbazol-9-yl)benzyl]-9-hydroxy-1*H*-phenalen-1-one (**CBHP**) are separated electronically by an aliphatic methylene bridge which introduces a twist angle between acceptor and donor and breaks the conjugation. In the following, single **CBHP** molecules will be analyzed on the Pt(111) surface by high-resolution STM in order to reveal their exact conformation and thus, their adsorption behavior. By analyzing the spatially resolved topographic and electronic features of this donor–bridge–acceptor dyad in comparison to Density Functional Theory (DFT) calculations we reveal two on-surface geometries characterized by the lateral extension of the donor and acceptor π-electron systems. We will show that adsorption on metallic surfaces induces a reduction, though not loss, of intrinsic molecular properties including the donor–acceptor character.

2. Results and discussion

2.1 Chemical synthesis of CBHP

The title compound **CBHP** was synthesized in a five-step sequence starting from carbazole (**1**) (Scheme 1). First, carbazole (**1**) was coupled with *p*-bromobenzaldehyde (**2**) under Ullmann conditions[18] to give 4-(9*H*-carbazol-9-yl)benzaldehyde (**3**) in 60% yield. The aldehyde was transformed to the benzyl alcohol **4** by sodium borohydride reduction in 83%, which was in turn reacted with PBr_3 to give benzyl bromide **5** in 99% yield. The benzyl bromide **5** was then transformed into the organozinc bromide–lithium chloride **6** by a literature known protocol,[19,20] which was directly submitted to Negishi coupling with 5-bromo-9-hydroxy-1*H*-phenalen-1-one (**7**) to give the dyad **CBHP** in 72% yield over two steps.

The fluorescence of the dyad is minimal and can be detected with a fluorescence quantum yield $\Phi_f < 0.01$ at 461 nm. Moreover, in the electronic ground state, as investigated by cyclic voltammetry, an electrochemically reversible one-electron

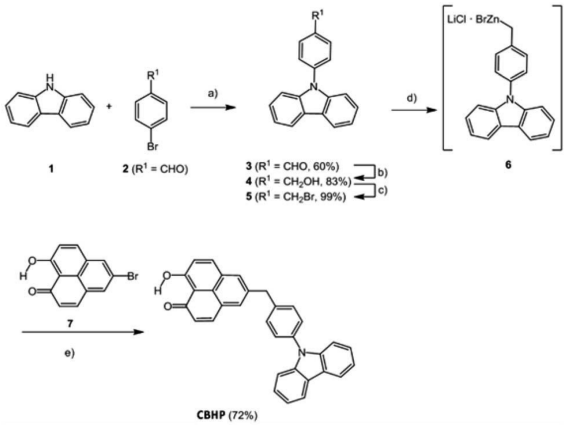

Scheme 1 Five-step synthesis of **CBHP**. (a) Cu (0.70 equiv.), K_2CO_3 (2.2 equiv.), [18]-crown-6 (0.14 equiv.), 1,2-dichlorobenzene, 185 °C, 3d, 60%. (b) $NaBH_4$ (1.20 equiv.), MeOH, 20 °C, 3 h, 83%. (c) PBr_3 (1.00 equiv.), THF, 20 °C, 23 h, 99%. (d) LiCl (1.12 equiv.), Zn (1.52 equiv.), 1,2-dibromoethane (0.35 equiv.), Me_3SiCl (0.35 equiv.), THF, 20 °C, 18 h. (e) 10 mol% $Pd(OAc)_2$, 10 mol% SPhos (2-dicyclohexylphosphano-2′,6′-dimethoxybiphenyl), THF, 65 °C, 24 h, 72%.

oxidation is found at $E_0^{0/+1} = 1290$ mV, as well as an electrochemically reversible one-electron reduction at $E_0^{0/-1} = -1160$ mV. From these redox potentials, an E_{00} transition $\lambda_{exc} = 453$ nm, and a mean donor–acceptor distance $r_{DA} = 0.82$ nm, a Gibbs free enthalpy of photoinduced electron transfer $\Delta G_{PET} = -0.487$ eV can be estimated by the Rehm–Weller approximation.[21]

$$\Delta G_{PET} = E_{Ox} - E_{red} - \Delta E_{00} - \frac{e^2}{4\pi\varepsilon_0\varepsilon_r r_{DA}} \quad (1)$$

2.2 Structure and topography of CBHP

Sublimation of **CBHP** from powder onto a clean Pt(111) surface leads to reproducible surface coverages controlled by duration and temperature. Using LT-UHV-STM we could identify single intact **CBHP** molecules in two different recurring structures, which we denote ConA and ConB, as well as a few molecular fragments. High resolution images of **CBHP** in both configurations are given in Fig. 1a and b. A large-scale image of a prototypical Pt(111) surface covered with **CBHP** is given in Fig. S1 (ESI†). The **CBHP** molecules exhibit no directionality with respect to the principal directions in the Pt(111) plane, which reflects the adsorption behavior of a non-planar, unsymmetrical molecule with three freely rotatable single bonds in the gas phase. Nevertheless, by means of the adsorption process the multiple degrees of freedom of the gas phase molecule (see red arrows in Fig. 2b) are reduced and the prochiral center located at the methylene linker becomes a chiral center in combination with the surface. This is reflected by the existence of the adsorption conformations ConA and ConB also in their mirror forms, that is, ConA′ and ConB′, like shown exemplarily for ConA′ in Fig. S1 (ESI†). Moreover, due to the on-surface reduced rotational degrees of freedom of the single

© 2021 The Author(s). Published by the Royal Society of Chemistry

Open Access Article. Published on 08 December 2020. Downloaded on 10/10/2021 7:52:07 PM.
This article is licensed under a Creative Commons Attribution-NonCommercial 3.0 Unported Licence.

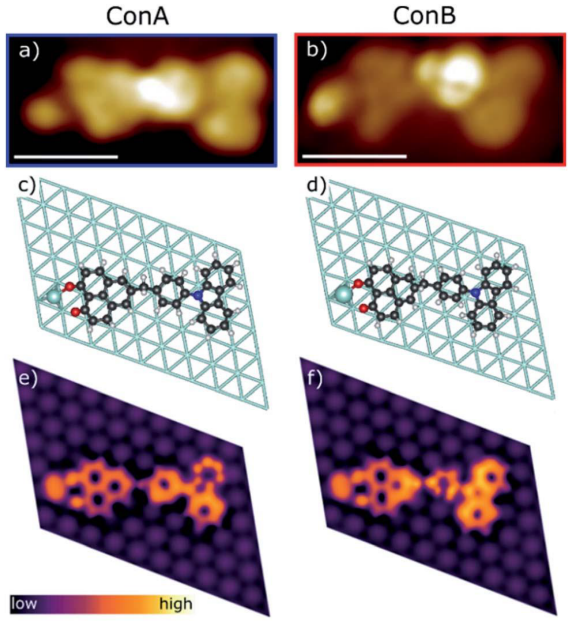

Fig. 1 Comparison of the two adsorption configurations of **CBHP**, ConA and ConB. (a and b) High resolution STM images ($U_{bias} = 50$ mV, $I_{set} = 200$ pA, scale bar = 1 nm). (c and d) Geometries of the **CBHP**–Pt complex on the Pt(111) surface corresponding to local minima from DFT calculations, where the Pt adatom has been highlighted from the substrate. (e and f) Simulated constant-current STM images around E_F.

bonds to the methylene linker and the need to provide enough space for the phenylene hydrogen atoms, the kink between the donor and the acceptor group only holds values from 140° to 160° deduced from 20 molecules adsorbed on Pt(111). However, the existence of this range of values points to multiple, nearly energetically equivalent rotational conformers of **CBHP** on Pt(111).

The two recurring adsorption configurations of the **CBHP** molecules (Fig. 1) exhibit the same general shape. They are identified as an elongated structure of 2.3 nm, a value which is in accordance with the dimension expected from the chemical structure given in Scheme 1. Three of the four main parts of the STM images can be identified by comparison of the orbital resolved structure with the chemical structure of **CBHP**. For both configurations we find from left to right in Fig. 1a and b, the rather flat HP acceptor, the brighter bridge unit (methylene and phenylene groups) which is the source for the conformational flexibility in the molecule, and the almost planar CB donor group. While the acceptor exhibits a width of only 0.9 nm perpendicular to the long molecular axis, this width amounts to 1.0 nm for the donor part (for details see ESI Fig. S2 and S3†). However, the single separated bright spot to the left of the acceptor cannot be explained in this way. Its position indicates an interaction with the HP group, but it is clearly not an orbital feature of **CBHP**. Indeed, each **CBHP** molecule observed on the surface shows this spot next to HP. Since HP is known to form multiple stable complex structures with metal atoms,[15,16] we hypothesize that deprotonation of the hydroxyl group and subsequent complexation leading to a **CBHP**–Pt complex takes place during adsorption of **CBHP** on the Pt(111) surface. Calculations for both conformers indicate that the adsorbed **CBHP**–Pt complex plus an individual H atom is more stable than the adsorbed **CBHP** plus an individual Pt atom by approximately 3.3 eV, thus supporting the formation of **CBHP**–Pt complexes. The Pt atoms might originate from adatoms diffusing on the surface or even substrate atoms extracted from the surface, since Pt(111) surfaces tend to reconstruct under the influence of adsorbed molecules.[22,23]

In order to verify this **CBHP**–Pt complex formation hypothesis during adsorption and to evaluate the **CBHP**/Pt(111) interface interactions, we performed thorough DFT calculations including van der Waals interactions on this molecular system. These calculations lead to a variety of adsorption geometries of **CBHP** or **CBHP**–Pt. Simulations showed that the strong C–Pt interaction and the large conformational flexibility of the molecule influenced the **CBHP** and **CBHP**–Pt geometries on the substrate. The calculated average height of C atoms above the Pt surface layer is 2.9 Å on the donor unit and 2.2 Å on the acceptor for ConA. For ConB these heights are 2.6 Å and 2.3 Å, respectively. These values are characteristic of strong metal-molecule chemical bonds.[24,25] Surface Pt atoms are also found to be displaced as a consequence of bonding to the adsorbate.[26,27] In our case, Pt atoms bonded to the molecule can be lifted up to 0.3 Å. The O–Pt adatom bond length is 2.2 Å in both configurations, ConA and ConB, which is a typical size for a donor–acceptor bond.[28] Both, C–Pt and O–Pt distances are close to previously computed values.[29,30] We obtained a considerable conformity between the measured STM images of ConA and ConB and the calculated constant-current STM images of the **CBHP**–Pt complex corresponding to the two most stable local energy minima (Fig. 1e and f). The aforementioned general shape of **CBHP** is reproduced in length and width and the four distinguishable parts of the **CBHP**–Pt complex are distinctly and visibly identified. The experimentally obtained appearance of the carbazole moiety, consisting of 2 large spots with small depressions in their center, and of the planar phenalenone moiety match in detail the calculated STM images. Even the differences in the general structures between ConA and ConB are distinguishable in the simulated STM images. The central region shows the brightest spot located at the position of the phenylene ring in the case of ConB (Fig. 1b) while it is located at the position of the methylene linker for ConA (Fig. 1a) indicating a rotation of the bridge between acceptor and donor part. This rotation of ConB relative to ConA is represented in the simulated STM images as well. Thus, the calculated on-surface configurations are representatives of the experimentally obtained conformations adopted by the **CBHP**–Pt complexes.

Additional simulations of the **CBHP** molecule without the Pt adatom were conducted and are given in ESI Fig. S4.† While in the experimental STM images one bright, distinct spot is observed on the edge of the HP acceptor, two smaller spots appear in the simulated constant-current image for the **CBHP** molecule, which can be assigned to the two oxygen atoms of HP. Thus, DFT calculations strongly suggest the formation of the

© 2021 The Author(s). Published by the Royal Society of Chemistry

Open Access Article. Published on 08 December 2020. Downloaded on 10/10/2021 7:52:07 PM.
This article is licensed under a Creative Commons Attribution-NonCommercial 3.0 Unported Licence.

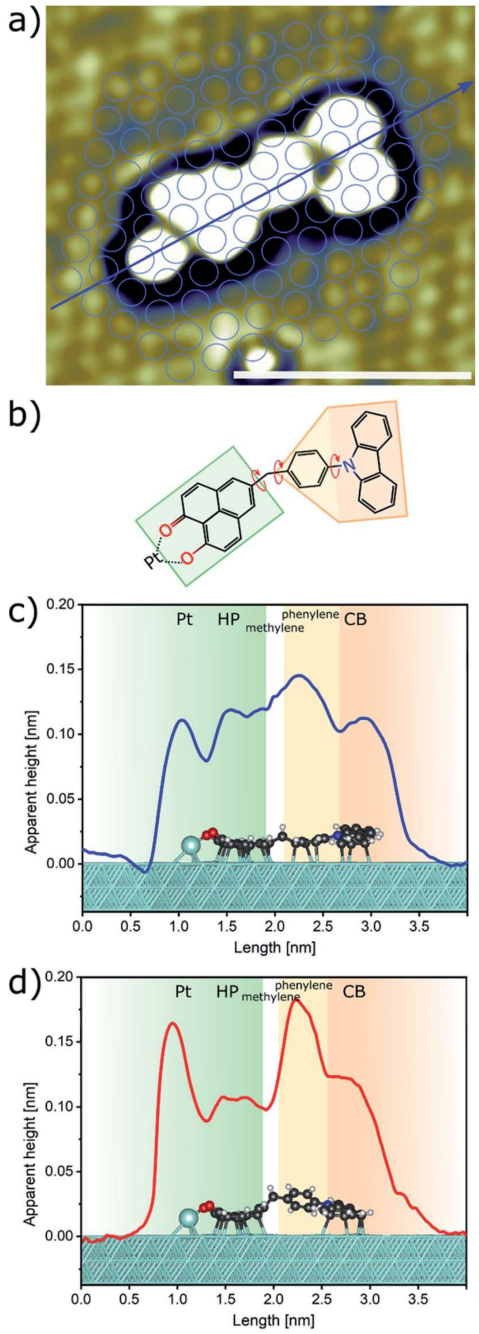

Fig. 2 Detailed on-surface geometry of **CBHP**. (a) High resolution STM image of ConA filtered as described in ESI, Fig. S5† (U_{bias} = 50 mV, I_{set} = 200 pA, scale bar = 2 nm). (b) Chemical structure of **CBHP**–Pt. The hydroxyphenalenone acceptor (HP) is marked by a green and the carbazolyl phenyl donor (CB) by an orange contour. A methylene linker is connecting donor and acceptor while introducing a kink to **CBHP**. Bonds with a rotational degree of freedom in the gas phase molecule are indicated by red arrows. (c and d) Averaged height profiles along the long molecular axis for ConA (blue) and ConB (red) as indicated exemplarily in (a) for ConA. The corresponding calculated **CBHP**–Pt complex geometries on a 3-layer Pt substrate are shown below the respective height profiles.

CBHP–Pt complexes, as presented in Fig. 1b–e, and we exclude the adsorption of single **CBHP** molecules without the formation of a Pt-complex on Pt(111).

A high-resolution image of **CBHP**–Pt with an atomically resolved Pt(111) surface is given in Fig. 2a, that enables the determination of the exact position of this molecule with respect to the substrate and shows the position of the averaged apparent height profile indicated by an arrow. In Fig. 2c and d the apparent height profiles through the molecule are overlaid with side views of the calculated on-surface geometries for ConA and ConB on three Pt layers. While the bridging phenylene group in ConA is only slightly rotated from an orientation parallel to the substrate, the one in ConB is rather upright. This rotation causes the methylene linker to be lifted from the surface in ConB as well. In consequence, this leads to an increased apparent height of the whole center of **CBHP**–Pt in ConB, consistent with the calculated geometries.

Based on these theoretically deduced insights the brightest features observed in the STM image of ConB (Fig. 1b) are interpreted as a phenylene ring standing obliquely to the substrate. This phenylene ring is represented by the two spots which differ by approximately 30 pm in their apparent height. They originate from the two lobes of the π-orbital (+π and −π) located above and below the phenylene ring which are separated by the atomic nodal plane located in the plane of the ring. A phenylene ring with an orientation exactly perpendicular to the substrate would be imaged as two equivalent spots related to the two parts of its π-orbital, as shown in a previous work.[14]

Different from the case of ConB, the slight asymmetry in the orbital appearance of the phenylene ring in ConA (Fig. 1a) can be attributed to the deviation from a parallel position to the substrate. The brighter side of the phenylene ring in ConA is found always at the inner side of the kink. This corresponds to a slight lifting of the inner side of the phenylene ring from the surface, owing to the steric hindrance introduced by the ring hydrogen atoms approaching the ones of HP and CB. ConB shows the rotation of the phenylene ring in the same direction but to a much higher extent. Here, always the outer side of the phenylene ring appears brighter, since in this configuration the geometry of the oblique π-orbital is recorded, as discussed above. Thus, the dominant differences in the appearance of ConA and ConB are mainly due to geometric effects. This has been verified by a series of high resolution STM images taken for ConA revealing no clear voltage dependent changes in the range between −2 V and 2 V (Fig. S6, ESI†). The simulated STM images in Fig. 1e and f show the differences in electronic and geometric properties of both conformers, while the latter are clearly visible in the side views of the calculated geometries (Fig. 2c and d).

While **CBHP**–Pt in ConB is chemisorbed to the Pt(111) surface through the HP acceptor and CB donor, all HP, the central part and CB units are chemisorbed in the case of ConA. The binding energy of the adsorbed **CBHP** molecule is −12.59 eV (ConA) and −11.10 eV (ConB). As a reference, values of 1.3–1.9 eV were measured and calculated previously for benzene on Pt(111),[31,32] approximately 6–10 times smaller than the calculated binding energies of ConA and ConB. Given that

© 2021 The Author(s). Published by the Royal Society of Chemistry

Open Access Article. Published on 08 December 2020. Downloaded on 10/10/2021 7:52:07 PM.
This article is licensed under a Creative Commons Attribution-NonCommercial 3.0 Unported Licence.

the total number of five- and six-membered rings in the **CBHP** molecule is seven (ignoring N and O heteroatoms), the calculated binding energies are consistent and indicative of a strong interaction with the substrate. The binding of C atoms to the Pt(111) substrate drives the lateral position of the CB and HP units on the surface and induces strain along the molecule in order to enable the binding of acceptor and donor to adequate positions of the Pt(111) surface, leading to the lifted molecule center in ConB and resulting in a smaller angle between HP and CB in experiment and theory. The difference in binding energy between both configurations, ConA and ConB, of 1.49 eV suggests that in thermal equilibrium only dyads in conformation ConA should be found on the Pt(111) surface. However, the observation of dyads in ConB in a considerable amount points clearly to a kinetically trapping during the deposition process.

2.3 Molecular orbitals in gas phase and on surface

The influence of the adsorption of **CBHP**–Pt on Pt(111) on the electronic structure is studied using voltage dependent STM images as well as scanning tunneling spectroscopy (STS) and is compared to the Local Density Of States (LDOS) from the DFT calculations. STM measurements exhibit a small voltage dependence and are given in ESI Fig. S6† for ConA. These STM images reveal that throughout the whole investigated voltage range (−2 V to +2 V) the unoccupied states appear brighter than the occupied states. In addition, the phenylene group becomes the brightest feature for voltages of more than 1 V, while otherwise the position of the methylene linker is the most intense spot of the molecule.

A full set of STS measurements was obtained for **CBHP**–Pt in configuration ConA, while this was not possible for ConB. **CBHP**–Pt in configuration ConB changed their appearance if voltage sweeps were applied indicating a considerable strain, as discussed above, so that voltage sweeps cause a strain release and thereby a change of the molecular conformation or even the decomposition of the molecule. Fig. 3a shows typical STS curves for ConA measured above four different positions of **CBHP** in comparison to the clean Pt(111) surface (gray background). Differential conductance spectra (dI/dV) were taken on the center of the acceptor, the benzyl group and both spots of the CB donor. Distinct differences are observed for the four positions. When the tip is positioned above the inner side of the donor (green curve) only small differential conductance values are obtained compared to the other parts of the molecule. However, this is the only tip position showing distinct features in the unoccupied part of the spectrum, at 0.9 eV (lowest unoccupied molecular orbital, LUMO) and 2.0 eV (LUMO+1). The dI/dV curve taken above the central part (purple) starts to rise at 1.0 eV, while on the other hand, the orange curve (outer part of the donor) begins to rise slowly not before 1.5 eV. Remarkably, the differential conductance characteristic of the HP acceptor (black curve) shows no distinct molecular features over the whole examined voltage range, which we attribute to a strong interaction with the Pt(111) surface. Occupied molecular orbital states can be identified by STS above the center of the molecule (purple curve) and the outer donor part (orange curve). The purple curve shows a first shoulder around −1.0 eV (highest occupied molecular orbital, HOMO) with a main peak at −1.9 eV while the orange curve has a feature at −2.1 eV. This is in accordance with occupied delocalized states over the CB donor inclusive the phenylene ring indicating the preservation of the donor character on Pt(111) in ConA. The thereof obtained HOMO–LUMO gap of **CBHP** adsorbed on Pt(111) amounts to 1.9 eV compared to 2.45 eV obtained from cyclic voltammetry investigations performed on **CBHP** in solution described above. This points to a reduction of the HOMO–LUMO gap during adsorption.

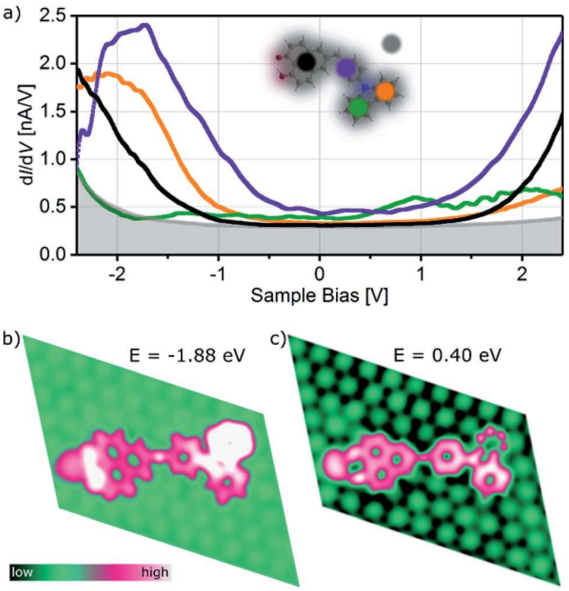

Fig. 3 STS spectra and calculated LDOS of **CBHP** in ConA. (a) Differential conductance (set-point: I_{set} = 3 nA, V_{mod} = 20 mV) obtained over four positions of ConA as indicated in the inset by colored circles: HP acceptor (black), central part (purple) and two spots over the donor CB (green and orange), Pt(111) substrate (grey background). (b) Calculated LDOS of ConA illustrating the spatial localization over the dyad of occupied and unoccupied electronic states.

Calculations for ConA capture some of the trends seen in the measured dI/dV curves for different tip positions, as shown in Fig. 3b. At energies below the Fermi level the calculated LDOS shows electronic states at −1.88 eV predominantly on the O atoms of the HP–Pt unit, the outer donor part and the central part (black, orange and purple lines in Fig. 3a, respectively). The calculated LDOS of the adsorbed ConA, for energies above the Fermi level, at 0.40 eV (Fig. 3c), exhibits bright LDOS features over the central phenylene ring and the inner CB unit and smaller features over the outer donor ring, in similarity with the purple, green, and orange curves of Fig. 3a for unoccupied states. Overall, spectral features of the adsorbed dyad reveal a high degree of hybridization with the Pt substrate leading to molecular states being significantly broadened in energy and distorted with respect to the isolated molecule. The calculated Projected Density Of States (PDOS) of ConA is given in Fig. S7

© 2021 The Author(s). Published by the Royal Society of Chemistry

Open Access Article. Published on 08 December 2020. Downloaded on 10/10/2021 7:52:07 PM.
This article is licensed under a Creative Commons Attribution-NonCommercial 3.0 Unported Licence.

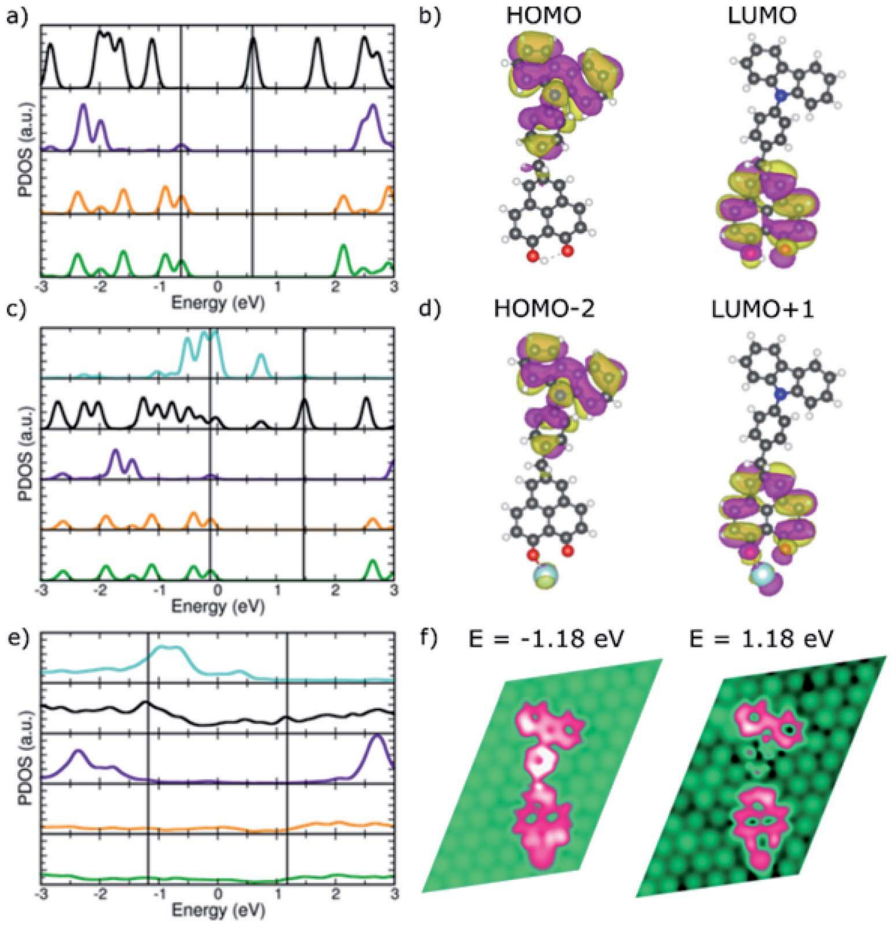

Fig. 4 PDOS of the donor–acceptor dyad in ConB. (a) **CBHP** in the gas phase. (c) **CBHP**–Pt in the gas phase. (e) **CBHP**–Pt adsorbed on Pt(111) (color code as in Fig. 3a, in addition Pt-adatom in turquoise). (b and d) Relevant frontier molecular orbitals marked by black lines in (a) and (c). (f) LDOS plots at selected energies marked by black lines in (e).

(ESI†) as well as LDOS images of ConA at additional positive and negative energies.

To investigate the preservation of the donor–acceptor character upon adsorption, electronic structure calculations were performed where the binding to the Pt adatom and then to the substrate were considered sequentially by calculating the isolated **CBHP** molecule, the isolated **CBHP**–Pt complex, and the **CBHP**–Pt complex adsorbed on the Pt(111) surface. Throughout, the positions of all atoms were kept frozen at the values of the metal-molecule junction, thus allowing us to disentangle electronic from geometric effects and analyze the former ones alone. Fig. 4 shows the results of this analysis for ConB.

The **CBHP** molecule in the gas phase (Fig. 4a) exhibits discrete molecular orbitals shown by well-separated PDOS peaks. The DOS projected over different donor and acceptor subunits are represented in different colors, like defined in Fig. 3. The calculated HOMO–LUMO gap of the molecule in the ConB geometry is 1.23 eV, close to the value of 1.37 eV in the ConA geometry and 1.40 eV in the fully relaxed isolated molecule geometry. These gap values, calculated with the vdW-DF exchange–correlation functional, are smaller than with other functionals which feature a more accurate description of electron–electron interaction (Fig. S8, ESI†) but which cannot be applied to the metal-molecule interface. The donor–acceptor character of the isolated dyad in geometry ConB can be seen in Fig. 4a, where PDOS peaks projected over the inner and outer donor regions are predominant at negative energies (green and orange lines), while the HP acceptor states abound in the unoccupied part of the spectrum. Bridge states are found mostly far from the gap for the unoccupied states.

Fig. 4b illustrates the donor–acceptor character of the isolated molecule by plotting selected molecular orbitals, whose energies are indicated in panel (a) with vertical lines. The HOMO is localized over the donor rings and the bridge phenylene and methylene units. In contrast, the LUMO is delocalized on the HP acceptor unit but has no significant amplitude on the phenylene bridge group or the CB acceptor.

© 2021 The Author(s). Published by the Royal Society of Chemistry

Open Access Article. Published on 08 December 2020. Downloaded on 10/10/2021 7:52:07 PM.
This article is licensed under a Creative Commons Attribution-NonCommercial 3.0 Unported Licence.

This is consistent with the donor–acceptor character of the **CBHP** dyad, which is clearly manifested in the gas phase, even in the somewhat constrained geometry ConB.

Fig. 4c shows the calculated PDOS after bond formation between a Pt atom (turquoise PDOS) and one of the HP oxygen atoms of **CBHP**, while keeping the geometry frozen to that of the ConB/Pt(111) interface. Additional features appear near the HOMO–LUMO gap due to the mixing of molecular states located at the HP acceptor with the states of this Pt atom. Several states of the complex have appreciable Pt PDOS contribution (turquoise line). In particular, the buildup slightly below the Fermi level leads to the edge of the Pt band in the slab. Many wave functions of the **CBHP**–Pt complex are delocalized over both species. However, the gas-phase orbitals selected in panel (b) still retain their characteristic nodal patterns (Fig. 4d) even though their ordering in the spectrum has changed as they are now HOMO−2 and LUMO+1, respectively. Thus, despite the mixing and rearranging introduced by the states of the Pt atom, the **CBHP**–Pt complex largely preserves the donor–acceptor characteristics of the isolated dyad (see ESI, Fig. S9 and S10†).

This situation, however, is significantly changed when the complex is adsorbed on the Pt(111) surface. Fig. 4e shows the calculated DOS projected onto the different donor and acceptor regions when **CBHP**–Pt is adsorbed on Pt(111). Molecular states are significantly broadened due to the strong hybridization with the Pt substrate. This is expected from the multiple bond formation established between C atoms of the CB and HP units and the Pt surface, as seen in the junction geometries (Fig. 2c and d). The spectral features of the molecule have significant amplitudes over a wide energy range around the Fermi level. CB donor features are present below the Fermi level, but also above it. Similarly, features derived from the HP acceptor are present in unoccupied energies, however, they also peak below the Fermi level. The donor–acceptor character is thus clearly reduced upon adsorption.

Over a wide range of energies above and below the Fermi level, calculated LDOS features are spread to some extent over donor, bridge, and acceptor units. We found no energies at which the distinctive localization and nodal patterns of panels (b) and (d) were preserved. Fig. 4f shows the calculated LDOS at two energies above and below the Fermi level. Electronic states at −1.18 eV involve dominantly the bridge and donor parts of the molecule, but also the Pt adatom bound to the HP unit and the HP unit. At 1.18 eV, there is no significant LDOS on the bridge group, however, it is spread over the HP acceptor including the Pt adatom and a part of the donor unit simultaneously. LDOS plots at additional energies are given in ESI Fig. S11† and exhibit similar characteristics. Thus, the donor–acceptor character of the **CBHP** dyad is significantly modified due to the hybridization and chemical bonds with the Pt(111) substrate.

2.4 Donor–acceptor character of CBHP upon adsorption on Pt(111)

The changes described previously can be analyzed in terms of the calculated electrostatic potential of the isolated **CBHP** molecule, isolated **CBHP**–Pt complex, and adsorbed **CBHP**–Pt complex. The results are plotted in Fig. 5 for both conformations. The plots show the evolution of the electrostatic potential along the sequential binding to the Pt adatom and then onto the Pt(111) substrate, while excluding effects due to changes in geometry. Electrostatic potential values (in mV) are projected on an isocontour of the electron density and are shown as a color scale.[33] High values of the electrostatic potential (blue) are related to a reduced electron density. Low electrostatic potential values (red) occur in electronegative regions and correspond to accumulation of electron density. The comparison between both conformers in Fig. 5 shows a similar pattern, indicating that the differences in geometry between ConA and ConB do not play an important role in determining the electrostatic distribution upon adsorption. The electrostatic potential of the isolated **CBHP** molecule (Fig. 5a and d) shows positive values near the peripheral H atoms, while negative values are found near the O atoms of the HP acceptor and, to a lesser extent, in the CB donor rings. Consequently, the planar carbon system forming the acceptor shows a lower electron density (green/blue) than the carbon system of the donor (yellow/green) confirming the donor–acceptor character of **CBHP** for both configurations in the gas phase. Binding of the complex to the Pt adatom (Fig. 5b and e) introduces changes in the O–Pt region but the potential in other parts of the molecule remains almost unchanged, thus the donor–acceptor character is maintained. This is consistent with the findings shown in Fig. 4, which indicate the introduction of Pt-related states but otherwise the preservation of the character of isolated molecular orbitals. Adsorption onto the

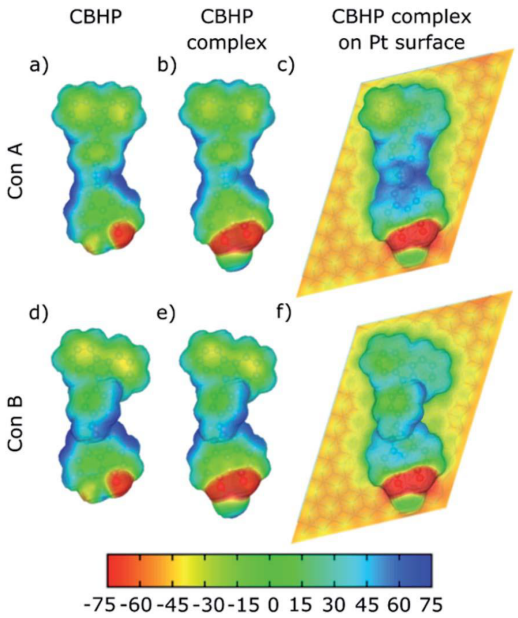

Fig. 5 Calculated electrostatic potential in mV plotted over an electron density contour of 10^{-3} e Å^{-3} for ConA (top panels) and ConB (bottom panels). (a and d) Gas-phase **CBHP**. (b and e) **CBHP**–Pt complex. (c and f) **CBHP**–Pt on Pt(111).

© 2021 The Author(s). Published by the Royal Society of Chemistry

Open Access Article. Published on 08 December 2020. Downloaded on 10/10/2021 7:52:07 PM.
This article is licensed under a Creative Commons Attribution-NonCommercial 3.0 Unported Licence.

Pt(111) substrate, however, leads to an increase of the electrostatic potential throughout the molecule. Negative values are only retained near the HP O atoms in both conformations, the center of ConB and on the donor rings of ConA and ConB which are detached from the substrate (see Fig. 2c). The Pt substrate has negative values. These findings reflect electron transfer from the molecule to the Pt substrate, resulting in the changes of the potential described. Therefore, the donor–acceptor character seems to be significantly changed but can be nevertheless identified at the surface.

To analyze the charge transfer in detail, we calculated the electron density difference upon adsorption. We computed the electron density of the junction minus the sum of the individual **CBHP**–Pt complex and the Pt(111) substrate. As before, the position of all atoms was kept fixed to their values at the interface throughout. Fig. 6 shows the results for ConA (panels a–c) and ConB (panels d–f). Positive (negative) values correspond to electron accumulation (depletion) and are shown in blue (yellow). For both ConA and ConB, electrons are transferred from the molecule to the substrate, mostly to the surface Pt layer. This follows from the formation of multiple molecule–substrate bonds involving many C atoms. The charge transfer between detached parts of the molecule and the Pt surface is minimal, like indicated by the real-space representation of the electron density difference (Fig. 6). For ConA, this applies to the outer donor ring, which is lifted above the inner one. In the case of the more twisted ConB, this corresponds to the bridge unit formed by the methylene group and one phenylene ring. Notably, electron density is transferred to the Pt surface from both donor and acceptor units, which changes the donor–acceptor character of the dyad upon adsorption.

Fig. 6c and f plot the plane-averaged electron density difference as a function of vertical distance for ConA and ConB. Both profiles exhibit oscillations and negative values in the molecular region and positive values below the Pt surface layer. The dashed horizontal lines indicate the mid height of the shortest C–Pt bond and are taken as a guide to separate the **CBHP**–Pt and Pt(111) subsystems. Integration of the charge difference above and below this dashed line gives a measure of the transferred charge. A value of 0.18*e* transferred from **CBHP**–Pt to the substrate is obtained for both ConA and ConB, which is in the size range found for other molecules.[34,35] However, for ConB only the CB and HP groups are involved, whereas in ConA the bridge also participates in the charge transfer. By cleaving the **CBHP**–Pt complex into separate donor, bridge, and acceptor–Pt units (all appropriately H-saturated), the charge transfer of each constituent can be computed. As expected, in both conformers electron transfer to Pt(111) from the CB donor unit is higher than from the HP–Pt acceptor (0.10–0.13 electrons compared to 0.06 electrons, respectively). This is consistent with the high work function of 5.8 eV for the Pt (111) substrate,[36] which possesses a higher acceptor character than either CB or HP. However, the analysis of Fig. 5 shows that the donor–acceptor character of the dyad does not disappear completely when adsorbed on Pt(111), although it is reduced.

These investigations indicate that the non-planarity of **CBHP** is the key factor, which enables the preservation of the donor–acceptor character upon adsorption on a metallic surface and in principle qualifies this kind of dyads to be employed in advanced devices. Further molecular engineering, like the introduction of bulky side groups, should lead to an increased decoupling of molecular parts from the surface und thus,

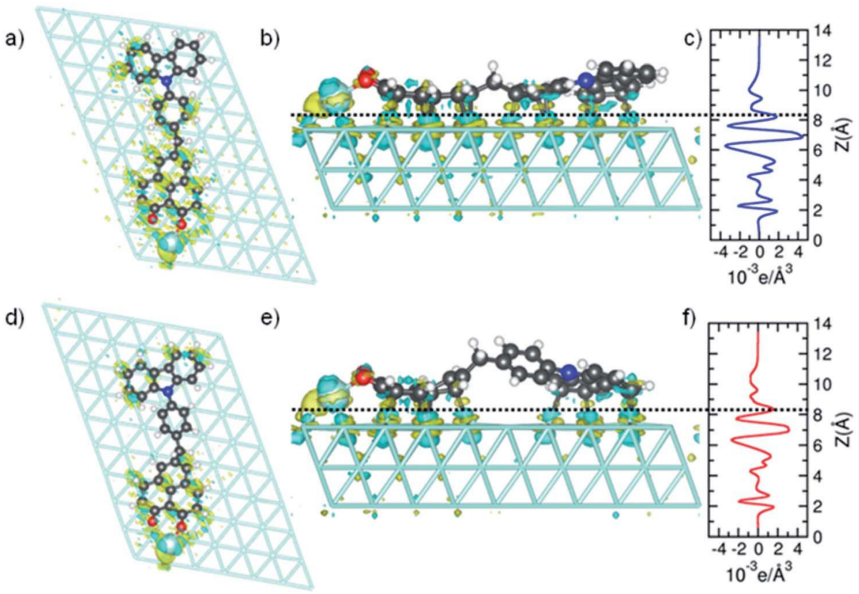

Fig. 6 Calculated electron density difference upon adsorption of ConA (top panels) and ConB (bottom panels). (a, b, d and e) Top and side views of the real-space difference. (c and f) Plane-averaged electron density difference.

© 2021 The Author(s). Published by the Royal Society of Chemistry

Open Access Article. Published on 08 December 2020. Downloaded on 10/10/2021 7:52:07 PM.
This article is licensed under a Creative Commons Attribution-NonCommercial 3.0 Unported Licence.

should be advantageous for the preservation of the intrinsic molecular properties. In addition, by tuning the energy level alignment of dyad and metal, undesired charge redistributions upon adsorption should be diminished and a significant on-surface donor–acceptor character should be possible.

3. Conclusions

In conclusion, a novel donor–bridge–acceptor dyad, **CBHP**, was synthesized, deposited on a Pt(111) surface, and studied by a combination of LT-UHV-STM measurements and DFT simulations. The geometry and electronic properties were investigated using STM and differential conductance measurements. Two recurring conformations, ConA and ConB, were identified in these measurements by comparison to the chemical structure. A bright spot close to the acceptor side on all STM images was ascribed to a Pt adatom. STS of ConA above different positions of the molecule revealed donor-related peaks below the Fermi level and acceptor-derived states at higher energies. DFT-based simulations were performed for two representative stable structures obtained from a broad sampling of junction configurations. The stronger bound was adsorbed nearly flat on Pt(111) (ConA) while the other conformation (ConB) exhibited a slightly twisted geometry with the phenylene bridge lifted from the substrate. Calculations rationalize the experimental findings and the nature of the donor–acceptor character of the adsorbed **CBHP** dyad. The donor–acceptor properties are significantly reduced upon adsorption. This is due to the strong hybridization between adsorbed molecular units and substrate orbitals, which substantially broadens and intermixes donor and acceptor states, as well as to the high work function of the Pt substrate, which acts as an acceptor to both CB and HP constituents. Nevertheless, calculated electrostatic potential and electron density difference indicate that the donor–acceptor character of this non-planar dyad is partially retained even after the formation of strong chemical contacts to the metal substrate. Thus, we conclude that despite the substantial changes of intrinsic molecular properties upon chemical adsorption the principle applicability of donor–bridge–acceptor molecules in functional devices is feasible.

4. Materials and methods

4.1 Chemical synthesis

4-(9*H*-Carbazol-9-yl)benzaldehyde (3). In an oven dried nitrogen-flushed screw-cap Schlenk tube with magnetic stir bar were placed 9*H*-carbazole (**1**) (1.23 g, 7.50 mmol) and dry 1,2-dichlorobenzene (20 mL) under nitrogen. To this solution was added 4-bromobenzaldehyde (**2**) (3.01 g, 16.3 mmol), copper powder (159 mg, 2.50 mmol), K_2CO_3 (1.66 g, 12.0 mmol), and [18]-crown-6 (264 mg, 1.00 mmol). The reaction mixture was stirred in the sealed reaction vessel at 185 °C for 72 h. After cooling to room temp. the mixture was filtered and the filtrate was evaporated under reduced pressure and absorbed on Celite®. Purification by flash chromatography on silica gel (*n*-hexane/ethyl acetate 19 : 1) and crystallization from hexane/ethyl acetate furnished 4-(9*H*-carbazol-9-yl)benzaldehyde (**3**) (814 mg, 60%) as colorless crystals, $R_f = 0.32$ (*n*-hexane/ethyl acetate 10 : 1), mp 158 °C (156–158 °C as given in ref. 37).

^{1}H NMR (600 MHz, $CDCl_3$): δ 7.34 (d, $^3J = 7.9$ Hz, 2H), 7.46–7.43 (m, 2H), 7.50 (s, 2H), 7.81–7.79 (m, 2H), 8.17–8.14 (m, 4H), 10.12 (s, 1H). ^{13}C NMR (151 MHz, $CDCl_3$): δ 109.9 (CH), 120.7 (CH), 121.0 (CH), 124.1 (C_{quat}), 126.4 (CH), 127.0 (CH), 131.5 (CH), 134.8 (C_{quat}), 140.2 (C_{quat}), 143.6 (C_{quat}), 191.1 (CH). MS (EI) (70 eV, *m*/*z* (%)): 272 (20), 271 (M^+, 100), 243 (5), 242 ([M − CHO]$^+$, 24), 241 (28), 240 (5), 120 (18). IR: $\tilde{\nu}$ = 2824 (w), 2733 (w), 1701 (m), 1595 (m), 1512 (w), 1479 (w), 1451 (m), 1362 (m), 1337 (m), 1317 (w), 1300 (w), 1227 (m), 1209 (w), 1182 (w), 1161 (m), 1125 (w), 1103 (w), 916 (w), 845 (w), 829 (w), 750 (s), 714 (m) cm^{-1}. Anal. calcd for $C_{19}H_{13}NO$ (271.1): C 84.11, H 4.83, N 5.16. Found: C 84.11, H 5.10, N 4.99.

[4-(9*H*-Carbazol-9-yl)phenyl]methanol (4). In an oven dried nitrogen-flushed screw-cap Schlenk tube with magnetic stir bar were placed 4-(9*H*-carbazol-9-yl)benzaldehyde (**3**) (712 mg, 2.62 mmol) in methanol (10 mL) under nitrogen. Under external cooling with ice-water sodium borohydride (119 mg, 3.15 mmol) was slowly added. The cooling was removed and the reaction mixture was stirred at 20 °C for 3 h. Then, deionized water (10 mL) was added to stop the reaction. The aqueous layer was extracted with dichloromethane (4 × 20 mL) and the combined organic phases were dried (anhydrous magnesium sulfate). The solvents were evaporated *in vacuo*, residue was absorbed on Celite® and purified by flash chromatography on silica gel (*n*-hexane/ethyl acetate 6 : 1 → 4 : 1 → 2 : 1) to give [4-(9*H*-carbazol-9-yl)phenyl]methanol (**4**) (592 mg, 83%) as a colorless solid, $R_f = 0.22$ (*n*-hexane/ethyl acetate 4 : 1), mp 123 °C.

^{1}H NMR (600 MHz, $CDCl_3$): δ 1.83 (s, 1H), 4.84 (s, 2H), 7.29 (ddd, J_{H-H} = 7.9 Hz, 5.7 Hz, 2.4 Hz, 2H), 7.45–7.38 (m, 4H), 7.64–7.54 (m, 4H), 8.15 (ddd, J_{H-H} = 7.8 Hz, 7.8 Hz, 1.0 Hz, 2H). ^{13}C NMR (151 MHz, $CDCl_3$): δ 65.1 (CH_2), 109.9 (CH), 120.1 (CH), 120.5 (CH), 123.5 (C_{quat}), 126.1 (CH), 127.4 (CH), 128.6 (CH), 137.2 (C_{quat}), 140.2 (C_{quat}), 141.0 (C_{quat}). MS (EI) (70 eV, *m*/*z* (%)): 274 (14), 273 (M^+, 68), 272 (6), 271 (14), 256 ([M − OH]$^+$, 18), 254 (21), 253 (7), 252 (25), 242 ([M − CH_2OH]$^+$, 8), 241 (12), 223 (8), 217 (8), 199 (12), 189 (10), 188 (89), 187 (90), 185 (16), 179 (10), 171 (42), 169 (43), 167 ([M − C_7H_7O]$^+$, 10), 159 (17), 157 (23), 152 ([M − C_7H_7NO]$^+$, 23), 149 (11), 108 (10), 107 (97), 91 (13), 90 ($C_6H_4N^+$, 18), 89 (17), 79 (100), 78 (36), 77 ($C_6H_4^+$, 96), 76 (12), 75 (13), 63 (10), 53 (13), 51 (25), 50 (20). IR: $\tilde{\nu}$ = 3233 (w), 1701 (w), 1607 (w), 1595 (w), 1518 (m), 1477 (w), 1451 (s), 1362 (w), 1335 (w), 1314 (w), 1229 (s), 1182 (w), 1171 (w), 1011 (s), 914 (w), 843 (m), 806 (w), 750 (s), 725 (s), 700 (w), 629 (m) cm^{-1}. Anal. calcd for $C_{19}H_{23}NO$ (281.2): C 83.49, H 5.53, N 5.12. Found: C 83.69, H 5.45, N 5.05.

9-[4-(Bromomethyl)phenyl]-9*H*-carbazole (5). In an oven dried nitrogen-flushed screw-cap Schlenk tube with magnetic stir bar were placed [4-(9*H*-carbazol-9-yl)phenyl]methanol (**4**) (1.88 g, 6.90 mmol) in dry THF (10 mL). To this solution was added dropwise and slowly phosphorus tribromide (650 µL, 6.90 mmol) and the reaction mixture was stirred at 20 °C for 24 h. Then, deionized water (5 mL) was added to stop the reaction. The aqueous layer was extracted with dichloromethane (4 × 30 mL) and the combined organic phases were dried (anhydrous magnesium sulfate). The solvents were

© 2021 The Author(s). Published by the Royal Society of Chemistry

Open Access Article. Published on 08 December 2020. Downloaded on 10/10/2021 7:52:07 PM.
This article is licensed under a Creative Commons Attribution-NonCommercial 3.0 Unported Licence.

evaporated *in vacuo*, residue was absorbed on Celite® and purified by flash chromatography on silica gel (*n*-hexane/ethyl acetate 19 : 1) to give 9-[4-(bromomethyl)phenyl]-9*H*-carbazole (**5**) (2.32 g, 99%) a colorless solid, R_f = 0.80 (*n*-hexane/ethyl acetate 4 : 1), mp 100 °C.

^{1}H NMR (600 MHz, $CDCl_3$): δ 4.62 (s, 2H), 7.33–7.29 (m, 2H), 7.45–7.40 (m, 4H), 7.57 (d, ^3J = 8.4 Hz, 2H), 7.64 (d, ^3J = 8.4 Hz, 2H), 8.16 (d, ^3J = 7.8 Hz, 1H). ^{13}C NMR (151 MHz, $CDCl_3$): δ 32.9 (CH_2), 109.9 (CH), 120.3 (CH), 120.5 (CH), 123.6 (C_{quat}), 126.1 (CH), 127.4 (CH), 130.7 (CH), 136.9 (C_{quat}), 137.9 (C_{quat}), 140.8 (C_{quat}). MS (EI) (70 eV, *m*/*z* (%)): 337 ($M(^{81}Br)^+$, 15), 335 ($M(^{79}Br)^+$, 13), 257 (23), 256 ([M − Br]$^+$, 100), 254 (16), 241 (6), 128 (19), 127 (12), 52 (6). IR: $\tilde{\nu}$ = 3061 (w), 3046 (w), 1593 (w), 1514 (m), 1478 (w), 1451 (s), 1418 (w), 1366 (w), 1335 (w), 1308 (m), 1287 (w), 1229 (s), 1206 (m), 1182 (m), 1169 (w), 1144 (w), 1119 (w), 1096 (w), 1020 (w), 995 (w), 916 (w), 831 (w), 812 (w), 747 (s), 721 (s), 702 (m), 644 (w), 629 (w) cm^{-1}. Anal. calcd for $C_{19}H_{14}BrN$ (335.0): C 67.87, H 4.20, N 4.17. Found: C 67.64, H 4.28, N 4.01.

5-[4-(9*H*-Carbazol-9-yl)benzyl]-9-hydroxy-1*H*-phenalen-1-one (CBHP). In an oven dried nitrogen-flushed screw-cap Schlenk tube with magnetic stir bar was placed lithium chloride (24 mg, 0.560 mmol) and dried at 150 °C *in vacuo* for an hour. Then, zinc powder (50 mg, 0.760 mmol) was added and drying *in vacuo* at 150 °C was continued for another hour. After cooling to room temp the Schlenk tube was flushed with nitrogen and evacuated for three times and finally flushed with nitrogen. Dry THF (2.00 mL), TMSCl (22 μL, 0.175 mmol), and 1,2-dibromoethane (15 μL, 0.350 mmol) were successively added to the reaction vessel. After stirring at room temp for 5 min at 20 °C 9-[4-(bromomethyl)phenyl]-9*H*-carbazole (**5**) 168 mg (0.500 mmol) was added and the reaction mixture was stirred at 20 °C for 18 h (92% of organozinc compound **6** determined by ^{1}H NMR integration with compound **5**).

In a second oven dried nitrogen-flushed screw-cap Schlenk tube with magnetic stir bar were placed 5-bromo-9-hydroxy-1*H*-phenalen-1-one (**7**) (69 mg, 0.250 mmol) and dry THF (2.00 mL) under nitrogen. To this solution palladium(II)acetate (6 mg, 25 μmol), and SPhos (21 mg, 50 μmol) were added. The decanted solution of the first Schlenk tube was placed in a syringe and by syringe pump this solution was added dropwise over 1.5 h to the stirred solution in the second Schlenk tube, which was warmed to 65 °C. Stirring was continued at 65 °C for 22.5 h. Then, after cooling to room temp the reaction was ended by addition of dichloromethane (5.00 mL), deionized water (10.0 mL), and 37% aqueous hydrochloric acid (2.00 mL). The aqueous layer was extracted with dichloromethane (3 × 10 mL) and the combined organic phases were dried (anhydrous magnesium sulfate), filtered and the solvents were removed *in vacuo*. The residue was purified by flash chromatography on reversed phase RP-18 (MeCN : H_2O 1 : 1 → MeCN) to furnish 5-[4-(9*H*-carbazol-9-yl)benzyl]-9-hydroxy-1*H*-phenalen-1-one (**CBHP**) (82 mg, 72%) as a yellow solid, mp 259 °C.

^{1}H NMR (600 MHz, $CDCl_3$): δ 4.36 (s, 2H), 7.19 (d, ^3J = 9.3 Hz, 2H), 7.30–7.27 (m, 2H), 7.42–7.36 (m, 4H), 7.47 (d, ^3J = 8.1 Hz, 2H), 7.52 (d, ^3J = 8.2 Hz, 2H), 7.94 (s, 2H), 8.09 (d, ^3J = 9.3 Hz, 2H), 8.14 (d, ^3J = 7.7 Hz, 2H), 15.89 (s, 1H). ^{13}C NMR (151 MHz, $CDCl_3$): δ 41.4 (CH_2), 109.8 (CH), 111.2 (C_{quat}), 120.1 (CH), 120.5 (CH), 123.5 (C_{quat}), 124.1 (CH), 125.8 (C_{quat}), 126.0 (CH), 126.1 (C_{quat}), 127.5 (CH), 130.4 (CH), 133.4 (CH), 136.3 (C_{quat}), 136.8 (C_{quat}), 139.9 (C_{quat}), 140.95 (CH), 140.97 (C_{quat}), 179.1 (C_{quat}). MS (EI) (70 eV, *m*/*z* (%)): 453 (7), 452 (35), 451 (M^+, 100), 285 (8), 284 (6), 256 (12), 255 (8), 254 (9), 241 (5), 239 (7), 226 (21), 211 (9). IR: $\tilde{\nu}$ = 3043 (w), 2963 (w), 2920 (w), 2361 (w), 1939 (w), 1632 (s), 1595 (s), 1558 (m), 1516 (s), 1477 (m), 1452 (s), 1418 (w), 1366 (m), 1335 (m), 1314 (w), 1267 (w), 1233 (s), 1184 (w), 1165 (m), 1144 (w), 1105 (m), 1022 (w), 930 (w), 914 (w), 893 (m), 833 (m), 812 (m), 746 (s), 723 (s), 692 (m), 638 (m) cm^{-1}. Anal. calcd for $C_{32}H_{21}NO_2 \cdot 1/5H_2O$ (451.2 + 3.6): C 84.45, H 4.74, N 3.08. Gef.: C 84.39, H 4.82, N 3.02. UV/Vis (MeCN): λ_{max} [nm] (ε [L mol^{-1} cm^{-1}]): 239 (73 400), 260 (29 300), 285 (19 900), 292 (21 500), 353 (21 600), 421 (7600), 446 (8200). Fluorescence (MeCN, λ_{exc} = 420 nm): λ_{max} = 461 nm (Φ_f < 0.01), Stokes shift: $\Delta\tilde{\nu}$ = 800 cm^{-1}. $E_0^{0/-1}$ = −1160 mV, $E_0^{0/+1}$ = 1290 mV.

4.2 SPM characterization

All low temperature scanning tunneling microscopy and spectroscopy experiments were performed with custom-made electrochemically etched tungsten tips using a commercial Createc STM (Germany) at 4.2 K. The LT-STM is operated under ultra-high vacuum (UHV) with a base pressure of 1 × 10^{-10} mbar. It is composed of three parts, *i.e.*, a load-lock, a preparation chamber, and a measurement chamber. Constant-current mode was used to record all STM images which are plotted after applying plane correction and optional noise filtering by a slight Fourier-filter using SPIP. Apparent heights are obtained from averaged height profiles in the corresponding images. The given length of molecules is the full width at half maxima obtained from the respective apparent height profiles. The precise current and voltage set-points are given in the caption of the respective STM images. STS experiments were performed with the feedback-loop switched off and the differential tunneling current was recorded using lock-in detection while the bias voltage was modulated. For each adsorption configuration several molecules were investigated on the Pt(111) surface. The differential conductance (dI/dV) spectra are usually averaged over five curves and their measurement parameters are given directly in the respective captions of the STS measurements.

The substrate used in this work was a polished Pt(111) single crystal (purity 99.999%) purchased from MaTeck (Germany). Remaining surface artifacts were removed by repeated cycles of Ne^+-ion sputtering (1 kV, 30 min, 2.5 μA), optional baking (600 °C, 30 min., 1 × 10^{-6} mbar, O_2 partial pressure) and subsequent annealing (900 °C, 10 min). The resulting Pt(111) surface was investigated by STM and LEED to confirm its cleanliness. The preparation cycles were repeated until the Pt(111) surface showed large clean terraces with a diameter up to several 100 nm and sharp spots with a hexagonal symmetry in the LEED patterns.

After outgassing of the **CBHP** molecules at 200 °C for at least 1 hour they were deposited onto the Pt(111) substrate using a Knudsen cell. Suitable evaporation temperatures were found with the help of TGA and DTA measurements (Fig. S12, ESI†). A

© 2021 The Author(s). Published by the Royal Society of Chemistry

Open Access Article. Published on 08 December 2020. Downloaded on 10/10/2021 7:52:07 PM.
This article is licensed under a Creative Commons Attribution-NonCommercial 3.0 Unported Licence.

submonolayer coverage was obtained by sublimation at 180 °C for 10 minutes with a background pressure in the 10^{-10} mbar range and the Pt(111) surface at room temperature (RT). Thereafter the sample was kept at RT for 105 s before it was cooled to 4.2 K for the STM and STS characterization.

4.3 Atomistic simulations

The structure and electronic properties of the metal/molecule interface were studied using the DFT-based code SIESTA.[38] A local-orbital pseudo-atomic basis was used. Molecular (substrate) atoms were described using double-(single-)zeta plus polarization bases. Exchange–correlation, including non-local dispersion interactions, was described with the vdW-DF functional of Dion *et al.* in the implementation of Román-Pérez and Soler.[39,40] The unit cell in the calculations consisted of the **CBHP**–Pt complex and three Pt(111) layers, each consisting of 70 atoms. Almost 50 initial geometries, each with different lateral positions and orientations with respect to the substrate, were screened. The positions of the **CBHP**–Pt complex and of the surface layer Pt atoms were optimized until the forces acting on them were smaller than 0.02 eV $Å^{-1}$. A real-space grid of 250 Ry was used. Reciprocal space was sampled using a single point for geometry optimization calculations, and a 5 × 5 Monkhorst–Pack grid to compute PDOS and LDOS. The LDOS at selected energies was obtained by integrating the electron density over 100 meV around that energy. Constant-current images were calculated from the LDOS within the Tersoff–Hamann approximation using a 0.25 Å Gaussian broadening to simulate the experimental broadening.[41,42]

Author contributions

S. K. and T. J. J. M. planned the experiments. L. B. synthesized and analyzed the molecular components and B. M. contributed to it. R. E. performed the STM/STS experiments and processed the data. B. S. L. contributed to the STM measurements. N. P. A. performed and H. V. planned the DFT calculations. The manuscript was written by R. E. with contributions of all authors. All authors have given approval to the final version of the manuscript.

Conflicts of interest

The authors declare no conflict of interest.

Acknowledgements

The authors gratefully acknowledge financial support from the Volkswagen-Stiftung through the 'Optically Controlled Spin Logic' project and the Czech Science Agency GAČR (grant number 19-23702S). Computational resources were supplied by the project "e-Infrastruktura CZ" (e-INFRA LM2018140) provided within the program Projects of Large Research, Development and Innovations Infrastructures.

References

1 A. B. Ricks, K. E. Brown, M. Wenninger, S. D. Karlen, Y. A. Berlin, D. T. Co and M. R. Wasielewski, *J. Am. Chem. Soc.*, 2012, **134**, 4581–4588.
2 Y. Olivier, M. Moral, L. Muccioli and J.-C. Sancho-García, *J. Mater. Chem. C*, 2017, **5**, 5718–5729.
3 T. J. J. Müller and U. H. Bunz, *Functional Organic Materials: Syntheses, Strategies and Applications*, Wiley-VCH, Weinheim, Germany, 2007.
4 S. Bay, T. Villnow, G. Ryseck, V. Rai-Constapel, P. Gilch and T. J. J. Müller, *ChemPlusChem*, 2013, **78**, 137–141.
5 L. Levi and T. J. J. Müller, *Chem. Soc. Rev.*, 2016, **45**, 2825–2846.
6 T. Benelli, M. Tomasulo and F. M. Raymo, in *Molecular Switches*, ed. B. L. Feringa and W. R. Browne, Wiley-VCH, Weinheim, Germany, 2011, pp. 697–717.
7 H. Kawauchi, S. Suzuki, M. Kozaki, K. Okada, D.-M. S. Islam, Y. Araki, O. Ito and K.-i. Yamanaka, *J. Phys. Chem. A*, 2008, **112**, 5878–5884.
8 O. S. Wenger, *Chem. Soc. Rev.*, 2011, **40**, 3538–3550.
9 M. Kuss-Petermann and O. S. Wenger, *Angew. Chem., Int. Ed.*, 2016, **55**, 815–819.
10 C. Tao, J. Sun, X. Zhang, R. Yamachika, D. Wegner, Y. Bahri, G. Samsonidze, M. L. Cohen, S. G. Louie, T. D. Tilley, R. A. Segalman and M. F. Crommie, *Nano Lett.*, 2009, **9**, 3963–3967.
11 B. Schuler, S.-X. Liu, Y. Geng, S. Decurtins, G. Meyer and L. Gross, *Nano Lett.*, 2014, **14**, 3342–3346.
12 A. Hinaut, T. Meier, R. Pawlak, S. Feund, R. Jöhr, S. Kawai, T. Glatzel, S. Decurtins, K. Müllen, A. Narita, S.-X. Liu and E. Meyer, *Nanoscale*, 2018, **10**, 1337–1344.
13 T. Meier, R. Pawlak, S. Kawai, Y. Geng, X. Liu, S. Decurtins, P. Hapala, A. Baratoff, S.-X. Liu, P. Jelínek, E. Meyer and T. Glatzel, *ACS Nano*, 2017, **11**, 8413–8420.
14 R. Ebeling, S. Tsukamoto, E. Dirksen, V. Caciuc, T. J. J. Müller, N. Atodiresei and S. Karthäuser, *J. Phys. Chem. C*, 2017, **121**, 26916–26924.
15 R. C. Haddon, R. Rayford and A. M. Hirani, *J. Org. Chem.*, 1981, **46**, 4587–4588.
16 X. Chi, M. E. Itkis, K. Kirschbaum, A. A. Pinkerton, R. T. Oakley, A. W. Cordes and R. C. Haddon, *J. Am. Chem. Soc.*, 2001, **123**, 4041–4048.
17 L. Bensch, I. Gruber, C. Janiak and T. J. J. Müller, *Chem.–Eur. J.*, 2017, **23**, 10551–10558.
18 K. Guzow, M. Czerwinska, A. Ceszlak, M. Kozarzewska, M. Szabelski, C. Czaplewski, A. Lukaszewicz, A. A. Kubicki and W. Wiczk, *Photochem. Photobiol. Sci.*, 2013, **12**, 284–297.
19 G. Manolikakes, C. Muñoz Hernandez, M. A. Schade, A. Metzger and P. Knochel, *J. Org. Chem.*, 2008, **73**, 8422–8436.
20 S. Xu, H. Kamada, E. H. Kim, A. Oda and E.-i. Negishi, in *Metal-Catalyzed Cross-Coupling Reactions and More*, ed. A. de Meijere, S. Bräse and M. Oestreich, Wiley-VCH, Weinheim, Germany, 2014, pp. 133–278.
21 A. Weller, *Z. Phys. Chem.*, 1982, **133**, 93–98.

© 2021 The Author(s). Published by the Royal Society of Chemistry

Open Access Article. Published on 08 December 2020. Downloaded on 10/10/2021 7:52:07 PM.
This article is licensed under a Creative Commons Attribution-NonCommercial 3.0 Unported Licence.

22 R. Felici, M. Pedio, F. Borgatti, S. Iannotta, M. Capozi, G. Ciullo and A. Stierle, *Nat. Mater.*, 2005, **4**, 688–692.
23 M. Huang, *Phys. Chem. Chem. Phys.*, 2012, **14**, 4959–4963.
24 M. Kiguchi, O. Tal, S. Wohlthat, F. Pauly, M. Krieger, D. Djukic, J. C. Cuevas and J. M. van Ruitenbeek, *Phys. Rev. Lett.*, 2008, **101**, 046801.
25 R. Otero, A. L. Vázquez de Parga and J. M. Gallego, *Surf. Sci. Rep.*, 2017, **72**, 105–145.
26 A. L. Pinardi, G. Biddau, K. van De Ruit, G. Otero-Irurueta, S. Gardonio, S. Lizzit, R. Schennach, C. F. Flipse, M. F. López, J. Méndez, R. Pérez and J. A. Martín-Gago, *Nanotechnology*, 2014, **25**, 385602.
27 A. Ugolotti, S. S. Harivyasi, A. Baby, M. Dominguez, A. L. Pinardi, M. F. López, J. A. Martín-Gago, G. Fratesi, L. Floreano and G. P. Brivio, *J. Phys. Chem. C*, 2017, **121**, 22797–22805.
28 T. Jacob, R. P. Muller and W. A. Goddard, III, *J. Phys. Chem. B*, 2003, **107**, 9465–9476.
29 G. Papoian, J. K. Norskov and R. Hoffmann, *J. Am. Chem. Soc.*, 2000, **122**, 4129–4144.
30 Z. Gu and P. B. Balbuena, *J. Phys. Chem. C*, 2007, **111**, 9877–9883.
31 H. Ihm, H. M. Ajo, J. M. Gottfried, P. Bera and C. T. Campbell, *J. Phys. Chem. B*, 2004, **108**, 14627–14633.
32 W. Liu, J. Carrasco, B. Santra, A. Michaelides, M. Scheffler and A. Tkatchenko, *Phys. Rev. B: Condens. Matter Mater. Phys.*, 2012, **86**, 245405.
33 V. P. Gupta, *Principles and Applications of Quantum Chemistry*, Academic Press, London, UK, 2016.
34 X. Jia and W. An, *J. Phys. Chem. C*, 2018, **122**, 21897–21909.
35 L. Vitali, G. Levita, R. Ohmann, A. Comisso, A. De Vita and K. Kern, *Nat. Mater.*, 2010, **9**, 320–323.
36 P. C. Rusu and G. Brocks, *Phys. Rev. B: Condens. Matter Mater. Phys.*, 2006, **74**, 073414.
37 X. Yang, R. Lu, F. Gai, P. Xue and Y. Zhan, *Chem. Commun.*, 2010, **46**, 1088–1090.
38 J. M. Soler, E. Artacho, J. D. Gale, A. García, J. Junquera, P. Ordejón and D. Sánchez-Portal, *J. Phys.: Condens. Matter*, 2002, **14**, 2745–2779.
39 M. Dion, H. Rydberg, E. Schröder, D. C. Langreth and B. I. Lundqvist, *Phys. Rev. Lett.*, 2004, **92**, 246401.
40 G. Román-Pérez and J. M. Soler, *Phys. Rev. Lett.*, 2009, **103**, 096102.
41 K. Momma and F. Izumi, *J. Appl. Crystallogr.*, 2011, **44**, 1272–1276.
42 J. Tersoff and D. R. Hamann, *Phys. Rev. B: Condens. Matter Mater. Phys.*, 1985, **31**, 805.

© 2021 The Author(s). Published by the Royal Society of Chemistry

Electronic Supplementary Material (ESI) for Nanoscale Advances.
This journal is © The Royal Society of Chemistry 2020

Electronic supplementary information (ESI) for Nanoscale

Preservation of the donor-acceptor character of a carbazol-phenalenone dyad upon adsorption on Pt(111)

René Ebeling, Narendra P. Arasu, Lisa Bensch, Bertram Schulze Lammers, Bernhard Mayer, Thomas J. J. Müller, Héctor Vázquez, and Silvia Karthäuser**

S1: STM overview of a prototypical Pt(111) surface after CBHP evaporation

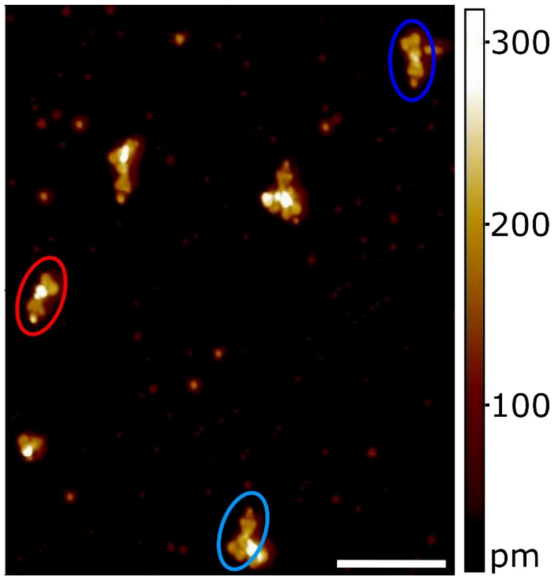

Fig. S1 STM image (U_{BIAS} = 50 mV, I_{SET} = 200 pA, scale bar = 5nm) showing a typical sample of CBHP adsorbed on Pt(111). Two different adsorption configurations, ConA marked by a blue and ConB by a red ellipse, can be assigned to single molecules. One of the mirror configurations of CBHP, ConA', is exemplarily marked by a light blue ellipse. A recurring type of fragment, consisting of three spots, one bright and two shallow, is observed below CBHP in configuration ConB. These fragments often show up close to our target molecules (see center of Fig. S1).

S2 and S3: Detailed measurements of CBHP dimensions in ConA and ConB

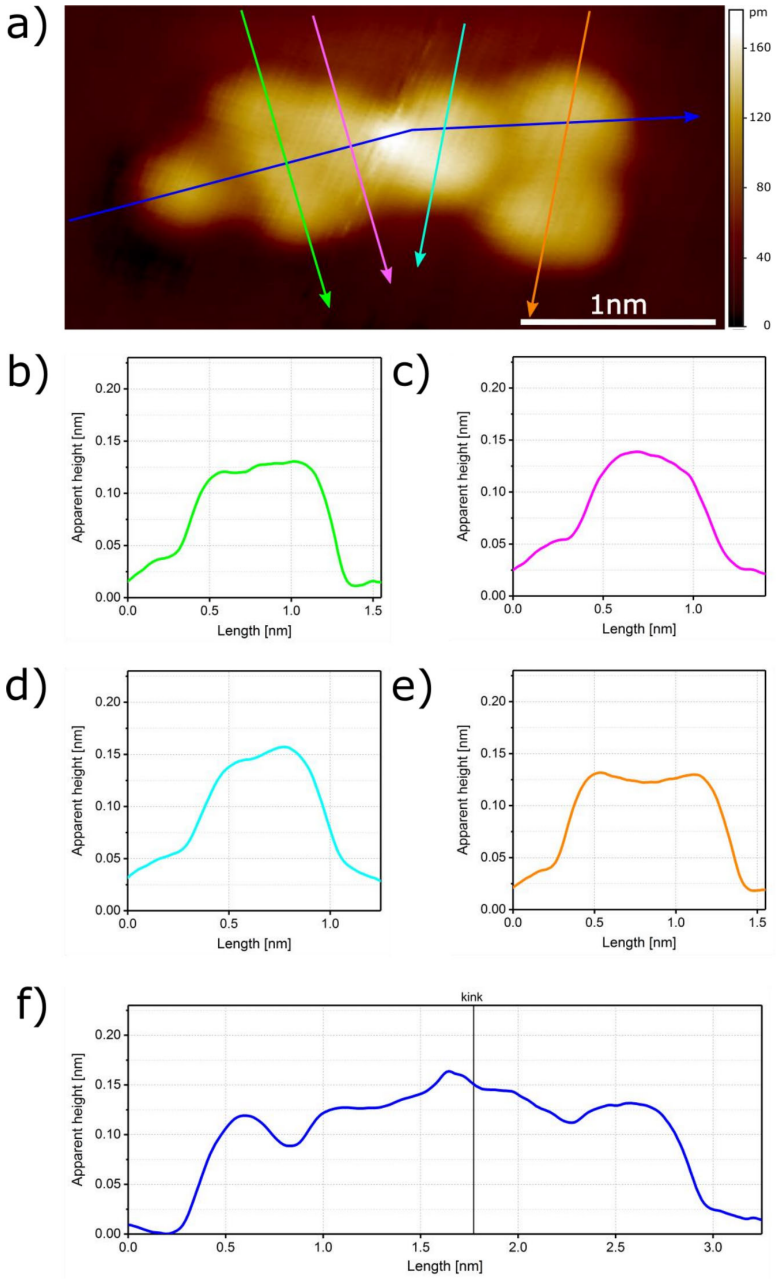

Fig. S2 (a) Unfiltered high resolution STM measurement (U_{BIAS} = 50 mV, I_{SET} = 200 pA) of Fig. 1a. An identical color scale is used in Fig. S3a. (b–f) Averaged apparent height profiles along different directions of configuration ConA of CBHP. Direction and position of the corresponding height profiles are given in a) in the same color scheme. (f) This profile follows a kink along the molecular axis.

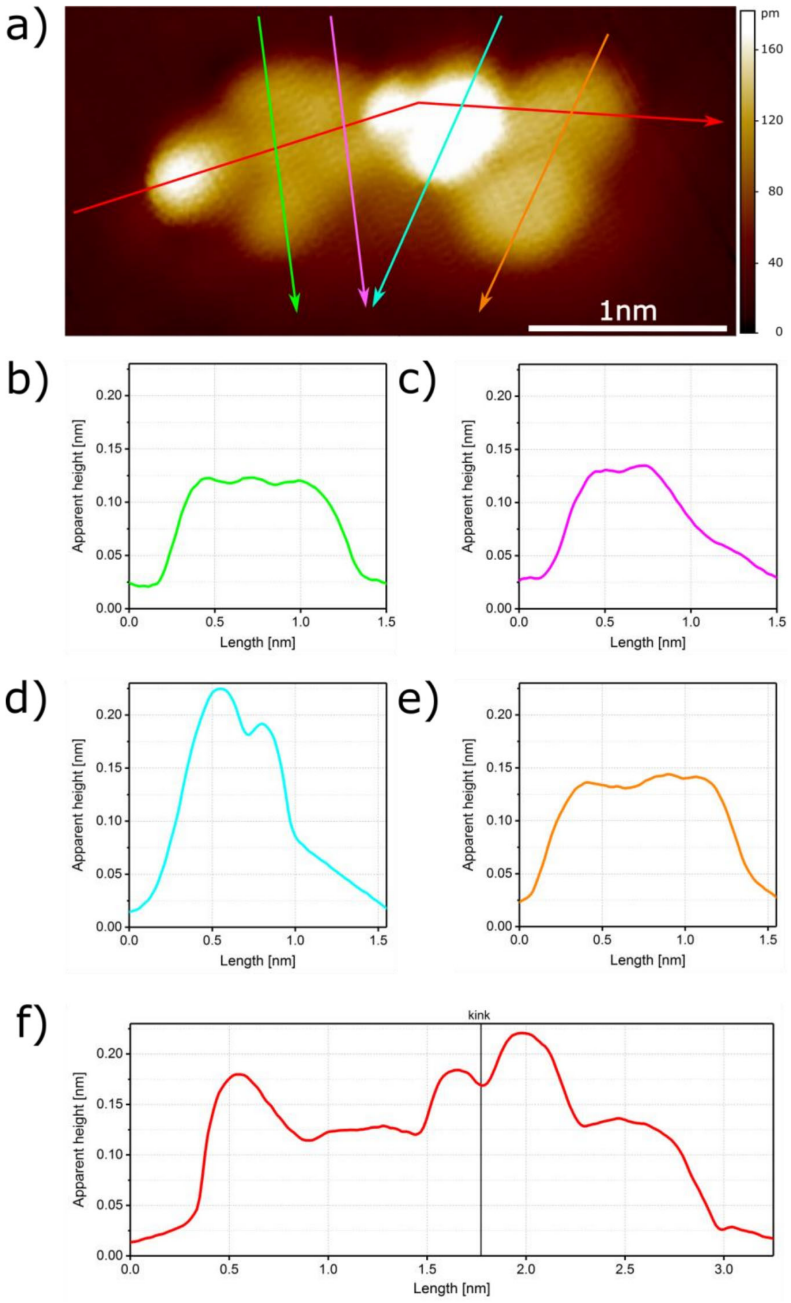

Fig. S3 (a) Unfiltered high resolution STM measurement (U_{BIAS} = 50 mV, I_{SET} = 200 pA) of Fig. 1b. An identical color scale is used in Fig. S2a. (b–f) show averaged apparent height profiles along different directions of configuration ConB of CBHP. Direction and position of the corresponding height profiles are given in a) in the same color scheme. (f) This profile follows a kink along the molecular axis.

S4: Calculated geometries and STM images of CBHP on Pt(111)

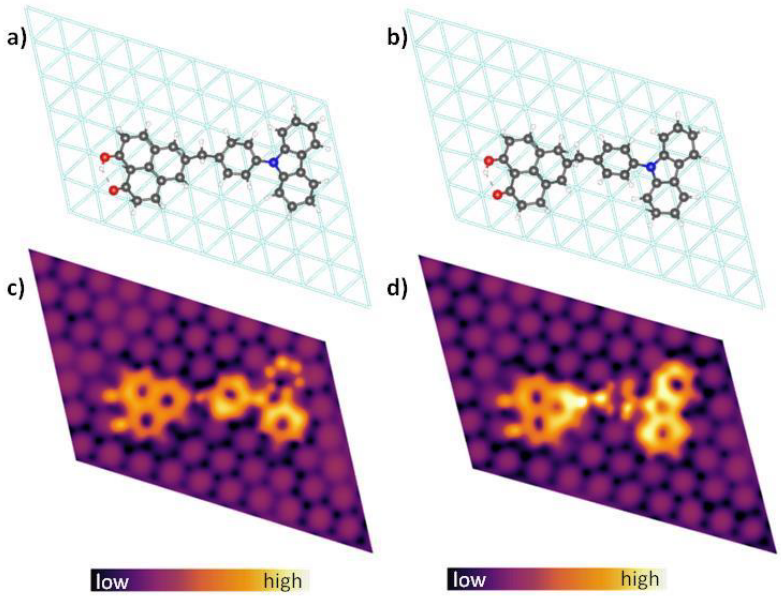

Fig. S4 (a, b) Geometries of the CBHP molecule, where no Pt adatom is present, on the Pt(111) surface corresponding to local minima from DFT calculations (c, d) Simulated constant-current STM images around the Fermi energy.

S5: Progress of a raw to a filtered STM image

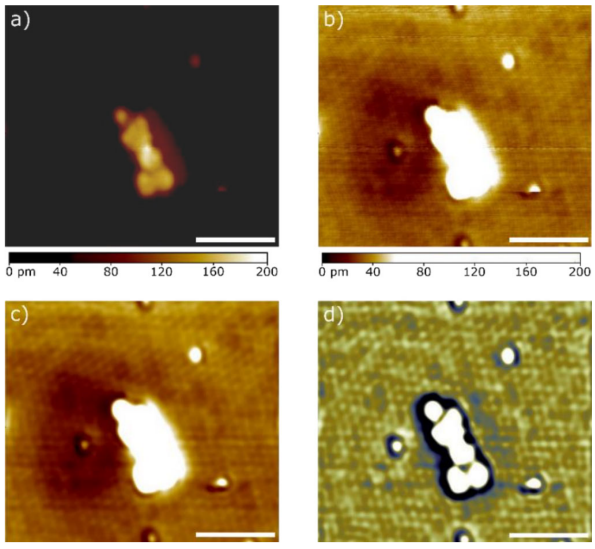

Fig. S5 Steps of image processing for Fig. 2a to present the atomic structure of the Pt(111) substrate combined with orbital molecular features of CBHP in the same STM image. (a, b) Raw STM measurements of a single molecule in ConA in different apparent height scales. The scale in a) puts the focus on the molecular structure while the scale chosen in b) emphasizes the atomic lattice of Pt(111). (c) Slight Fourier filtering of b) reduces the noise. (d) In a last step an ISO 11562 Gaussian Profile Filter is applied to c).

S6: Voltage dependent STM images of CBHP in ConA

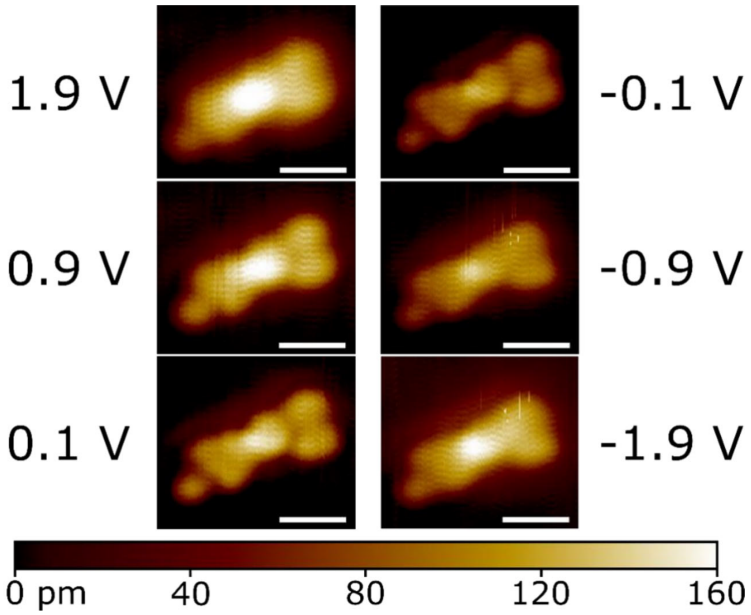

Fig. S6 Voltage dependent STM measurement (I_{SET} = 200 pA) of ConA. An identical color scale is used for all unfiltered Images. The scale bar is 1 nm.

S7: PDOS of ConA together with LDOS at selected energies

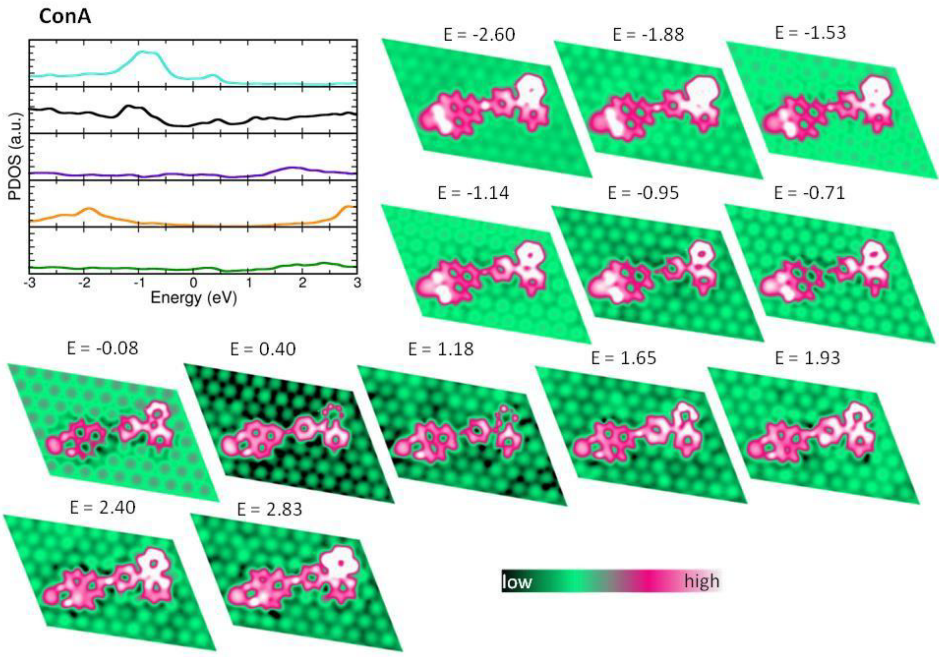

Fig. S7 Calculated PDOS of the CBHP-Pt donor-acceptor dyad adsorbed in ConA and LDOS at selected energies (in eV). Color code like indicated in Fig. 3 and 4: HP acceptor (black), central part (purple), two spots over the donor CB (green and orange), Pt adatom (turquoise).

S8: Kohn-Sham frontier molecular orbitals (FMOs) for CBHP in acetonitril

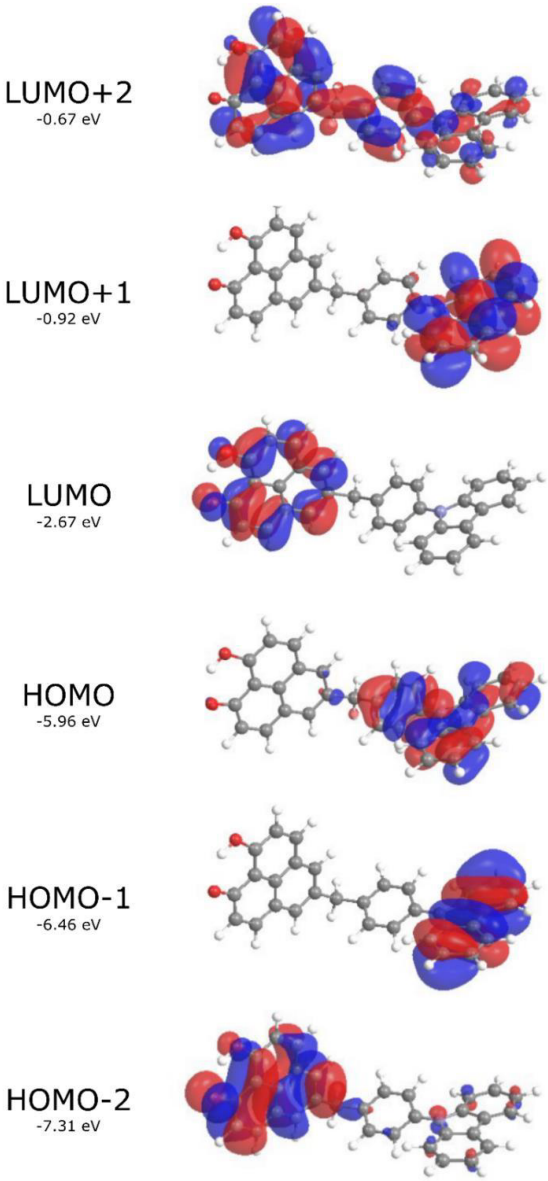

Fig. S8: Chosen Kohn-Sham Frontier Molecular Orbital (FMOs) for CBHP. A polarizable continuum model was used for its calculation (*Gaussian 09 PBEh1PBE/6-311+G***) with acetonitrile as solvent.

S9 and S10: Frontier molecular orbitals of CBHP and CBHP-Pt in ConA and ConB

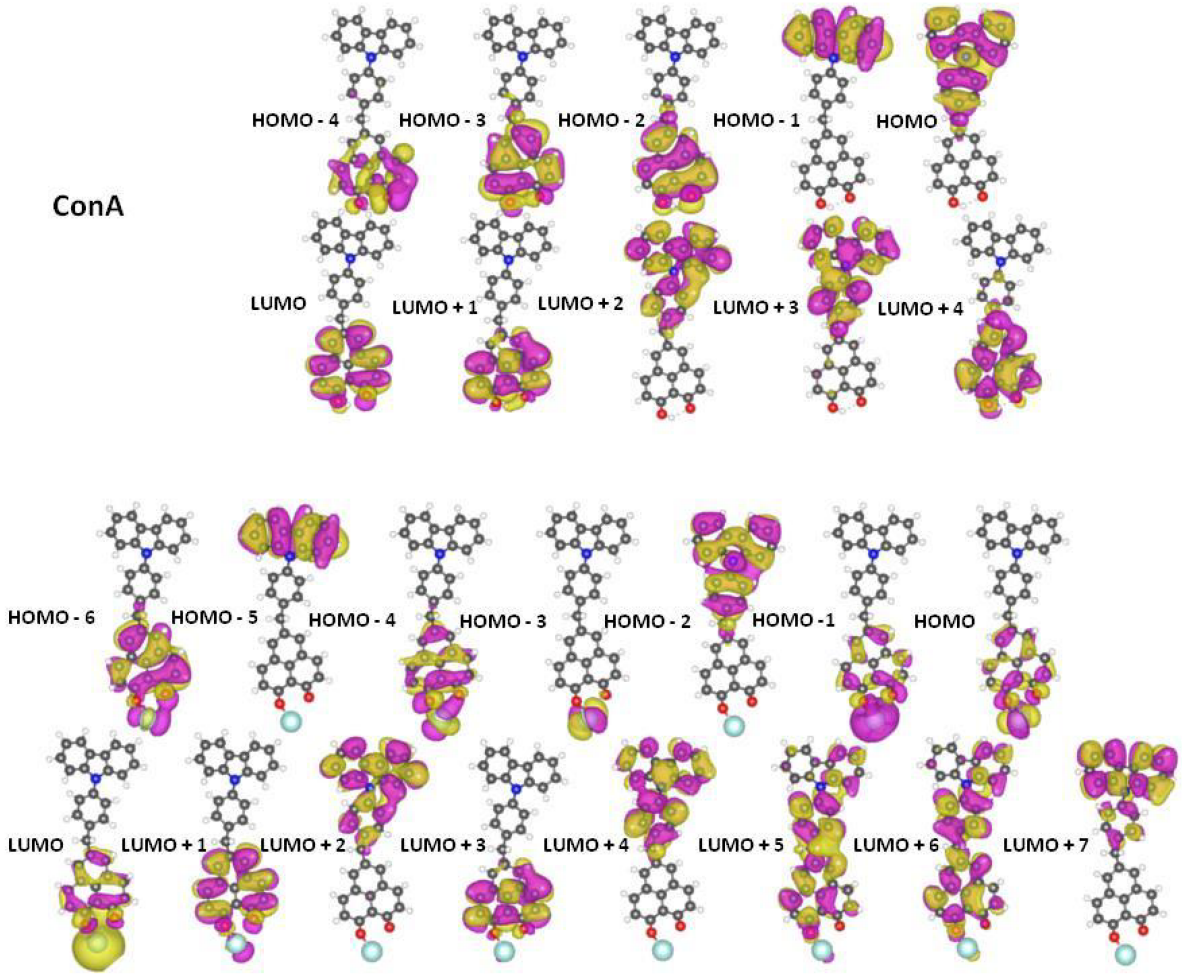

Fig. S9 Occupied and unoccupied frontier molecular orbitals of the isolated CBHP molecule (top) and of the CBHP-Pt complex (bottom) in ConA.

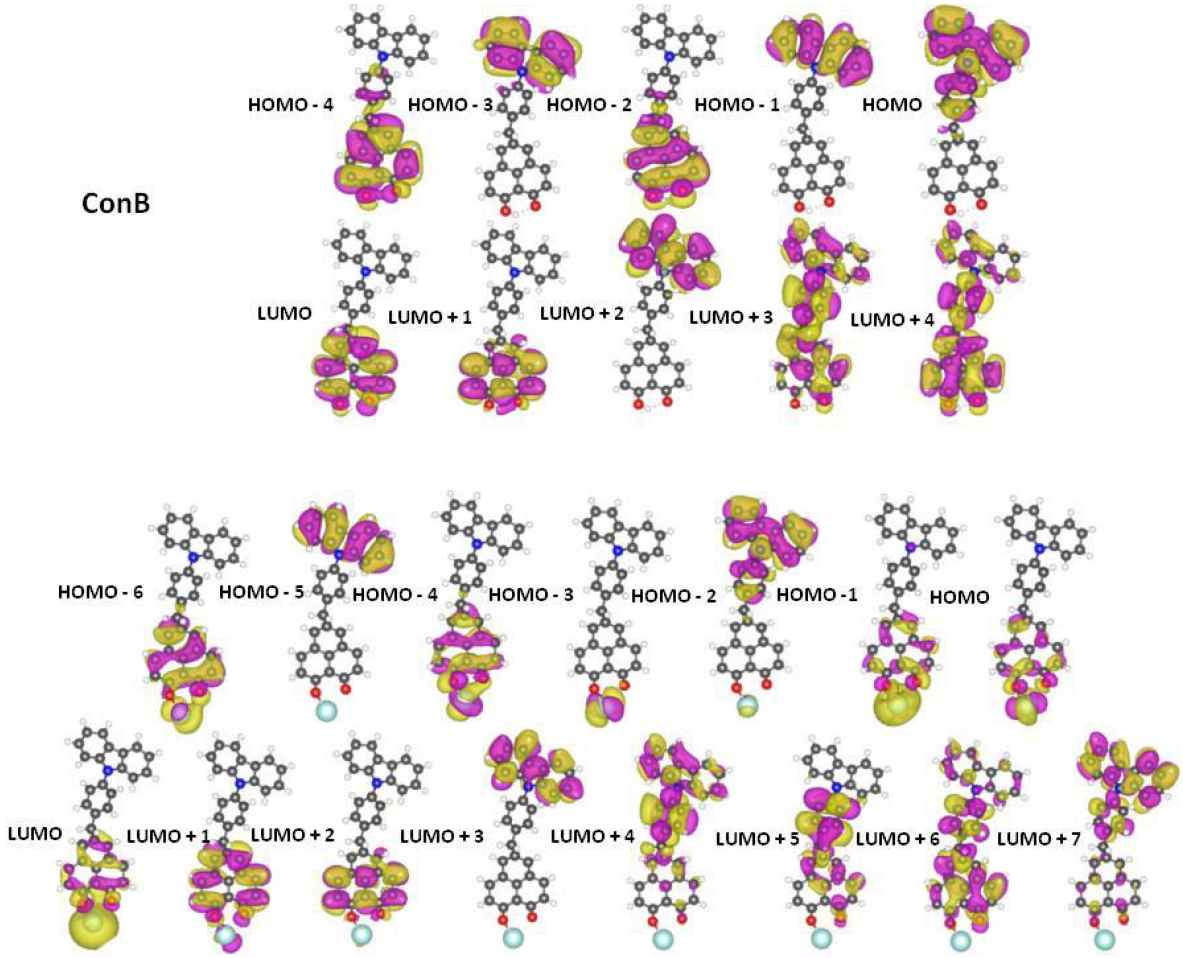

Fig. S10 Occupied and unoccupied frontier molecular orbitals of the isolated CBHP molecule (top) and of the CBHP-Pt complex (bottom) in ConB.

S11: PDOS of ConB together with LDOS at selected energies

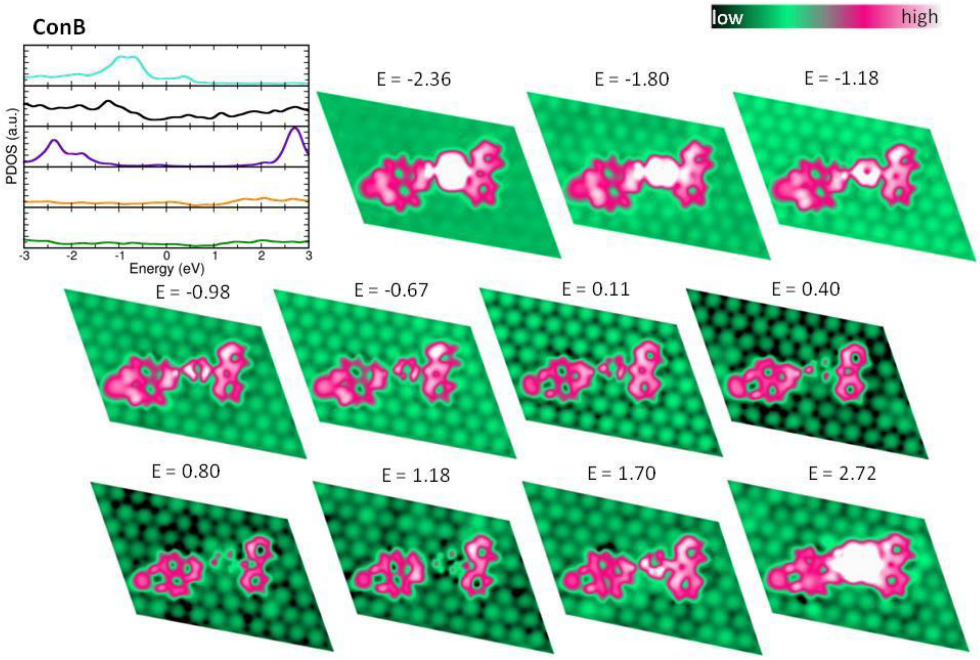

Fig. S11 Calculated PDOS of the CBHP-Pt donor-acceptor dyad adsorbed in ConB and LDOS at selected energies (in eV). Color code like indicated in Fig. 3 and 4: HP acceptor (black), central part (purple), two spots over the donor CB (green and orange), Pt adatom (turquoise).

S12: TGA and DTA of CBHP

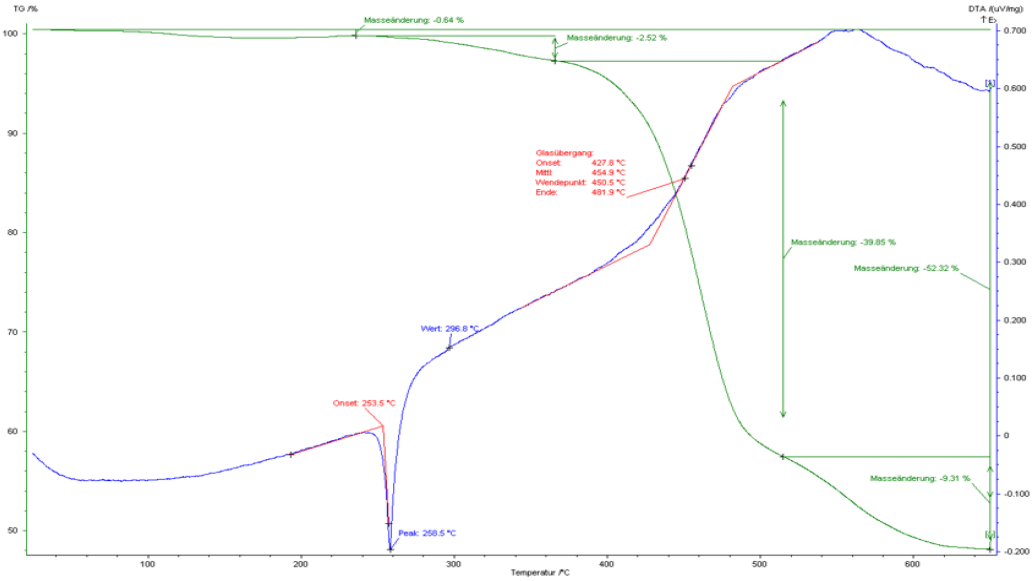

Fig. S12: Thermogravimetric (TGA) and differential thermal analysis (DTA) of CBHP measured using simultaneous thermal analyzer NETZSCH STA 449C.

3. Adsorption of a novel carbene molecule on the Au surface

3.1 Introduction

In chemistry, carbenes are traditionally known as highly reactive, and short-lived intermediate compounds [73] that are useful to add a carbon atom into a molecule [74]. The reactivity of carbenes comes from the electronic unsaturation of a carbon atom in the molecular ring. Two of the four valance electrons of the unsaturated carbon atom contribute to form one bond, each with the neighboring atom. The two remaining electrons are either left unpaired (triplet carbene), or both electrons stay together as a lone pair (singlet carbene) as shown in figure 3.1. Both singlet and triplet carbenes are highly reactive and proved to be a challenge for synthetic chemists.

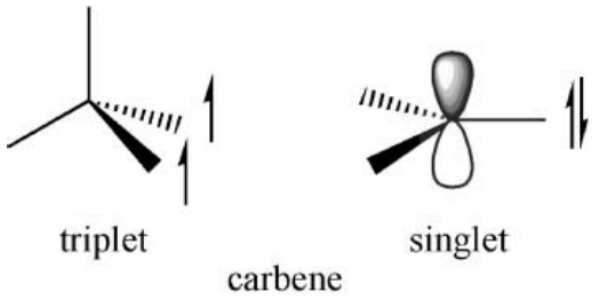

Figure 3.1: Electronic structure of singlet and triplet carbenes. The figure is same as Fig. 1 of [75].

For over a century, all attempts to synthesis stable uncoordinated carbenes were unsuccessful. At last, in 1991, Arduengo et al. managed to synthesize the first stable carbene molecule. The stability is incorporated by placing the carbene molecule between nitrogen heterocycles, and hence the molecule is termed as N-heterocyclic carbene (NHC) [76]. The core of the NHC molecule is a pentagonal ring in which a carbon atom has two C-N bonds and a lone pair, as shown in figure 3.2. NHCs were found to be more electron-rich ligands than the conventional phosphines, leading to great interest in NHC-based catalysis [77]. The presence of a lone pair in the plane of NHC makes the molecule suitable for forming coordination bonds with transition metals. The instant binding to transition metal ions led to the development of NHC-based molecular devices [78–80]. Further studies show that the exceptional stability of the metal-NHC coordination results in uniform monolayer coverage of NHC on metal surface [81, 82]. The discovery and subsequent studies of NHC molecules showed the large potential of carbenes in organometallic applications.

The quest for other carbene molecules with different catalytic behavior than NHCs lead to the discovery of a more stable bis(dialkylamino)cyclopropenylidenes (BAC) molecule [83]. The core of BAC is a triangular structure made of carbon

atoms, as shown in figure 3.2. Bulky side groups stabilize the molecule. The chemical reactions induced by BACs are different from those observed from NHCs. For example, NHCs promote the aggregation of phosphorous, whereas BACs degrade phosphorous to elementary compounds [84, 85]. BACs exhibit better σ-donor properties than NHCs [86], providing promise for higher surface coverage than NHCs. We studied for the first time BAC molecules deposited on a metal surface [87].

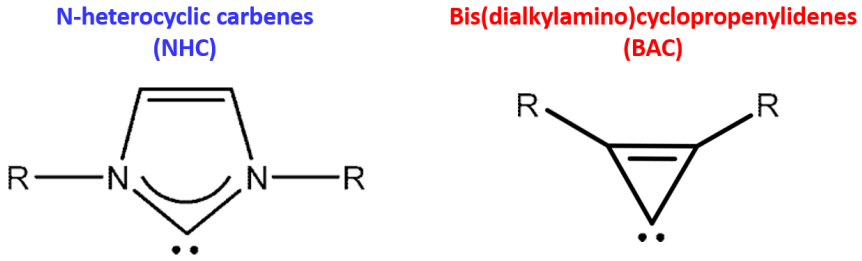

Figure 3.2: Chemical structures of NHC and BAC molecules. R represents bulky side group attached to the molecule. Lone pairs are indicated by two dots.

The synthesis of BAC molecule was carried out by our collaborators from the group of Xavier Roy, Columbia University (USA). The molecule was deposited on Au(111), and surface absorption was measured through high-resolution X-ray photoelectron spectroscopy (XPS) and near-edge X-ray absorption fine structure (NEXAFS). Both XPS and NEXAFS experiments use X-ray radiation from a synchrotron source to detect the adsorption configuration on the surface. XPS and NEXAFS experiments were carried out by associates from the University of Ljubljana, Slovenia. Atomic-scale adsorption configurations of BAC on Au(111) were probed with STM and AFM spectroscopy by our collaborators from Brookhaven National Laboratory and the group of Latha Venkataraman at Columbia University (USA). We performed DFT calculations to investigate the adsorption properties of BAC on Au(111) substrate. We compare adsorption configurations of NHC and BAC core structures. Our study is the first work on BAC molecules deposited on a metal surface.

Experiments reveal that BAC forms uniform monolayer coverage over Au(111) upon annealing, as shown in figure 3.3. NEXAFS results suggest that the BAC molecule adsorbs at a tilt angle, whereas NHC stands vertical on the surface. To reveal the angular adsorption of the BAC molecule, we performed a potential energy scan along the angle (θ) between the molecular plane and the vertical direction. Our calculations show that the binding energy of BAC molecule reaches a maximum at $\theta = 40°$, while NHC the favorable binding is when $\theta = 0°$. To elucidate the contribution of the BAC core on adsorption angle, in our calculations, we replaced the bulky side groups of BAC molecules with H atoms. The 40° tilted adsorption was true for the truncated BAC structure as well, showing no role of side groups in the adsorption angle.

We further investigated the reason behind the tilt angle of the BAC molecule. We calculated the binding of gas-phase BAC and NHC core structures bound to Au adatom to check if the tilt angle was inherent to the Au-BAC bond. Our

calculations showed that the angled adsorption of BAC is indeed inherent to the electronic structure of the BAC core. The BAC lone pair is more electronegative than the NHC lone pair leading to flexible adsorption of the Au-molecule bond. Our study shows that BAC molecules' high electronegativity and flexible tilted adsorption provide an excellent platform for carbene-based molecular layers on metal surfaces.

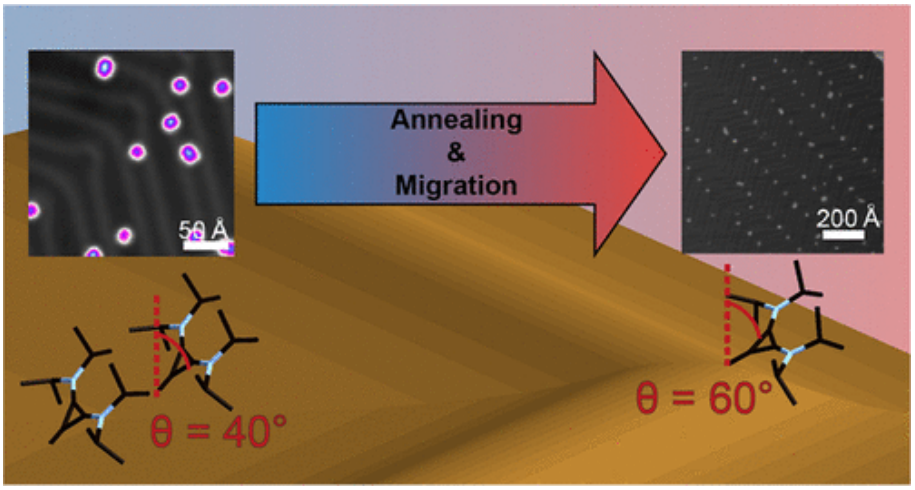

Figure 3.3: Insets show the bis(dialkylamino)cyclopropenylidenes (BAC) molecules forming a uniform coverage on the Au (111) surface upon annealing. The tilted adsorption of BAC is shown as graphical illustration. The figure is taken from the TOC of the article [87].

3.2 My contribution to the article

I performed the gas phase calculations of BAC and NHC molecules and molecule Au adatom complexes. I performed the calculation using Gaussian ab-initio code with B3LYP functional and 6-31G* basis set. I contributed to making computational figures in both the main text and supplementary information.

JACS
JOURNAL OF THE AMERICAN CHEMICAL SOCIETY
pubs.acs.org/JACS
Communication

Cyclopropenylidenes as Strong Carbene Anchoring Groups on Au Surfaces

Evan A. Doud,◆ Rachel L. Starr,◆ Gregor Kladnik,◆ Anastasia Voevodin,◆ Enrique Montes, Narendra P. Arasu, Yaping Zang, Percy Zahl, Alberto Morgante,* Latha Venkataraman,* Héctor Vázquez,* Dean Cvetko,* and Xavier Roy*

Cite This: J. Am. Chem. Soc. 2020, 142, 19902−19906

Read Online

ACCESS | Metrics & More | Article Recommendations | Supporting Information

ABSTRACT: The creation of stable molecular monolayers on metallic surfaces is a fundamental challenge of surface chemistry. N-Heterocyclic carbenes (NHCs) were recently shown to form self-assembled monolayers that are significantly more stable than the traditional thiols on Au system. Here we theoretically and experimentally demonstrate that the smallest cyclic carbene, cyclopropenylidene, binds even more strongly than NHCs to Au surfaces without altering the surface structure. We deposit bis(diisopropylamino)cyclopropenylidene (BAC) on Au(111) using the molecular adduct BAC−CO_2 as a precursor and determine the structure, geometry, and behavior of the surface-bound molecules through high-resolution X-ray photoelectron spectroscopy, atomic force microscopy, and scanning tunneling microscopy. Our experiments are supported by density functional theory calculations of the molecular binding energy of BAC on Au(111) and its electronic structure. Our work is the first demonstration of surface modification with a stable carbene other than NHC; more broadly, it drives further exploration of various carbenes on metal surfaces.

Downloaded via CHARLES UNIV IN PRAGUE on October 10, 2021 at 18:53:10 (UTC).
See https://pubs.acs.org/sharingguidelines for options on how to legitimately share published articles.

Cyclopropenylidene, the smallest aromatic molecule displaying a carbene center, has received widespread theoretical and experimental interest due to its unique electronic structure, chemical reactivity, and existence in interstellar space.[1−5] Cyclopropenylidene, however, is too unstable to be isolated as a free carbene. First reported as a stable crystalline solid by Bertrand and co-workers, bis(dialkylamino)cyclopropenylidenes (Figure 1a) consist of the cyclopropenylidene ring functionalized with two dialkylamino groups.[2,3,6] The presence of these dialkylamino groups stabilizes the free carbene and, combined with the highly strained nature of the ring and the resulting small angle at the carbenic carbon, produce a molecule capable of remarkably strong σ-donation. Most experimental and theoretical investigations indicate that bis(dialkylamino)cyclopropenylidenes are in fact better σ-donors than N-heterocyclic carbenes (NHCs) while having a smaller footprint.[7] Carbenes have recently received intense attention due to their rich coordination chemistry[8−10] and ability to form ultrastable self-assembled monolayers on metal surfaces.[11−16] While diazomethane derivatives have been used to assemble carbene molecules on Ru surfaces,[16] most recent studies have focused on NHCs, prompting the question whether carbenes such as bis(dialkylamino)cyclopropenylidenes could strongly bind to metal surfaces.

In this work, we investigate for the first time the functionalization of metal surfaces with bis(diisopropylamino)-cyclopropenylidene (BAC). Using density functional theory (DFT), we first present a detailed theoretical picture of the bonding energetics and geometry of BAC to a Au(111) surface. We then develop a simple synthetic approach to

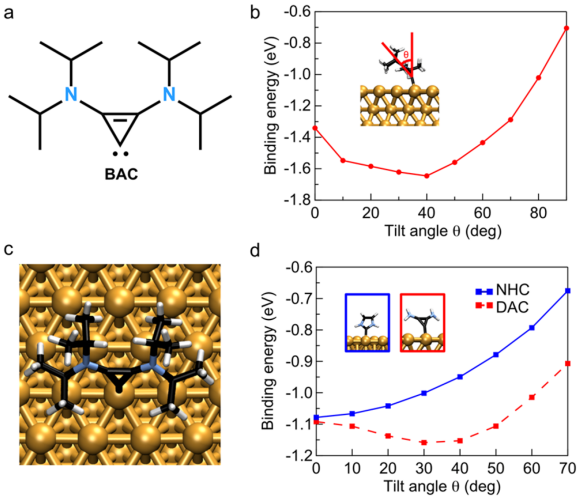

Figure 1. (a) Chemical structure of BAC. (b) Calculated binding energy of BAC as a function of tilt angle θ. (c) Structure of BAC absorbed on the Au(111) surface for θ = 40°. (d) Calculated binding energy of DAC and NHC cores on the Au(111) surface as a function of tilt angle θ.

Received: October 9, 2020
Published: November 11, 2020



ACS Publications
© 2020 American Chemical Society

https://dx.doi.org/10.1021/jacs.0c10743
J. Am. Chem. Soc. 2020, 142, 19902−19906

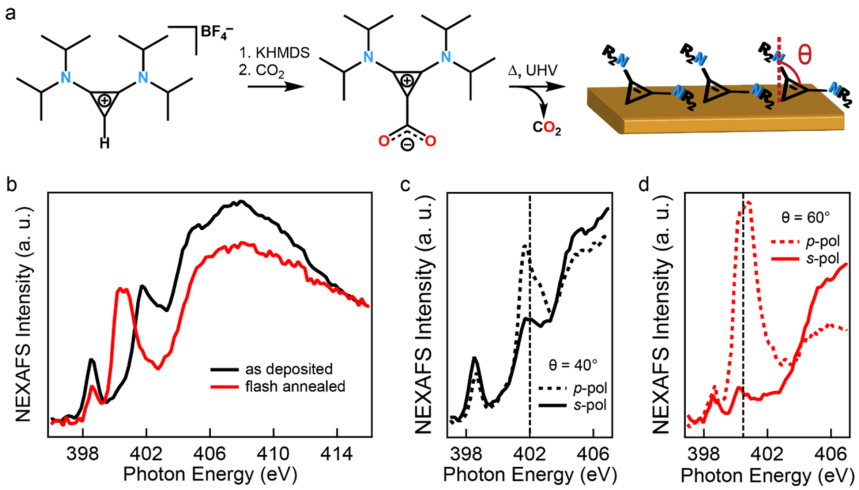

Figure 2. (a) Synthesis of BAC−CO_2 and subsequent vapor deposition onto Au(111). (b) Magic angle NEXAFS spectra collected at the N K-edge of the BAC deposited on the Au(111) substrate at 100 °C (black) and then annealed at 200 °C (red). (c, d) NEXAFS N K-edge spectra of the BAC deposited at 100 °C (c) and annealed at 200 °C (d) collected with the electric field of the incident photons perpendicular (*p*-pol) and parallel (*s*-pol) to the surface. The dashed vertical black line indicates the N 1s → π^* LUMO absorption peak in both (c) and (d).

deposit BAC on Au(111) surfaces in ultrahigh vacuum (UHV) and use synchrotron radiation to probe the geometry of the carbenes on the surface through high-resolution X-ray photoelectron spectroscopy (XPS) and near-edge X-ray absorption fine structure (NEXAFS). To support these measurements, we image the surface-bound BACs using high-resolution scanning tunneling microscopy and atomic force microscopy (STM and AFM). Overall, our results indicate that cyclopropenylidenes are attractive anchoring groups to modify metal surfaces.

We first model the bonding of BAC to a Au(111) surface using atomistic DFT-based simulations with van der Waals interactions. We start by determining the orientation of the cyclopropenylidene ring relative to the Au(111) surface, which is modeled as three Au layers, each containing 36 atoms (section 2 of the Supporting Information (SI)). For these simulations, the tilt angle (θ) of the ring relative to the surface normal is fixed and all other atoms, including the surface Au atoms, are fully relaxed. This is done by allowing the C atoms in the cyclopropenylidene ring to shift rigidly in any direction. The resulting energy profile is shown in Figure 1b. In the vertical orientation (θ = 0°), the binding energy is −1.34 eV, close to that of NHC on a Au(111) surface (−1.49 eV).[15] The favored adsorption site for BAC is an atop site with a Au−C distance of 2.2 Å. As the molecule is tilted and θ increases, the binding energy increases due to the contributions from the Au−C dative bond and the van der Waals interactions with the surface. The binding energy reaches a maximum at θ = 40° (Figure 1b, c) and decreases for larger θ due to a reduction of the BAC−Au orbital overlap and steric repulsion between the isopropyl N-substituents and the surface. The calculated binding energy at θ = 40° is −1.65 eV, larger than the reported value of −1.49 eV for ^{Me}NHC on Au(111).[15]

To quantify the steric role of the isopropyl N-substituents, we calculate the adsorption properties of a BAC molecule in which the isopropyl groups are replaced with H atoms (diaminocyclopropenylidenes, DAC). The binding energy is shown in Figure 1d as a function of tilt angle up to θ = 70° (for θ > 70°, the Au contact atom is extracted from the surface and these geometries are thus excluded). Comparison with Figure 1b reveals that both BAC and DAC adopt roughly similar tilt angles on the Au(111) surface but the binding energy of BAC is significantly larger (by 0.2−0.4 eV) than that of DAC. When the tilt angle is large, however, the binding energy decreases more rapidly for BAC due to the increased steric repulsion with the surface. Similar to observations of NHCs bound to Au,[17] we find that dispersive interactions between the surface and the cyclopropenylidene core and pendent isopropyl groups contribute significantly to the binding energy. These results suggest that the binding energy of cyclopropenylidenes to a Au substrate could be further increased by functionalizing the ring with amino groups bearing substituents that can strongly interact with the surface.

We also compare the binding energies of DAC and dihydroimidazol-2-ylidene (NHC) to understand the effect of the ring structure. Figure 1d presents the calculated binding energy of both model carbenes as a function of tilt angle. When θ = 0°, the binding energies of both molecules are similar and close to −1.10 eV. However, the DAC ring can sustain a stable geometry for larger θ whereas the NHC core cannot. This is seen even when calculated DAC or NHC rings are bound to a single Au atom (Figure S2). These results suggest that cyclopropenylidene rings can form stronger and less constrained bonds to a Au(111) surface.

To validate these predictions and experimentally probe the binding of BAC to a Au surface, the BAC−CO_2 adduct was synthesized and used as a precursor that thermally decomposes in UHV to generate free BAC, which can be deposited from the gas phase onto the Au(111) surface (Figure 2a). We deposited BAC by thermal decomposition/sublimation of the BAC−CO_2 precursor on Au(111) surfaces and performed X-ray calculations of the C 1s core-electron binding energies for BAC on a Au surface (Figure S8). We performed XPS measurements on as-deposited and annealed monolayers.[15] The XPS reveals the presence of C and N on the Au(111) surface and the absence of O, consistent with the BAC anchored to the surface without the CO_2 moiety (Figure S4). Moreover, the C 1s photoemission spectrum is well

https://dx.doi.org/10.1021/jacs.0c10743
J. Am. Chem. Soc. 2020, 142, 19902−19906

reproduced by DFT calculations of the C 1s core-electron binding energies for BAC on a Au surface (Figure S8). We performed X-ray polarization dependent NEXAFS measurements to determine the average orientation of the BAC ring relative to the Au(111) surface normal (Figure 2a). For this measurement, we focus on the N K-edge NEXAFS spectra because the C K-edge NEXAFS spectrum contains a complex fine structure with significant contribution from the isopropyl groups (Figure S9).

We then examine the electronic structure of the unoccupied molecular orbitals in both the as-deposited and annealed films by comparing NEXAFS spectra in the magic angle configuration (Figure 2b). Under these specific conditions, the orientations of the molecules do not influence the NEXAFS signal.[18] We notice a substantial change of the measured NEXAFS spectra between the two films, with a shift of the main absorption peak from ~402 to ~400.5 eV after annealing at 200 °C. Note that the peak at ~398.5 eV, which grows with X-ray exposure, is likely due to molecular fragmentation caused by the beam and not an intrinsic property of the BAC. DFT-based half-core-hole calculations of the X-ray absorption spectra of the BAC molecule coupled to a Au dimer (Figure S10a) allow us to assign the absorption peaks at ~402 eV in the as deposited film and at ~400.5 eV in the annealed film to the same N 1s → π^* LUMO transition (Figure S10b). Of particular note, our DFT calculations reveal that the excitation energy of this transition strongly depends on the Au−C distance (Figure S10a). Although the observed energy difference is not fully reproduced by DFT, our calculations show a clear trend toward lower excitation energies with decreasing Au−C distances, indicating a stronger binding of the BAC to Au surface upon annealing. Annealing may enable molecular migration to undercoordinated Au sites, e.g., adatoms, enhancing electronic coupling.

We next measure NK-edge NEXAFS spectra of a BAC monolayer deposited on Au(111) at 100 °C with the incident photon electric field directed either perpendicular (*s*-polarization) or parallel (*p*-polarization) to the surface normal to determine the average molecular surface orientation.[18] From the intensity difference of the N 1s → π^* LUMO transition absorption peaks (at ~402 eV) measured using *s*- and *p*-polarizations (Figure 2c), we calculate an average $\theta \sim 40°$, consistent with our DFT calculations (Figure 1b). After annealing the sample to 200 °C, the linear dichroism of the N 1s → π^* LUMO transition (at ~400.5 eV) is enhanced (Figure 2d), resulting in $\theta \sim 60°$. This average tilt angle is larger than DFT-based predictions, suggesting that annealing encourages BAC migration to undercoordinated Au sites, thus energetically favoring larger angles.

The orientation of NHCs on the surface is primarily determined by the N-substituents.[15] For BAC, the increased distance between the N-substituted and the carbenic carbon allows for relaxation of the molecule onto the surface and thus a greater tilt angle θ. NHCs can pull adatoms from the Au(111) substrate, forming flat-lying bis(NHC) complexes with the adatom on the surface.[15,19,20] These adatoms can be spectroscopically identified as satellite peaks in the XPS Au 4f spectrum.[15,21] By contrast, we see no evidence for such adatom formation when BAC is deposited on Au(111). The XPS Au 4f spectrum has no satellite peaks indicative of adatom formation (Figure S4).[22]

To support our spectroscopic and theoretical data, we imaged individual BAC molecules anchored to the Au surface with STM and AFM. Using the BAC−CO_2 precursor, we deposited a sub-monolayer of BAC on a Au(111) surface at ~5 K in ultrahigh vacuum. Figure 3a shows an STM image of the

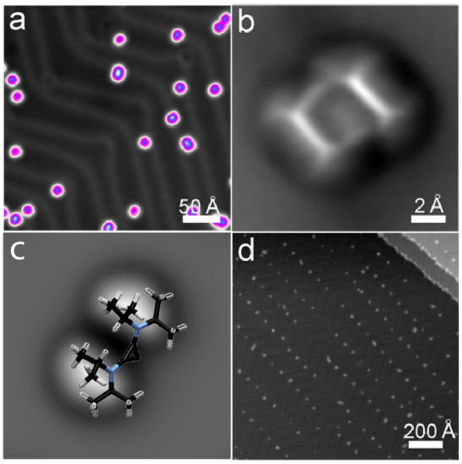

Figure 3. (a) STM image of BACs on the Au(111) surface (where the herringbone reconstruction is visible) (0.2 V, 50 pA). (b) High-resolution AFM image of a single BAC molecule. (c) Simulated AFM image for a single BAC. (d) STM image of the BAC molecules on the Au(111) surface after annealing to 110 °C for a few seconds (0.2 V, 50 pA).

BACs affixed to the surface. Although a few dimers or clusters are visible, the molecules are generally well dispersed and separated with no preferred anchoring sites. We performed high resolution AFM imaging at 5 K of a single BAC using a CO-functionalized tip (Figure 3b). The BAC features two bright lobes attributed to the isopropyl groups. We simulated AFM images of the adsorbed molecule taken with a CO-functionalized tip using a probe particle model.[23] The simulation of the most stable geometry ($\theta = 40°$) reproduces the main experimental observations (Figure 3c). The two bright features, separated by ~5 Å, result from the repulsion of the hydrogen atoms in the terminal methyl groups of the diisopropyl substituents furthest from the surface. The molecule measures ~10 Å across, the confirmed diameter of BAC bound to reported metal-BAC complexes.[24] The three-membered ring is hidden underneath the bulky alkyl groups, expected for $\theta = 40°$.

The BAC-functionalized surface was heated at 110 °C for a few seconds and imaged again using STM to examine changes to the bound BACs. Figure 3d details the rearrangement of the molecules on the surface. At this temperature, the molecules are clearly mobile on the surface and relocate to the herringbone edges. The undercoordinated elbow sites of the herringbone structure are more favorable binding sites for BACs, corroborating the NEXAFS results.

In summary, we have studied for the first time the functionalization of a Au surface with cyclopropenylidene carbenes. Our results indicate that BACs bind more strongly to the surface than NHCs, making them highly suitable as surface binding ligands. Compared to NHCs, BACs have a unique structure with the bulky substituents away from the carbenic carbon. High resolution X-ray absorption spectroscopy supported by DFT-based calculations and single molecule imaging reveal how this structure allows BACs to adopt tilted

https://dx.doi.org/10.1021/jacs.0c10743
J. Am. Chem. Soc. 2020, 142, 19902−19906

orientations that maximize their binding energy without Au-adatom formation. This work opens an exciting new area of investigation in the rapidly developing field of self-assembled carbene monolayers on surfaces.

■ ASSOCIATED CONTENT

Supporting Information

The Supporting Information is available free of charge at https://pubs.acs.org/doi/10.1021/jacs.0c10743.

Synthetic details, DFT calculations, XPS and NEXAFS details, STM and AFM details (PDF)

■ AUTHOR INFORMATION

Corresponding Authors

Alberto Morgante − *CNR-IOM Laboratorio Nazionale TASC, 34149 Trieste, Italy; Department of Physics, University of Trieste, 34127 Trieste, Italy;* orcid.org/0000-0001-9021-2944; Email: morgante@iom.cnr.it

Latha Venkataraman − *Department of Chemistry and Department of Applied Physics, Columbia University, New York, New York 10027, United States;* orcid.org/0000-0002-6957-6089; Email: lv2117@columbia.edu

Héctor Vázquez − *Institute of Physics, Czech Academy of Sciences, Prague 16200, Czech Republic;* orcid.org/0000-0002-3865-9922; Email: vazquez@fzu.cz

Dean Cvetko − *CNR-IOM Laboratorio Nazionale TASC, 34149 Trieste, Italy; Faculty of Mathematics and Physics, University of Ljubljana, 1000 Ljubljana, Slovenia; J. Stefan Institute, SI-1000 Ljubljana, Slovenia;* Email: cvetko@iom.cnr.it

Xavier Roy − *Department of Chemistry, Columbia University, New York, New York 10027, United States;* orcid.org/0000-0002-8850-0725; Email: xr2114@columbia.edu

Authors

Evan A. Doud − *Department of Chemistry, Columbia University, New York, New York 10027, United States;* orcid.org/0000-0003-4561-4105

Rachel L. Starr − *Department of Chemistry, Columbia University, New York, New York 10027, United States;* orcid.org/0000-0002-0098-7920

Gregor Kladnik − *CNR-IOM Laboratorio Nazionale TASC, 34149 Trieste, Italy; Faculty of Mathematics and Physics, University of Ljubljana, 1000 Ljubljana, Slovenia;* orcid.org/0000-0002-8675-4756

Anastasia Voevodin − *Department of Chemistry, Columbia University, New York, New York 10027, United States*

Enrique Montes − *Institute of Physics, Czech Academy of Sciences, Prague 16200, Czech Republic;* orcid.org/0000-0002-7852-7350

Narendra P. Arasu − *Institute of Physics, Czech Academy of Sciences, Prague 16200, Czech Republic*

Yaping Zang − *Department of Applied Physics, Columbia University, New York, New York 10027, United States;* orcid.org/0000-0002-5665-7605

Percy Zahl − *Center for Functional Nanomaterials, Brookhaven National Laboratory, Upton, New York 11973, United States*

Complete contact information is available at: https://pubs.acs.org/10.1021/jacs.0c10743

Author Contributions

◆E.A.D., R.L.S., G.K., and A.V. contributed equally.

Notes

The authors declare no competing financial interest.

■ ACKNOWLEDGMENTS

Experimental work was supported primarily by the National Science Foundation Award Grant CHE-1807654 (X.R. and L.V.) and CAREER Award DMR-1751949 (X.R.). E.M., N.P.A., and H.V. gratefully acknowledge financial support from the Czech Science Foundation GACR (19-23702S). D.C. and G.K. acknowledge the financial support from the Slovenian Research Agency (Research Core funding No. P1-0112 and No. P1-0044). A.M. acknowledges support from the Ministero dell'Universita e della Ricerca MUR (PRIN 2017KFY7XF_002). This research used resources of the Center for Functional Nanomaterials, which is a U.S. DOE Office of Science Facility, at Brookhaven National Laboratory under Contract No. DE-SC0012704.

■ REFERENCES

(1) Kaiser, R. I. Experimental investigation on the formation of carbon-bearing molecules in the interstellar medium via neutral-neutral reactions. *Chem. Rev.* **2002**, *102*, 1309−1358.

(2) Lavallo, V.; Canac, Y.; Donnadieu, B.; Schoeller, W. W.; Bertrand, G. Cyclopropenylidenes: From interstellar space to an isolated derivative in the laboratory. *Science* **2006**, *312*, 722−724.

(3) Lavallo, V.; Ishida, Y.; Donnadieu, B.; Bertrand, G. Isolation of cyclopropenylidene-lithium adducts: The Weiss-Yoshida reagent. *Angew. Chem., Int. Ed.* **2006**, *45*, 6652−6655.

(4) Schoeller, W. W.; Frey, G. D.; Bertrand, G. Tuning the Nucleophilicity in Cyclopropenylidenes. *Chem. - Eur. J.* **2008**, *14*, 4711−4718.

(5) Johnson, L. E.; DuPre, D. B. Topological and orbital-based mechanisms of the electronic stabilization of bis(diisopropylamino)-cyclopropenylidene. *J. Phys. Chem. A* **2008**, *112*, 7448−7454.

(6) Kinjo, R.; Ishida, Y.; Donnadieu, B.; Bertrand, G. Isolation of Bicyclopropenylidenes: Derivatives of the Smallest Member of the Fulvalene Family. *Angew. Chem., Int. Ed.* **2009**, *48*, 517−520.

(7) Kuchenbeiser, G.; Donnadieu, B.; Bertrand, G. Stable bis-(diisopropylamino)cyclopropenylidene (BAC) as ligand for transition metal complexes. *J. Organomet. Chem.* **2008**, *693*, 899−904.

(8) Jazzar, R.; Soleilhavoup, M.; Bertrand, G. Cyclic (Alkyl)- and (Aryl)-(amino)carbene Coinage Metal Complexes and Their Applications. *Chem. Rev.* **2020**, *120*, 4141−4168.

(9) Sau, S. C.; Hota, P. K.; Mandal, S. K.; Soleilhavoup, M.; Bertrand, G. Stable abnormal N-heterocyclic carbenes and their applications. *Chem. Soc. Rev.* **2020**, *49*, 1233−1252.

(10) Guisado-Barrios, G.; Soleilhavoup, M.; Bertrand, G. 1H-1,2,3-Triazol-5-ylidenes: Readily Available Mesoionic Carbenes. *Acc. Chem. Res.* **2018**, *51*, 3236−3244.

(11) Crudden, C. M.; Horton, J. H.; Ebralidze, I. I.; Zenkina, O. V.; McLean, A. B.; Drevniok, B.; She, Z.; Kraatz, H. B.; Mosey, N. J.; Seki, T.; Keske, E. C.; Leake, J. D.; Rousina-Webb, A.; Wu, G. Ultra stable self-assembled monolayers of N-heterocyclic carbenes on gold. *Nat. Chem.* **2014**, *6*, 409−414.

(12) Zhukhovitskiy, A. V.; MacLeod, M. J.; Johnson, J. A. Carbene Ligands in Surface Chemistry: From Stabilization of Discrete Elemental Allotropes to Modification of Nanoscale and Bulk Substrates. *Chem. Rev.* **2015**, *115*, 11503−11532.

(13) Crudden, C. M.; Horton, J. H.; Narouz, M. R.; Li, Z.; Smith, C. A.; Munro, K.; Baddeley, C. J.; Larrea, C. R.; Drevniok, B.; Thanabalasingam, B.; McLean, A. B.; Zenkina, O. V.; Ebralidze, I. I.; She, Z.; Kraatz, H. B.; Mosey, N. J.; Saunders, L. N.; Yagi, A. Simple direct formation of self-assembled N-heterocyclic carbene monolayers on gold and their application in biosensing. *Nat. Commun.* **2016**, *7*, 12654.

(14) Man, R. W. Y.; Li, C. H.; MacLean, M. W. A.; Zenkina, O. V.; Zamora, M. T.; Saunders, L. N.; Rousina-Webb, A.; Nambo, M.; Crudden, C. M. Ultrastable Gold Nanoparticles Modified by Bidentate N-Heterocyclic Carbene Ligands. *J. Am. Chem. Soc.* **2018**, *140*, 1576−1579.
(15) Lovat, G.; Doud, E. A.; Lu, D. Y.; Kladnik, G.; Inkpen, M. S.; Steigerwald, M. L.; Cvetko, D.; Hybertsen, M. S.; Morgante, A.; Roy, X.; Venkataraman, L. Determination of the structure and geometry of N-heterocyclic carbenes on Au(111) using high-resolution spectroscopy. *Chem. Sci.* **2019**, *10*, 930−935.
(16) Tulevski, G. S.; Myers, M. B.; Hybertsen, M. S.; Steigerwald, M. L.; Nuckolls, C. Formation of catalytic metal-molecule contacts. *Science* **2005**, *309*, 591−594.
(17) Kim, H. K.; Hyla, A. S.; Winget, P.; Li, H.; Wyss, C. M.; Jordan, A. J.; Larrain, F. A.; Sadighi, J. P.; Fuentes-Hemandez, C.; Kippelen, B.; Bredas, J. L.; Barlow, S.; Marder, S. R. Reduction of the Work Function of Gold by N-Heterocyclic Carbenes. *Chem. Mater.* **2017**, *29*, 3403−3411.
(18) Stohr, J. *NEXAFS Spectroscopy*; Springer, Heidelberg, 1992.
(19) Wang, G.; Ruhling, A.; Amirjalayer, S.; Knor, M.; Ernst, J. B.; Richter, C.; Gao, H. J.; Timmer, A.; Gao, H. Y.; Doltsinis, N. L.; Glorius, F.; Fuchs, H. Ballbot-type motion of N-heterocyclic carbenes on gold surfaces. *Nat. Chem.* **2017**, *9*, 152−156.
(20) Jiang, L.; Zhang, B.; Medard, G.; Seitsonen, A. P.; Haag, F.; Allegretti, F.; Reichert, J.; Kuster, B.; Barth, J. V.; Papageorgiou, A. C. N-Heterocyclic carbenes on close-packed coinage metal surfaces: bis-carbene metal adatom bonding scheme of monolayer films on Au. *Ag and Cu. Chem. Sci.* **2017**, *8*, 8301−8308.
(21) Chaudhuri, A.; Lerotholi, T. J.; Jackson, D. C.; Woodruff, D. P.; Dhanak, V. Author reply to: Comment on "Local Methylthiolate Adsorption Geometry on Au(111) from Photoemission Core-Level Shifts". *Phys. Rev. Lett.* **2009**, *103*, 119602.
(22) Cossaro, A.; Floreano, L.; Verdini, A.; Casalis, L.; Morgante, A. Comment on Local Methylthiolate Adsorption Geometry on Au(111) from Photoemission Core-Level Shifts. *Phys. Rev. Lett.* **2009**, *103*, 119601.
(23) Hapala, P.; Kichin, G.; Wagner, C.; Tautz, F. S.; Temirov, R.; Jelinek, P. Mechanism of high-resolution STM/AFM imaging with functionalized tips. *Phys. Rev. B: Condens. Matter Mater. Phys.* **2014**, *90*, 085421.
(24) Tamm, M.; Grzegorzewski, A.; Ekkehardt Hahn, F. Pentacarbonylchromium(0) and -tungsten(0) complexes with the bis(diisopropylamino) cyclopropenylidene ligand. *J. Organomet. Chem.* **1995**, *501*, 309−313.

https://dx.doi.org/10.1021/jacs.0c10743
J. Am. Chem. Soc. 2020, 142, 19902−19906

Supporting Information

Cyclopropenylidenes as Strong Carbene Anchoring Groups on Au Surface

Evan A. Doud[1†], Rachel L. Starr[1†], Gregor Kladnik[4,5†], Anastasia Voevodin[1†], Enrique Montes[3], Narendra P. Arasu[3], Yaping Zang[2], Percy Zahl[8], Alberto Morgante[4,7*], Latha Venkataraman[1,2*], Héctor Vázquez[3*], Dean Cvetko[4,5,6*], Xavier Roy[1*]

[1] *Department of Chemistry and* [2] *Department of Applied Physics, Columbia University, New York, New York, 10027, United States*
[3] *Institute of Physics, Czech Academy of Sciences, Cukrovarnická 10, Prague 16200, Czech Republic*
[4] *CNR-IOM Laboratorio Nazionale TASC, Basovizza SS-14, km 163.5, Italy*
[5] *Faculty of Mathematics and Physics, University of Ljubljana, Jadranska 19, Ljubljana, Slovenia*
[6] *J. Stefan Institute, Jamova 39, SI-1000, Ljubljana, Slovenia*
[7] *Department of Physics, University of Trieste, via A. Valerio 2, 34127, Trieste, Italy*
[8] *Center for Functional Nanomaterials, Brookhaven National Laboratory, Upton, NY, 11973, USA*

[†] These authors contributed equally

[*]Correspondence:
morgante@iom.cnr.it (A. M.)
lv2117@columbia.edu (L. V.)
vazquez@fzu.cz (H. V.)
cvetko@iom.cnr.it (D. C)
xr2114@columbia.edu (X. R.)

Table of Contents:

1. Synthesis of BAC–CO_2 Precursor

2. DFT Calculations of Binding on Au(111)

3. Details of XPS and NEXAFS Measurements

4. Details of DFT Calculations of X-ray Photoemission and Absorption Spectra

5. High-resolution Scanning Tunneling Microscopy and Atomic Force Microscopy

6. References

1. Synthesis of BAC–CO_2 Precursor

BAC–CO_2 was synthesized following a previously reported literature procedure[1] starting from bis(diisopropylamino)cyclopropenium tetrafluoroborate [BAC][BF_4], also prepared via a literature procedure.[2] Briefly, [BAC][BF_4] was deprotonated with potassium bis(trimethylsilyl)amide (KHMDS) in diethyl ether to form the free BAC. After removal of the solvent in vacuo, the free carbene was dissolved in hexanes and filtered. Carbon dioxide was bubbled through the hexanes solution to generate the adduct, BAC–CO_2, which precipitates from solution as a white solid. Unlike the free carbene, BAC–CO_2 is air stable, affording new opportunities as a precursor in various synthetic strategies.

2. Computational Details

Calculation of carbene molecules adsorbed on the Au(111) surface.

The adsorption properties and electronic structure of BAC and NHC molecules on the Au(111) surface were calculated using the SIESTA implementation of density functional theory (DFT).[3] The non-local vdW-DF functional of Dion *et al.* which includes van der Waals (vdW) interactions in the implementation of Román-Pérez and Soler[4-5] was employed. The unit cell for calculations consists of three Au(111) layers, each containing 36 atoms, plus the molecule, and a vacuum gap of at least 10 Å (Figure S1). Molecular (gold) atoms were described using a double-ζ (single-ζ) polarized basis set. Reciprocal space was sampled using a 2×2×1 Monkhorst pack grid and a real-space grid was defined with an equivalent cut-off energy of 250 Ry. The coordinates of molecular and Au surface atoms were relaxed until the Hellmann-Feynman forces acting on these atoms were smaller than 0.02 eV/Å. The tilt angle (θ) is fixed by constraining the relative position of the atoms in the cyclopropenylidene ring. The position of these atoms was kept fixed relative to each other, without restricting their displacement as a rigid unit. The tilt angle is defined as the angle between the plane of the cyclopropenylidene ring and the z axis. For the calculation of the binding energy, corrections to basis set superposition errors were taken into account. The binding energy for the fully unconstrained geometry is -1.72 eV, slightly higher than the geometries with constrained angle. The contribution of dispersion interactions to the binding energy was computed for the most

stable BAC geometry (θ = 40°) from the difference to a PBE calculation at the same geometry. We found a contribution of -1.40 eV to the total binding energy of -1.65 eV of BAC at θ = 40°. The binding energy of DAC at the same angle (θ = 40°) was calculated to be -1.16 eV, of which -0.93 eV corresponds to van der Waals interactions.

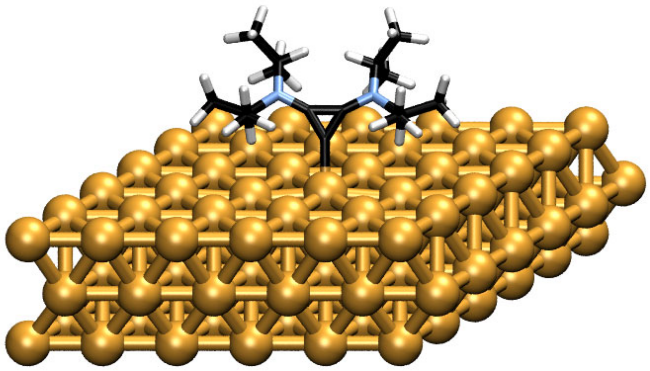

Figure S1: Unit cell used in the DFT calculations of the adsorbed molecule.

Calculation of isolated molecule and carbene-Au atom complexes.

The electronic properties of diaminocyclopropenylidene (DAC) and dihydroimidazol-2-ylidene (NHC) molecules as well as DAC-Au_1 and NHC-Au_1 complexes in the gas phase were calculated with Gaussian.[6] Exchange-correlation was approximated with the B3LYP functional. 6-31G* (LANL2DZ) basis sets were used to describe the Au atoms. The total energy of DAC-Au_1 and NHC-Au_1 complexes was calculated as a function of the angle between the C-Au bond and the carbene planes, as shown in Figure S2a for the DAC-Au_1 complex. This angle was constrained while all other degrees of freedom were optimized. Figure S2b shows the calculated energy profiles, with the energy at 0 degrees in each case set to zero for ease of comparison. While the most stable geometry of NHC-Au is found for 0 degrees, the lowest energy of the DAC-Au complex is obtained when the C-Au bond is tilted 24 degrees from the carbene plane. Thus, the possibility of DAC to bind at a tilted angle develops already with a single Au atom.

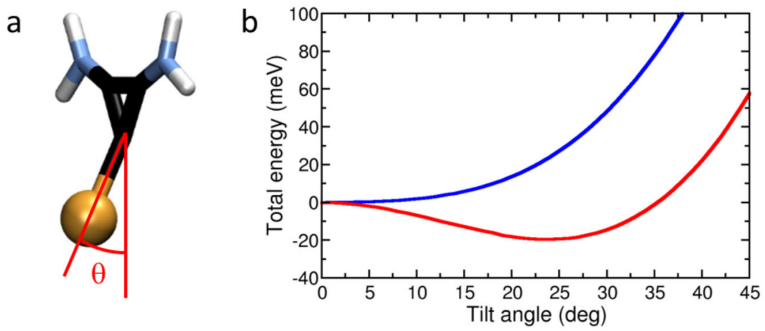

Figure S2: a) Structure of the DAC -Au complex used in the calculations. b) Energy of DAC -Au (red curve) and NHC-Au (blue curve) complexes as a function of tilt angle, relative to the value at 0 degrees.

To elucidate the origin of the out of plane binding in DAC but not in NHC, the electrostatic potential of isolated DAC and NHC molecules was calculated. Figure S3a shows the calculated electrostatic potential of DAC (top) and NHC (bottom) isolated molecules. Contour lines are plotted at 1, 10, and 20 eV. The position of the Au atom at its most stable conformation in Figure S3 is indicated by a cross. In Figure S3b, the three-dimensional electrostatic potential is represented in real-space projected onto an isosurface of the electron density (10^{-3} e/Å^3). Positive (negative) values of the potential, corresponding to blue (red) regions, indicate electron-deficient (electron-rich) regions of the molecule. The broader angular distribution in DAC compared to NHC evidences its ability to bond to Au in a tilted conformation.

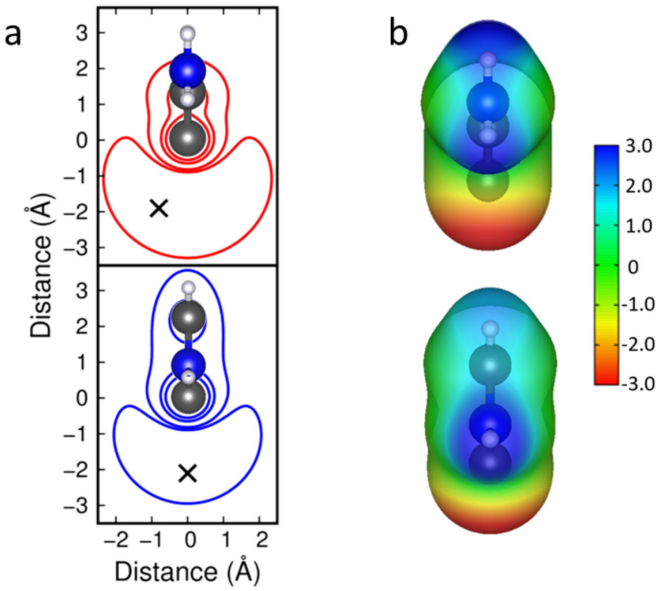

Figure S3: a) Electrostatic potential contour lines of DAC and NHC. b) Real-space representation for DAC (top) and NHC (bottom) of the electrostatic potential (in V) projected over the electron density isocontour (10^{-3} e/Å^3) .

3. Details of XPS and NEXAFS Measurements

The X-ray photoemission (XPS) and absorption (NEXAFS) measurements were performed at the ALOISA beamline[7] of the Elettra synchrotron. The Au(111) surface was prepared by cycles of Ar^+ sputtering (1.5 keV) and thermal annealing up to ~750 K. Absence of surface contaminants was checked by XPS prior to molecule deposition. The BAC precursor was loaded into a pyrex cell and pumped down to high vacuum resulting in decarboxylation and sublimation of the carbene compounds for deposition. During the deposition the cell was heated to ~380 K and the sample chamber pressure reached 2 × 10^{-8} mbar. The temperature of the Au substrate was controlled during the deposition (as reported in the text) and then cooled down to ~200 K for the X-ray absorption measurement.

XPS spectra were taken at grazing incidence angle (4°) using a photon energy of 500 eV with the photon electric field aligned 4° off the surface normal. The emitted electrons were detected by a hemispherical electron analyzer in normal emission geometry, with overall energy resolution

better than 220 meV. The binding energy scale has been calibrated using bulk spectral component of the Au $4f_{7/2}$ peak at 84.0 eV.[8]

Figure S4 shows the XPS measurement of the BAC film deposited on Au(111) surface held at 370 K sample temperature. We detect no oxygen spectral features indicating that the CO_2 moiety in the precursor molecules is cleaved off leaving just the BAC molecule deposited on the substrate.

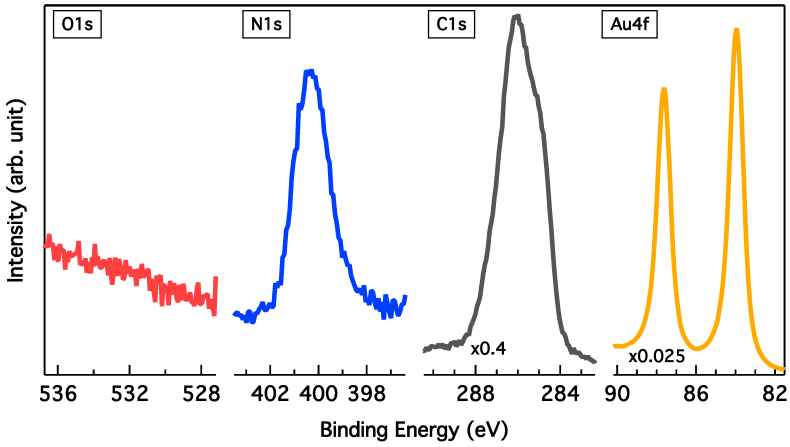

Figure S4: XPS measurement of the as-deposited BAC film at 370 K sample temperature. Lack of any oxygen signal indicates that CO_2 moiety is cleaved from the precursor molecules. Intensities of the C1s and Au4f spectral features are scaled as indicated for better comparison.

The effect of temperature annealing the BAC film is further shown in Figure S5 and S6. Some N1s and C1s signals are reduced after annealing to 430 K and 470 K, pointing to a partial desorption of the BAC. The C1s peak shape in the as deposited film displays two distinct components at 285.2 and 286.0 eV, with the higher binding energy component likely due to bilayer formation where substrate screening of the core hole is less efficient. The C1s peak profile of the 430 K and 470 K annealed film demonstrates that predominantly the high binding energy component is reduced, whereas the low binding energy component is preserved. The slight increase of the Au4f signal upon temperature annealing also indicates that some of the BAC molecules desorb, leaving just the monolayer.

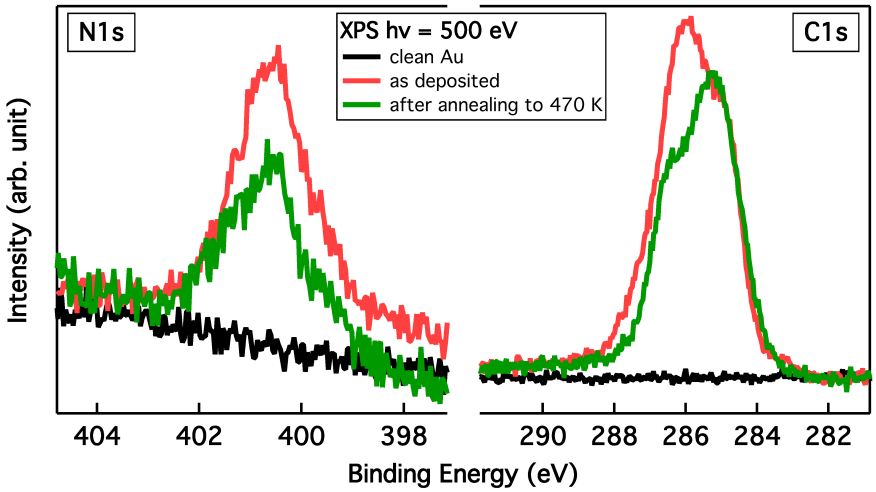

Figure S5: N1s and C1s XPS data of BAC film deposited on Au(111) (red) and after temperature annealing to 470 K (green). Changes in the C 1s peak shape indicate desorption of the second layer leaving just a single layer of BAC on Au. Clean gold substrate XPS scans are also shown (black) as a reference.

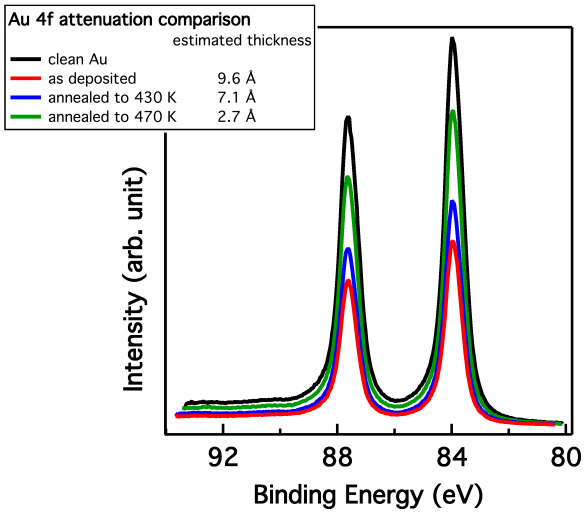

Figure S6: Comparison of Au 4f intensity attenuation due to different thicknesses of the BAC film remaining after temperature annealing the pristine (as deposited) film.

The NEXAFS N K-edge spectra were acquired in partial electron yield mode by a wide acceptance angle channeltron detector. A grid placed in front of the channeltron was polarized to -370 V, acting as a high-pass filter rejecting electrons with kinetic energies lower than 370 eV. The photon energy resolution was better than 150 meV. Polarization dependent NEXAFS spectra were taken in two polarizations, in *p*-polarization (photon electric field normal to the surface) and *s*-polarization (electric field parallel to the surface), to measure the molecular adsorption geometry.[9] Magic angle NEXAFS spectra were measured with the surface normal at 55 degrees from the photon polarization.

4. Details of DFT Calculations of X-ray Photoemission and Absorption Spectra

We simulate the effect of gold adatoms or step edges by introducing a gold dimer as shown in Figure S7 and optimizing the geometry using density functional theory (DFT) with the B3LYP functional and the double-zeta correlation-consistent basis set (cc-pVDZ) implemented in the NWChem computational chemistry package.[10] The optimized geometry then served as input to GPAW, a DFT Python code based on the projector-augmented wave (PAW) method to calculate the core electron binding energies (CEBEs) as well as the X-ray absorption spectra (XAS).[11-13]

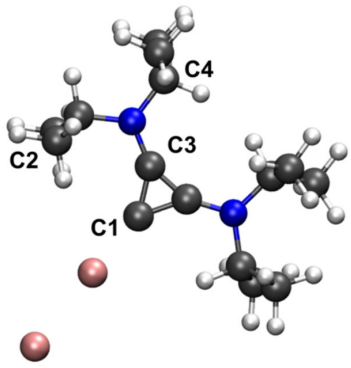

Figure S7: Optimized geometry of the BAC molecule with a gold dimer near the C1 carbene carbon.

We calculated the CEBEs of all inequivalent C1s sites with the PBE functional with a cell size of 25.6 Å and grid spacing of 0.2 Å using the delta Kohn-Sham scheme. The full core-hole PAW setups were created with GPAW and default parameter values. The inequivalent C1s sites are marked in Figure S7 and correspond to the carbene carbon (C1), aromatic carbons bound to nitrogen (C3), aliphatic carbons also bound to nitrogen (C4) and aliphatic carbons (C2) in the propyl groups. Figure S8a shows a comparison of the calculated C1s (blue) CEBEs with the measured XPS (green) after flashing the deposited film to 420K. The shape of the C1s peak changed significantly upon flashing to 430 K (compare with Figure S4) probably indicating desorption of the second layer. This is further corroborated by the DFT calculation of the C1s CEBEs. The calculated CEBEs were offset to match the measured XPS for better comparison and the intensities were set to follow the expected stoichiometric ratios. The simulated peak shapes were obtained by gaussian convolution with FWHM = 0.4 eV.

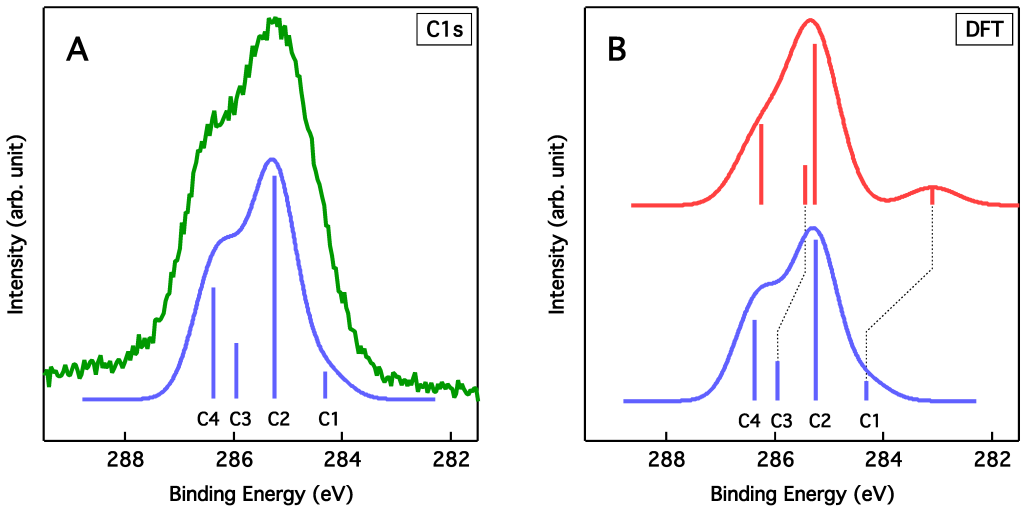

Figure S8: **a)** Comparison of the measured C1s peak (green) with the calculated CEBEs, which are shifted to match the measured peak position. **b)** Comparison of the calculated CEBEs for isolated BAC molecule (red) and the BAC molecule with a gold dimer placed near the carbene (C1) carbon.

The overall peak shape is well reproduced in the DFT calculation of the BAC molecule with an Au dimer. The effect of the Au dimer on the spectra are shown in the Figure S8b with the isolated BAC molecule CEBEs shown in red and the BAC with Au dimer CEBEs shown in blue. The calculated energies were offset to match the main (C2) component position belonging to the propyl group atoms presumably least prone to modification due to coupling with the Au dimer. The CEBEs of the peaks corresponding to the carbons closest to the Au dimer (C1 and C3) are found shifted towards higher binding energies relative to the positions of the other two peaks indicating a charge redistribution from the molecule's carbene core to the Au dimer.

X-ray absorption spectra (NEXAFS) were performed using the half core-hole transition potential method as implemented in GPAW. The calculation parameters were the same as for the CEBE calculations described above. The calculated NEXAFS spectra were obtained by gaussian convolution of the calculated transition intensities represented in the corresponding figures by sticks. We focus only on nitrogen K-edge NEXAFS spectra, since the measured carbon K-edge spectrum, Figure S9b, has a rich fine structure, due to the different initial states (C1-C4) where the majority of the signal stems from the aliphatic carbons. The contribution of the aromatic (and carbene) carbons is minimal and their effect on the measured absorption spectra is experimentally difficult to evaluate.

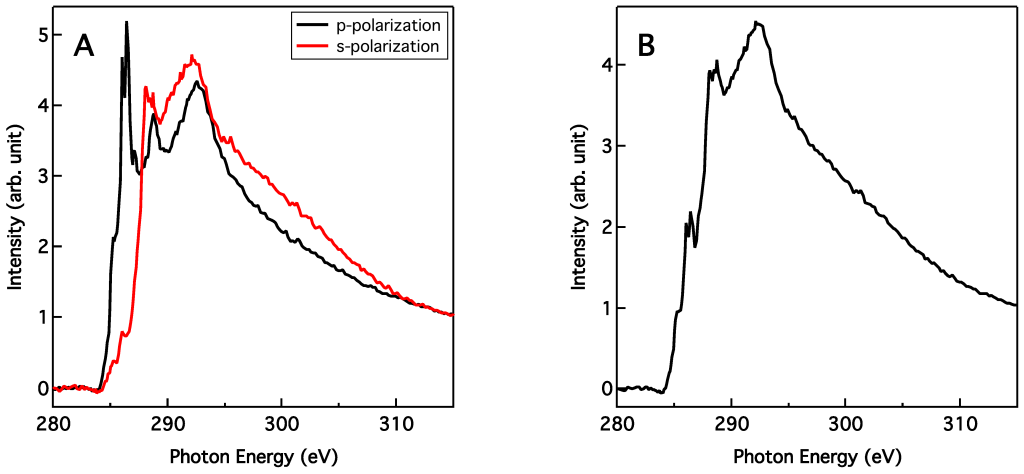

Figure S9: **a)** Polarization dependent carbon K-edge NEXAFS of the flashed BAC film and **b)** the corresponding magic angle NEXAFS.

Nitrogen K-edge spectra are easier to simulate since both N atoms in the molecule are equivalent. Moreover, the N atoms are directly bound to the aromatic (carbene) core indicating that electronic structure changes localized on the aromatic core should manifest also in nitrogen related unoccupied orbitals. Additionally, as noted in the main text, the DFT calculations of the BAC geometry show that the aromatic carbons (C1 and C3) and the nitrogens lie almost in the same plane, which allows us to use the measured dichroism in the polarization dependent N K-edge NEXAFS to estimate the orientation of the aromatic (carbene) core of the molecule relative to the substrate plane.

We calculate NEXAFS in magic angle conditions, i.e. absorption spectra independent of the molecular orientation, since we are specifically interested in the unoccupied molecular states and the corresponding transition energies. Experimentally we observe a significant change in the absorption spectra, where it appears that the LUMO peak position shifts toward lower excitation energy upon flash annealing the deposited film to 430 K (see main text Figure 2b). We attribute this to reorganization of the BAC molecules on the Au substrate surface toward more reactive sites (Au adatoms, step edges). This is further corroborated by our DFT simulations where we investigate the effect of the distance between the gold dimer and the C1 (carbene) carbon on the simulated N K-edge NEXAFS, Figure S10.

In Figure S10a we compare the experimentally derived magic angle N K-edge NEXAFS data (top black and red traces) with the DFT calculated NEXAFS spectra for isolated BAC molecule and BAC molecule with a gold dimer positioned at different distances to the C1 (carbene) carbon. Of immediate note, the peak at ~398 eV in the measured spectra is attributed to synchrotron beam induced modification of the amino groups and is therefore not reproduced in the DFT calculations. The calculated NEXAFS spectra were obtained by gaussian convolution of the calculated transition intensities represented in the figure by sticks. The calculated absorption spectrum of isolated BAC molecule (yellow trace) reproduces the NEXAFS measured just after deposition very well. The as deposited film is a multilayer, as established from the XPS data, therefore no features induced by molecule-substrate interactions are expected in the spectrum and is confirmed by the DFT calculation. The addition of a gold dimer induces some charge delocalization from the molecule to the gold dimer as indicated by the bubble plots shown in the Figure S10b. This further induces a transition energy shift of the LUMO orbital to lower energies, which reaches a minimum

for a gold – carbon distance of about 2.0Å (red trace). This shift is indeed observed in the measured spectra, where after flashing to 430 K the NEXAFS changes significantly, with a shift of the peak at ~402 eV (black trace) to an energy of ~400.5 eV. Our DFT calculations show that this shift can be attributed to stronger Au substrate – BAC molecule interaction. Although the full -1.5 eV shift is not reproduced with our calculations, the trend is clear – stronger interaction, i.e. smaller distance between the C1 carbene carbon and the gold dimer, yields a larger shift of the LUMO excitation energy towards lower values.

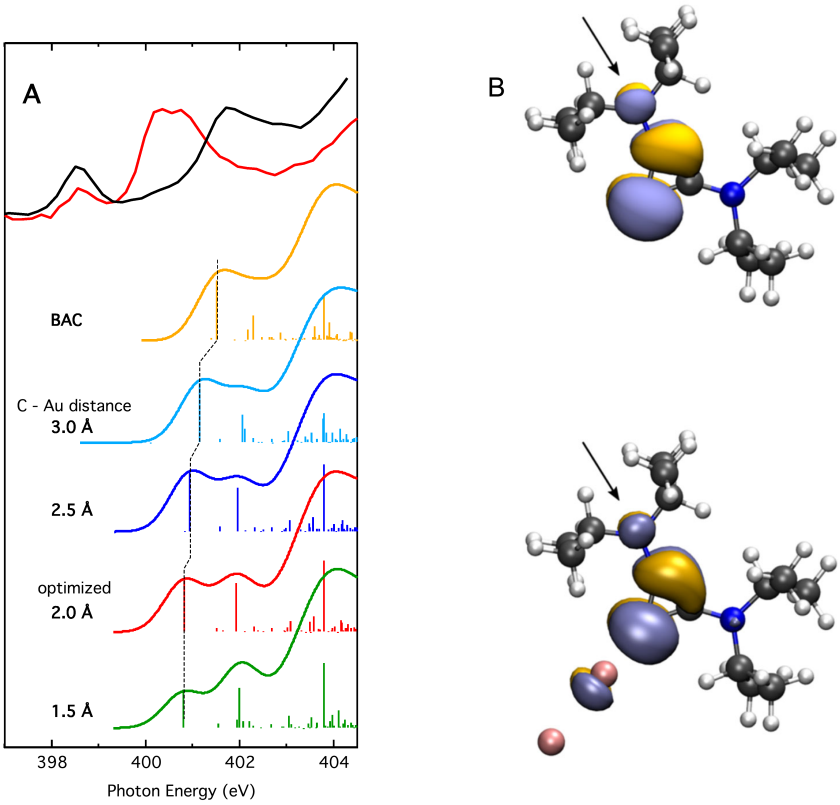

Figure S10: **a)** Comparison of experimentally derived magic-angle N K-edge NEXAFS (top black after BAC deposition, top red after flash to 430 K) and DFT calculated NEXAFS spectra of isolated BAC molecule (yellow) and BAC molecule with a gold dimer at different distances from the C1 (carbene) carbon. **b)** Bubble plot of the calculated "LUMO" with a half-core-hole on the nitrogen atom pointed on with an arrow for the isolated BAC molecule (top right) and the BAC molecule with a gold dimer (bottom right).

5. Scanning probe microscopy experiments:

Measurements were performed with a Createc-based low-temperature (LT)-STM system custom upgraded (by the author P. Zahl) with NC-AFM capability and operated using the open source GXSM control software.[14-16] Our Q-Plus sensor used for the STM/NC-AFM measurements has a 25 μm PtIr tip wire attached which was cut and sharpened by a focused ion beam (FIB) milling following a final cleaning procedure in UHV using Ar^+ sputtering from three directions before mounting on the SPM scanner.

Simulation of AFM images.

AFM images were calculated using the probe particle model[17] for the BAC structure at $\theta = 40°$. The parameters of the tip were chosen to simulate a CO-functionalized tip (lateral stiffness of 0.24 N/m). Images were generated by scanning the tip over BAC on a three-dimensional grid with a spacing of 0.1 Å. At each grid position of the vertical approach, the tip position was allowed to relax. An oscillation amplitude of around 1 Å was used.

6. References

(1) Kuchenbeiser, G.; Soleilhavoup, M.; Donnadieu, B.; Bertrand, G. Reactivity of Cyclic (Alkyl)(amino)carbenes (CAACs) and Bis(amino)cyclopropenylidenes (BACs) with Heteroallenes: Comparisons with their N-Heterocyclic Carbene (NHCs) Counterparts. *Chem. Asian J.* **2009,** *4*, 1745-1750. DOI: 10.1002/asia.200900338.

(2) Lavallo, V.; Ishida, Y.; Donnadieu, B.; Bertrand, G. Isolation of cyclopropenylidene-lithium adducts: The Weiss-Yoshida reagent. *Angew. Chem. Int. Ed.* **2006,** *45*, 6652-6655. DOI: 10.1002/anie.200602701.

(3) Soler, J. M.; Artacho, E.; Gale, J. D.; Garcia, A.; Junquera, J.; Ordejon, P.; Sanchez-Portal, D. The SIESTA method for ab initio order-N materials simulation. *J. Phys. Condens. Matter.* **2002,** *14*, 2745-2779. DOI: 10.1088/0953-8984/14/11/302.

(4) Dion, M.; Rydberg, H.; Schroder, E.; Langreth, D. C.; Lundqvist, B. I. Van der Waals density functional for general geometries. *Phys. Rev. Lett.* **2004,** *92*, 246401. DOI: 10.1103/PhysRevLett.92.246401.

(5) Roman-Perez, G.; Soler, J. M. Efficient Implementation of a van der Waals Density Functional: Application to Double-Wall Carbon Nanotubes. *Phys. Rev. Lett.* **2009,** *103*, 096102. DOI: 10.1103/PhysRevLett.103.096102.

(6) Frisch, M. J.; Trucks, G. W.; Schlegel, H. B.; Scuseria, G. E.; Robb, M. A.; Cheeseman, J. R.; Scalmani, G.; Barone, V.; Petersson, G. A.; Nakatsuji, H.; Li, X.; Caricato, M.; Marenich, A. V.; Bloino, J.; Janesko, B. G.; Gomperts, R.; Mennucci, B.; Hratchian, H. P.; Ortiz, J. V.; Izmaylov, A. F.; Sonnenberg, J. L.; Williams; Ding, F.; Lipparini, F.; Egidi, F.; Goings, J.; Peng, B.; Petrone, A.; Henderson, T.; Ranasinghe, D.; Zakrzewski, V. G.; Gao, J.; Rega, N.; Zheng, G.; Liang, W.; Hada, M.; Ehara, M.; Toyota, K.; Fukuda, R.; Hasegawa, J.; Ishida, M.; Nakajima, T.; Honda, Y.; Kitao, O.; Nakai, H.; Vreven, T.; Throssell, K.; Montgomery Jr., J. A.; Peralta, J. E.; Ogliaro, F.; Bearpark, M. J.; Heyd, J. J.; Brothers, E. N.; Kudin, K. N.; Staroverov, V. N.; Keith, T. A.; Kobayashi, R.; Normand, J.; Raghavachari, K.; Rendell, A. P.; Burant, J. C.;

Iyengar, S. S.; Tomasi, J.; Cossi, M.; Millam, J. M.; Klene, M.; Adamo, C.; Cammi, R.; Ochterski, J. W.; Martin, R. L.; Morokuma, K.; Farkas, O.; Foresman, J. B.; Fox, D. J. *Gaussian 16 Rev. A.03*, Wallingford, CT, 2016.

(7) Floreano, L.; Naletto, G.; Cvetko, D.; Gotter, R.; Malvezzi, M.; Marassi, L.; Morgante, A.; Santaniello, A.; Verdini, A.; Tommasini, F.; Tondello, G. Performance of the grating-crystal monochromator of the ALOISA beamline at the Elettra Synchrotron. *Rev. Sci. Instrum.* **1999,** *70*, 3855-3864. DOI: 10.1063/1.1150001.

(8) Cossaro, A.; Floreano, L.; Verdini, A.; Casalis, L.; Morgante, A. Comment on ``Local Methylthiolate Adsorption Geometry on Au(111) from Photoemission Core-Level Shifts". *Phys. Rev. Lett.* **2009,** *103*, 119601. DOI: 10.1103/PhysRevLett.103.119601.

(9) Stöhr, J., *NEXAFS Spectroscopy*. Springer-Verlag Berlin Heidelberg: New York, 1992; Vol. 25.

(10) Valiev, M.; Bylaska, E. J.; Govind, N.; Kowalski, K.; Straatsma, T. P.; Van Dam, H. J. J.; Wang, D.; Nieplocha, J.; Apra, E.; Windus, T. L.; de Jong, W. NWChem: A comprehensive and scalable open-source solution for large scale molecular simulations. *Comput. PHys. Commun.* **2010,** *181*, 1477-1489. DOI: 10.1016/j.cpc.2010.04.018.

(11) Bahn, S. R.; Jacobsen, K. W. An object-oriented scripting interface to a legacy electronic structure code. *Comput. Sci. Eng.* **2002,** *4*, 56-66. DOI: 10.1109/5992.998641.

(12) Mortensen, J. J.; Hansen, L. B.; Jacobsen, K. W. Real-space grid implementation of the projector augmented wave method. *Phys. Rev. B.* **2005,** *71*, ARTN 035109. DOI: 10.1103/PhysRevB.71.035109.

(13) Enkovaara, J.; Rostgaard, C.; Mortensen, J. J.; Chen, J.; Dulak, M.; Ferrighi, L.; Gavnholt, J.; Glinsvad, C.; Haikola, V.; Hansen, H. A.; Kristoffersen, H. H.; Kuisma, M.; Larsen, A. H.; Lehtovaara, L.; Ljungberg, M.; Lopez-Acevedo, O.; Moses, P. G.; Ojanen, J.; Olsen, T.; Petzold, V.; Romero, N. A.; Stausholm-Moller, J.; Strange, M.; Tritsaris, G. A.; Vanin, M.; Walter, M.;

Hammer, B.; Hakkinen, H.; Madsen, G. K. H.; Nieminen, R. M.; Norskov, J.; Puska, M.; Rantala, T. T.; Schiotz, J.; Thygesen, K. S.; Jacobsen, K. W. Electronic structure calculations with GPAW: a real-space implementation of the projector augmented-wave method. *J. Phys. Condens. Matter.* **2010,** *22*. DOI 10.1088/0953-8984/22/25/253202.

(14) Zahl, P.; Wagner, T. GXSM - Smart & Customizable SPM Control. *Imaging & Microscopy* **2015,** 1, 38-41. DOI: 10.1002/imaging.4840.

(15) Zahl, P.; Klust, A. GXSM Software Project Homepage. http://gxsm.sourceforge.net/.

(16) Reineke, S.; Lindner, F.; Schwartz, G.; Seidler, N.; Walzer, K.; Lussem, B.; Leo, K. White organic light-emitting diodes with fluorescent tube efficiency. *Nature* **2009,** *459*, 234-U116. 10.1038/nature08003.

(17) Hapala, P.; Kichin, G.; Wagner, C.; Tautz, F. S.; Temirov, R.; Jelinek, P. Mechanism of high-resolution STM/AFM imaging with functionalized tips. *Phys. Rev. B.* **2014,** *90*. DOI: 10.1103/PhysRevB.90.085421

4. Proposal for a biphenylene based molecular junction

4.1 Introduction

Linker groups are functionalized organic molecules units that provide mechanical stability and electronic coupling at the electrode-molecule-electrode interface in a molecular junction. Gold is the most commonly used electrode element in molecular electronic devices. The chemical inertness of gold helps surface preparation and molecule deposition. Interestingly Au atoms on the surface are known to be catalytically active and form chemical bonds with organic substances [88].

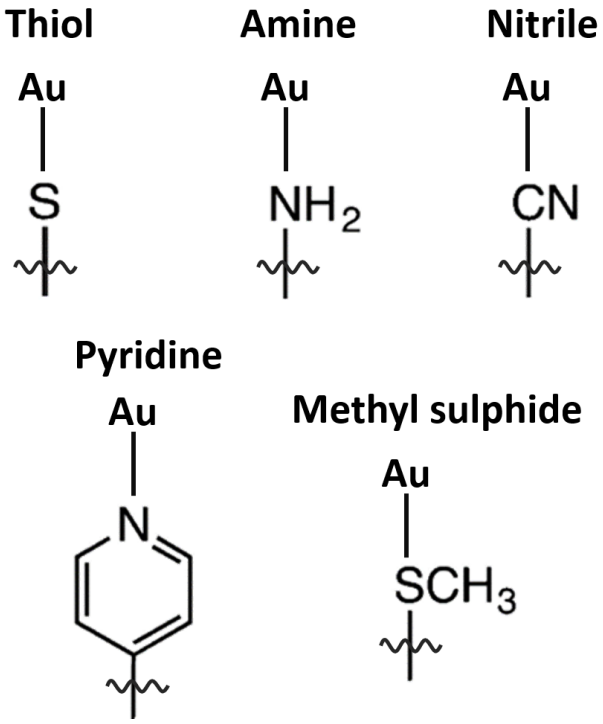

Figure 4.1: Typical anchoring groups for single-molecule electronics.

Mechanical stability and electronic coupling (strong or weak) must be considered when choosing an organic device's linker group. Thiol (-SH) is the most explored linker group on gold surfaces [89, 90]. In addition, amine (-NH_2) [17, 32], methyl sulphide (-SCH_3) [91], nitrile (-CN) [92] and pyridine [93] linkers have good affinity towards gold, as shown in figure 4.1. Thiol bonds can be established on Au(111) in several geometries. Each of them leads to a different conductance. This led to many problems interpreting the early experiments with thiols [94].

Venkataraman et al. proposed amine group as an alternative to thiol linker for molecular devices [32]. Amine forms a unidirectional bond to under-coordinated Au adatoms on the surface, providing highly reproducible molecular junctions. Amines bind weakly to the electrode creating instability at high bias voltages. Various studies show that the stability of linker groups follows the trend: pyridine $>$ SCH_3 $>$ NH_2 [95, 96].

In addition to mechanical stability, different anchor groups provide different transport mechanisms due to differences in the coupling of HOMO-LUMO levels to the substrate and the level alignment at the interface. Previous studies show that the HOMO of a molecule with an amine linker group to the Fermi level of gold. Hence, amine-linked molecules are usually HOMO conducting [17]. Thiol and methyl sulphide linkers are also shown to provide HOMO-derived conductance similar to amine [91, 97]. Nitrile and pyridine give weak conductance occurring through the tail of the LUMO orbital, as LUMO is closer to E_F for those linkers [98–100].

In 2011 Cheng et al. constructed single-molecule junctions with direct Au-C linkers [101], the linker exhibit high HOMO derived conductance and exceptional stability [102, 103] when compared to all previous linkers. Usually, molecules are closed-shell structures at the gas phase. Au-C linked molecules were initially synthesized with trimethyl tin end groups, removed in situ at the junction. Thus, forming a direct Au-C bond requires breaking an intramolecular bond and creating a new metal-molecule bond [101]. Another possibility involves the alkynyl group's deprotonation, where an open bond is occupied by a gold atom [104]. The disadvantages of these approaches are that they involve toxic precursor residues and rapid dimer formation.

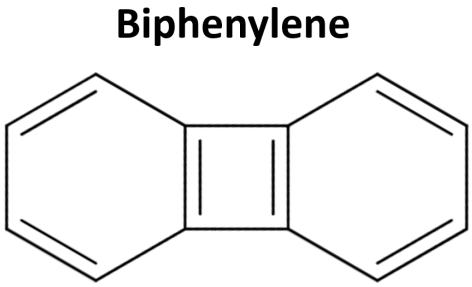

Figure 4.2: Chemical structure of biphenylene molecule. Two benzene rings are connected together through two C=C bonds.

In this work, we propose a new approach to achieve Au-C bonds with less footprints. We propose a biphenylene-based surface reaction approach to form two (bipod) direct Au-C bonds on Au(111) surface [105]. Molecules with more than one contact to the electrodes have been previously reported [106, 107]. Biphenylene is an antiaromatic molecule with two benzene rings connected through two covalent C=C bonds (see 4.2). Antiaromatic molecules are highly reactive compounds [108–110]. Electron-rich transition metal complexes are capable of cleaving the C=C bond of biphenylene [111]. We assume that upon perturbation, for example, by adsorption or through external stimulation, the biphenylene molecule breaks one of the two C=C intermolecular bonds. Subsequently, due to steric repulsion and substrate lattice arrangement, we assume both benzene rings twist with respect to each other, and each free carbon atom will form a direct Au-C bond to the Au(111) surface as shown in figure 4.3.

We theoretically study the mechanical and transport properties of the bipodal biphenylene platform standing vertical on Au(111) surface. To investigate the transport properties, we need to contact the bipodal molecule from the other

end. We included a third benzene ring to create a site for linker functionalization, as shown in figure 4.3. We functionalized the third benzene ring with five different linker groups. We considered both HOMO and LUMO conducting linkers. For HOMO conducting linkers, we chose amine, Au-C, and methyl sulphide as they have different atomic species at the metal-molecule contact. For LUMO conductance, we chose nitrile and pyridine, linker groups. The structures of all five linker groups are shown in figure 4.3.

The strong biphenylene-based bipodal platform at the bottom enabled us to compare five different linkers' mechanical and transport properties at the top contact. We quantified the mechanical properties by approaching the molecule with a tip. The force-displacement plot reveals four different mechanical processes undergone by the junction. The slope of the force-displacement curve around equilibrium gives the stiffness of the molecule. Change in stiffness of the molecule with respect to different linker groups follows the trend, pyridine > Au-C > amine > nitrile > methyl sulphide. Based on the reactivity to the tip, we classify into low and high reactive linkers. Low reactive linkers (amine and methyl sulphide) and high reactive linkers (nitrile and pyridine).

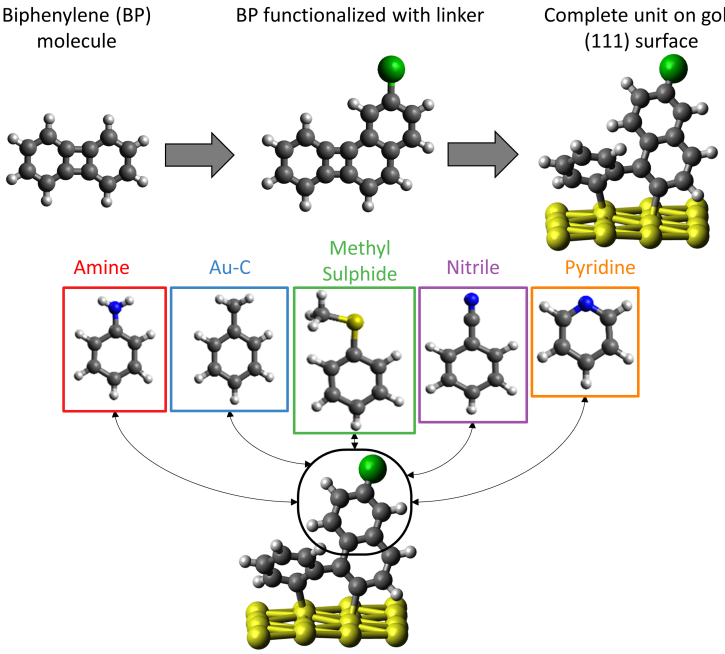

Figure 4.3: Biphenylene molecule forming two direct Au-C bonds on an Au(111) surface. The top side of the molecule shows the chemical functionalization of five different linker groups. The mechanical and transport properties of five linker groups were studied over the strong bipodal biphenylene platform. The figure is the same as the TOC figure of the article [105].

We study the transport properties of the five linker groups using DFT-NEGF calculations. Our results show that the low reactive amine and methyl sulphide linkers exhibit high HOMO-derived conductance. On the contrary, the highly reactive nitrile and pyridine linker show low LUMO-derived conductance. As expected, the Au-C linker has the highest conductance among all the linkers. Examining electronic hybridization at the point of contact shows the overlap of Au 6s orbital to either π or σ orbital of the molecule. Interestingly, less

reactive (high conducting) amine, methyl sulphide, and Au-C linker groups have π overlap, whereas high reactive (low conducting) pyridine and methyl sulphide have σ overlap.

The theoretical work proposes a new efficient strategy to form two direct Au-C bonds to the Au substrate. Our subsequent calculations demonstrate the relationship between mechanical and transmission properties of different linker groups, thereby providing valuable design rules for building molecular junctions.

4.2 My contribution to the article

I performed all the calculations discussed in the article. I developed a Python script to approach/retract a tip above a molecule to study mechanical properties. The results were analyzed, and conclusions were drawn collaboratively with Héctor Vázquez. I plotted the figures and prepared an advanced draft of the article.

PCCP

PAPER

View Article Online
View Journal | View Issue

Check for updates

Cite this: *Phys. Chem. Chem. Phys.*, 2018, **20**, 10378

Direct Au–C contacts based on biphenylene for single molecule circuits†

Narendra P. Arasu [ab] and Héctor Vázquez [*a]

Received 27th January 2018,
Accepted 22nd March 2018

DOI: 10.1039/c8cp00613j

rsc.li/pccp

We propose a novel platform for stable and highly conducting single molecule electronics and characterize its mechanical, electronic and conducting properties using *ab initio* simulations. We study a biphenylene-based molecular architecture on gold and consider that the antiaromatic instability of biphenylene leads to the breaking of internal carbon–carbon bonds and subsequent formation of Au–C covalent bonds with the substrate. In the resulting conformation the conjugated rings have a large twist angle and stand almost upright on the surface. The top contact is realized by functionalizing one end of the biphenylene unit with a chemical linker group, which in the adsorbed geometry is positioned far from the surface. We consider several linker terminations for this top contact, which is approached in our simulations by a gold tip. Using Density-Functional Theory (DFT) and Non-Equilibrium Green's Function (NEGF) methods, we quantify the mechanical and electron transport properties of the molecular junction and discuss their relationship with the nature of the linker group. Our results show that this biphenylene-based platform is very stable and provides high electronic transparency to current flow, demonstrating its potential in single molecule conductance studies.

Published on 23 March 2018. Downloaded by Charles University on 10/10/2021 7:49:43 PM.

1. Introduction

Nanoscale circuits in which single molecules act as the active elements represent the ultimate step in electronic miniaturization. Molecules can be characterized and manipulated with sub-nanometer precision, placing them between two electrodes so that their conducting properties can be measured reliably. At the same time, atomistic simulation methods are able to provide a detailed picture of the main physical and chemical principles that govern electron transport across single molecules. Through chemical synthesis, molecular circuits with different properties and functionalities can be designed. Research has shown that, among these chemical properties, metal–molecule contacts play an essential role in electron transport.[1–4] They not only affect the geometry and mechanical properties at the junction but also often act as bottlenecks for electron flow. Thus, designing and realizing optimal metal–molecule contacts is essential for the development of efficient and reliable single molecule circuits.

Usually, each end of the molecule is functionalized with a chemical linker group, and each linker group binds to an electrode, bridging the nanogap. Recently, however, asymmetric molecules with more than one bond to the substrate electrode have been investigated and reported to have many advantages for single molecule conductance studies. Thiol-terminated tripodal terminations were shown to provide strong electronic coupling to the substrate.[5] In another study, a molecular switch was realized in a molecule having a tripodal platform to the substrate and a cantilever arm protruding from the surface.[6] The electronic and transport properties of these molecules with tripodal wires were shown to depend on the orientation and conformation of the wires.[7] An ideal linker should be electronically transparent in order to result in high conductance, as well as mechanically stable and selective. Direct Au–C bonds were shown to be highly-conducting and reproducible metal–molecule contacts for single molecule transport. The conductance of alkanes or oligophenyls with Au–C bonds is much higher than with other terminations. Formation of Au–C bonds in single molecule transport was first demonstrated from trimethyltin end groups that cleave off *in situ*, resulting in covalent Au–C bonds between electrode tip atoms and the terminal Carbon atoms of the molecule.[8–10] Subsequently, other synthetic strategies were demonstrated, using trimethylsilyl groups[11] or the deprotonation of alkynyl groups, where an open bond is occupied by Au atom.[12] However, these approaches involve toxic precursors or residues, or rapid dimer formation.

In this paper we propose a bipodal molecular architecture for single molecule transport studies on gold having stable and highly-conducting metal–molecule links. From calculations based on Density-Functional Theory (DFT) and Non-Equilibrium Green's Functions (NEGF), we demonstrate the excellent mechanical, electronic and conducting properties of the proposed architecture.

[a] *Institute of Physics, Academy of Sciences of the Czech Republic, Cukrovarnická 10, Prague 6, Czech Republic. E-mail: vazquez@fzu.cz*
[b] *Department of Condensed Matter Physics, Faculty of Mathematics and Physics, Charles University, Ke Karlovu 5, Prague 2, Czech Republic*

† Electronic supplementary information (ESI) available. See DOI: 10.1039/c8cp00613j

This journal is © the Owner Societies 2018

Published on 23 March 2018. Downloaded by Charles University on 10/10/2021 7:49:43 PM.

This molecular platform is based on biphenylene, a conjugated molecule consisting of two benzene rings connected by single bonds exhibiting an antiaromatic electronic structure. Aromaticity is a key concept describing the stability of conjugated systems. According to Hückel's rule, cyclic and planar conjugated systems are said to be aromatic if they have $4n + 2\pi$ electrons (where n is an integer), and antiaromatic if this number is $4n$. Antiaromatic molecules exhibit remarkable electronic properties[13–18] but are known to be very reactive and unstable. Antiaromatic instability makes these complexes likely to experience bending or rotation, or bond alternation and rearrangement leading to more stable structures.[13] As such, antiaromatic molecules are more prone to bond breaking and reformation than, for instance, aromatic counterparts. For instance, the breaking of the central C–C σ bonds in biphenylene was recently demonstrated,[19] where oxidative addition of biphenylene to Au resulted in stable organogold complexes.

Here we explore the consequences of antiaromatic instability for single molecule transport contacts. We assume that these central C–C bonds in the biphenylene structure can be broken due to an external perturbation such as thermal annealing or a voltage pulse from an STM tip, and that the two C atoms form bonds with a Au(111) substrate. In this conformation, steric repulsion results in a large twist angle between the conjugated rings of biphenylene and the rings stand almost upright on the substrate. This constitutes the contact to one electrode. In order to address molecular transport, we functionalize one end of the biphenylene molecule, which in the adsorbed conformation points away from the surface, with an additional benzene ring which we functionalize with several linker groups (Fig. 1). This provides the contact to the other electrode (*e.g.* an STM tip). In our study, we consider several alternatives for the linker groups in this top contact so as to compare their mechanical and conducting properties with those of the bottom biphenylene-based contact. In particular, we analyze amine ($-NH_2$), methyl sulphide ($-SCH_3$), nitrile (–CN) and pyridine linkers, as well as direct Au–C bonds. Amine, nitrile, and pyridine groups form donor–acceptor bonds with Au, involving electron donation from N to Au. In amine bonds, the N lone pair is directed perpendicular to the molecular π system and, as a result, couples strongly with π orbitals. In single molecule transport, amine links have been shown to result in Highest Occupied Molecular Orbital (HOMO)-dominated transport.[20,21] Pyridine and nitrile groups have a σ (in-plane) lone pair which is poorly coupled to the π system. In molecular transport studies, these linkers have been shown to conduct *via* the Lowest Unoccupied Molecular Orbital (LUMO).[22–24] Methyl sulphide groups result in HOMO-dominated transport,[25] similar to amines. Au–C links are covalent metal–molecule bonds directed perpendicularly to the π system, resulting in very high conductance *via* occupied orbitals.[8] The mechanical properties of these linkers in Au junctions have also been investigated previously in symmetric molecules. Smaller rupture forces have been reported for alkanes with amine and methyl sulphide terminations than for bipyridine.[26–28]

Using DFT-based methods, we study the elastic and conducting properties of the biphenylene-based junction with five different chemical terminations in the top contact. From this analysis we show that the proposed bipodal platform presents very good mechanical and transport properties.

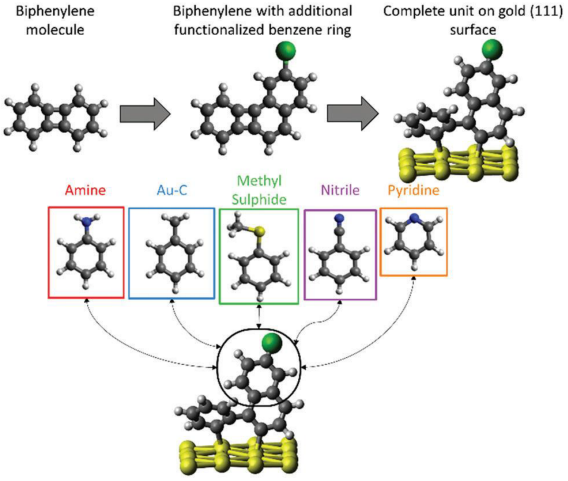

Fig. 1 Schematic illustration of the formation of a bipodal platform on Au(111) based on the antiaromatic instability of biphenylene and breaking of internal C–C bonds. An additional functionalized benzene ring is added to act as a top contact. Five different linker groups are considered.

2. Methods and simulations

In this work we do not address the process of internal C–C bond breaking and formation of Au–C bonds. Instead, we assume this process can be stimulated *via*, *e.g.* thermal annealing or from voltage pulses using an STM tip, and study the geometry and electronic properties of the adsorbed biphenylene-based species on the Au surface.

The functionalized biphenylene-based molecule is shown adsorbed on the substrate in the bottom panel of Fig. 1. We considered the Au(111) surface. Each Au layer consist of 16 atoms. The adsorbed molecule is contacted by an STM tip modelled as a pyramidal structure. The electronic properties are carried out using the SIESTA code.[29] Norm-conserving non-local Kleinman–Bylander type pseudopotentials are used. Exchange–correlation is described using the semi-local generalised gradient approximation (GGA) in the PBE implementation. A local-orbital basis set is used in the calculations. Au atoms are described using a single-ζ polarized basis while a double-ζ polarized basis is used for molecular atoms.

Mechanical properties were investigated by approaching the tip to the molecule in steps of 0.2 Å and optimizing the geometry at each step for each linker considered. The position of molecular, tip and bottom surface atoms are relaxed at each displacement step until the forces fall below 0.02 eV $Å^{-1}$. A unit cell consisting of three Au layers is used and electronic properties are evaluated at the Γ point.

Transport calculations were performed using the DFT-NEGF formalism.[30] Additional Au layers were added to the optimized

Published on 23 March 2018. Downloaded by Charles University on 10/10/2021 7:49:43 PM.

geometries to calculate the transport properties The unit cell for transmission calculations consists of 6 Au layers on each side (ESI,† Fig. S1). The junction electronic structure was calculated using a $5 \times 5 \times 1$ Monkhorst–Pack k-point grid. For transmission spectra, a $15 \times 15 \times 1$ k-point grid is used. Transmission eigenchannels are calculated at the center of the Brillouin zone using the method of by Paulsson and Brandbyge.[31,32]

3. Results and discussion

3.1 Mechanical properties

Fig. 2 shows the calculated mechanical properties of biphenylene-based junction with the five top linkers considered. The force is calculated as the derivative of the total energy with respect to the vertical displacement. Positive (negative) values mean that the tip-molecule interaction is attractive (repulsive). Because of the height of the molecule changes with the different linkers, we choose to shift the curves horizontally, as discussed below. Across the different functional groups in the top contact, we can distinguish four different regimes. (a) When the tip is far, there is little tip-molecule interaction the calculated forces are small. The exception to this is the Au–C link in the top contact. Being a covalent bond, the interaction is strong and the calculated force is not small at large distances. We therefore chose to restrict the simulations to within a certain tip height given the nontrivial experimental realization of this top Au–C contact. As the tip approaches, interaction with the top linker increases until this attractive interaction reaches a maximum (b), signalling the formation of a metal–molecule bond. As the tip is further approached, the molecule relaxes by tilting and compressing until an equilibrium configuration with both contacts is established (c). At this distance the forces on the tip and substrate are minimized and the system is in equilibrium. At this equilibrium distance we carry out the transport calculations. In Fig. 2 we shift the calculated F *vs.* z curves horizontally so that relative displacement is defined with respect to this equilibrium distance. This allows us to unify the force analysis since the height of the molecule, and thus inter-electrode vertical distances, is different for each top termination. If the tip is approached further, the system enters in the repulsive regime, indicated by negative forces, and the junction is compressed (d). Snapshots of the calculated geometries illustrating these regimes are shown in Fig. 2 for the molecule with a pyridine top contact.

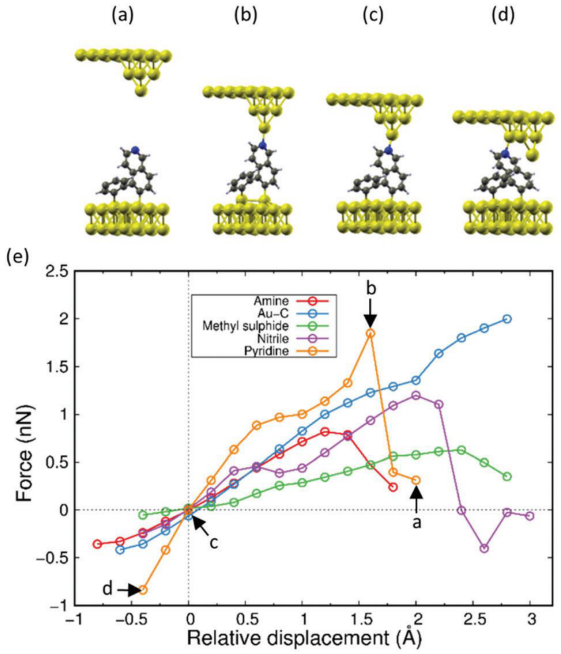

Fig. 2 (a–d) Snapshots of the tip approach trajectory for a pyridine-terminated top contact illustrating different interaction regimes. (e) Calculated forces as a function of tip displacement for the five linker terminations considered, measured from equilibria.

The slope of the calculated force *vs.* distance curves gives the junction stiffness. The values of the stiffness at equilibrium for the different functionalizations are shown in Table 1. In agreement with the trend previously reported[26] we find the pyridine-terminated molecule to have a high stiffness. In the biphenylene-based platform considered, the calculated stiffness decreases along the following series: pyridine, nitrile, Au–C, amine, and methyl sulphide. A similar trend is found in the calculated maximum force sustained by the junction. For pyridine, nitrile, amine and methyl sulphide terminations, it is 1.84, 1.19, 0.81 and 0.62 nN, respectively. This establishes pyridine and nitrile linkers as presenting a stronger interaction with the Au tip, while amine and methyl sulphide terminations are weakly interacting. A higher rupture force in bipyridine- than amine-terminated junctions was previously demonstrated.[24] However, in our case the binding to both electrodes in these biphenylene-based platforms is strongly asymmetric: the top contact is very different to the bipodal bonds to the substrate. Since rupture forces were shown to depend on the nature of the molecular backbone,[26,33] quantitative agreement should not be expected with symmetric molecules which have the same metal–molecule contact on both ends.

The trends observed in the calculated stiffness and maximum force sustained by the junction are consistent with the angle with respect to the π system at which the tip binds. Fig. 3 shows the evolution of the molecule-linker-tip angle along the approach trajectory. It is defined by the apical Au atom at the tip, the linker atom X (where X = N for pyridine, nitrile and amine links, S for methyl sulphide and C for Au–C bond), and the C atom in the top benzene ring. We see clear differences which match the trend observed in the calculated forces. For amine, methyl sulphide and Au–C links, the molecule gradually tilts to accommodate the increasing interaction with the tip. This is reflected in the

Table 1 Stiffness and conductance of the biphenylene-based junction with five different linkers

Linker	Amine	Au–C	Methyl sulphide	Nitrile	Pyridine
Stiffness nN Å^{-1}	0.61	0.77	0.18	0.84	1.31
$G(E_F)/G_0$ ($\times 10^{-2}$)	2.05	14.70	2.51	0.47	0.58

This journal is © the Owner Societies 2018

Published on 23 March 2018. Downloaded by Charles University on 10/10/2021 7:49:43 PM.

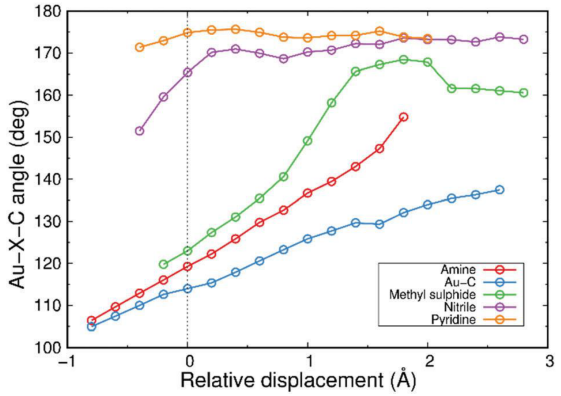

Fig. 3 Angle defined by the apical Au tip atom, the linker atom X, and a molecular backbone C atom in the benzene ring as a function of tip height, measured from equilibria.

continuous change in the C–X–Au angle to ~120 degrees at equilibrium (Fig. 3). On the other hand, for nitrile and pyridine contacts, this value remains more or less constant around 170 degrees, indicative of in-plane binding *via* the σ lone pair until a clearly repulsive interaction is established between tip and molecule.

Taken together, the calculated mechanical properties provide a picture of stiff and more reactive contacts to Au for nitrile and pyridine through the σ system and soft contacts to Au for amine, methyl sulphide and Au–C links, which are also less reactive for the first two.

So far we have discussed the mechanical properties of the metal-tip top contact but we now address the bottom Au–C bonds to the substrate. The binding energy of the biphenylene molecule to the Au surface, calculated by cleaving the bonds in an amine-functionalized molecule and keeping the molecular geometry fixed in a structure similar to that of Fig. 2a, where interaction with the top contact is small, is 1.2 eV per Au–C bond. In this geometry, analysis of charge rearrangement upon bond formation reveals it to be localized mostly at the biphenylene-substrate interface (ESI,† Fig. S2). C atoms closest to the surface are most affected by the formation of Au–C links. Electron density is displaced from the bonding C atoms towards the Au–C bond regions and, to a smaller extent, towards the benzene rings. Importantly, this charge rearrangement upon Au–C bond formation has a σ symmetry pattern since it takes place in the plane of the benzene rings. The biphenylene HOMO and LUMO experience minor changes from the isolated molecule to the adsorbed environment (ESI,† Fig. S3). The states at the cleaved C atoms hybridize with Au atoms at the surface and the spectral features of the contact C atoms are smoothened out when adsorbed.

As the tip is approached in the simulations, the surface Au contact atoms in the bottom contact can be lifted (ESI,† Fig. S4). This happens for the more reactive pyridine and nitrile linkers and corresponds to the sudden jumps in the calculated force displayed on Fig. 2. Amine- and methyl sulphide-terminated junctions show no such jumps. The case of a Au–C bond in the top contact is special, since this breaking this covalent bond would result in a radical. Instead, when the tip is far, the molecule is lifted from the substrate. In all cases, the bond lengths of the bottom two Au–C bonds remain almost unaltered and no changes in the adsorption geometry of the bottom contact are seen (ESI,† Fig. S5). Additional structural relaxations of the adsorbed molecule where the initial geometry was shifted parallel to the surface resulted in similar final structures (ESI,† Fig. S6). These results highlight the stability and directionality of the Au–C bonds to the substrate.

3.2 Transmission properties

The calculated transmission spectra for the biphenylene-based molecule with are shown in Fig. 4 for the five different top linkers considered. First, we address zero bias conductance. The conductance is highest with a top Au–C bond. This is followed by amine and methyl sulphide linkers, whose conductance is similar to each other and ~6–7 × smaller than with the top Au–C bond. Nitrile and pyridine contacts provide the lowest conductance, a factor ~35–30 lower than for Au–C (Table 1).

From Fig. 4 a pattern is immediately apparent, since the linkers for which conductance is HOMO-dominated result also in higher conductance values. Nitrile and pyridine terminated molecules yield LUMO-derived transport and low conductance values. This relation of linker termination and dominant conducting state (empty or occupied) agrees with previous reports.[3] The Au–X–C contact angle of ~120 degrees for Au–C, amine and methyl sulphide is indicative of out of plane bonding and concomitant strong electronic coupling. These linkers result in high calculated conductance values. On the other hand, the in-plane tip binding by nitrile and pyridine contacts results is driven by the σ system and consequently the degree of electronic coupling provided by

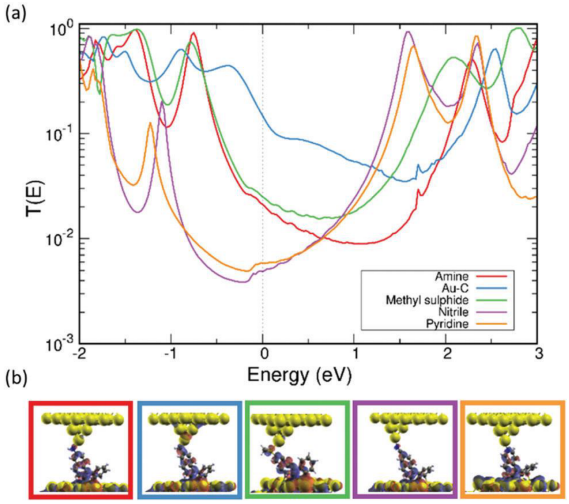

Fig. 4 (a) Calculated transmission spectra of biphenylene-based junction with the five linker terminations considered in for the top contact. (b) Real-space representation of the most conducting scattering states at the Fermi energy.

Published on 23 March 2018. Downloaded by Charles University on 10/10/2021 7:49:43 PM.

these links is rather low since the tip is poorly coupled to the π system. The degree of electronic coupling provided by the different top terminations is reflected transmission eigenchannels at the Fermi energy shown in Fig. 4 and ESI,† Fig. S7.

We also note that the strong dependence of the transport properties with the top metal–molecule contact highlights its role as bottleneck for electron transport. The bottom bipodal Au–C bonds to the substrate provide strong electronic coupling, and the conducting molecular state is strongly determined by the top contact (ESI,† Fig. S8).

Finally, we comment on the role played by each of the bottom benzene rings derived from the biphenylene unit that are forming bonds with the substrate. An analysis of the Projected Density of States (PDOS) of each ring shows (ESI,† Fig. S9) that only the ring connected to the top contact is in the conducting pathway. The spectral features of the other benzene ring play a smaller role near the Fermi energy, especially in the conducting frontier orbital. This is reflected in the transmission eigenchannels involving mostly only one of the bottom benzene rings (Fig. 4 and ESI,† Fig. S7).

To quantify the role in conductance of the 'side' benzene ring not bonded to the top contact, we removed this ring and saturated the C atom it was bonded to, and fixed the positions of all other atoms in the junction. This allows us to calculate the contribution of the second benzene ring while excluding any possible effects of geometrical changes in conductance. We find that the calculated transmission spectrum is almost unchanged (ESI,† Fig. S10), demonstrating that conducting properties derive from the benzene ring in the tunnelling pathway alone. Thus, while both rings provide mechanical stability to the molecule through the two Au–C bonds to the substrate, only one of them (the one bonded to the top contact) plays a role in electron transport.

4. Conclusions

In this work, we proposed a new bipodal platform based on biphenylene for single molecule transport. The molecule has two covalent Au–C bonds to the Au substrate. We considered five different possibilities for the other contact to the electrodes and calculated the junction mechanical and conducting properties.

Our results show that the biphenylene-based structure provides a strong attachment to the substrate, which remained stable in all cases when a Au tip was approached to the molecule. We observed trends in the mechanical properties with the top linker termination consistent with previous results. We then calculated the conducting properties of the junctions with the different functionalizations. The observed trend in transport properties with the nature of the top contact was related to the calculated force and stiffness in terms of the electronic states (π or σ) of the tip-linker bond, which determines the electronic coupling of this top metal–molecule contact. We also showed that electron transport was limited by the chemical characteristics of the top contact. This makes the proposed biphenylene-based platform a mechanically robust and electronically transparent molecular architecture.

Our work paves the way for the development of new strategies for stable and highly conducting metal–molecule platforms for single molecule transport.

Conflicts of interest

There are no conflicts to declare.

Acknowledgements

We thank Ivo Starý, Irena G. Stará and Jaroslav Vacek for fruitful discussions. We gratefully acknowledge financial support from the Purkyně Fellowship program of the Czech Academy of Sciences and the Czech Science Foundation (15-19672S). Computational resources were provided by the National Grid Infrastructure MetaCentrum and the "Projects of Large Research, Development, and Innovations Infrastructures" CESNET LM2015042 and LM2015087.

References

1 L. Sun, Y. A. Diaz-Fernandez, T. A. Gschneidtner, F. Westerlund, S. Lara-Avila and K. Moth-Poulsen, Single-molecule electronics: from chemical design to functional devices, *Chem. Soc. Rev.*, 2014, **43**, 7378–7411.
2 F. Schwarz and E. Lörtscher, Break-junctions for investigating transport at the molecular scale, *J. Phys.: Condens. Matter*, 2014, **26**, 424201.
3 R. J. Nichols and S. J. Higgins, Single-Molecule Electronics: Chemical and Analytical Perspectives, *Annu. Rev. Anal. Chem.*, 2015, **8**, 389–417.
4 T. A. Su, M. Neupane, M. L. Steigerwalsd, L. Venkataraman and C. Nuckolls, Chemical principles of single-molecule electronics, *Nat. Rev. Mater.*, 2016, **1**, 16002.
5 J. Šebera, V. Kolivoška, M. Valášek, J. Gasior, R. Sokolová, G. Mészáros, W. Hong, M. Mayor and M. Hromadová, Tuning Charge Transport Properties of Asymmetric Molecular Junctions, *J. Phys. Chem. C*, 2017, **121**, 12885–12894.
6 L. Gerhard, K. Edelmann, J. Homberg, M. Valášek, S. G. Bahoosh, M. Lukas, F. Pauly, M. Mayor and W. Wulfhekel, An electrically actuated molecular toggle switch, *Nat. Commun.*, 2017, **8**, 14672.
7 M. Lukas, K. Dössel, A. Schramm, O. Fuhr, C. Stroh, M. Mayor, K. Fink and H. V. Löhneysen, A tripodal molecule on a gold surface: orientation-dependent coupling and electronic properties of the molecular legs, *ACS Nano*, 2013, **7**, 6170–6180.
8 W. Chen and J. R. Widawsky, Highly Conducting π-Conjugated Molecular Junctions Covalently Bonded to Gold Electrodes, *J. Am. Chem. Soc.*, 2011, **43**, 17160.
9 Z.-L. Cheng, R. Skouta, H. Vazquez, J. R. Widawsky, S. Schneebeli, W. Chen, M. S. Hybertsen, R. Breslow and L. Venkataraman, In situ formation of highly conducting covalent Au–C contacts for single-molecule junctions, *Nat. Nanotechnol.*, 2011, **6**, 353–357.
10 J. R. Widawsky, W. Chen, H. Vázquez, T. Kim, R. Breslow, M. S. Hybertsen and L. Venkataraman, Length-dependent

 This journal is © the Owner Societies 2018

Published on 23 March 2018. Downloaded by Charles University on 10/10/2021 7:49:43 PM.

thermopower of highly conducting Au–C bonded single molecule junctions, *Nano Lett.*, 2013, **13**, 2889–2894.
11 W. Hong, H. Li, S. X. Liu, Y. Fu, J. Li, V. Kaliginedi, S. Decurtins and T. Wandlowski, Trimethylsilyl-terminated oligo(phenylene ethynylene)s: an approach to single-molecule junctions with covalent Au–C σ-bonds, *J. Am. Chem. Soc.*, 2012, **134**, 19425–19431.
12 I. J. Olavarria-contreras, M. L. Perrin, Z. Chen, S. Klyatskaya, M. Ruben and H. S. J. Van Der Zant, C–Au covalently bonded molecular junctions using nonprotected alkynyl anchoring groups, *J. Am. Chem. Soc.*, 2016, **138**, 8465.
13 R. Breslow, Antiaromaticity, *Acc. Chem. Res.*, 1973, **6**, 393–398.
14 R. Breslow and F. W. Foss Jr, Charge transport in nanoscale aromatic and antiaromatic systems, *J. Phys.: Condens. Matter*, 2008, **20**, 374104.
15 S. Schneebeli, M. Kamenetska, F. Foss, H. Vazquez, R. Skouta, M. Hybertsen, L. Venkataraman and R. Breslow, The electrical properties of biphenylenes, *Org. Lett.*, 2010, **12**, 4114–4117.
16 S. Fujii, S. Marqués-González, J. Y. Shin, H. Shinokubo, T. Masuda, T. Nishino, N. P. Arasu, H. Vázquez and M. Kiguchi, Highly-conducting molecular circuits based on antiaromaticity, *Nat. Commun.*, 2017, **8**, 4–11.
17 X. Yin, Y. Zang, L. Zhu, J. Z. Low, Z.-F. Liu, J. Cui, J. B. Neaton, L. Venkataraman and L. M. Campos, A reversible single-molecule switch based on activated antiaromaticity, *Sci. Adv.*, 2017, **3**, aao2615.
18 S. Kawai, K. Takahashi, S. Ito, R. Pawlak, T. Meier, P. Spijker, F. F. Canova, J. Tracey, K. Nozaki, A. S. Foster and E. Meyer, Competing Annulene and Radialene Structures in a Single Anti-Aromatic Molecule Studied by High-Resolution Atomic Force Microscopy, *ACS Nano*, 2017, **11**, 8122–8130.
19 M. Joost, L. Estévez, K. Miqueu, A. Amgoune and D. Bourissou, Oxidative addition of carbon–carbon bonds to gold, *Angew. Chem., Int. Ed.*, 2015, **54**, 5236–5240.
20 T. A. Su, M. Neupane, M. L. Steigerwald, L. Venkataraman and C. Nuckolls, Chemical principles of single-molecule electronics, *Nat. Rev. Mater.*, 2016, **1**, 16002.
21 L. Venkataraman, J. E. Klare, I. W. Tam, C. Nuckolls, M. S. Hybertsen and M. L. Steigerwald, Single-molecule circuits with well-defined molecular conductance, *Nano Lett.*, 2006, **6**, 458–462.
22 M. Mayor, H. B. Weber, J. Reichert, M. Elbing, C. Von Hänisch, D. Beckmann and M. Fischer, Electric Current through a Molecular Rod – Relevance of the Position of the Anchor Groups, *Angew. Chem., Int. Ed.*, 2003, **42**, 5834–5838.
23 M. Kamenetska, S. Y. Quek, A. C. Whalley, M. L. Steigerwald, H. J. Choi, S. G. Louie, C. Nuckolls, M. S. Hybertsen, J. B. Neaton and L. Venkataraman, Conductance and geometry of pyridine-linked single-molecule junctions, *J. Am. Chem. Soc.*, 2010, **132**, 6817–6821.
24 A. Mishchenko, L. A. Zotti, D. Vonlanthen, M. Bürkle, F. Pauly, J. C. Cuevas, M. Mayor and T. Wandlowski, Single-molecule junctions based on nitrile-terminated biphenyls: a promising new anchoring group, *J. Am. Chem. Soc.*, 2011, **133**, 184–187.
25 Y. S. Park, A. C. Whalley, M. Kamenetska, M. L. Steigerwald, M. S. Hybertsen, C. Nuckolls and L. Venkataraman, Contact chemistry and single-molecule conductance: a comparison of phosphines, methyl sulfides, and amines, *J. Am. Chem. Soc.*, 2007, **129**, 15768–15769.
26 M. Frei, S. V. Aradhya, M. Koentopp, M. S. Hybertsen and L. Venkataraman, Mechanics and chemistry: single molecule bond rupture forces correlate with molecular backbone structure, *Nano Lett.*, 2011, **11**, 1518–1523.
27 M. Frei, S. V. Aradhya, M. S. Hybertsen and L. Venkataraman, Linker dependent bond rupture force measurements in single-molecule junctions, *J. Am. Chem. Soc.*, 2012, **134**, 4003–4006.
28 S. V. Aradhya, M. Frei, M. S. Hybertsen and L. Venkataraman, van der Waals interactions at metal/organic interfaces at the single-molecule level, *Nat. Mater.*, 2012, **11**, 872–876.
29 J. M. Soler, E. Artacho, J. D. Gale, A. García, J. Junquera, P. Ordejón and D. Sánchez-Portal, The SIESTA method for simulation, *J. Phys.: Condens. Matter*, 2002, **14**, 2745–2779.
30 M. Brandbyge, J. L. Mozos, P. Ordejón, J. Taylor and K. Stokbro, Density-functional method for nonequilibrium electron transport, *Phys. Rev. B: Condens. Matter Mater. Phys.*, 2002, **65**, 165401.
31 T. Frederiksen, M. Paulsson, M. Brandbyge and A.-P. Jauho, Inelastic transport theory from first principles: methodology and application to nanoscale devices, *Phys. Rev. B: Condens. Matter Mater. Phys.*, 2007, **75**, 205413.
32 M. Paulsson and M. Brandbyge, Transmission eigenchannels from nonequilibrium Green's functions, *Phys. Rev. B: Condens. Matter Mater. Phys.*, 2007, **76**, 1–9.
33 S. V. Aradhya and L. Venkataraman, Single-molecule junctions beyond electronic transport, *Nat. Nanotechnol.*, 2013, **8**, 399.

Electronic Supplementary Material (ESI) for Physical Chemistry Chemical Physics.
This journal is © the Owner Societies 2018

Electronic Supplementary Information for

Direct Au-C contacts based on biphenylene for single molecule circuits

Narendra P. Arasu,[a,b] and Héctor Vázquez *,[a]

[a.] Institute of Physics, Academy of Sciences of the Czech Republic. Cukrovarnická 10, Prague 6, Czech Republic.

[b.] Department of Condensed Matter Physics, Faculty of Mathematics and Physics, Charles University, Ke Karlovu 5, Prague 2, Czech Republic.

* vazquez@fzu.cz

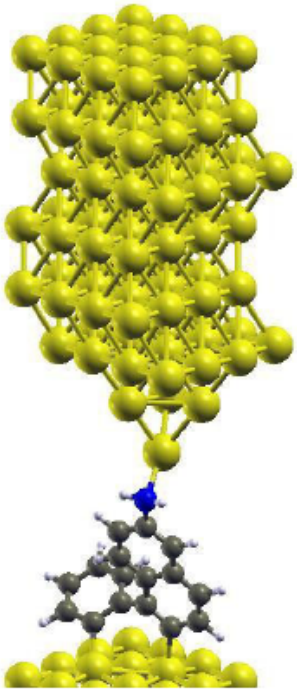

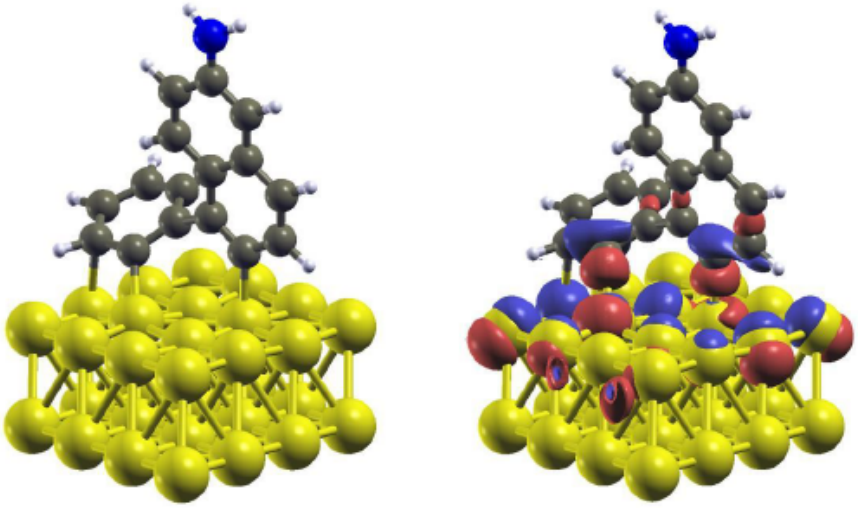

SI Fig.2 Electron density difference upon adsorption for an amine-terminated biphenylene-based molecule in a geometry similar to that of Fig. 2a (tip not visible). The structure is shown on the left for clarity. Electron density accumulation (depletion) is shown in red (blue) with respect to the isolated molecule plus Au surface. Electron density is displaced from the contact C atoms mainly towards the regions of the Au-C bonds. The nodal pattern of charge rearrangement upon adsorption has σ symmetry and is confined to the plane of the benzene rings.

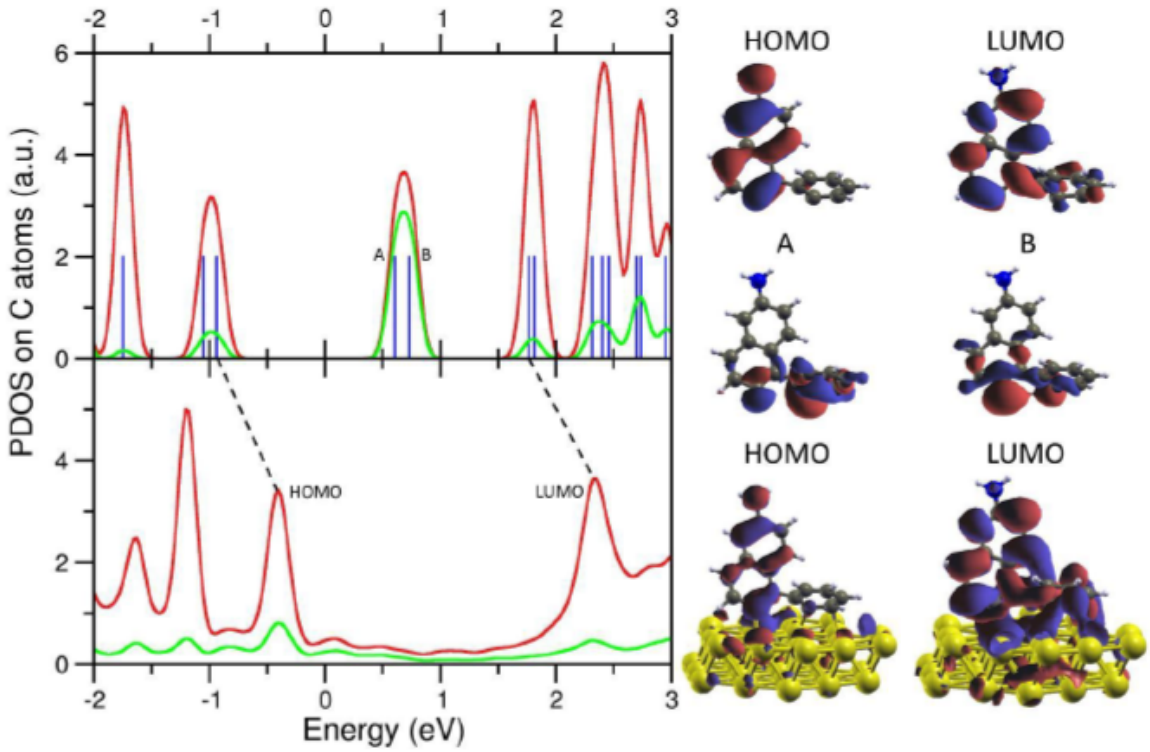

SI Fig.3 PDOS on the molecular C atoms (red) of the isolated molecule (top panel, spin polarised) and at the junction (bottom panel). The PDOS on the contact C atoms is shown in green. Contour plots to the right show relevant wave functions: C radicals (labelled A and B), HOMO and LUMO of the isolated molecule, and the latter two at the junction.

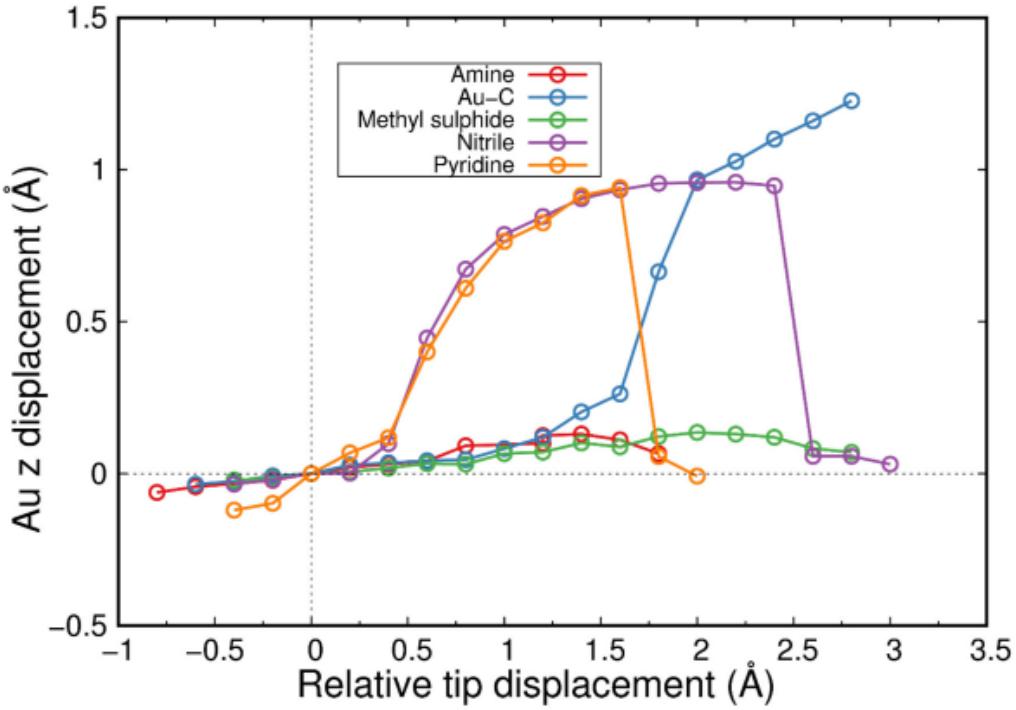

SI Fig.4 Height of the contact Au atom in the substrate measured from its position at equilibrium as a function of tip displacement. Since the height of the molecule changes with the top linker termination, the horizontal axis is measured with respect to the equilibrium distance for each linker. For nitrile, pyridine and Au-C links, the substrate Au atom is lifted from the surface.

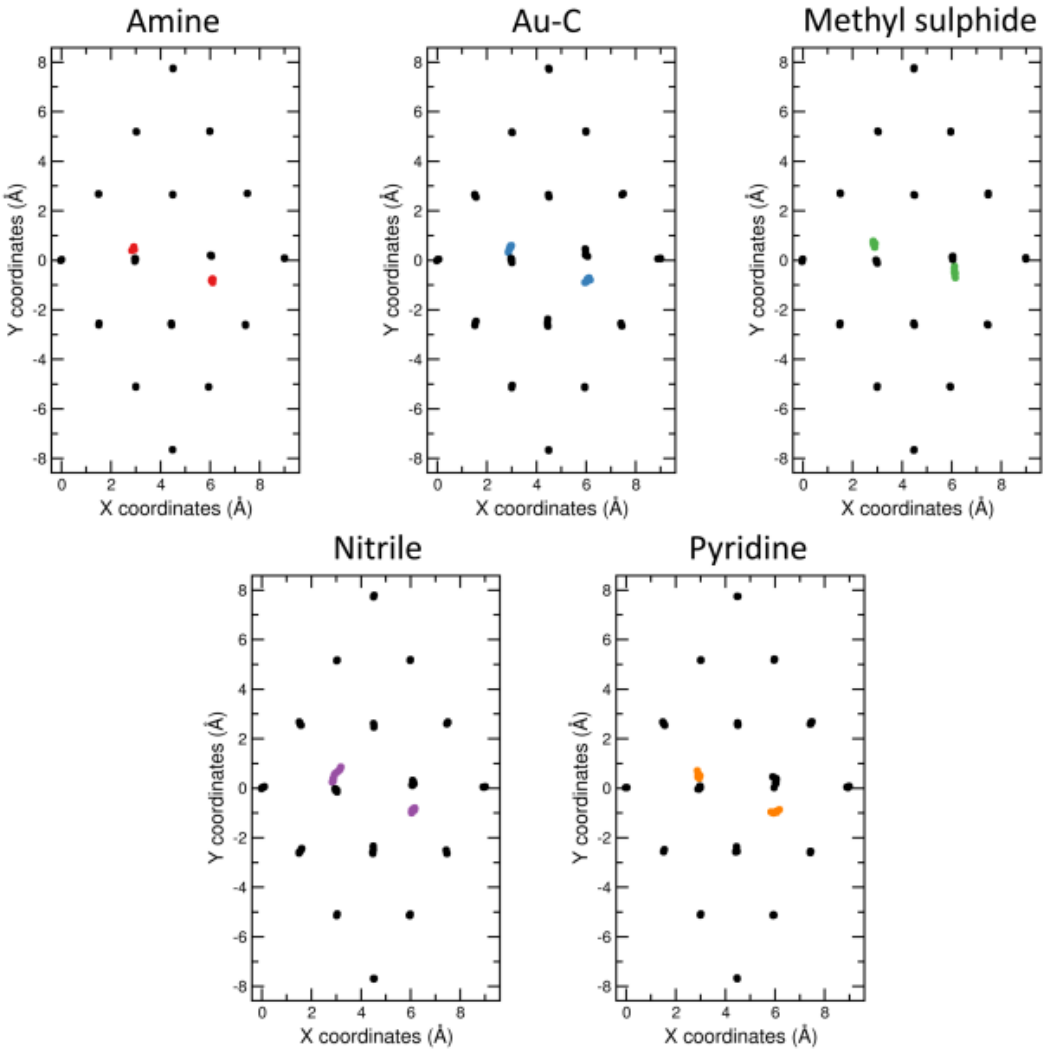

SI Fig.5 X and y coordinates of the surface Au atoms (black) and contact C atoms (color) during the tip approach simulations of Figs. 2 and 3 in the main text.

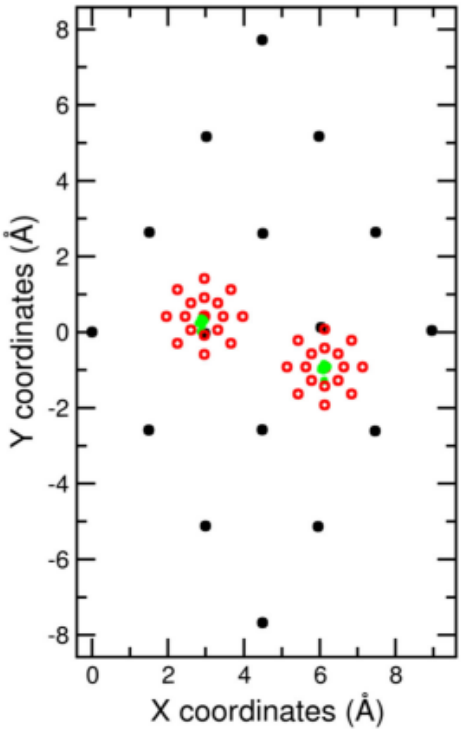

SI Fig.6 X and y coordinates of initial and final atomic positions during additional structural relaxations of an amine-terminated molecule where the initial molecular geometry was shifted laterally by 0.5Å or 1.0Å from the structure similar to that of Fig. 2a. In all cases, the contact C atoms relax to a final geometry close to that of the tip approach simulations. Black circles: Au surface atoms; open red circles: initial positions of the contact C atoms; filled red circle: (final) positions of the contact C atoms in Fig. 2 (tip far); filled green circles: final positions of the contact C atoms. All molecular and Au surface atoms were allowed to move.

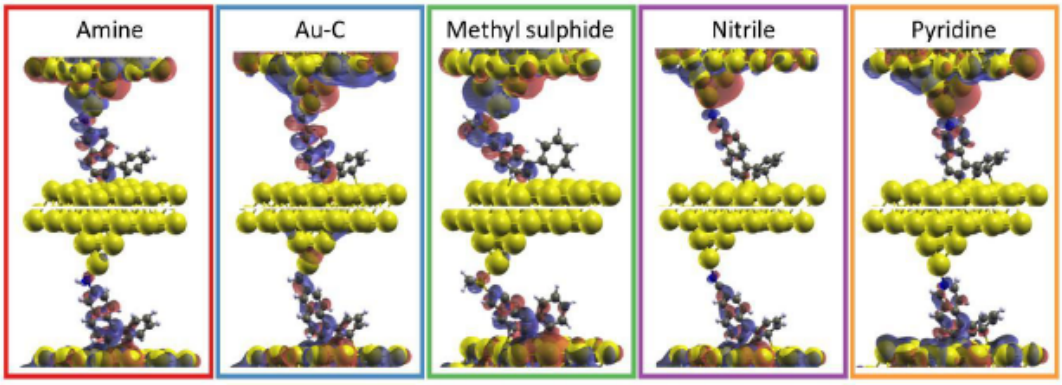

SI Fig.7 Calculated transmission eigenchannels at the Fermi energy incident from above (top panels) or below (bottom panels). In the bottom biphenylene-derived contacts, the side benzene ring is not in the tunnelling pathway.

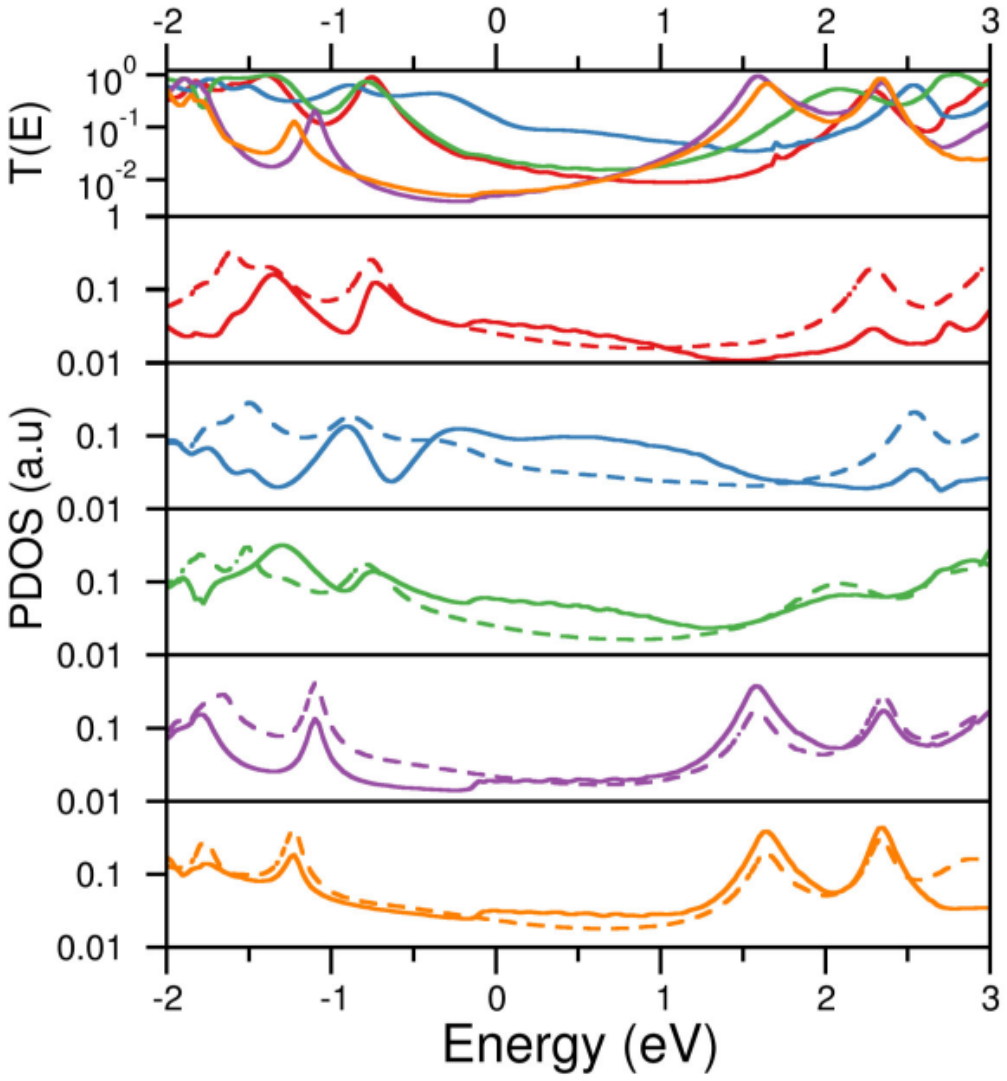

SI Fig. 8 Calculated transmission spectra (top panel) and PDOS over the top contact atom X (dashed lines) and bottom contact C atom (solid lines) for the five linker terminations considered for the top contact. The top

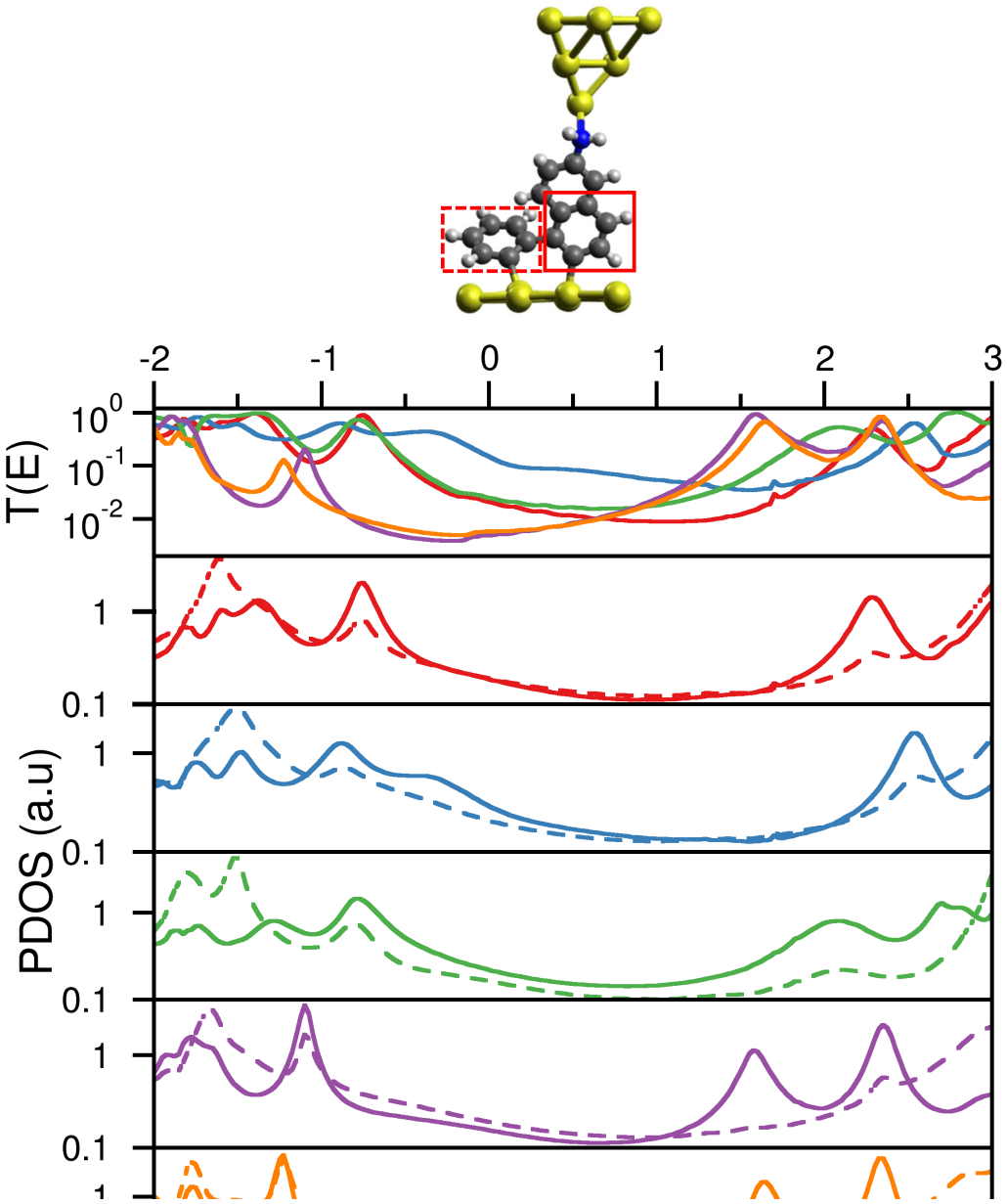
-2
-1
0
1
2
3
T(E)
10^{0}
10^{-1}
10^{-2}
PDOS (a.u)
1
0.1

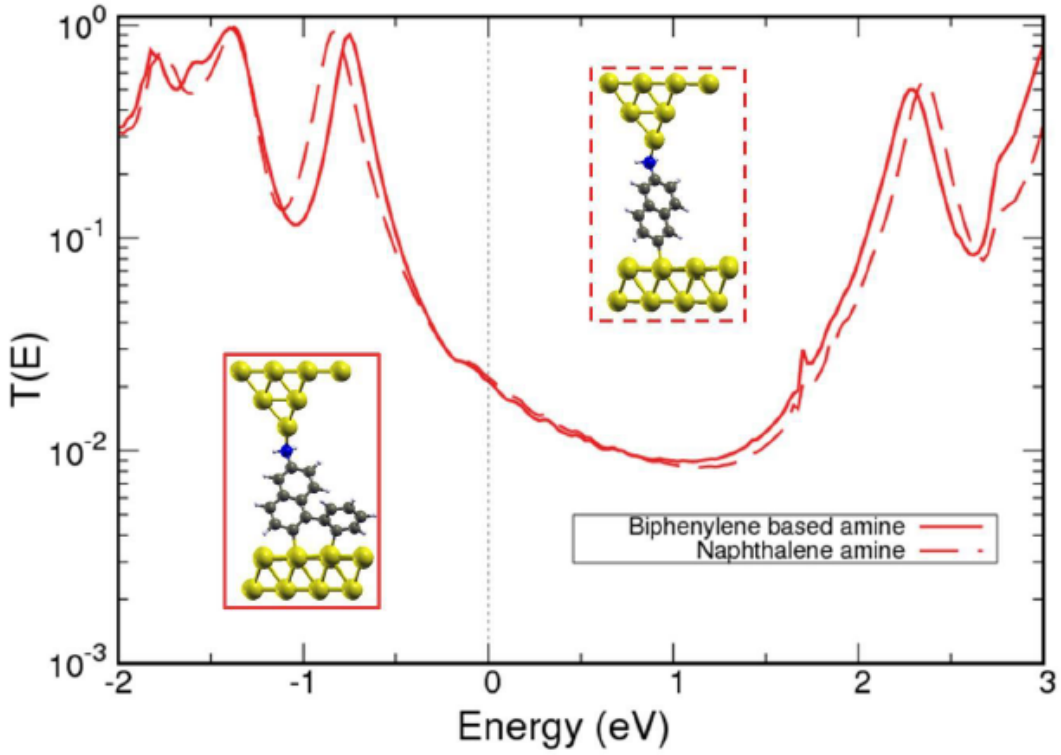

SI Fig.10 Calculated transmission spectra for the amine-terminated junction and for a molecule in the same geometry but missing the side benzene ring in the bottom contact. The contribution to conductance of this side ring is small.

5. Conductance of aromatic and antiaromatic molecules

5.1 Introduction

Conjugated molecules are useful and promising materials for a variety of applications such as organic photovoltaics[112], organic light-emitting diodes[113], and organic transistors[114]. The stability of conjugated molecules strongly depends on the number and arrangement of π bonds. Aromaticity is a key concept in chemistry that describes the stability of conjugated systems. According to Hückel's rule, conjugated systems with 4n+2 π-electrons are very stable, while those with 4n π-electrons are unstable. He termed the first kind of compounds "aromatic". Aromaticity is often associated with molecular stability provided by delocalized electrons. Benzene is a typical example of an aromatic molecule with 6 π-electrons contributing to molecular conjugation. It is more stable than molecules with a fewer number of π-electrons[115]. The stability of aromatic molecules makes them widely used in organic optoelectronic devices [17, 21]. Various studies have been reported on charge transport properties of aromatic molecules such as porphyrins [24, 116] and oligophenyls [117].

The relationship between aromaticity and conductance provides valuable insights for organic devices based on conjugated molecules. Chen et al. showed that more aromatic molecules lead to lower conductance [118]. The increase in energy gaps due to increasing aromaticity is attributed to a decrease in conductance. Since then molecules with less aromaticity gained interest in the field of organic devices.

Molecules with reduced aromaticity were known for a long time. In particular, Breslow [119] introduced the term "antiaromatic" for molecules in which the delocalization of electrons is destabilizing. Following Hückel's rule, antiaromatic molecules are conjugated compounds with 4n π electrons. For example, cyclobutadiene with 4 π-electrons is a highly unstable intermediate compound. The (anti)aromaticity of molecules can be measured through nuclear magnetic resonance (NMR) technique [120]. When a magnetic field is applied aromatic rings generate an induced magnetic field opposite to the applied field ('diatropic'), resulting in a shielding effect and lower NMR chemical shifts. Antiaromatic molecules lead to the deshielding effect and reinforce the applied magnetic field ('paratropic'), indicated by higher NMR chemical shifts.

In electrochemical studies, molecules with narrow energy gaps exhibit exceptional charge carrier properties and easily tunable molecular orbitals. The first electrochemical study on antiaromatic molecules was conducted by Breslow in 1967, [119]. Further electrochemical studies by Breslow et al., showed that electron passage through the cyclobutadiene ring is promoted by antiaromaticity [121]. It was anticipated that antiaromatic molecules conduct more than aromatic molecules. Despite knowing antiaromaticity for a long time, the synthesis of antiaromatic molecules remained a challenge owing to their high instability.

Recently, Ito et al. succeeded in the large-scale synthesis of the first stable antiaromatic molecule [122]. The high stability of the Ni-norcorrole in ambient

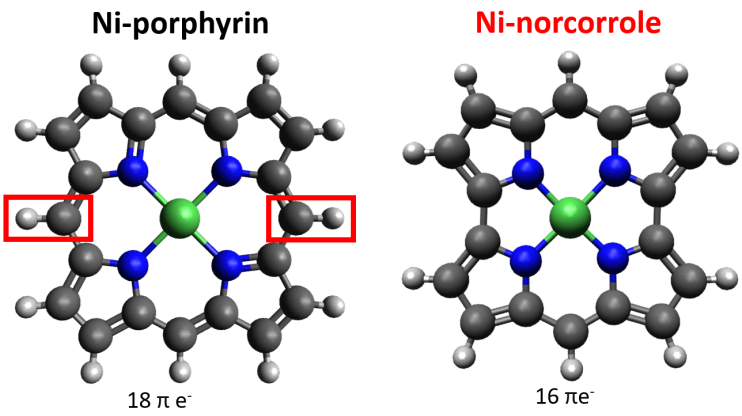

Figure 5.1: Core structures of first stable antiaromatic molecule synthesized (Ni-norcorrole, right) and its aromatic counterpart (Ni-porphyrin, left). The difference comes from two pairs of C-H atoms missing in Ni-norcorrole, marked as red boxes in Ni-porphyrin.

conditions is provided by heavy side groups with large steric demand. The Ni-norcorrole is a conjugated molecule with two fewer C-H groups than its aromatic counterpart Ni-porphyrin, as highlighted in figure 5.1. Following Hückel's rule, Ni-norcorrole is antiaromatic (16 π-electrons), whereas, Ni-porphyrin is aromatic (18 π-electrons).

We carried out the first study of single-molecule transport across a genuinely antiaromatic molecule (Ni-norcorrole). In collaboration with the chemists and experimentalists from Japan, we studied the transport properties of the antiaromatic Ni-norcorrole and compared it with its aromatic analogue Ni-porphyrin [102]. Our collaborators carried out the synthesis, deposition, and STM-BJ measurements of the Ni-norrcorrole and Ni-porphyrin molecules. We performed DFT-NEGF simulations to rationalize the transport properties of molecules. We calculated the zero-bias transmission spectra of both molecules. Our results show that the conductance of the Ni-norcorrole molecule is fourteen times higher than aromatic Ni-porphyrin. The higher conductance of the antiaromatic molecule is due to the LUMO-derived resonance of Ni-norcorrole, which is closer to the Fermi level than the LUMO resonance of the Ni-porphyrin molecule. The values are in excellent agreement with STM-BJ experiments. In our calculations, we apply a correction to the calculated conductance due energy level alignment errors intrinsic to DFT. We apply self-energy based corrections, accounting for errors intrinsic to DFT in the calculation of electron affinity, and polarization by the metal substrate. The corrected DFT molecular levels improve on the overestimation of conductance by DFT. Our work demonstrates the potential of the antiaromatic Ni-norcorrole molecules as highly conducting molecular devices.

In the process of analyzing the electronic structure of Ni-norcorrole, we noticed that the antiaromatic electronic structure is strikingly similar to that of the aromatic Ni-porphyrin. The HOMO and LUMO of Ni-norcorrole resemble HOMO-1 and HOMO of Ni-porphyrin respectively. The one orbital difference in occupation between aromatic-antiaromatic molecules comes from the fact that the Ni-porphyrin has two more π electrons, i.e, aromatic with 4n+2 against antiaromatic with 4n πelectrons. To see how general this phenomenon is, we quantified similari-

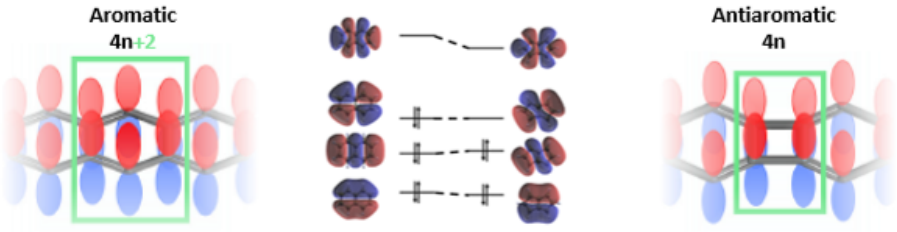

Figure 5.2: Antiaromaticity is shown to be double p-doping of the electronic structure of the aromatic analogue, whereby the HOMO of the aromatic molecule is fully depleted. These general principles have wide consequences on electron transport, quantum interference, and molecular design rules. The figure is the same as the table of the content figure of article 2 [123].

ties between aromatic and antiaromatic electronic structures. We wanted to know if this relationship is true for other pairs of aromatic-antiaromatic molecules. In our calculations, we compared aromatic-antiaromatic wavefunctions by computing the dot product of every aromatic molecular orbital with every antiaromatic molecular orbital. If an antiaromatic wavefunction is similar to an aromatic wavefunction, the dot product is close to one, and if the wavefunctions are orthogonal to each other, the dot product is zero.

The best match for every antiaromatic wavefunction is almost always the aromatic wavefunction with the same occupation number. As we traverse through the wavefunction spectra, states of both the molecules resemble each other in the same order. That is, the first antiaromatic wavefunction matches the first aromatic wavefunction, the second matches the second, and so on as illustrated in figure 5.2. Exceptions happen in the unoccupied orbitals at higher energy where the most similar aromatic and antiaromatic wavefunction does not have the same occupation number. The analysis shows that the electronic structure of an antiaromatic molecule is remarkably similar to its aromatic analogue. However, the antiaromatic molecules have one fewer (doubly) occupied state than its analogous aromatic molecule. Our results showed that the antiaromatic electronic structure could be perceived as a double p-doped aromatic molecule. Similar to double p-doped organic semiconductor, antiaromaticity completely depletes the aromatic HOMO.

In chemistry, cross-conjugation is a strategy to partially p-dope aromatic electronic structure[124]. Quinones are cross-conjugated derivatives of aromatic molecules. They are characterized by carbonyl substitution of two C atoms in an aromatic molecule. The two carbonyl groups extract one π-electron each, and only 4n π-electrons are left in the molecular conjugation. To explore the relationship between cross-conjugated molecule and antiaromaticity, we extended our wavefunction comparison to aromatic-quinoidal molecular pairs shown in figure 5.3. We found that the quinoidal molecules closely resemble the electronic structure of their analogous antiaromatic molecule by removing two π electrons from the conjugated system and localizing them on the carbonyl units.

We compared the transport properties of aromatic, antiaromatic, and quinoidal conjugated systems. Conjugated molecules can exhibit destructive quantum interference (DQI), introduced in section 1.9.2.

In our DFT-NEGF calculations, molecules are connected to the Au electrodes

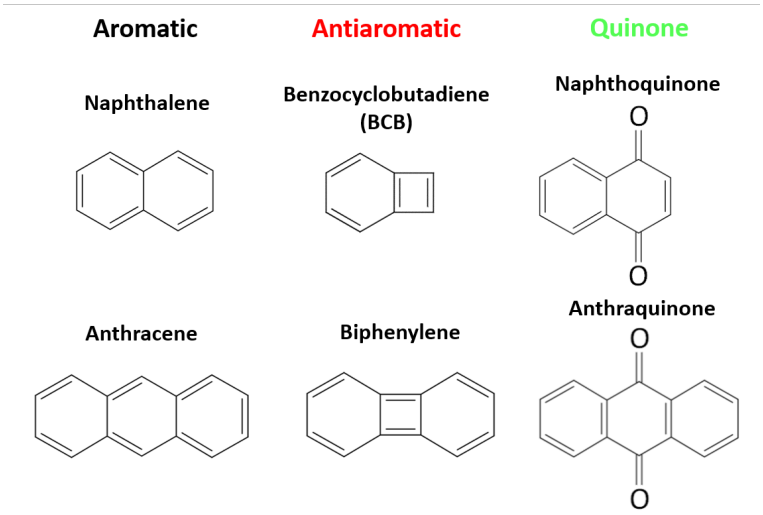

Figure 5.3: Aromatic, antiaromatic, and quinoidal molecular structures. Quinones are oxidized derivatives of aromatic molecules. The bond order of quinones is similar to antiaromatic molecules.

on either side through nitrile and methyl sulfide functionalized linkers. We calculated transmission spectra at zero bias. Our DFT-NEGF calculations show that the property of an antiaromatic molecule acting as a p-doped aromatic molecule is preserved at the metal-molecule junction. We found a close relationship between (anti)aromaticity and DQI.

Our transport calculation shows that, if DQI is present (absent) in an antiaromatic molecule then DQI is absent (present) in its aromatic counterpart for similar attachment points. For antiaromatic molecules connected to electrodes in the cis configuration, the DQI feature appears, whereas there is no DQI feature in aromatic molecules with the cis connection. Through calculations, we showed that by tuning metal-molecule contact chemistry, the aromatic-antiaromatic conductance relationship could be reversed.

To summarize, we showed that the antiaromatic electronic structure resembles a double p-doped aromatic molecule and that the electronic structure of a quinoidal molecule is similar to its analogous antiaromatic molecule, with additional orbitals localized on the carbonyl groups. We addressed the long-standing question of the enhancement of conductance in antiaromatic structures. We showed that it is favored due to the reduced energy gap, but also closely related to DQI and connectivity. Our work showed how the relative conductance of aromatic and antiaromatic pairs could be tuned through linker chemistry [123].

5.2 My contribution to article 1

I performed all DFT calculations. The nature of the experiment is such that the chemistry of the linker group was not well understood. We tested several linker groups before arriving at the appropriate bonding of sulphur acetate-linked molecular junctions. The final optimized structure was calculated by considering the minimum energy geometry of several electrode separation distances. Héctor Vázquez performed the NEGF calculations from the optimized geometry I pro-

vided. I wrote a Python script to calculate a correction to the DFT energy level. I applied the correction to the transmission peak and obtained the final conductance values. The results of the calculations were interpreted and analyzed together with Héctor Vázquez. I contributed to plotting the theory and simulation figures of the article.

5.3 My contribution to article 2

I carried out all the calculations. I calculated the electronic structure of several molecules at the gas phase using B3LYP exchange-correlation functional with a 6-31G basis set. I developed a Python script to compare wavefunctions of any two molecules. The script generates a ranked list of best-matching wavefunctions. I carried out the DFT-NEGF calculations. I prepared the figures and an advanced draft of the article.

nature COMMUNICATIONS

ARTICLE

Received 24 Jan 2017 | Accepted 17 May 2017 | Published 19 Jul 2017

DOI: 10.1038/ncomms15984 OPEN

Highly-conducting molecular circuits based on antiaromaticity

Shintaro Fujii[1], Santiago Marqués-González[1], Ji-Young Shin[2], Hiroshi Shinokubo[2], Takuya Masuda[3], Tomoaki Nishino[1], Narendra P. Arasu[4], Héctor Vázquez[4] & Manabu Kiguchi[1]

Aromaticity is a fundamental concept in chemistry. It is described by Hückel's rule that states that a cyclic planar π-system is aromatic when it shares $4n+2$ π-electrons and antiaromatic when it possesses $4n$ π-electrons. Antiaromatic compounds are predicted to exhibit remarkable charge transport properties and high redox activities. However, it has so far only been possible to measure compounds with reduced aromaticity but not antiaromatic species due to their energetic instability. Here, we address these issues by investigating the single-molecule charge transport properties of a genuinely antiaromatic compound, showing that antiaromaticity results in an order of magnitude increase in conductance compared with the aromatic counterpart. Single-molecule current–voltage measurements and *ab initio* transport calculations reveal that this results from a reduced energy gap and a frontier molecular resonance closer to the Fermi level in the antiaromatic species. The conductance of the antiaromatic complex is further modulated electrochemically, demonstrating its potential as a high-conductance transistor.

[1] Department of Chemistry, Graduate School of Science and Engineering, Tokyo Institute of Technology, Ookayama, Meguro-ku, Tokyo 152-8551, Japan. [2] Department of Molecular and Macromolecular Chemistry, Graduate School of Engineering, Nagoya University, Aichi 464-8603, Japan. [3] Global Research Center for Environment and Energy Based on Nanomaterials Science (GREEN), National Institute for Materials Science (NIMS), Tsukuba 305-0044, Japan. [4] Institute of Physics, Academy of Sciences of the Czech Republic, Cukrovarnicka 10, Prague CZ-162 00, Czech Republic. Correspondence and requests for materials should be addressed to S.F. (email: fujii.s.af@m.titech.ac.jp) or to H.S. (email: hshino@chembio.nagoya-u.ac.jp) or to H.V. (email: vazquez@fzu.cz) or to M.K. (email: kiguti@chem.titech.ac.jp).

The concept of aromaticity[1–3] is of fundamental importance in the chemistry of π-electrons that play an essential role in many organic materials relevant for nanoscale chemical, physical and biological studies. The stability and electronic properties of the π-system depend sensitively on the geometry and connectivity of the molecule. For instance, when a linear π-conjugated system adopts a cyclic and planar framework, the molecule gains additional energetic or resonance stabilization. This resonance or aromatic stabilization energy represents the energy difference with the best canonical structure that can be drawn for the molecule and is thus a measure of molecular stability. The greater this energy, the more stable the compound is. In addition to topology, this quantity also depends on the number of π-electrons in the cyclic conjugated system. Cyclic and planar molecules with $4n+2$ π-electrons present the highest resonance energy (stability) and are referred to as aromatic within Hückel's rule[4]. On the other hand, cyclic and planar molecules sharing $4n$ π-electrons feature a remarkable energetic destabilization and are referred to as antiaromatic[1,5]. For example, the lower resonance energy in cyclobutadiene makes it more energetic (and far more reactive) than its open-chain counterpart 1,3-butadiene. Higher stability and lower reactivity are reflected in larger molecular gaps and aromatic molecules generally have larger gaps than antiaromatic ones[6,7]. From a fundamental and simplified viewpoint, cyclic molecules with $4n+1$ and $4n+3$ π-electrons obviously possess unpaired electron(s) and become nonaromatic. These compounds exhibit open shell character and cannot be chemically isolated in a controlled manner.

Aromatic and antiaromatic π-systems have attracted wide attention in the field of the organic synthesis and materials science[8–11]. Aromatic molecules such as oligoacenes[8], porphyrins[9], tetrathiafulvalenes[10,11] and related compounds play an important role in organic electronic components such as electroluminescent devices and organic photovoltaic devices. In contrast, the characteristic instability and smaller gap of antiaromatic molecules brings to the π-system a great ability to donate and accept charge carriers and eases electrochemical tunability of the molecular orbitals, making antiaromatic compounds well suited for organic electronic components. Indeed, antiaromatic compounds had been predicted by Breslow to be more conducting. Early electrochemical measurements of oxidation/reduction potentials had shown that electron transfer from donor to acceptor groups in a molecule was amplified when connected through an antiaromatic structure[12,13]. Advances in electronic characterization make it possible to measure an electronic current through individual molecules, probing their inherent charge transport properties at the single-molecule scale[14–16]. Recent single-molecule electronics studies of a series of molecules with varying degrees of aromaticity established a negative relation between aromaticity and conductance. More aromatic rings with higher resonance energies were seen to correlate with HOMO (highest occupied molecular orbital) positions further from the Fermi level and lower conductance (which in these molecules is HOMO dominated)[17]. Subsequent transport calculations verified this trend and reported smaller molecular gaps and HOMO positions closer to the Fermi level with decreasing aromaticity[18]. However, the chemical instability of the antiaromatic molecules and unfavourable intermolecular interaction in the bulk has restricted transport studies to aromatic systems or species with no aromaticity. While these works clearly established the negative relationship of aromaticity with conductance, the positive relationship of conductance and antiaromaticity remained to be demonstrated[19].

The present study aims to address the long-standing issue of the electronic properties of antiaromatic molecules by investigating the single-molecule transport properties of an antiaromatic compound and exploring the effect of antiaromaticity on the charge transport properties at the single-molecule scale. To that end, a recently developed, antiaromatic norcorrole-based Ni(II) complex is studied (Fig. 1). Ni(nor) features a chemically stable, structurally rigid antiaromatic porphyrinoid moiety[20–22] where antiaromaticity can be preserved due in no small part to its molecular rigidity. The electronic properties of Ni(nor) are benchmarked against a porphyrin-based aromatic counterpart, Ni(porph) (Fig. 1). The antiaromatic molecule Ni(nor) exhibits enhanced charge transport properties in which single-molecule conductance is more than one order of magnitude higher than that of its aromatic counterpart. This makes Ni(nor) the most conductive organometallic complex reported to date, to the best of our knowledge. The *ab initio* transport calculations show that the remarkable conductance of Ni(nor) originates from the smaller gap and more favourable frontier orbital alignment with respect to the aromatic species. Through electrochemical gating, the conductance of the antiaromatic molecule Ni(nor) is further modulated by more than a factor of five. This work ultimately expands the current synthetic guidelines for the design of highly conducting and functional organic electronic materials using antiaromaticity.

Results

Conductance studies. To assess the impact of antiaromaticity in molecular conductance, single-molecule transport studies were performed on two structurally similar complexes, Ni(nor) and Ni(porph) (Fig. 1, Supplementary Figs 1,2, and Supplementary Note 1). The thioacetate groups bind to Au electrodes through the S lone pair, a strategy that has been shown to result in selective bonding and clear experimental conductance signatures (see Supplementary Note 3 for further details)[23]. The scanning tunnelling microscope-based break-junction (STM-BJ) technique was used to obtain 2,500 conductance–distance traces for each molecule (see Methods and Supplementary Fig. 3). Measurements were repeated on analogue samples of both complexes to ensure reproducibility. All recorded traces were employed to build logarithmically binned conductance histograms with no data selection (Fig. 2a). Conductance histograms display well-defined peaks denoting the most probable molecular conductance value at 4.2×10^{-4} and $1.7\times10^{-5}\,G_0$ for Ni(nor) and Ni(porph), respectively. No additional molecular signatures were observed in the high conductance regime 10^{-2}–1 G_0 (Supplementary Fig. 5). The measured conductance of the antiaromatic complex Ni(nor) was found to be an order of magnitude higher than that of Ni(porph). The comparatively low conductance of the aromatic counterpart is in good agreement with previous studies on closely related porphyrin-based complexes[24,25]. The structural similarities between both complexes suggest that the enhanced conductance of Ni(nor) arises from the antiaromatic nature of the norcorrole moiety. A two dimensional conductance–distance histogram constructed with traces featuring Ni(nor) molecular plateaus extracted from the same data set reveals junction lengths of ∼0.8–1.0 nm (Fig. 2b; Supplementary Figs 6 and 7), ruling out the possibility of molecular junctions being formed perpendicularly to the norcorrole plane[26]. Slightly longer junction dimensions of ∼1.0–1.2 nm were typically observed for Ni(porph) (Supplementary Fig. 8) in good agreement with previous reports[25]. Similar junction lengths were obtained for both complexes at different voltages (Supplementary Figs 9 and 10). The comparatively shorter length of Ni(nor) junctions reflects the marked structural constraints of the antiaromatic norcorrole moiety, in sharp contrast with porphyrin moiety known to adopt both buckled and twisted conformations (Supplementary Fig. 11)[20,27,28]. Additional STM-BJ experiments were performed in ultrahigh vacuum (UHV) to confirm the

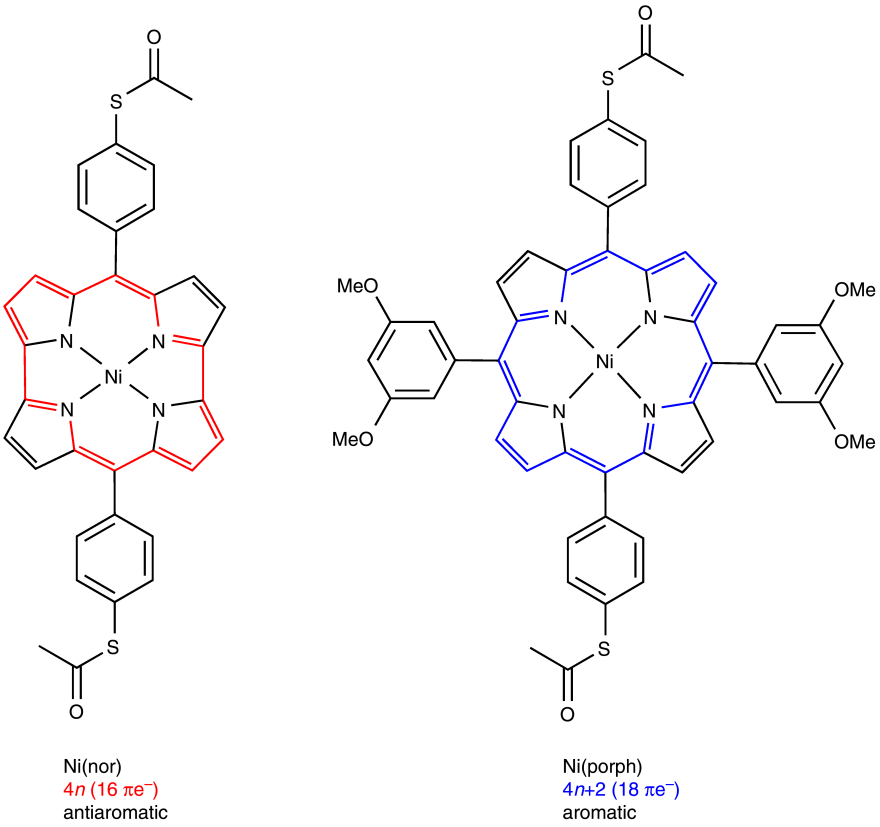

Figure 1 | Antiaromatic and aromatic molecules. Antiaromatic Ni norcorrole Ni(nor) and its porphyrin-based aromatic counterpart Ni(porph) (Supplementary Note 1).

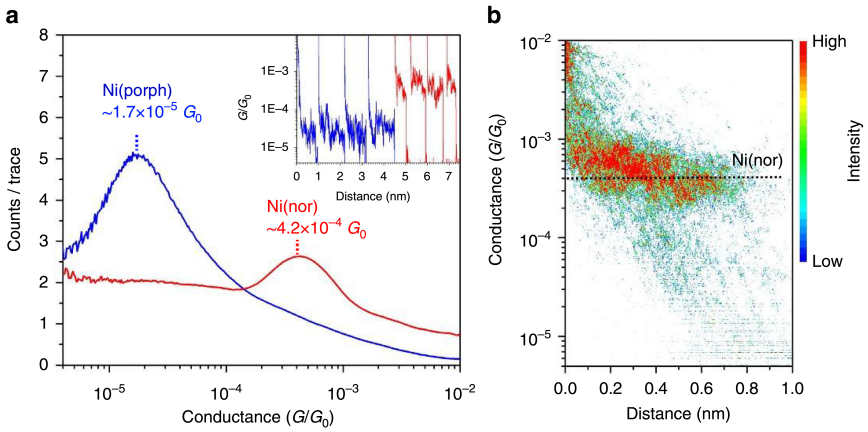

Figure 2 | Measured single-molecule conducting properties. (**a**) Logarithmically binned conductance histograms (111 bins per decade) of Ni(nor) and Ni(porph) at 100 mV in air. The peaks at 4.2×10^{-4} and $1.7 \times 10^{-5}\,G_0$ denote the most probable molecular conductance values of Ni(nor) and Ni(porph), respectively. Histograms were built from 2,500 conductance traces with no data selection. Inset: representative examples of STM-BJ conductance–distance traces of Ni(nor) and Ni(porph) featuring molecular conductance plateaus. Traces were laterally offset for clarity. (**b**) Two-dimensional (2D) conductance–distance histogram of Ni(nor). Traces showing a conventional tunnelling decay were removed for clarity. For additional conductance measurements and histograms see Supplementary Figs 4–11.

remarkable charge transport properties and chemical stability observed for Ni(nor). In UHV, a well-defined molecular conductance peak was observed at $4.6 \times 10^{-4}\,G_0$ (Supplementary Note 9), demonstrating the robustness of the electronic transport probabilities of the chemically stable antiaromatic compound of Ni(nor).

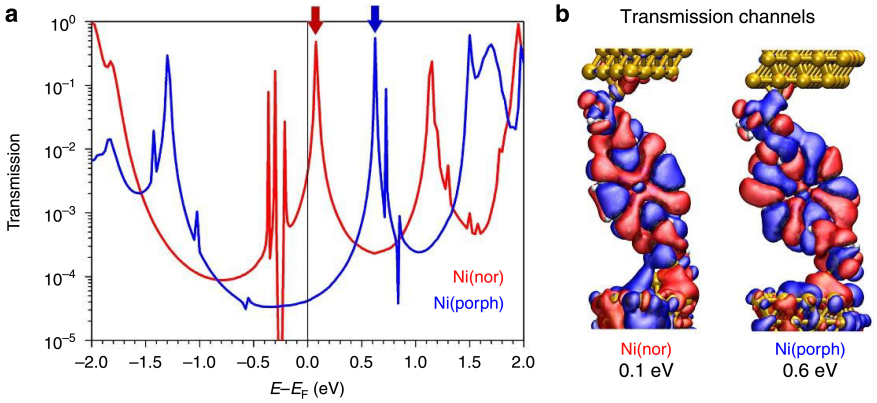

Figure 3 | Calculated transport properties. (**a**) DFT transmission spectra of Ni(nor) and Ni(porph). Peaks at 0.1 and 0.6 eV are indicated by arrows. (**b**) Real part of the most conducting channels of Ni(nor) at 0.1 eV and Ni(porph) at 0.6 eV. In both cases, current is carried by a single channel.

Table 1 | Comparison of resonance-corrected calculated and measured conductance (in units of G_0) and molecular-level offsets (in eV) of Ni(nor) and Ni(porph).

	Ni(nor)		Ni(porph)		Ratio G(nor)/G(porph)
	E_{LUMO}-E_F	G(E_F)	E_{LUMO}-E_F	G(E_F)	
Calculations	0.47	2.1×10^{-4}	0.93	1.5×10^{-5}	14
Experiment	0.48	4.2×10^{-4}	0.85	1.7×10^{-5}	25

Transport calculations. To clarify the origin of the higher conductance of the antiaromatic Ni(nor) complex and understand the effect of antiaromaticity on the charge transport properties, transmission calculations based on density functional theory (DFT) and nonequilibrium Green's functions, including corrections to the DFT resonance positions, were performed (see Supplementary Notes 4,5 and Supplementary Figs 12–15). As discussed in the previous section, the Ni(nor) and Ni(porph) molecules bind to Au electrodes using acetyl groups at the molecular termini and form single-molecule junctions (see also Supplementary Note 4). Figure 3a shows the DFT spectra of the Ni(nor) and Ni(porph) species. The spectrum of the Ni(porph) complex shows a peak slightly above $\sim+0.6$ eV while that of the Ni(nor) features a low-lying peak at $\sim+0.1$ eV. For both Ni(porph) and Ni(nor), zero-bias conductance is determined by an unoccupied molecular frontier orbital that tails into the Fermi level and the current is carried by a single transmission channel. The width of the transmission peaks measures the degree of electronic coupling of the conducting orbital to the electrodes. From the spectra, we obtain full-width at half-maximum of $\Gamma_{Ni(nor)}=16$ meV and $\Gamma_{Ni(porph)}=10$ meV (Supplementary Table 2). Analysis of the most conducting transmission channel at that energy shows that it is a state delocalized over the conjugated core and linker rings (Fig. 3b) deriving from the lowest unoccupied molecular orbital (LUMO). It should be noted that the series of peak-dip features in the occupied part of the Ni(nor) spectrum close to the Fermi level are very sharp and do not influence zero-bias conductance (Supplementary Note 4).

It is well known that DFT calculations inherently overestimate conductance due to errors in the position of frontier molecular orbitals[29–33]. Corrections to the positions of DFT molecular resonances, which include a molecular self-interaction term as well as a contribution arising from the polarization of the interface, were applied to the Ni(nor) and Ni(porph) junctions (details are available in Supplementary Note 5 and Supplementary Table 1). Table 1 summarizes these results and compares the measured conductance to the calculated values after the corrections to the DFT molecular-level positions are taken into account. The corrections to the molecular resonance positions bring the calculated values into very good agreement with experiment, as previously seen for porphyrins[25]. Calculations show that the higher conductance of the antiaromatic species results from a LUMO-derived resonance closer to the Fermi level.

Current–voltage (I–V) measurements. To confirm the theoretical prediction that the higher conductance of the antiaromatic compound Ni(nor) is due to the energetically closer lying resonance, the I–V characteristics of Ni(nor) and Ni(porph) were measured using a variation of the STM-BJ technique. Briefly, upon formation of a single-molecule junction, the tip is momentarily held in position and the tunnelling current is monitored as the voltage is swept in the ±1 V range (see Methods, Supplementary Fig. 16 and Supplementary Notes 6–8 for details). The process is repeated until a statistically significant data set is obtained. The selected profiles were compiled into logarithmically binned two-dimensional plots to obtain a statistical description of the I–V characteristics of Ni(nor) and Ni(porph) (Fig. 4a,b). The steeper slope of the Ni(nor) I–V profiles in the linear regime ±0.1 V ($I/V=\sim4\times10^{-4}G_0$) is in good agreement with the aforementioned STM-BJ studies. The nonlinear I–V response is evident in the I–V profiles at the high bias voltage-range above 0.5 V. Each nonlinear I–V profile was individually fitted to a single-level tunnelling model[34,35] described by

$$I(V)=\frac{2e\Gamma}{h}\left\{\tan^{-1}\left[\frac{eV/2-\varepsilon_0}{\Gamma}\right]+\tan^{-1}\left[\frac{eV/2+\varepsilon_0}{\Gamma}\right]\right\}, \quad (1)$$

where ε_0 is the energy difference between the chemical potential of

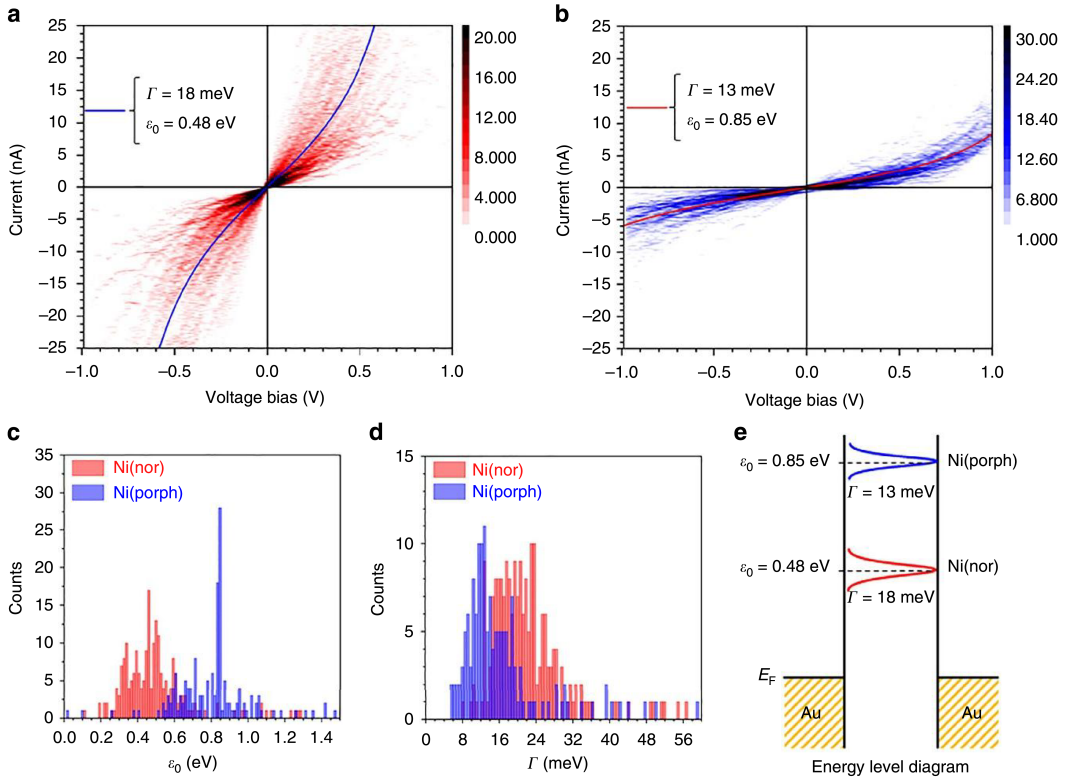

Figure 4 | Experimental determination of transmission resonance positions and electronic couplings. (**a**) Two-dimensional (2D) histogram built from 216 *I*–*V* profiles collected from single-molecule junctions of Ni(nor). (**b**) Current–voltage histogram constructed with 168 profiles of Ni(porph). Overlaid lines show the most probable *I*–*V* profile. All current–voltage profiles were recorded during single-molecule conductance plateaus in the correlated BJ trace. Bin sizes of 0.02 V and 0.075 nA were employed. (**c**) Statistical distribution of transmission peak position Ni(nor) and Ni(porph) extracted from the fitting of each individual *I*–*V* response to a single-level tunnelling model. (**d**) Statistical distribution of metal–molecule coupling for Ni(nor) and Ni(porph) single-molecule junctions. (**e**) Schematic representation of the orbital alignment and metal–molecule electronic coupling for Ni(nor) and Ni(porph) assuming a single-level model.

the electrode and the dominant molecular transport orbital and Γ is the metal–molecule coupling (full-width at half-maximum) (see Supplementary Figs 17–19). The statistical distribution of ε_0 and Γ for Ni(nor) and Ni(porph) is shown in Fig. 4b,c. Both complexes show a comparable degree of metal–molecule electronic coupling with $\Gamma \sim 18$ meV and ~ 13 meV for Ni(nor) and Ni(porph), respectively. The experimentally obtained electronic couplings are in very good agreement with the theoretical ones of 16 and 10 meV for Ni(nor) and Ni(porph), respectively. The similarity between values obtained for the metal–molecule couplings of both complexes can be rationalized in terms of their structural similarity and the use of identical thioacetate linkers. These results confirm the weakly binding nature of the thioacetate linkers, compared with previously reported studies on 1,4-benzenedithiol featuring the archetypal-SH linkers (10–130 meV)[36]. The moderate metal–molecule interaction displayed by the thioacetate moiety plays a crucial role in the preservation of the antiaromatic character of the complex, avoiding possible counterbalancing electronic effects[19,37] The energy difference between the Fermi level and the dominant molecular transport orbital was found to be much smaller ($\varepsilon_0 \sim 0.48$ eV) for the antiaromatic compound Ni(nor) than for the aromatic compound Ni(porph) ($\varepsilon_0 \sim 0.85$ eV). The *I*–*V* analysis indicates that the origin of the increased conductance of Ni(nor) is the closer-lying frontier orbital ($\varepsilon_0 \sim 0.48$ eV) that is directly related to the narrow HOMO–LUMO gap caused by the antiaromatic destabilization of the norcorrole moiety.

Electrochemical conductance modulation. The ambient and UHV STM-BJ studies and transport calculations described above revealed the LUMO-mediated enhanced charge transport capabilities of Ni(nor). Here we demonstrate tunability of the single-molecule conductance of Ni(nor) by electrochemically gating the position of this orbital with respect to the electrode potential.

Before single-molecule studies, cyclic voltammetry of Ni(nor) adsorbed on Au(111) was measured. The first electrochemical reduction, attributable to a reaction from Ni(nor) to Ni(nor)$^{\bullet -}$ (ref. 21), appeared at -0.65 V versus Ag/AgCl (Supplementary Note 10). Subsequent electrochemical single-molecule conductance experiments brought the LUMO-mediated transport channel closer to the electrode potential as the electrochemical potential was changed from $+0.45$ to -0.30 V versus Ag/AgCl. The STM-BJ technique was employed to collect conductance–distance traces of Ni(nor) in a pH 7 aqueous phosphate buffer at different electrochemical potentials (E) while keeping the tip–substrate voltage constant at 0.1 V (see Methods and Supplementary Figs 20 and 21 for details). The accessible electrochemical potential window was determined experimentally ensuring that the background tunnelling current would not affect the single-molecule measurements.

Logarithmically binned histograms show an increase in the molecular conductance of Ni(nor) as E takes more negative values in the reduction direction and display well-defined peaks shifting from $6.9 \times 10^{-4} G_0$ at $E = -0.30$ V to $1.3 \times 10^{-4} G_0$ at $E = +0.45$ V (Fig. 5a and Supplementary Fig. 21). Under the

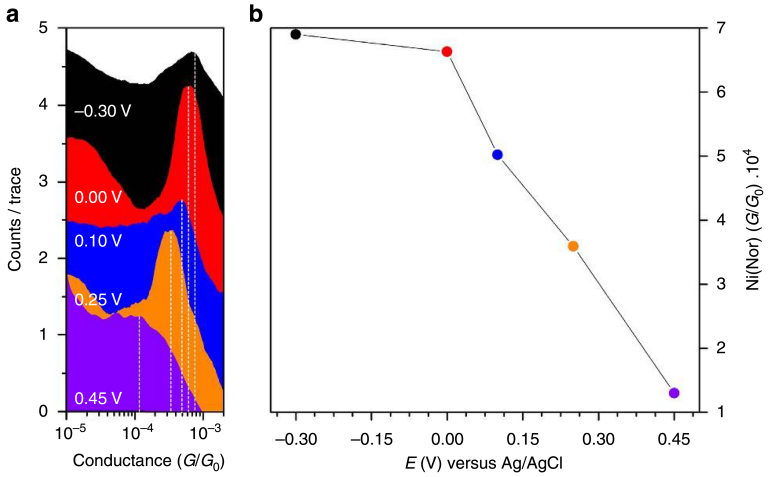

Figure 5 | Electrochemical gating of the charge transport properties. (**a**) Logarithmically binned conductance histograms of Ni(nor) built from STM-BJ traces at different electrochemical potentials. An approximately fivefold conductance modulation was attained for the antiaromatic complex Ni(nor) under electrochemical environment. Histograms were built from STM-BJ traces collected at a different electrochemical potential (*E*), while holding a constant tip-substrate bias of 0.1 V. Experiments were performed using a Ag/AgCl reference ($\Delta E_{ref} = \pm 1$ mV). (**b**) Ni(nor) conductance as a function of electrochemical potential. For details on the experimental setup, individual histograms and reproducibility see Supplementary Figs 20–24.

electrochemical potential control, the single-molecule conductance of Ni(nor) exhibits a fivefold modulation. Comparable results were obtained on an analogue sample (Supplementary Figs 23 and 24). In both cases, a substantial conductance modulation was observed for Ni(nor) (Fig. 5b and Supplementary Fig. 23). The measured conductance modulation results from the movement of the LUMO position of the neutral species with respect to the Fermi level of the electrodes.

The observed behaviour with the quasi-sigmoidal shape of the conductance modulation is similar to one of two distinct profiles recurrently found in the literature for both organic and organometallic derivatives in aqueous electrolytes[38–40]. A sigmoidal shape of the molecular conductance modulation has been observed previously in studies of electrochemically gated conductance of viologen-based single-molecule junctions in aqueous electrolytes and attributed to a 'soft' electrochemical gating of the conductance response[40,41]. A second behaviour, less frequently reported, features a bell-shaped conductance modulation profile[40,42] with a conductance peak centred at a threshold electrochemical potential that predicted to be shifted by typically a few hundred mV (corresponding to the reorganization energy of the molecule) from the redox potential[43]. Although both modulation profiles (that is, sigmoidal and bell-shaped profiles) have been rationalized for both direct tunnelling and redox-mediated hopping transport mechanisms, the origin of the sigmoidal profile remains a matter of debate. The absence of a maximum in the modulation profile within the potential range (from $+0.45$ to -0.3 V versus Ag/AgCl) may suggest that the resonance between the Fermi level and the Ni(nor) orbitals has not been reached. Recent studies have demonstrated that the sigmoidal profile may arise from the broadening of the bell-shaped gating response[40]. This result was rationalized in terms of the comparatively low gating efficiency of the aqueous electrolytes, roughly 20% that of the ionic liquid electrolytes. By replacing the aqueous electrolyte for an ionic liquid electrolyte the gating profile of a viologen derivative changed from sigmoidal to bell shaped[40]. While the origin of the profile in the electrochemical modulation remains to be solved, the present study revealed that the antiaromaticity is preserved in the aqueous electrochemical conditions and Ni(nor) displays well-defined single-molecule conductance that enabled us to attain a fivefold conductance modulation.

Discussion

We have used STM-BJ and *I*–*V* measurements, supported by theoretical calculations, to explore the effect of antiaromaticity on the charge transport properties of single-molecule junctions. The rational molecular design of the antiaromatic Ni(nor) and aromatic Ni(porph) featuring weakly interacting thioacetate linkers enabled direct comparison between the single-molecule junctions of antiaromatic and aromatic characters. We compared an antiaromatic compound with its aromatic counterpart and showed that the antiaromatic species is an order of magnitude more conducting. Antiaromatic destabilization results in a smaller molecular gap and drives the LUMO closer to the Fermi level. The conductance of the antiaromatic species was further modulated by a factor of five by means of electrochemical gating. Our work demonstrates the potential of analogue derivatives as highly conducting molecular materials and provides relevant guidelines for the design of molecular materials for highly conducting single-molecule electronics.

Methods

Synthesis and characterization. The general procedure to synthesize Ni(nor) and Ni(porph) is as follows (see the Supplementary Note 1 for details). For the preparation of Ni(nor), 4-(*S*-acetylthio)benzaldehyde was prepared in 80% yield according to the literature method by Lindsey and colleagues[44]. The formyl group of *p*-(methylthio)benzaldehyde was protected by treatment with neopentyl glycol[45]. The methylthio group was converted into the acetylthio group upon the reaction with the methanethiolate anion followed by the introduction of acetyl chloride. Deprotection of the acetal group with trifluoroacetic acid at –10 °C afforded 4-(*S*-acetylthio)benzaldehyde that was transformed to *p*-(*S*-acetylthio)phenyl-2,2′-dipyrromethane in ~30% yield by treatment with pyrrole. Bromination with NBS at –75 °C followed by DDQ (2,3-dichloro-5,6-dicyanobenzoquinone) oxidation gave 1,9-dibromo-5-(*S*-acetylthio phenyl)dipyrrin in 67%. The work-up was conducted using neutral or weak acidic conditions while avoiding alumina filtration. The conventional protocol involving the use of aqueous NaOH solutions and alumina filtration was found to produce a large number of side-products including the deprotected merchaptophenyl-substituted dipyrrin. The dipyrrin was metalated in the reaction with $Ni(OAc)_2 \cdot 4H_2O$ and purified by recrystallization from CH_2Cl_2/hexane to get greenish black crystals in 79% yield. Finally, the

dibromodipyrrin Ni(II) complex was converted to Ni(nor) by Ni(0)-mediated homo-coupling in 10% yield. For the synthesis of Ni(porph), the 5,15-di(S-acetyl thiphenyl)-10,20-di(3,5-dimethoxyphenyl)porphyrin was prepared by the trifluoroacetic acid catalysed condensation of *S*-acetylthiobenzaldedhyde and 3,5-dimethoxyphenyl-2,2′-dipyrromethane. The free-base porphyrin was then metalated with $Ni(acac)_2$ to obtain Ni(porph).

Conductance measurements. Molecular conductance was measured using the STM-BJ technique on a Nanoscope V (Bruker, Santa Barbara, CA, USA) running a custom-made dataflow program. Scanners featuring $10\,nA\,V^{-1}$ preamplifiers were used throughout. The tunnelling current (I) is measured between a gold tip and a gold-on-mica substrate while they are repeatedly brought into and out of contact ($23.3\,nm\,s^{-1}$) at a constant voltage bias of 100 mV. In the absence of molecules bridging the tip–substrate gap an exponential current decay is recorded. On the contrary, if a molecule gets suspended between tip and substrate a characteristic region of constant current (plateau) is observed. Current values are transformed into conductance ($G = I/V$) and referenced to the conductance quantum ($G_0 = 2e^2/h = 77{,}481$ nS). The Au(111) substrates were prepared by means of thermal deposition at 625–675 K under vacuum, and flame annealed before use. Tips were prepared by mechanical cutting of commercially available Au wire (>99%, ø–0.3 mm). Molecular adsorption was achieved by casting a small aliquot (~20 µl) of 0.1 mM CH_2Cl_2 solutions of the target molecules on freshly annealed substrates. Conductance measurements were performed before and after molecular deposition. Measurements were repeated until a statistically significant data set was obtained.

Current–voltage measurements. The aforementioned BJ protocol was modified to record the I–V response of individual molecules. Upon formation of a single-molecule junction, the tip was briefly held in position and the voltage scanned (±1.0 V in 2.5 ms). A detailed description of the experimental protocol as well as the analysis and fitting of the I–V profiles to a single-level tunnelling model is included in the Supplementary Information.

Electrochemical conductance modulation. Electrochemical control on the single-molecule conductance of Ni(nor) was exerted using a 4-electrode setup controlled by a Bruker Universal Bipotentiostat. The BJ studies were performed at different electrochemical potentials, with respect to a Ag/AgCl reference, while holding a constant tip–substrate voltage bias of 100 mV. A purpose-built three-dimensional printable cell was used to accommodate the four-electrode setup (See Supplementary Fig. 20). Gold tips were electrochemically etched in 3 M NaCl and coated in polydimethylsiloxane following a dipping/baking procedure[46]. Substrates and molecular deposition were performed following the aforementioned procedure. Experiments were performed in a pH 7 aqueous electrolyte (0.1 M, NaH_2PO_4/Na_2HPO_4).

Transmission calculations. We carried out first-principles simulations based on DFT nonequilibrium Green's functions to calculate the electronic and transport properties[47,48]. Exchange correlation was described using the generalized gradient approximation in the Perdew–Burke–Ernzerhof implementation. Au atoms were described using a single-zeta polarized basis while a double-zeta polarized basis was used for molecular atoms. Both molecules bind to tip structures via the S lone pair. In the case of the aromatic compound, we removed the side dimethoxy phenyl groups not connected to the electrodes and replaced them with H atoms to minimize the computational cost. The electronic coupling between these side groups and the central aromatic core is weak due to the large dihedral angle (~110°) between them. In a large unit cell (42 Au atoms per layer) we verified that the projected density of states on the central aromatic core plus binding conjugated linkers was essentially unchanged upon removal of the dimethoxy phenyl groups. We used a unit cell with 16 Au atoms per layer and optimized the vertical separation between the electrodes, relaxing the position of the molecular and tip atoms until all forces were $<0.02\,eV\,Å^{-1}$. We then carried out transmission calculations at optimized geometries. Monkhorst-Pack grids ($5 \times 5 \times 1$ and $15 \times 15 \times 1$) were used for the calculations of the electronic structure and transmission spectra, respectively. Transmission eigenchannels were computed at the centre of the Brillouin zone[49].

Data availability. The data that support the findings of this study are available from the corresponding authors on request.

References

1. Schleyer, P. V. R. Introduction: aromaticity. *Chem. Rev.* **101,** 1115–1118 (2001).
2. Randić, M. Aromaticity of polycyclic conjugated hydrocarbons. *Chem. Rev.* **103,** 3449–3606 (2003).
3. Krygowski, T. M., Szatylowicz, H., Stasyuk, O. A., Dominikowska, J. & Palusiak, M. Aromaticity from the viewpoint of molecular geometry: application to planar systems. *Chem. Rev.* **114,** 6383–6422 (2014).
4. Hückel, E. Quantentheoretische Beiträge zum Benzolproblem. *Z. Physik* **70,** 204–286 (1931).
5. Breslow, R. Antiaromaticity. *Acc. Chem. Res.* **6,** 393–398 (1973).
6. De Proft, F. & Geerlings, P. Conceptual and computational DFT in the study of aromaticity. *Chem. Rev.* **101,** 1451–1464 (2001).
7. Aihara, J.-I. Reduced HOMO–LUMO gap as an index of kinetic stability for polycyclic aromatic hydrocarbons. *J. Phys. Chem. A* **103,** 7487–7495 (1999).
8. Anthony, J. E. Functionalized acenes and heteroacenes for organic electronics. *Chem. Rev.* **106,** 5028–5048 (2006).
9. Jurow, M., Schuckman, A. E., Batteas, J. D. & Drain, C. M. Porphyrins as molecular electronic components of functional devices. *Coord. Chem. Rev.* **254,** 2297–2310 (2010).
10. Wang, C., Dong, H., Hu, W., Liu, Y. & Zhu, D. Semiconducting pi-conjugated systems in field-effect transistors: a material odyssey of organic electronics. *Chem. Rev.* **112,** 2208–2267 (2012).
11. Bendikov, M., Wudl, F. & Perepichka, D. F. Tetrathiafulvalenes, oligoacenenes, and their buckminsterfullerene derivatives: the brick and mortar of organic electronics. *Chem. Rev.* **104,** 4891–4946 (2004).
12. Breslow, R., Murayama, D. R., Murahashi, S. & Grubbs, R. Quantitative assessment of the antiaromatic city of cyclobutadiene by electrochemical studies on quinone derivatives. *J. Am. Chem. Soc.* **95,** 6688–6699 (1973).
13. Breslow, R. & Foss, Jr F. W. Charge transport in nanoscale aromatic and antiaromatic systems. *J. Phys. Condens. Matter* **20,** 374104 (2008).
14. Reed, M. A. Conductance of a molecular junction. *Science* **278,** 252–254 (1997).
15. Smit, R. H. M. *et al.* Measurement of the conductance of a hydrogen molecule. *Nature* **419,** 906–909 (2002).
16. Xu, B. & Tao, N. J. Measurement of single-molecule resistance by repeated formation of molecular junctions. *Science* **301,** 1221–1223 (2003).
17. Chen, W. *et al.* Aromaticity decreases single-molecule junction conductance. *J. Am. Chem. Soc.* **136,** 918–920 (2014).
18. Xie, Z., Ji, X.-L., Song, Y., Wei, M.-Z. & Wang, C.-K. More aromatic molecular junction has lower conductance. *Chem. Phys. Lett.* **639,** 131–134 (2015).
19. Mahendran, A., Gopinath, P. & Breslow, R. Single molecule conductance of aromatic, nonaromatic, and partially antiaromatic systems. *Tetrahedron Lett.* **56,** 4833–4835 (2015).
20. Ito, T. *et al.* Gram-scale synthesis of nickel(II) norcorrole: the smallest antiaromatic porphyrinoid. *Angew. Chem. Int. Ed. Engl.* **51,** 8542–8545 (2012).
21. Shin, J. Y., Yamada, T., Yoshikawa, H., Awaga, K. & Shinokubo, H. An antiaromatic electrode-active material enabling high capacity and stable performance of rechargeable batteries. *Angew. Chem. Int. Ed. Engl.* **53,** 3096–3101 (2014).
22. Nozawa, R., Yamamoto, K., Shin, J. Y., Hiroto, S. & Shinokubo, H. Regioselective nucleophilic functionalization of antiaromatic nickel(II) norcorroles. *Angew. Chem. Int. Ed. Engl.* **54,** 8454–8457 (2015).
23. Park, Y. S. *et al.* Contact chemistry and single-molecule conductance: a comparison of phosphines, methyl sulfides, and amines. *J. Am. Chem. Soc.* **129,** 15768–15769 (2007).
24. Sedghi, G. *et al.* Long-range electron tunnelling in oligo-porphyrin molecular wires. *Nat. Nanotechnol.* **6,** 517–523 (2011).
25. Liu, Z. F. *et al.* Control of single-molecule junction conductance of porphyrins via a transition-metal center. *Nano Lett.* **14,** 5365–5370 (2014).
26. Perrin, M. L. *et al.* Influence of the chemical structure on the stability and conductance of porphyrin single-molecule junctions. *Angew. Chem. Int. Ed. Engl.* **50,** 11223–11226 (2011).
27. Maji, S. & Sarkar, S. HOMO based two electrons and one-electron oxidation in planar and nonplanar methoxy-substituted nickel tetraphenylporphyrins. *Inorg. Chim. Acta* **363,** 2778–2785 (2010).
28. Tu, Y. J. *et al.* Intriguing electrochemical behavior of free base porphyrins: effect of porphyrin-meso-phenyl interaction controlled by position of substituents on meso-phenyls. *J. Phys. Chem. A* **116,** 1632–1637 (2012).
29. Neaton, J. B., Hybertsen, M. S. & Louie, S. G. Renormalization of molecular electronic levels at metal-molecule interfaces. *Phys. Rev. Lett.* **97,** 216405 (2006).
30. Quek, S. Y. *et al.* Amine – gold linked single-molecule circuits: experiment and theory. *Nano Lett.* **7,** 3477–3482 (2007).
31. Toher, C. & Sanvito, S. Effects of self-interaction corrections on the transport properties of phenyl-based molecular junctions. *Phys. Rev. B* **77,** 155402 (2008).
32. Flores, F., Ortega, J. & Vazquez, H. Modelling energy level alignment at organic interfaces and density functional theory. *Phys. Chem. Chem. Phys.* **11,** 8658–8675 (2009).
33. Strange, M., Rostgaard, C., Häkkinen, H. & Thygesen, K. S. Self-consistent GW calculations of electronic transport in thiol- and amine-linked molecular junctions. *Phys. Rev. B* **83,** 115108 (2011).
34. Kim, Y., Pietsch, T., Erbe, A., Belzig, W. & Scheer, E. Benzenedithiol: a broad-range single-channel molecular conductor. *Nano Lett.* **11,** 3734–3738 (2011).
35. Cuevas, J. C. & Scheer, E. *Molecular Electronics: An Introduction to Theory and Experiment* (World Scientific Publishing Co. Pte. Ltd, 2010).

36. Komoto, Y. *et al.* Resolving metal-molecule interfaces at single-molecule junctions. *Sci. Rep.* **6,** 26606 (2016).
37. Schneebeli, S. *et al.* The electrical properties of biphenylenes. *Org. Lett.* **12,** 4114–4117 (2010).
38. Baghernejad, M. *et al.* Electrochemical control of single-molecule conductance by Fermi-level tuning and conjugation switching. *J. Am. Chem. Soc.* **136,** 17922–17925 (2014).
39. Zhou, X. S. *et al.* Do molecular conductances correlate with electrochemical rate constants? Experimental insights. *J. Am. Chem. Soc.* **133,** 7509–7516 (2011).
40. Osorio, H. M. *et al.* Electrochemical single-molecule transistors with optimized gate coupling. *J. Am. Chem. Soc.* **137,** 14319–14328 (2015).
41. Haiss, W. *et al.* Redox state dependence of single molecule conductivity. *J. Am. Chem. Soc.* **125,** 15294–15295 (2003).
42. Chappell, S. *et al.* Evidence for a hopping mechanism in metal | single molecule | metal junctions involving conjugated metal–terpyridyl complexes; potential-dependent conductances of complexes $[M(pyterpy)_2]^{2+}$ (M = Co and Fe; pyterpy = 4'-(pyridin-4-yl)-2,2':6',2''-terpyridine) in ionic liquid. *Faraday Discuss.* **193,** 113–131 (2016).
43. Pobelov, I. V., Li, Z. & Wandlowski, T. Electrolyte gating in redox-active tunneling junctions—an electrochemical stm approach. *J. Am. Chem. Soc.* **130,** 16045–16054 (2008).
44. Gryko, D. T., Clausen, C. & Lindsey, J. S. Thiol-derivatized porphyrins for attachment to electroactive surfaces. *J. Org. Chem.* **64,** 8635–8647 (1999).
45. Tiecco, M., Tingoli, M., Testaferri, L., Chianelli, D. & Maiolo, F. Selective dealkylation of bis[alkylthio]benzenes: elimination-substitution competition with methoxide and methanethiolate ions in hexamethylphosphoric triamide. *Synthesis* (1982 478–480 (1982).
46. Kuroda, M. & Nishino, T. Preparation of tips coated with poly(dimethyl-siloxane) for scanning tunneling microscopy in aqueous solutions. *Rev. Sci. Instrum.* **82,** 063707 (2011).
47. Soler, J. M. *et al.* The SIESTA method for ab initio order-N materials simulation. *J. Phys. Condens. Matter.* **14,** 2745 (2002).
48. Brandbyge, M., Mozos, J.-L., Ordejón, P., Taylor, J. & Stokbro, K. Density-functional method for nonequilibrium electron transport. *Phys. Rev. B* **65,** 165401 (2002).
49. Paulsson, M. & Brandbyge, M. Transmission eigenchannels from nonequilibrium Green's functions. *Phys. Rev. B* **76,** 115117 (2007).

Acknowledgements

S.M.-G. gratefully acknowledges an International Research Fellowship from the Japan Society for the Promotion of Science. This work was financially supported by Grants-in-Aid for Scientific Research in Innovative Areas (Nos. 26102013, 2511008, 26102002) and Grants-in-Aid for Scientific Research (A) (No. 21340074), (B) (No. 26288020), (C) (No. 25410124) from the Ministry of Education, Culture, Sports, Science and Technology (MEXT) of Japan. N.P.A. and H.V. gratefully acknowledge financial support from the Czech Science Foundation (GAČR) under project 15-19672S and from the Purkyně Fellowship program. We thank CESNET LM2015042 and CERIT Scientific Cloud LM2015085, under the programme 'Projects of Large Research, Development, and Innovations Infrastructures' for computational resources.

Author contributions

S.F., T.N., M.K, and H.S. conceived and designed the experiments. S.M.-G. performed the single-molecule experiments and the data analysis. T.M. performed cyclic voltammetry measurements. J.-Y.S. and H.S. synthesized and characterized the organometallic complexes. N.P.A and H.V. performed the computational studies. H.V. designed the calculations. All authors contributed to the discussion of the results. S.M.-G., S.F. and M.K. wrote the paper with contributions from all authors.

Additional information

Supplementary Information accompanies this paper at http://www.nature.com/naturecommunications

Competing interests: The authors declare no competing financial interests.

Reprints and permission information is available online at http://npg.nature.com/reprintsandpermissions/

How to cite this article: Fujii, S. *et al.* Highly-conducting molecular circuits based on antiaromaticity. *Nat. Commun.* **8,** 15984 doi: 10.1038/ncomms15984 (2017).

Publisher's note: Springer Nature remains neutral with regard to jurisdictional claims in published maps and institutional affiliations.

Open Access This article is licensed under a Creative Commons Attribution 4.0 International License, which permits use, sharing, adaptation, distribution and reproduction in any medium or format, as long as you give appropriate credit to the original author(s) and the source, provide a link to the Creative Commons license, and indicate if changes were made. The images or other third party material in this article are included in the article's Creative Commons license, unless indicated otherwise in a credit line to the material. If material is not included in the article's Creative Commons license and your intended use is not permitted by statutory regulation or exceeds the permitted use, you will need to obtain permission directly from the copyright holder. To view a copy of this license, visit http://creativecommons.org/licenses/by/4.0/

© The Author(s) 2017

Supplementary Note 4. Transmission studies

As mentioned in Supplementary Note 3, in the single-molecule junctions, the thioacetate groups (-SAc) of the Ni(nor) and Ni(porph) molecules are preserved and bind to Au electrodes through the S lone pair. Several tip motifs were investigated in the calculations.

The total conductance can be decomposed in terms of eigenchannel contributions. [11] For both Ni(nor) and Ni(porph), we find that only one transmission channel is dominant at the Fermi level and thus current is carried by a single channel. Interestingly, for both compounds the calculated spectra show a series of three sharp peaks close to each other, located in the 0.6~0.9 eV range for Ni(porph) and −0.4~−0.2 eV for Ni(nor). These sharp peak-dip structures reflect the crossing of different transmission channels, which are derived from quasi-degenerate molecular orbitals [12] of the aromatic and antiaromatic cores.

The energy of molecular projected self-consistent Hamiltonian (MPSH) [13] orbitals matches that of peaks or peak-dip features in the transmission spectra. The molecular gap is significantly smaller for the antiaromatic species. Notably, this arises from the conjugated cores and is not related to the metal atom. In both complexes the central Ni atom was replaced by two H atoms, whose positions were optimized while keeping all other coordinates constant. The transmission spectra of the complexes do not change significantly upon removal of the metal atom, but they exhibit fewer peaks or peak-dip features, consistent with the absence of Ni-derived states. The position of MPSH orbitals, displayed as solid diamonds in the Supplementary Figures shows a smaller gap in the antiaromatic species for both Ni- and Ni-free complexes.

We apply corrections to DFT-based conductance by taking into account errors in the DFT alignment of relevant frontier orbitals current.[14-17] For each species, we shift the position of the LUMO-derived resonance by an amount which includes self-energy corrections to the position of the isolated molecular level as well as screening effects at the junction. The magnitude of the self-energy corrections was obtained from total energy differences of the neutral and negatively charged species, making sure that the excitation populated the N-electron LUMO.[16,17] Screening effects at the metal interface were calculated using a classical image-charge model, taking into account the charge distribution of the LUMO and an image plane 1Å above the Au(111) surface.[15] We fitted the calculated transmission spectra to a lorentzian, which was then shifted in energy according to the corrections calculated above.

Corrected conductance values are in good agreement with experiment, as seen before for porphyrins.[14]

4-1. DFT transmission spectra with different tip structures

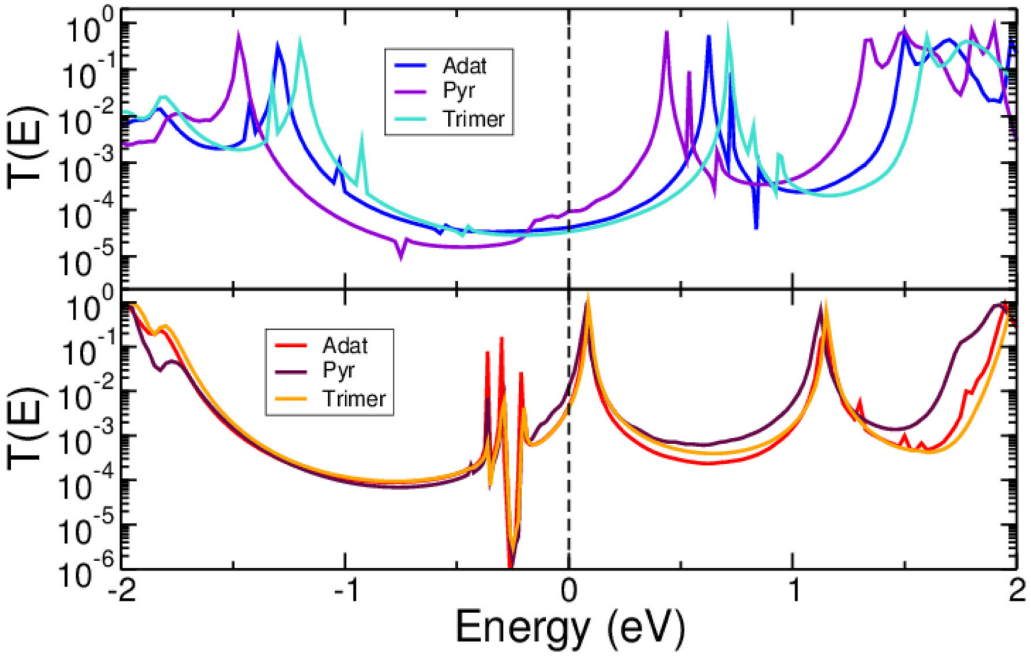

Supplementary Figure 12 | DFT transmission spectra with different tip structures. DFT transmission spectra for (top panel) Ni(porph) and (bottom panel) Ni(nor) complexes bound to gold *via* adatom, pyramidal or trimer tip motifs.

4-2. Eigenchannel decomposition

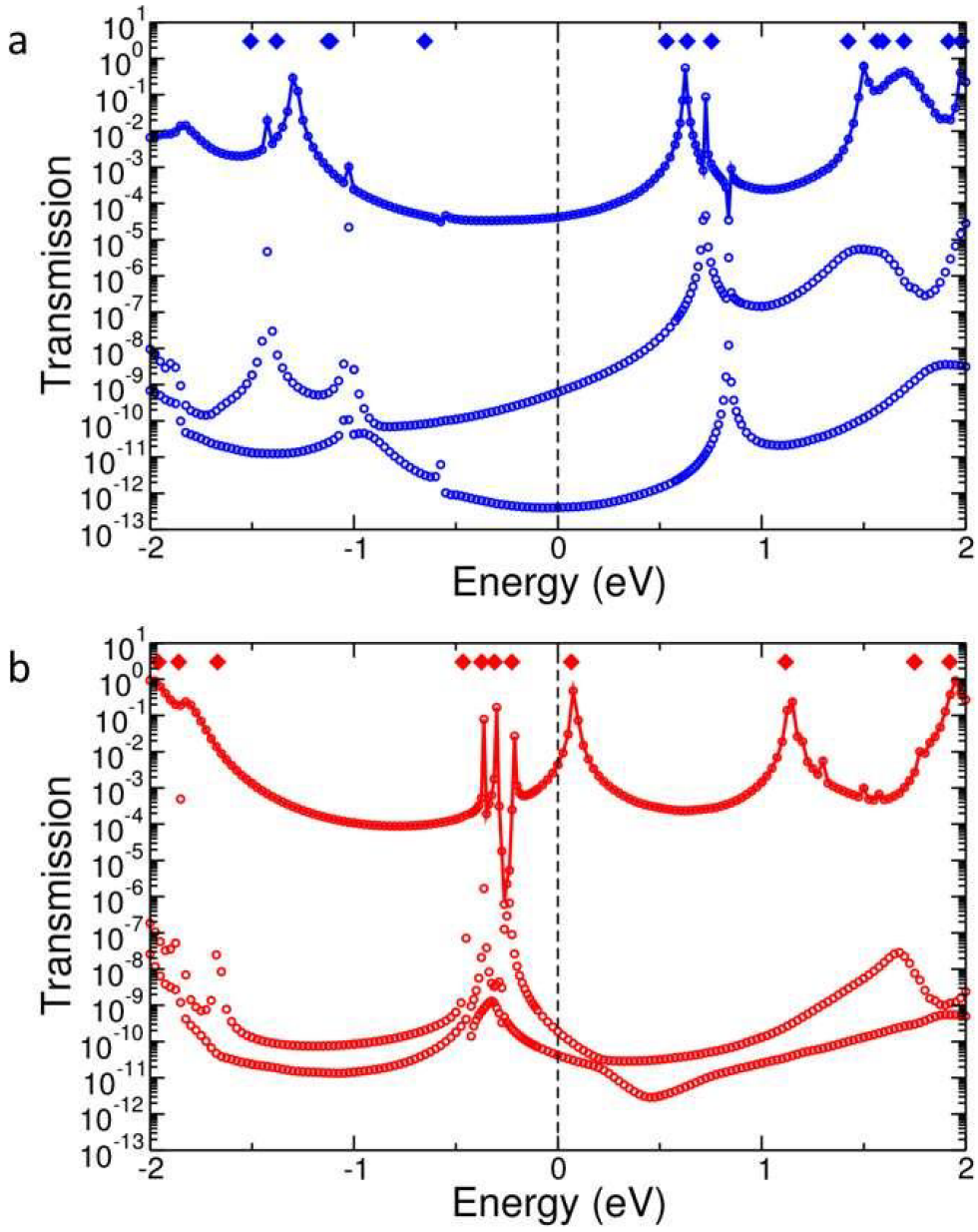

Supplementary Figure 13 | Eigenchannel decomposition. DFT transmission spectra of (**a**) Ni(porph) and (**b**) Ni(nor) with adatom tips. Solid diamonds indicate positions of MPSH orbitals. Total transmission (solid lines) and contribution of the 3 most conducting eigenchannels (open circles).

4-3. Molecular gap of aromatic and antiaromatic species

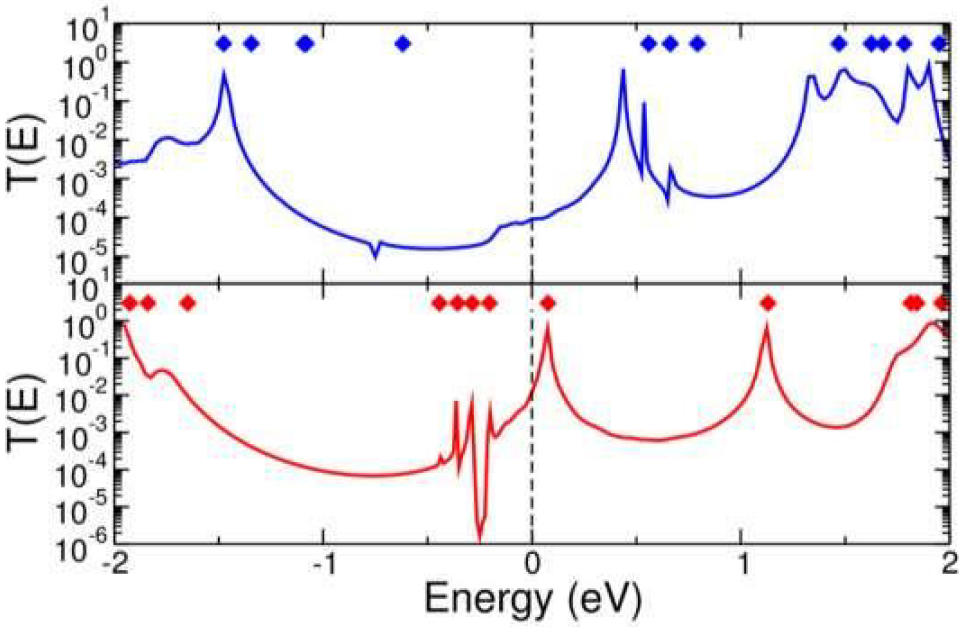

Supplementary Figure 14 | Molecular gap of aromatic and antiaromatic species. DFT transmission spectra for (top panel) Ni(porph) and (bottom panel) Ni(nor) complexes with pyramidal tip structures. Solid diamonds indicate positions of MPSH orbitals.

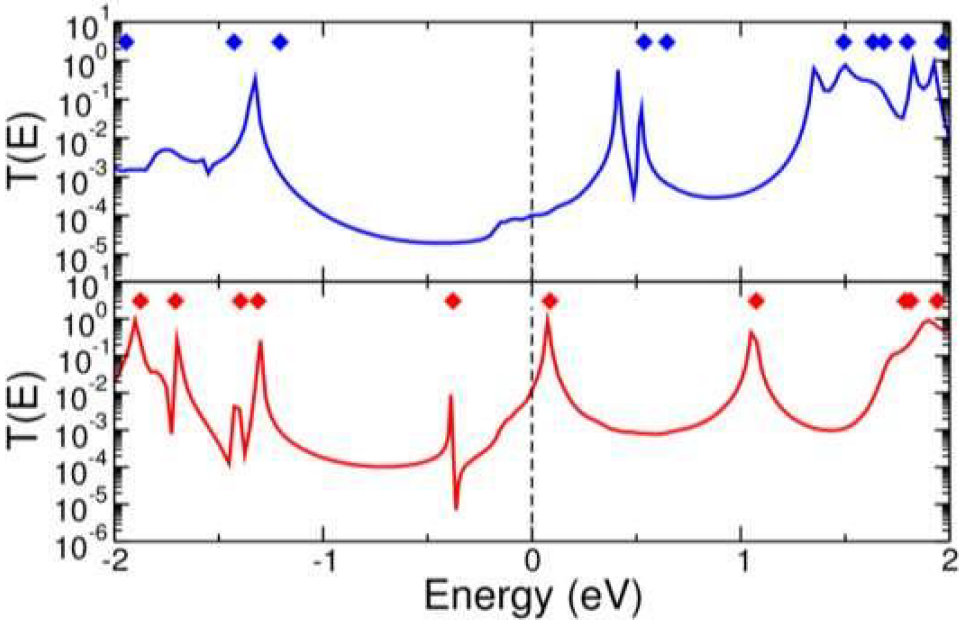

Supplementary Figure 15 | Molecular gap of metal-free aromatic and antiaromatic species. DFT transmission spectra for (top panel) H_2(porph) and (bottom panel) H_2(nor) metal-free complexes with pyramidal tip structures. Solid diamonds indicate positions of MPSH orbitals.

Supplementary Note 5. Corrections to the position of DFT molecular resonances

Transmission resonances were shifted in energy, while keeping the DFT-based peak height.

		Ni(nor)		Ni(porph)		Ratio
		E_{LUMO}-E_F	$G(E_F)$	E_{LUMO}-E_F	$G(E_F)$	G(nor)/G(porph)
DFT	Pyramids	0.08	1.2×10^{-2}	0.43	9.2×10^{-5}	130
	Trimers	0.09	4.2×10^{-3}	0.71	3.4×10^{-5}	124
	Adatoms	0.08	4.4×10^{-3}	0.63	4.2×10^{-5}	105
Corrected	Pyramids	0.68	1.4×10^{-4}	0.98	1.5×10^{-5}	9
	Trimers	0.37	2.6×10^{-4}	0.93	1.5×10^{-5}	17
	Adatoms	0.37	2.2×10^{-4}	0.87	1.6×10^{-5}	14
	Average	0.47	2.1×10^{-4}	0.93	1.5×10^{-5}	13
Experiment		0.48	4.2×10^{-4}	0.85	1.7×10^{-5}	25

Supplementary Table 1 | Comparison of calculated and measured conductance (in units of G_0) and molecular level offsets (in eV) of Ni(nor) and Ni(porph).

		Ni(nor)	Ni(porph)
		Γ	Γ
Corrected	Pyramids	20	9
	Trimers	13	11
	Adatoms	15	9
	Average	16	10
Experiment		18	13

Supplementary Table 2 | Comparison of calculated and experimentally determined electronic couplings (in units of meV).

13697641, 2021, 24, Downloaded from https://chemistry-europe.onlinelibrary.wiley.com. By Narendra Prabhakar Arasu - <Shibboleth>-member@cuni.cz- on [10/10/2021]. Re-use and distribution is strictly not permitted, except for Open Access arti

Origin of the Electron Transport Properties of Aromatic and Antiaromatic Single Molecule Circuits

Narendra P. Arasu[a, b] and Héctor Vázquez*[a]

Antiaromatic molecules have been predicted to exhibit increased electron transport properties when placed between two nanoelectrodes compared to their aromatic analogues. While some studies have demonstrated this relationship, others have found no substantial increase. We use atomistic simulations to establish a general relationship between the electronic spectra of aromatic, antiaromatic, and quinoidal molecules and illustrate its implications for electron transport. We compare the electronic properties of a series of aromatic-antiaromatic counterparts and show that antiaromaticity effectively p-dopes the aromatic electronic spectra. As a consequence, the conducting properties of aromatic-antiaromatic analogues are closely related. For similar attachment points to the electrodes, an interference feature is expected in the HOMO-LUMO gap of one whenever it is absent in the other one. We demonstrate how the relative conductance of aromatic-antiaromatic pairs can be tuned and even reversed through the choice of chemical linker groups. Our work provides a general picture relating connectivity, (anti) aromaticity, and quantum interference and establishes new design rules for single molecule circuits.

1. Introduction

Aromaticity is a key concept which describes the stability and electronic properties of π-conjugated molecules. Aromatic backbones such as oligoacenes, porphyrins, or polycyclic aromatic hydrocarbons display large stabilization energies and are thus commonly used in many fields of electronics, photovoltaics, and materials science at the molecular scale.[1–7] In other cyclic planar conjugated 'antiaromatic' molecules, the arrangement of π electrons is very destabilizing.[8] However, these antiaromatic molecules were long proposed to exhibit increased electron transport properties.[8–10] Single molecule electronics, where individual molecules can be controllably placed between two nanoscale electrodes to act as active components in nanoscale circuits, opens the way to investigating the effects of molecular properties such as (anti)aromaticity on the electron transport properties.

Over the past decades, many aromatic compounds have featured in single molecule conductance studies.[1,2] On the basis of electrochemical measurements of oxidation/reduction potentials, antiaromatic compounds were long predicted to lead to higher conductance than aromatic backbones, but their instability hindered their study.[8–10] Aromaticity was shown to negatively correlate with conductance[11] as the least aromatic compounds had molecular resonances closer to the Fermi level,[12] leading to increased conductance. In the few experimental studies of genuinely antiaromatic molecules available so far, some showed increased conductance compared with aromatic analogues,[13,14] but in other cases this expected effect was not observed.[15,16] Model calculations of molecular structure and connectivity[17] were proposed to explain this lack of increased conductance, but no general picture has emerged. At the same time, quantum chemical calculations on expanded aromatic and antiaromatic porphyrins[18,19] provided examples of aromaticity increasing, rather than decreasing, conductance and observed quantum interference features depending on number of C atoms separating the molecular contacts to the electrodes. Atomistic simulations based on Density-Functional Theory and Non-Equilibrium Green's Functions (DFT-NEGF) are ideally suited to study the effect on conductance of molecular chemical properties due to their accurate description of junction electronic and conducting properties,[20,21] particularly given the formidable synthetic challenges of antiaromatic compounds.

Here we use DFT-NEGF calculations to provide a comprehensive view of the electronic and conducting properties of (anti)aromatic molecules and address the longstanding question of when the conductance of antiaromatic molecules can be expected to be higher than that of aromatic analogues. By analyzing a series of representative conjugated backbones, we show that antiaromaticity can be considered as double p-doping of the analogue aromatic electronic structure, resulting in the full depletion of the HOMO, and investigate the implications of this relationship for conductance. We demonstrate that (anti)aromaticity, connectivity to the electrodes, and destructive quantum interference are closely related and all influence conductance. We show that, for similar connectivities to the electrodes, the presence (absence) of destructive interference features in the aromatic or antiaromatic compound leads to the absence (presence) in the other one, a relationship which follows from the notion of antiaromaticity as p-doping.

[a] N. P. Arasu, Dr. H. Vázquez
Institute of Physics Academy of Sciences of the Czech Republic
Cukrovarnická 10, 16200 Prague, Czech Republic
E-mail: vazquez@fzu.cz
[b] N. P. Arasu
Department of Condensed Matter Physics
Faculty of Mathematics and Physics, Charles University
Ke Karlovu 5, 12000 Prague, Czech Republic

Supporting information for this article is available on the WWW under https://doi.org/10.1002/cphc.202100010

© 2021 Wiley-VCH GmbH

13977641, 2021, 24, Downloaded from https://chemistry-europe.onlinelibrary.wiley.com. By Narendra Prabhakar Arasu - <Shibboleth>-member@cuni.cz- on [10/10/2021]. Re-use and distribution is strictly not permitted, except for Open Access artic

We further show how the position of the Fermi level relative to the interference feature within the gap, and thus the relative conductance of aromatic-antiaromatic pairs, can be changed through the choice of metal-molecule linkers. Our results provide insight into the concept of antiaromaticity and show the way to tune the conductance of (anti)aromatic single molecule circuits through molecular design.

2. Results and Discussion

We study several pairs of aromatic-antiaromatic and antiaromatic-quinoidal molecules (Figure 1) which represent prototypical backbones for electron transport studies.[1,2,9–18,22–29] Calculation of their Nucleus-Independent Chemical Shifts (NICS), establishing their (anti)aromatic character, are given in SI section 1. We derive antiaromatic oligoacenes by removing two C atoms from a benzene ring, effectively replacing a benzene ring in the aromatic molecule with a cyclobutadiene ring. Quinoidal species are formed by carbonyl functionalization of an aromatic benzene ring in the para positions. We first establish the spectral relationships in isolated molecules. We consider the wave function coefficients of each molecular orbital (MO) of π symmetry. We write $|\psi^A\rangle = \sum_i c_i^A |\phi_i\rangle$, where c_i^A are the real-valued coefficients on an orthonormal basis $|\phi_i\rangle$, A labels an aromatic MO, and index i runs over all basis states. We write a similar expression for antiaromatic wave functions $|\psi^{AA}\rangle = \sum_i c_i^{AA} |\phi_i\rangle$ where AA is a label for antiaromatic MOs and c_i^{AA} are the wavefunction coefficients. We quantify the similarity of the electronic structures between molecules to the left and right of Figure 1 by calculating the dot product of each antiaromatic MO $|\psi^{AA}\rangle$ with every aromatic orbital $|\psi^A\rangle$. Since the global phase of wave functions is not well defined, we take the absolute values.

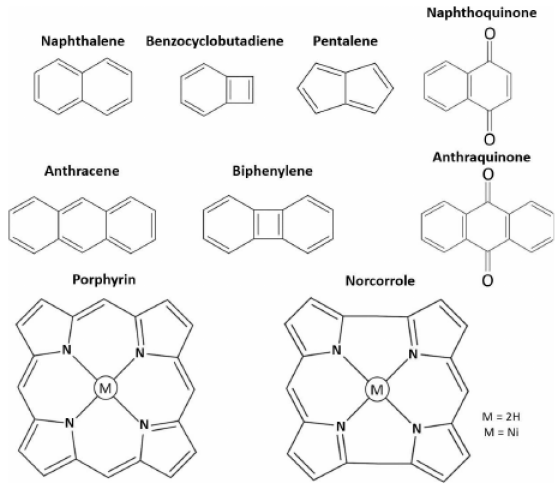

Figure 1. Aromatic molecules (left), and their antiaromatic and quinoidal counterparts (right). Antiaromatic molecules have two fewer C and H atoms than aromatic analogues.

$$|\langle\psi^{AA}|\psi^{A}\rangle| = \sum_i \left| c_i^{AA}\ c_i^{A} \right| \tag{1}$$

This product quantifies the similarity in the nodal patterns of molecular orbitals A and AA. Aromatic molecules have two more C and H atoms than their antiaromatic analogues and, on a local-orbital basis, c_i^A arrays are thus longer than c_i^{AA}. We therefore truncate the arrays c_i^A by excluding the coefficients when i corresponds to one of these atoms and renormalize the aromatic MO. By considering the wave function coefficients on atoms common to both aromatic and antiaromatic molecules, both pairs of wave functions have the same dimension. This truncation merely rescales the dot product so that its maximum value is 1 but does not otherwise alter the matching of MOs.

Figure 2 a shows the products $|\langle\psi^{AA}|\psi^{A}\rangle|$ near the gap between all naphthalene aromatic π MOs and every benzocyclobutadiene π MO. The products are shown in the three-dimensional plot as vertical bars. Values close to 0 mean that the nodal pattern and amplitude of states A and AA are very different. Values close to 1, on the other hand, imply that molecular orbitals A and AA are very similar. From the three-dimensional plot, we see that most antiaromatic MOs are similar to one or, at most, a few aromatic orbitals. The best match for every antiaromatic MO is projected onto the horizontal plane, with values in the range of 0.7-1. The fact that these best-matching pairs of orbitals lie along lines with a slope of 1 (solid lines) in the two-dimensional projection implies that, as the spectra are traversed, states of both molecules closely resemble each other in the same order. That is, the first, second, third π orbitals of the antiaromatic molecule best match the first, second, third MO of its aromatic counterpart, respectively, and so on. Exceptions happen when the most similar aromatic and antiaromatic MOs do not have the same orbital index. For example, the 6th benzocyclobutadiene MO best matches the 8th (not 6th) naphthalene MO. In other cases, an aromatic MO is not the best match of any antiaromatic orbital, such as naphthalene MO 6. In this case, the solid line in the two-dimensional projection plot of Figure 2a is displaced upwards. The energy

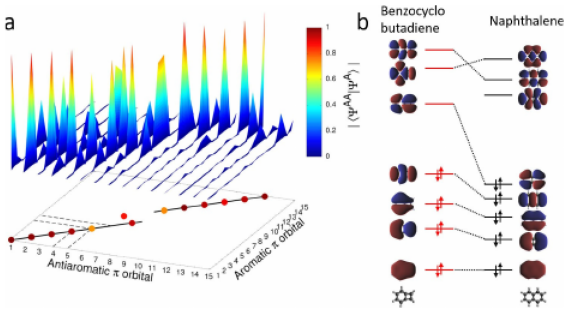

Figure 2. (a) Three-dimensional plot of the dot product between benzocyclobutadiene and naphthalene π molecular orbitals. Best-matching pairs, projected onto the horizontal plane, have a slope of 1 (solid lines). Dashed lines indicate the HOMO and LUMO of each molecule. (b) π MO diagrams. Lines connect best-matching orbitals of each molecule.

© 2021 Wiley-VCH GmbH

1397641, 2021, 24, Downloaded from https://chemistry-europe.onlinelibrary.wiley.com. By Narendra Prabhakar Arasu - <Shibboleth>-member@cuni.cz- on [10/10/2021]. Re-use and distribution is strictly not permitted, except for Open Access arti

level diagram and spatial representation of each π MO are shown in Figure 2b. Dashed lines connect the best-matching orbital pairs. This analysis shows that, despite differing in the number of atoms, the π electronic structure of benzocyclobutadiene and naphthalene are remarkably similar as the nodal pattern and symmetry of MOs are largely preserved across both species. However, since benzocyclobutadiene has one fewer (doubly) occupied MO than naphthalene, the benzocyclobutadiene LUMO matches the naphthalene HOMO. This situation, in which the HOMO of the aromatic species is fully depleted, is analogous to doping of molecular semiconductors, where dopants can add (n-doping) or remove (p-doping) electrons from the host material.[30] From Figure 2, the benzocyclobutadiene electronic structure can be considered as that of naphthalene after double p-doping. This relationship is also observed for the other pairs of aromatic-antiaromatic molecules in Figure 1 (SI section 2), showing that it is a general and robust property.

To investigate how this analysis applies to quinoidal molecules, we carried out a similar study between antiaromatic species and quinoidal counterparts. The C and O carbonyl atoms are not present in the antiaromatic species, which results in c_i^{AA} and c_i^{Q} arrays having different lengths. As before, we truncate the wavefunction coefficients of the quinoidal MO to contain only those atoms also present in the antiaromatic species. Figure 3 compares the electronic spectra of benzocyclobutadiene and naphthoquinone. There is a large similarity between most antiaromatic and quinoidal MOs, evidenced by the values close to 1 of most $|\langle\psi^{AA}|\psi^{Q}\rangle|$ best-matching products depicted in Figure 3a. Again, these most similar pairs tend to lie along a line of slope 1, which is shifted upwards whenever no quinoidal MO is the best match of a given antiaromatic orbital. The diagram in Figure 3b shows that these unmatched quinoidal MOs (blue lines) have significant amplitude on the O atoms. SI section 3 shows that this relationship also holds for the anthraquinone-biphenylene pair. These results demonstrate that the spectra of quinoids and antiaromatic analogues whose structure is the same except for additional C=O groups, are closely related. The electronic structure of the quinoidal molecule can be thought of as that of the corresponding antiaromatic species, plus some additional molecular orbitals with significant amplitude on the quinoidal carbonyl groups. This analysis shows that an antiaromatic electronic structure can be obtained through quinoidal functionalization of the structurally similar aromatic compound, substantiating the interest in the conducting properties of quinones in the past.[8,9]

To illustrate how these relationships in the spectra of aromatic, antiaromatic, and quinoidal molecules translate into profound changes in the electron transport properties of these molecules, we calculate their conducting properties when placed between two metallic electrodes. We calculate electron transport across these molecules using DFT-NEGF.[20,21] We build single molecule junctions by placing naphthalene or benzocyclobutadiene between two atomically sharp Au electrodes and optimizing the junction geometry (see Computational Details). Both molecules are connected to the electrodes at similar positions, i.e. on opposite sides of the molecular long axis (Figure 4 insets).

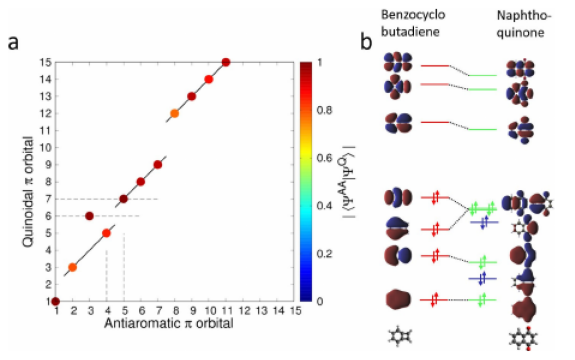

Figure 3. (a) Best-matching benzocyclobutadiene and naphthoquinone π orbitals. (b) Corresponding MO diagrams. Some quinoidal MOs, localized on the C=O atoms, are not matched.

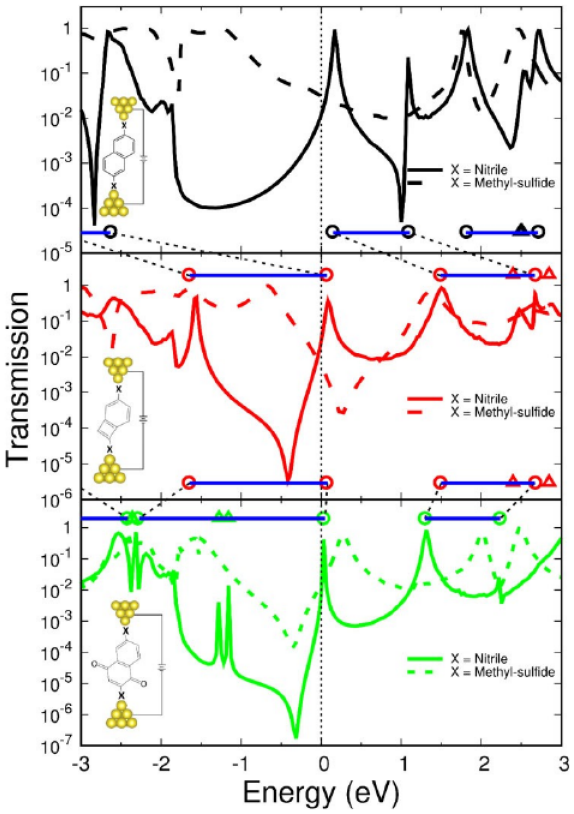

Figure 4. Calculated transmission spectra of naphthalene (top panel), its antiaromatic counterpart benzocyclobutadiene (center panel), and naphthoquinone (bottom panel) with nitrile (solid lines) or methyl-sulfide linkers (dashed lines). Open circles (triangles) represent π (in-plane) resonances of nitrile-linked molecules. Blue lines denote energy ranges where an interference feature is present.

© 2021 Wiley-VCH GmbH

13697641, 2021, 24, Downloaded from https://chemistry-europe.onlinelibrary.wiley.com. By Narendra Prabhakar Arasu - <Shibboleth>-member@cuni.cz- on [10/10/2021]. Re-use and distribution is strictly not permitted, except for Open Access arti

The calculated transmission spectra of nitrile-functionalized[31] naphthalene, benzocyclobutadiene, and naphthoquinone are shown in Figure 4 (solid lines) on a semi-logarithmic scale. The spectra exhibit peaks with transmission close to unity, corresponding to molecular resonances. However, there are also sharp dips at certain energies, indicative of destructive quantum interference (DQI), where transmission is significantly suppressed.[32–37] We first address the comparison between aromatic and antiaromatic spectra. While benzocyclobutadiene exhibits a DQI feature within the HOMO-LUMO gap at - 0.4 eV, naphthalene does not. Open circles in Figure 4 mark the energies of π molecular resonances, calculated as the eigenvalues of the molecular projected self-consistent Hamiltonian.[38] Best-matching naphthalene and benzocyclobutadiene orbitals are connected with dashed lines. For each species, blue lines connect resonances that have a DQI feature between them. The notion of antiaromaticity as effective double p-doping is reflected in the transmission spectra of Figure 4. Going from naphthalene to benzocyclobutadiene, the transmission spectrum shifts to higher energies by one peak. Concomitantly, a DQI feature now appears close to the Fermi level for the benzocyclobutadiene junction. The existence of DQI in the transmission properties of π conjugated systems, or its absence, sometimes called constructive interference, is a rich topic which has attracted considerable attention in the past years. It sensitively depends on the attachment points of the molecule to the electrodes, for which analyses based on graphical rules,[35–37] curly arrows,[39] connectivity,[18,19,40–43] diradical character,[44–47] or the phases of molecular orbital coefficients[32–34] have been developed. The appearance of a DQI feature in the HOMO-LUMO gap going from naphthalene to benzocyclobutadiene is consistent with the orbital rule for electron transport,[32–34] according to which DQI is expected when the relative sign on the molecular atoms connected to the leads is the same for HOMO and LUMO. The MO nodal patterns in Figures 2b and 3b show this is the case for the antiaromatic and quinoidal species. Antiaromaticity as p-doping implies that, when predicting the conducting properties of antiaromatic species, one can consider the relative sign of HOMO and HOMO-1 of the aromatic analogue, which for the molecules of Figure 1 anticipate the appearance of DQI (see SI section 4). These results are also consistent with the graphical rules of DQI,[35–37] which predict DQI within the gap when no path between the atoms coupled to the electrodes can be drawn across the molecule such that all other sites can be paired. The antiaromatic analogue has one fewer atom outside of the path, so the expectation of DQI is opposite that for the aromatic counterpart. The HOMO of the aromatic and antiaromatic counterparts differ from each other in the number of nodes or their direction (along the long or short molecular axes). The same happens with the LUMO. This change in the nodal pattern arising from the removal of two C atoms from the aromatic analogue, is induced in the quinoidal structures by the carbonyl bonds (see Figures 2b, 3b, SI section 2 and 3). This agrees with previous findings in expanded porphyrins predicting the appearance of DQI features when the separation between contacts atoms in the cycle is changed from an even to an odd number of C.[19]

The bottom panel of Figure 4 shows the calculated transmission spectrum of naphthoquinone. The LUMO is close to the Fermi level and there is a DQI feature at - 0.3 eV within the HOMO-LUMO gap. Although cross-conjugation in quinoids can lead to DQI features,[27,28,35] electron transfer induced by O atoms shifts carbonyl states out of resonance with the rest of the π system. The naphthoquinone spectrum also shows two sharp resonances at ~- 1.2 eV, which derive from in-plane molecular states (see SI Figure S10). The shape and features of the naphthoquinone spectrum are very similar to those of benzocyclobutadiene. In particular, the matching of molecular π resonances and quantum interference pattern, given by open circles and solid blue lines in Figure 4, are preserved between both species. This shows that the transmission spectra of antiaromatic and quinoidal analogues are closely related.

The calculated transmission spectra of the metal-free porphyrin and norcorrole are shown in Figure 5. In this connectivity, the aromatic molecule exhibits no DQI features within the gap and transport is LUMO-dominated, as reported previously for other porphyrins.[13] In the norcorrole spectrum, on the other hand, HOMO and LUMO are both very close to the Fermi level. Between them, a sharp interference feature is

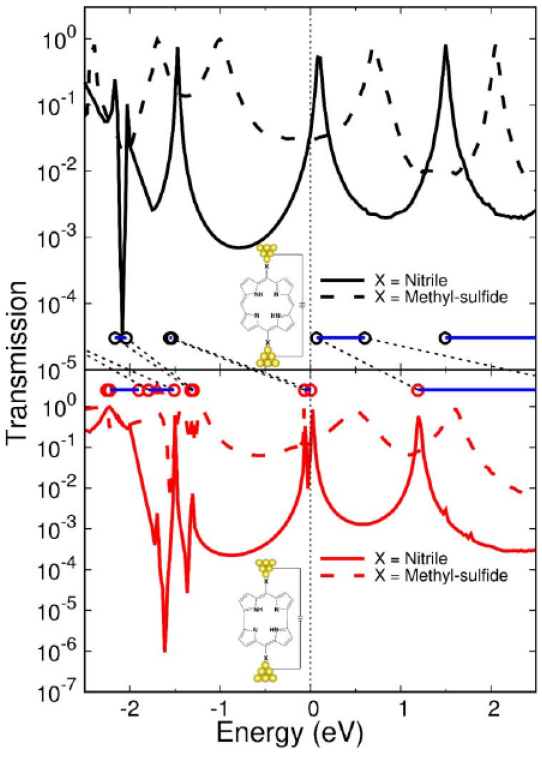

Figure 5. Calculated transmission spectra of metal-free porphyrin (top panel) and its antiaromatic norcorrole analogue (bottom panel) functionalized with nitrile (solid lines) or methyl-sulfide linkers (dashed lines). Open circles (triangles) represent π (in-plane) resonances of nitrile-linked molecules. Blue lines denote energy ranges where an interference feature is present.

© 2021 Wiley-VCH GmbH

13697641, 2021, 24, Downloaded from https://chemistry-europe.onlinelibrary.wiley.com. By Narendra Prabhakar Arasu - <Shibboleth>-member@cuni.cz- on [10/10/2021]. Re-use and distribution is strictly not permitted, except for Open Access arti

visible. The calculated transmission at the Fermi energy is higher for the antiaromatic norcorrole compound, despite this sharp DQI feature. The matching of transmission resonances in this porphyrin-norcorrole pair, defined by the dashed lines in Figure 5, is again consistent with the concept of antiaromaticity as double p-doping of the analogue aromatic structure and the full depletion of the aromatic HOMO.

Thus, if an aromatic molecule is well-conducting with no interference feature in the gap (a reasonable requirement for molecular electronics candidates), its antiaromatic or quinoidal analogue with similar attachment points (eg., with respect to the molecular long axis) can be expected to exhibit DQI and the suppression of transmission across the molecule. In Figure 4, the higher conductance of the antiaromatic compound arises from the low-lying benzocyclobutadiene LUMO-derived peak. This agrees with previous experimental reports of higher transmission of antiaromatic species due to more favorable level alignment,[13,14] a scenario assisted by the smaller antiaromatic HOMO-LUMO gaps (see SI section 5). However, one can expect an interference feature in the antiaromatic spectrum, which could strongly suppress conductance compared to the aromatic counterpart. In Figure 4 the DQI dip is relatively far for nitrile linkers (solid lines) but using methyl-sulfide linkers (dashed lines) brings the benzocyclobutadiene interference dip closer to the Fermi level and makes naphthalene more conducting than benzocyclobutadiene. For other connectivities to the electrodes, the opposite scenario can happen, namely that the aromatic molecule exhibits a DQI feature in the gap, while the antiaromatic counterpart does not (see SI Figure S11). Other linker groups may similarly modulate molecular resonance and DQI energies with respect to the Fermi level. For quinones, hybridization between carbonyl and linker groups may reduce these shifts in peak and DQI energies compared to their aromatic and antiaromatic counterparts.

The high conductance is therefore not an intrinsic property of antiaromaticity. On one hand, it is clearly favored by the smaller HOMO-LUMO gaps of antiaromatic complexes. However, compared to well-conducting aromatic analogues (i.e., with no DQI features in the gap), an interference dip may develop close to the Fermi level depending on the connectivity, which could lead to conductance suppression. The relative conductance of aromatic-antiaromatic pairs hinges on the position of the Fermi level within the gaps. These can be tuned through the choice of metal-molecule linker groups or via gating of the molecular junctions.[48]

3. Conclusion

To conclude, we considered a series of representative aromatic molecules and their antiaromatic analogues, obtained by replacing a benzene ring with a cyclobutadiene unit. Analysis of aromatic and antiaromatic molecular orbitals shows that their nodal pattern is very similar, and their ordering is largely preserved. As a consequence, antiaromaticity can be considered as double p-doping of the electronic structure of the aromatic analogue. The spectra of quinones resemble those of the antiaromatic counterpart plus carbonyl-localized states. These general relationships have important consequences for electron transport and molecular design rules. For similar attachment points to the electrodes, interference features should be present in the antiaromatic gap when absent in the aromatic species, and vice-versa. Antiaromatic or quinoidal analogues of well-conducting aromatic species are thus expected to present interference features close to the Fermi level and a smaller HOMO-LUMO gap. Their conductance depends sensitively on the position of the Fermi level in the gap, which can be tuned through the choice of chemical linkers. Our work provides new insight on the electronic spectra of aromatic, antiaromatic and quinoidal counterparts and highlights the implication of this relationship for (anti)aromaticity, connectivity, and quantum interference in single molecule circuits.

Computational Details

Calculation of Isolated Molecules

Geometry optimization and electronic structure calculations for molecules in the gas phase were carried out using Gaussian.[49] The simulations were performed using the B3LYP exchange-correlation functional and the 6-31G basis set. To obtain orthonormal wave function coefficients, we performed a Löwdin transformation.

Calculation of Conducting Properties of Molecular Junctions

Conductance calculations were carried out within DFT and Non-equilibrium Green's functions (NEGF) using TranSIESTA.[20,21] Single molecule junctions were constructed by placing the molecule between two atomically sharp Au electrodes, bonded through 3-atom Au structures protruding from Au(111) layers. Each layer consisted of 16 atoms. Double-ζ (single- ζ) polarized local orbitals were used for the description of molecular (gold) atoms. Exchange-correlation was described using the PBE functional. Junction structures were obtained by first minimizing the forces acting on molecular and tip atoms until these were smaller than 0.02 eV/Å. Optimized junction geometries were then used to calculate zero-bias transmission spectra. A dense 15×15 Monkhorst-Pack grid was used to sample the Brillouin zone in the parallel direction.

Acknowledgements

We gratefully acknowledge financial support from the Czech Science Foundation GAČR (19-23702S). Computational resources were supplied by the project "e-Infrastruktura CZ" (e-INFRA LM2018140) provided within the program Projects of Large Research, Development and Innovations Infrastructures.

Conflict of Interest

The authors declare no conflict of interest.

© 2021 Wiley-VCH GmbH

1397641, 2021, 24, Downloaded from https://chemistry-europe.onlinelibrary.wiley.com. By Narendra Prabhakar Arasu - <Shibboleth>-member@cuni.cz- on [10/10/2021]. Re-use and distribution is strictly not permitted, except for Open Access arti

Keywords: molecular electronics · electron transport · electronic structure · aromaticity · density functional calculations

[1] T. A. Su, M. Neupane, M. L. Steigerwald, L. Venkataraman, C. Nuckolls, *Nat. Rev. Mater.* **2016**, *1*, 16002.
[2] P. Gehring, J. M. Thijssen, H. S. J. van der Zant, *Nat. Rev. Phys.* **2019**, *1*, 381–396.
[3] M. D. Peeks, M. Jirasek, T. D. W. Claridge, H. L. Anderson, *Angew. Chem. Int. Ed.* **2019**, *58*, 15717–15720.
[4] M. D. Peeks, T. D. W. Claridge, H. L. Anderson, *Nature* **2017**, *541*, 200–203.
[5] A. C. Aragonès, N. Darwish, J. Im, B. Lim, J. Choi, S. Koo, I. Díez-Pérez, *Chem. A Eur. J.* **2015**, *21*, 7716–7720.
[6] A. Etcheverry-Berríos, I. Olavarría, M. L. Perrin, R. Díaz-Torres, D. Jullian, I. Ponce, J. H. Zagal, J. Pavez, S. O. Vásquez, H. S. J. van der Zant, D. Dulić, N. Aliaga-Alcalde, M. Soler, *Chem. A Eur. J.* **2016**, *22*, 12808–12818.
[7] M. U. Winters, J. Kärnbratt, H. E. Blades, C. J. Wilson, M. J. Frampton, H. L. Anderson, B. Albinsson, *Chem. A Eur. J.* **2007**, *13*, 7385–7394.
[8] R. Breslow, *Acc. Chem. Res.* **1973**, *6*, 393–398.
[9] R. Breslow, F. W. Foss Jr, *J. Phys. Condens. Matter* **2008**, *20*, 374104.
[10] R. Breslow, S. T. Schneebeli, *Tetrahedron* **2011**, *67*, 10171–10178.
[11] W. Chen, H. Li, J. R. Widawsky, C. Appayee, L. Venkataraman, R. Breslow, *J. Am. Chem. Soc.* **2014**, *136*, 918–920.
[12] Z. Xie, X. L. Ji, Y. Song, M. Z. Wei, C. K. Wang, *Chem. Phys. Lett.* **2015**, *639*, 131–134.
[13] S. Fujii, S. Marqués-González, J. Y. Shin, H. Shinokubo, T. Masuda, T. Nishino, N. P. Arasu, H. Vázquez, M. Kiguchi, *Nat. Commun.* **2017**, *8*, 4–11.
[14] X. Yin, Y. Zang, L. Zhu, J. Z. Low, Z.-F. Liu, J. Cui, J. B. Neaton, L. Venkataraman, L. M. Campos, *Sci. Adv.* **2017**, *3*, aao2615.
[15] S. Schneebeli, M. Kamenetska, F. Foss, H. Vazquez, R. Skouta, M. Hybertsen, L. Venkataraman, R. Breslow, *Org. Lett.* **2010**, *12*, 4114–4117.
[16] M. Gantenbein, X. Li, S. Sangtarash, J. Bai, G. Olsen, A. Alqorashi, W. Hong, C. J. Lambert, M. R. Bryce, *Nanoscale* **2019**, *11*, 20659–20666.
[17] A. Borges, G. C. Solomon, *J. Phys. Chem. C* **2017**, *121*, 8272–8279.
[18] T. Stuyver, M. Perrin, P. Geerlings, F. De Proft, M. Alonso, *J. Am. Chem. Soc.* **2018**, *140*, 1313–1326.
[19] T. Stuyver, S. Fias, P. Geerlings, F. De Proft, M. Alonso, *J. Phys. Chem. C* **2018**, *122*, 19842–19856.
[20] J. M. Soler, E. Artacho, J. D. Gale, A. García, J. Junquera, P. Ordejón, D. Sánchez-Portal, *J. Phys. Condens. Matter* **2002**, *14*, 2745–2779.
[21] M. Brandbyge, J. L. Mozos, P. Ordejón, J. Taylor, K. Stokbro, *Phys. Rev. B: Condens. Matter Mater. Phys.* **2002**, *65*, 1654011–16540117.
[22] T. Yelin, R. Korytar, N. Sukenik, R. Vardimon, B. Kumar, C. Nuckolls, F. Evers, O. Tal, R. Korytár, N. Sukenik, R. Vardimon, B. Kumar, C. Nuckolls, F. Evers, O. Tal, *Nat. Mater.* **2016**, *15*, 444–449.
[23] Z. F. Liu, S. Wei, H. Yoon, O. Adak, I. Ponce, Y. Jiang, W. D. Jang, L. M. Campos, L. Venkataraman, J. B. Neaton, *Nano Lett.* **2014**, *14*, 5365–5370.
[24] G. Sedghi, V. M. García-Suárez, L. J. Esdaile, H. L. Anderson, C. J. Lambert, S. Martín, D. Bethell, S. J. Higgins, M. Elliott, N. Bennett, J. E. Macdonald, R. J. Nichols, *Nat. Nanotechnol.* **2011**, *6*, 517–523.
[25] Y. Tanaka, M. Kiguchi, M. Akita, *Chem. A Eur. J.* **2017**, *23*, 4741–4749.
[26] D. Stefani, M. Perrin, C. Gutiérrez-Cerón, A. C. Aragonès, J. Labra-Muñoz, R. D. C. Carrasco, Y. Matsushita, Z. Futera, J. Labuta, T. H. Ngo, K. Ariga, I. Díez-Pérez, H. S. J. van der Zant, D. Dulić, J. P. Hill, *ChemistrySelect* **2018**, *3*, 6473–6478.
[27] D. Fracasso, H. Valkenier, J. C. Hummelen, G. C. Solomon, R. C. Chiechi, *J. Am. Chem. Soc.* **2011**, *133*, 9556–9563.
[28] M. Koole, J. M. Thijssen, H. Valkenier, J. C. Hummelen, H. S. J. V. Der Zant, *Nano Lett.* **2015**, *15*, 5569–5573.
[29] N. Darwish, I. Díez-Pérez, S. Guo, N. Tao, J. J. Gooding, M. N. Paddon-Row, *J. Phys. Chem. C* **2012**, *116*, 21093–21097.
[30] K. Walzer, B. Männig, M. Pfeiffer, K. Leo, *Chem. Rev.* **2007**, *107*, 1233–1271.
[31] A. Mishchenko, L. A. Zotti, D. Vonlanthen, M. Bürkle, F. Pauly, J. C. Cuevas, M. Mayor, T. Wandlowski, *J. Am. Chem. Soc.* **2011**, *133*, 184–187.
[32] K. Yoshizawa, T. Tada, A. Staykov, *J. Am. Chem. Soc.* **2008**, *130*, 9406–9413.
[33] K. Yoshizawa, *Acc. Chem. Res.* **2012**, *45*, 1612–1621.
[34] J. Koga, Y. Tsuji, K. Yoshizawa, *J. Phys. Chem. C* **2012**, *116*, 20607–20616.
[35] T. Markussen, R. Stadler, K. S. Thygesen, *Nano Lett.* **2010**, *10*, 4260–4265.
[36] K. G. L. Pedersen, A. Borges, P. Hedegård, G. C. Solomon, M. Strange, *J. Phys. Chem. C* **2015**, *119*, 26919–26924.
[37] Y. Tsuji, E. Estrada, R. Movassagh, R. Hoffmann, *Chem. Rev.* **2018**, *118*, 4887–4911.
[38] K. Stokbro, J. Taylor, M. Brandbyge, P. Ordejón, *Ann. N. Y. Acad. Sci.* **2003**, *1006*, 212–226.
[39] J. Alqahtani, H. Sadeghi, S. Sangtarash, C. J. Lambert, *Angew. Chem. Int. Ed.* **2018**, *57*, 15065–15069.
[40] P. W. Fowler, B. T. Pickup, T. Z. Todorova, W. Myrvold, *J. Chem. Phys.* **2009**, *131*, 044104.
[41] T. Stuyver, S. Fias, F. De Proft, P. Geerlings, *J. Phys. Chem. C* **2015**, *119*, 26390–26400.
[42] Y. Tsuji, R. Hoffmann, R. Movassagh, S. Datta, *J. Chem. Phys.* **2014**, *141*, 224311.
[43] Y. Geng, S. Sangtarash, C. Huang, H. Sadeghi, Y. Fu, W. Hong, T. Wandlowski, S. Decurtins, C. J. Lambert, S. X. Liu, *J. Am. Chem. Soc.* **2015**, *137*, 4469–4476.
[44] Y. Tsuji, R. Hoffmann, M. Strange, G. C. Solomon, *Proc. Natl. Acad. Sci. USA* **2016**, *113*, E413–E419.
[45] T. Stuyver, T. Zeng, Y. Tsuji, P. Geerlings, F. De Proft, *Nano Lett.* **2018**, *18*, 7298–7304.
[46] T. Stuyver, S. Fias, F. De Proft, P. Geerlings, Y. Tsuji, R. Hoffmann, *J. Chem. Phys.* **2017**, *146*, 092310.
[47] M. H. Garner, W. Bro-Jørgensen, P. D. Pedersen, G. C. Solomon, *J. Phys. Chem. C* **2018**, *122*, 26777–26789.
[48] B. Capozzi, J. Xia, O. Adak, E. J. Dell, Z.-F. Liu, J. C. Taylor, J. B. Neaton, L. M. Campos, L. Venkataraman, *Nat. Nanotechnol.* **2015**, *10*, 522–527.
[49] M. J. Frisch, G. W. Trucks, H. B. Schlegel, G. E. Scuseria, M. A. Robb, J. R. Cheeseman, G. Scalmani, V. Barone, G. A. Petersson, H. Nakatsuji, X. Li, M. Caricato, A. V. Marenich, J. Bloino, B. G. Janesko, R. Gomperts, B. Mennucci, H. P. Hratchian, J. V. Ortiz, A. F. Izmaylov, J. L. Sonnenberg, D. Williams-Young, F. Ding, F. Lipparini, F. Egidi, J. Goings, B. Peng, A. Petrone, T. Henderson, D. Ranasinghe, V. G. Zakrzewski, J. Gao, N. Rega, G. Zheng, W. Liang, M. Hada, M. Ehara, K. Toyota, R. Fukuda, J. Hasegawa, M. Ishida, T. Nakajima, Y. Honda, O. Kitao, H. Nakai, T. Vreven, K. Throssell, J. A. Montgomery Jr, J. E. Peralta, F. Ogliaro, M. J. Bearpark, J. J. Heyd, E. N. Brothers, K. N. Kudin, V. N. Staroverov, T. A. Keith, R. Kobayashi, J. Normand, K. Raghavachari, A. P. Rendell, J. C. Burant, S. S. Iyengar, J. Tomasi, M. Cossi, J. M. Millam, M. Klene, C. Adamo, R. Cammi, J. W. Ochterski, R. L. Martin, K. Morokuma, O. Farkas, J. B. Foresman, D. J. Fox, *Gaussian 16, Revision A.03*, Gaussian, Inc., Wallingford CT, 2016, www.gaussian.com.

Manuscript received: January 8, 2021
Revised manuscript received: February 12, 2021
Accepted manuscript online: March 3, 2021
Version of record online: April 7, 2021

© 2021 Wiley-VCH GmbH

ChemPhysChem

Supporting Information

Origin of the Electron Transport Properties of Aromatic and Antiaromatic Single Molecule Circuits

Narendra P. Arasu and Héctor Vázquez*

Table of contents

1. Nucleus-Independent Chemical Shifts (NICS) 2

2. Comparison of electronic properties of aromatic and antiaromatic molecules 3

3. Comparison of electronic properties of anthraquinone and biphenylene molecules 5

4. Transmission spectra of aromatic, antiaromatic, and quinoidal molecules functionalized with nitrile and methyl-sulfide linkers 6

5. Table: HOMO-LUMO gaps of aromatic, antiaromatic, and quinoidal molecules 8

6. Table: Conductance of aromatic, antiaromatic, and quinoidal molecules with nitrile and methyl-sulfide linkers at opposite sides of the molecular long axis 9

1. Nucleus-Independent Chemical Shift (NICS)

Different NICS were calculated[1]:

i) NICS(0), at the geometric center of the molecular rings

ii) NICS(1), 1 Å above and below the geometrical center of the rings

iii) NICSzz(1), the out of plane component of the tensor

NICS(1) and NICSzz(1) are the averages of the values calculated above and below the molecular plane.

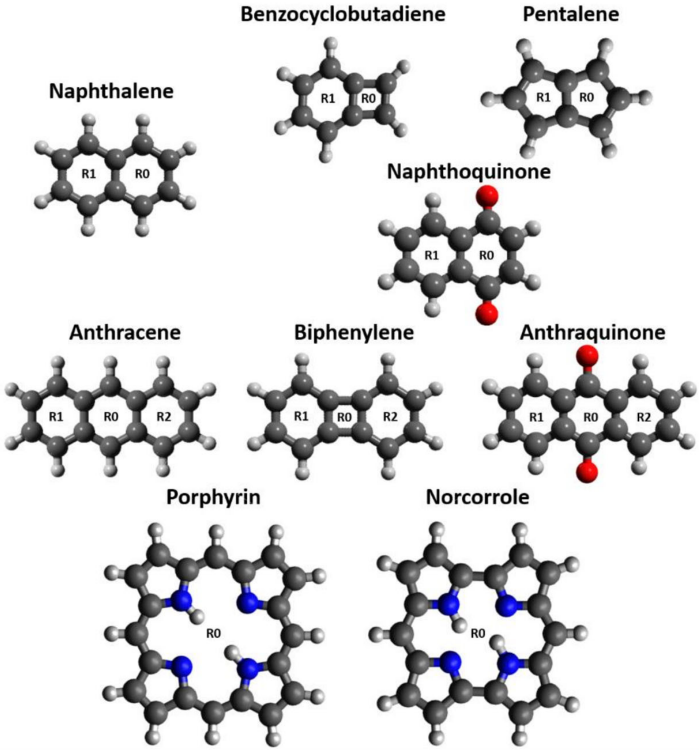

Figure S1. Structures for which NICS are calculated.

R0

Molecule	NICS(0) (ppm)	NICS(1) (ppm)	$NICS_{zz}(1)$ (ppm)
Naphthalene	-7.74	-10.75	-25.98
Benzocyclobutadiene	23.94	12.88	49.68
Naphthoquinone	6.26	0.47	5.42
Pentalene	24.03	17.46	60.07
Anthracene	-10.16	-12.81	-31.19
Biphenylene	19.55	8.92	38.72
Anthraquinone	8.73	1.74	9.64
Metal-free porphyrin	-13.49	-11.83	-31.02
Metal-free norcorrole	26.47	22.95	73.78

R1

Molecule	NICS(0) (ppm)	NICS(1) (ppm)	$NICS_{zz}(1)$ (ppm)
Naphthalene	-7.74	-10.75	-25.98
Benzocyclobutadiene	-0.80	-3.64	-4.93
Naphthoquinone	-5.88	-9.42	-21.78
Pentalene	24.04	17.47	60.08
Anthracene	-6.82	-9.91	-23.20
Biphenylene	-2.32	-5.36	-10.01
Anthraquinone	-5.74	-9.31	-21.18

R2

Molecule	NICS(0) (ppm)	NICS(1) (ppm)	$NICS_{zz}(1)$ (ppm)
Anthracene	-6.82	-9.91	-23.20
Biphenylene	-2.32	-5.36	-10.01
Anthraquinone	-5.74	-9.31	-21.18

2. Comparison of electronic properties of aromatic and antiaromatic molecules

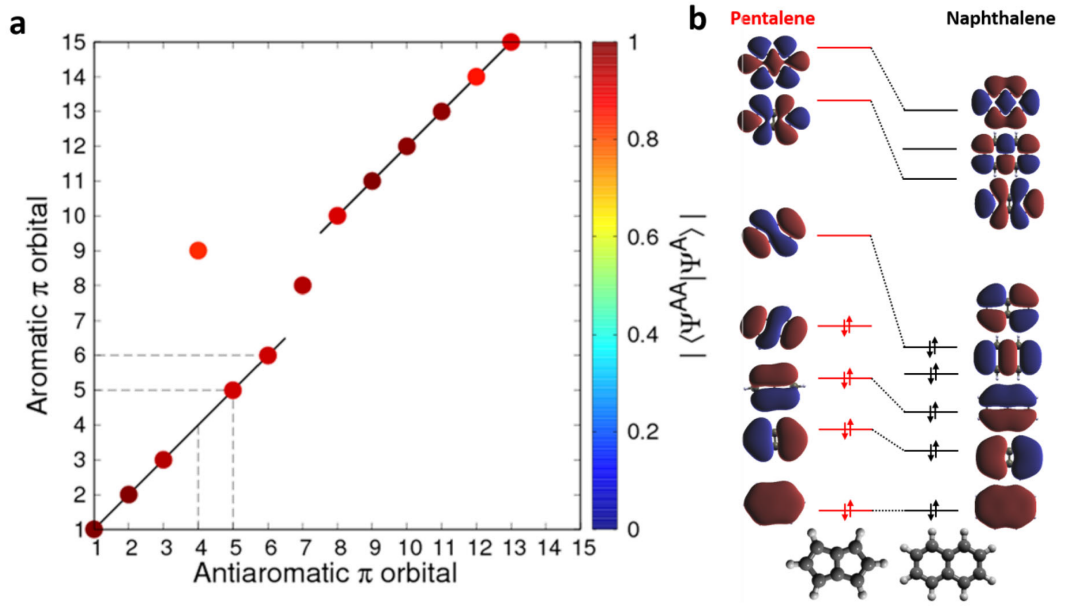

Figure S2. (a) Best-matching 2D plot of pentalene and naphthalene π molecular orbitals. Dashed lines indicate the HOMO and LUMO of each molecule. (b) π MO diagrams. Lines connect the best-matching orbitals of each molecule.

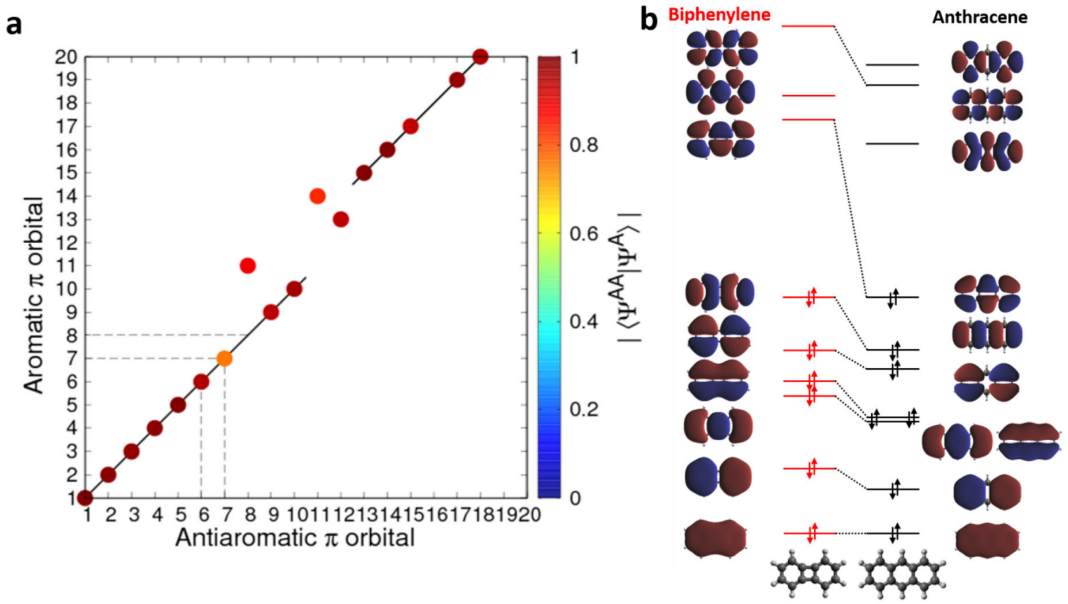

Figure S3. Same as S2 for biphenylene and anthracene.

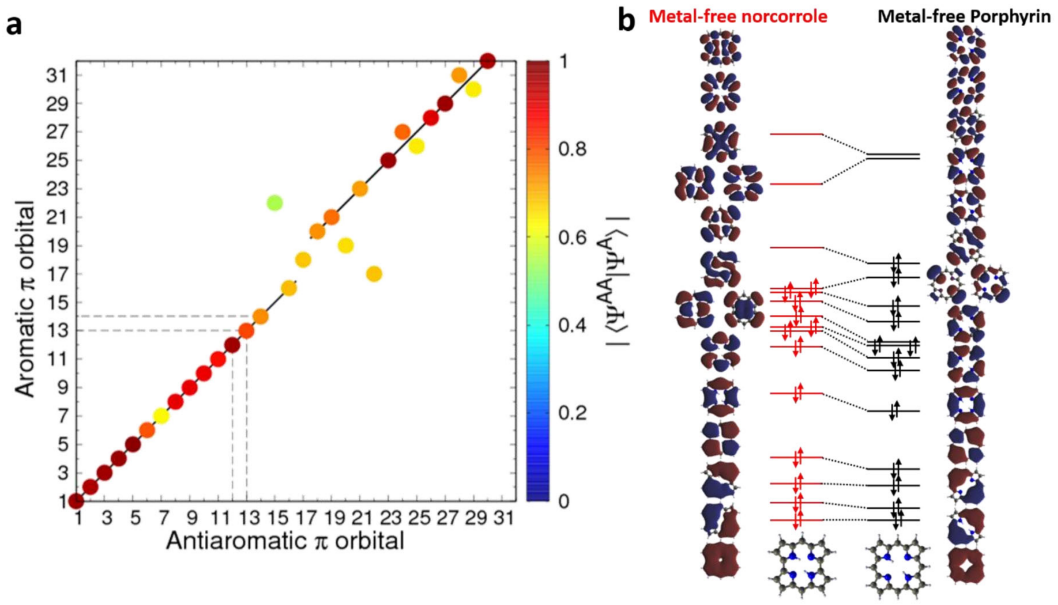

Figure S4. Same as S2 for metal-free norcorrole and porphyrin.

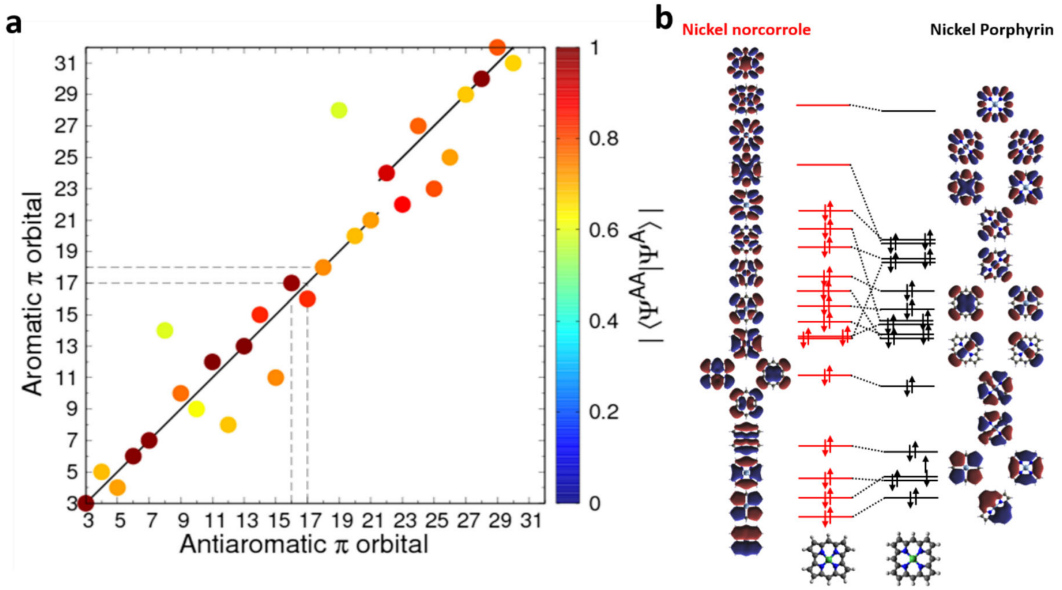

Figure S5. Same as S2 for nickel norcorrole and porphyrin.

3. Comparison of electronic properties of anthraquinone and biphenylene molecules

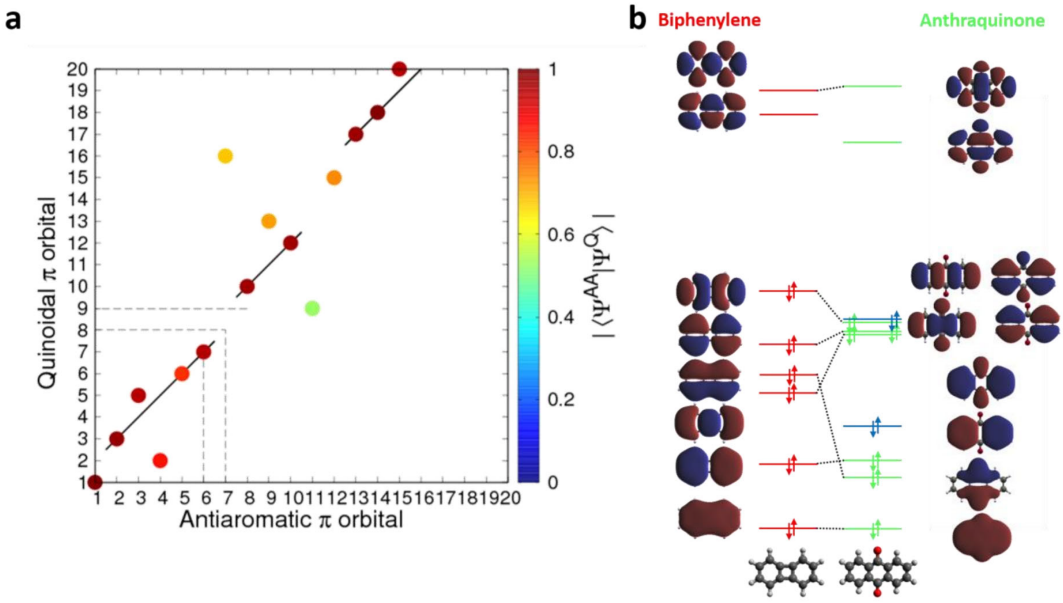

Figure S6. (a) Best-matching biphenylene and anthraquinone π orbitals. (b) Corresponding MO diagrams. Some quinoidal MOs localized on the C=O atoms are not matched.

4. Transmission spectra of aromatic, antiaromatic, and quinoidal molecules functionalized with nitrile and methyl-sulfide linkers

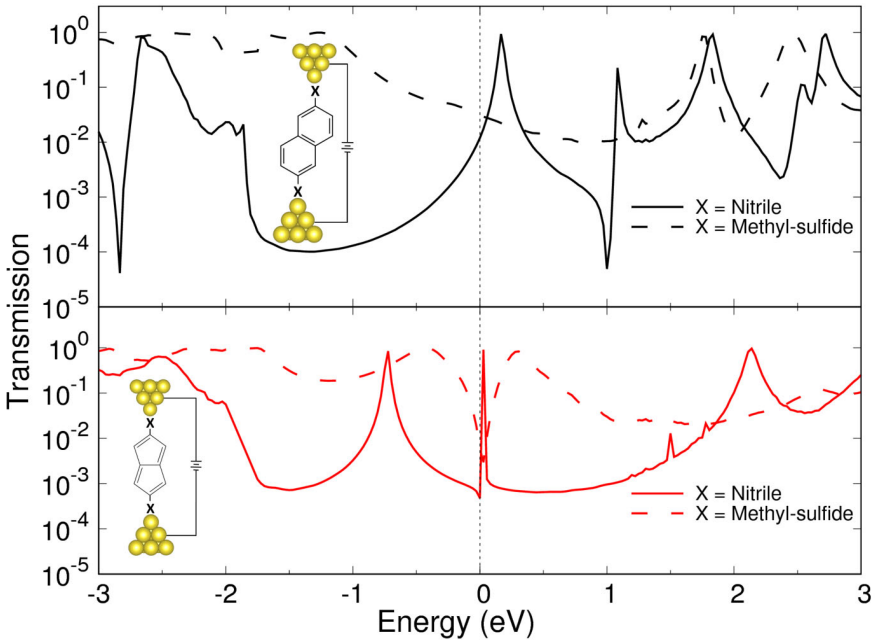

Figure S7. Calculated transmission spectra of naphthalene (top) and its antiaromatic counterpart pentalene (bottom) for nitrile and methyl sulphide linkers.

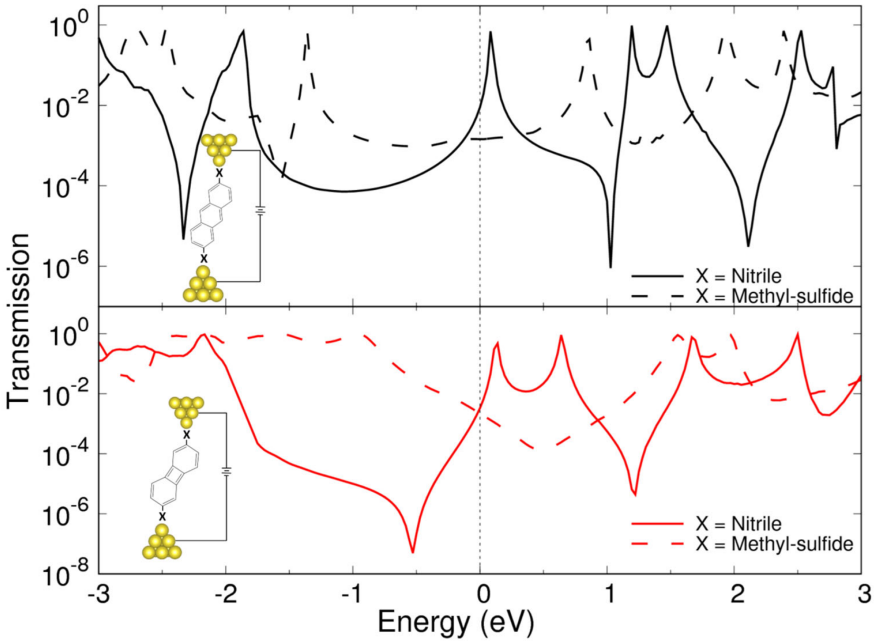

Figure S8. Calculated transmission spectra of anthracene (top) and its antiaromatic counterpart biphenylene (bottom).

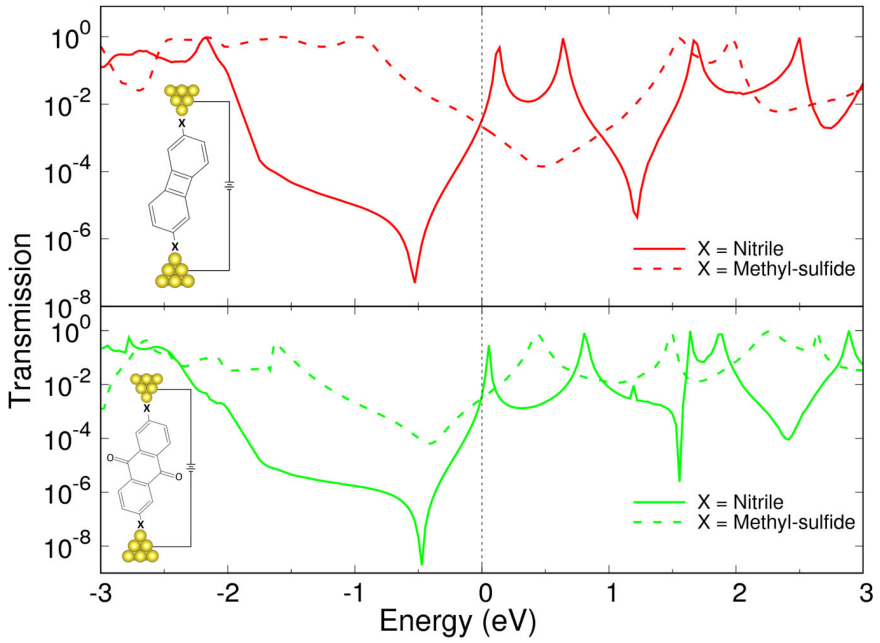

Figure S9. Calculated transmission spectra of biphenylene (top) and its quinoidal counterpart anthraquinone (bottom).

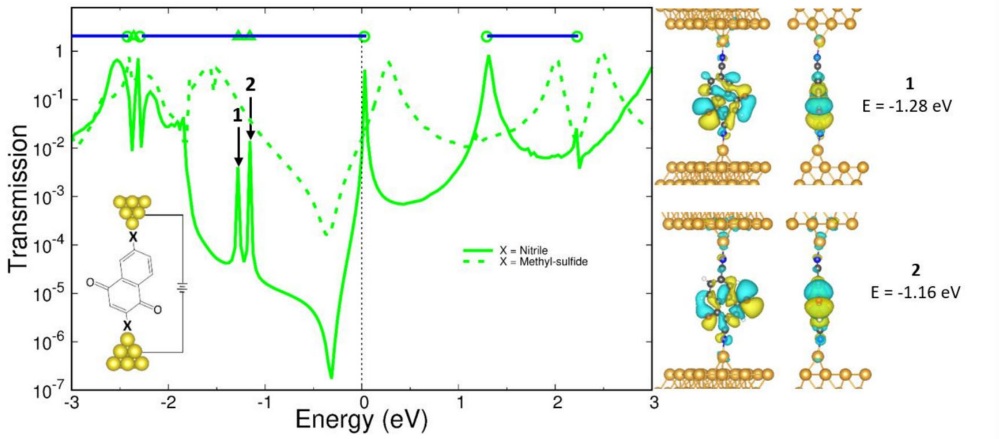

Figure S10. Real-space representation of transmission eigenchannels at selected energies, showing their in-plane character.

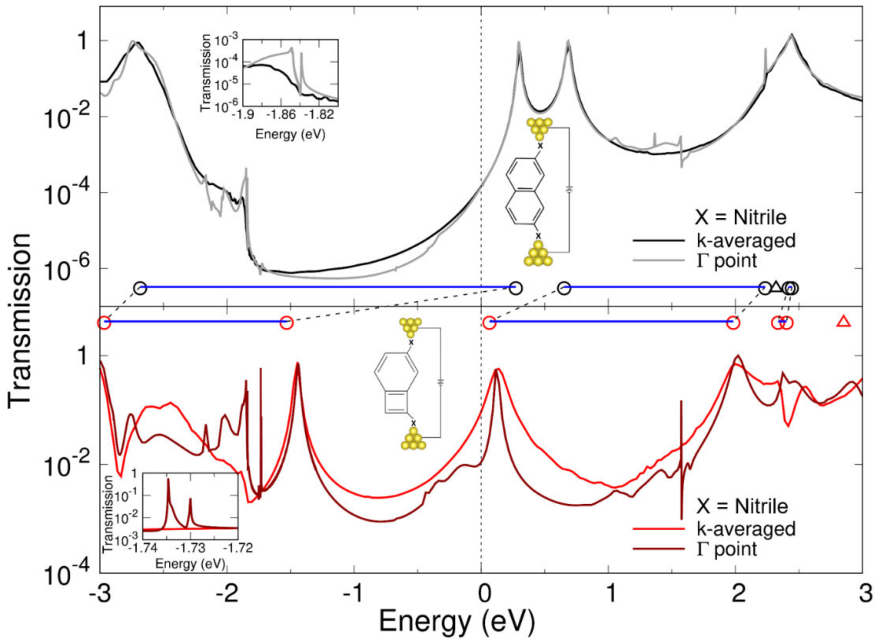

Figure S11. Calculated transmission spectra of nitrile-functionalized naphthalene (top) and its antiaromatic counterpart benzocyclobutadiene (bottom). Here both molecules bind to electrodes on the same side of the molecular long axis. Panels show transmission spectra calculated on a 15x15 reciprocal-space mesh and at the Γ point. Insets highlight DQI features.

5. Table: HOMO-LUMO gaps of aromatic, antiaromatic, and quinoidal molecules

Calculated HOMO-LUMO gap of isolated molecules using B3LYP/6-31G.

	HOMO-LUMO gap (eV)
Naphthalene	4.86
Benzocyclobutadiene	3.87
Pentalene	2.60
Naphthoquinone	3.86
Anthracene	3.62
Biphenylene	4.20
Anthraquinone	4.08
Metal-free porphyrin	2.87
Metal-free norcorrole	1.66
Ni-Porphyrin	3.19
Ni-Norcorrole	1.48

6. Table: Conductance of aromatic, antiaromatic, and quinoidal molecules with nitrile and methyl-sulfide linkers at opposite sides of the molecular long axis.

	Conductance ($\times 10^{-2}$ G_0)	
	Nitrile	**Methyl-sulfide**
Naphthalene	1.19	3.08
Benzocyclobutadiene	2.80	0.53
Pentalene	0.05	0.59
Naphthoquinone	1.01	1.54
Anthracene	0.90	0.14
Biphenylene	0.33	0.22
Anthraquinone	0.38	0.30
Metal-free porphyrin	3.84	2.92
Metal-free norcorrole	9.50	12.80

References

[1] Gaussian 16, Revision A.03, M. J. Frisch, G. W. Trucks, H. B. Schlegel, G. E. Scuseria, M. A. Robb, J. R. Cheeseman, G. Scalmani, V. Barone, G. A. Petersson, H. Nakatsuji, X. Li, M. Caricato, A. V Marenich, J. Bloino, B. G. Janesko, R. Gomperts, B. Mennucci, H. P. Hratchian, J. V Ortiz, A. F. Izmaylov, J. L. Sonnenberg, D. Williams-Young, F. Ding, F. Lipparini, F. Egidi, J. Goings, B. Peng, A. Petrone, T. Henderson, D. Ranasinghe, V. G. Zakrzewski, J. Gao, N. Rega, G. Zheng, W. Liang, M. Hada, M. Ehara, K. Toyota, R. Fukuda, J. Hasegawa, M. Ishida, T. Nakajima, Y. Honda, O. Kitao, H. Nakai, T. Vreven, K. Throssell, J. A. Montgomery Jr., J. E. Peralta, F. Ogliaro, M. J. Bearpark, J. J. Heyd, E. N. Brothers, K. N. Kudin, V. N. Staroverov, T. A. Keith, R. Kobayashi, J. Normand, K. Raghavachari, A. P. Rendell, J. C. Burant, S. S. Iyengar, J. Tomasi, M. Cossi, J. M. Millam, M. Klene, C. Adamo, R. Cammi, J. W. Ochterski, R. L. Martin, K. Morokuma, O. Farkas, J. B. Foresman, D. J. Fox, Gaussian,Inc., Wallingford, CT **2016**.

Conclusion

Molecular junctions are nanoscale electronic circuits where individual molecules act as active components. Molecular circuits are powerful tools to study the physical and chemical properties at the atomic scale. This thesis presents the theoretical works I did on molecular junctions I did as part of my Ph.D. The results include experiments that our collaborators carried out. Our results and discussions helped to explain new phenomena in the field of molecular junctions. I have studied molecules of diverse nature such as donor-acceptor, carbenes, aromatic and antiaromatic molecules. I have theoretically studied novel molecular junctions with the molecules and thus creating a unique design manual in this field.

The thesis started with an introduction to the background in the field. In this theoretical overview, I derived the expression for electronic transmission in a molecular junction. I presented an overview of the fundamentals of quantum mechanics related to molecules and junctions, including the concepts of resonance transmission through a potential barrier, fundamentals of DFT, and interface electronic structure. I also included a brief overview of experimental techniques used in the field of molecular junctions.

In the subsequent chapter, I showed our study on a carbazol and phenalenon based donor-bridge-acceptor molecule. I discussed the charge transfer properties of the molecule adsorbed over the platinum substrate. Our results suggest that the molecule retains many donor-acceptor characteristics even upon adsorption to a highly reactive surface such as platinum. Our study demonstrated that the donor-acceptor dyad separated by a methylene bridge is a promising candidate for organic energy harvesting devices.

I then showed our study on a previously synthesized novel molecule, which is also the smallest carbene molecule. I studied the adsorption properties of the molecule over a Au surface. Our study attributed the tilted adsorption of the novel carbene molecule to the high electronegativity of the carbene core. The molecule showed stronger adsorption than any other carbene previously studied, paving the way for new carbene-based surface science studies.

In the final chapter 4, I showed our work on a biphenylene-based bipodal molecular junction, I analyzed the mechanical and electron transport properties with respect to different linker groups. I proposed a new strategy to form two direct Au-C bonds to the Au substrate using our calculations. I established a relationship between mechanical and transmission properties of different linker groups, thereby providing valuable design rules for building molecular junctions.

Finally, I showed our study on aromatic and antiaromatic molecules. We proved a long speculated concept of antiaromaticity enhanced conductance to be true. I carried out the theoretical study of the first stable antiaromatic molecule, Ni-norcorrole. The higher conductance of the antiaromatic molecule comes from the lowest occupied molecular orbital (LUMO) derived resonance being closer to the Fermi level when compared to its aromatic counterpart. Our subsequent study showed that the antiaromatic electronic structure resembles a double p-doped aromatic molecule. I also showed how aromaticity, antiaromaticity, and destructive quantum interference (DQI) are related. We also showed how to tune

the relative conductance of aromatic and antiaromatic compounds through linker choice. Our study proposed new design rules for single-molecule circuits based on characteristics of (anti)aromatic conjugated systems.

I believe that the projects I was involved in have contributed to advance knowledge in the field of single-molecule junctions. I hope that the donor-acceptor characteristics of the CBHP molecule are utilized in solar-energy cells. Our study on BAC opens a pathway for new carbene-based surface science studies. In addition, the design rules we proposed through biphenylene molecule served as a guide for me throughout my research. I am confident that it will be equally helpful for designing molecular junctions in future studies. The research on conjugated molecules based on antiaromaticity is in its early stage. Our work is the first demonstration of an antiaromatic-based molecular junction. I am confident that antiaromaticity will be used in various fields in the future, and I am glad to have contributed to this exciting area of research.

Bibliography

[1] M. Ratner, "A brief history of molecular electronics," *Nat. Nanotechnol.*, vol. 8, no. 6, pp. 378–381, 2013.

[2] A. Aviram and M. A. Ratner, "Molecular rectifiers," *Chem. Phys. Lett.*, vol. 29, no. 2, pp. 277–283, 1974.

[3] G. Binnig, H. Rohrer, C. Gerber, and E. Weibel, "Surface studies by scanning tunneling microscopy," *Phys. Rev. Lett.*, vol. 49, no. 1, p. 57, 1982.

[4] G. Binnig, H. Rohrer, C. Gerber, and E. Weibel, "Tunneling through a controllable vacuum gap," *Appl. Phys. Lett.*, vol. 40, no. 2, pp. 178–180, 1982.

[5] L. A. Bumm, J. J. Arnold, M. T. Cygan, T. D. Dunbar, T. P. Burgin, L. Jones, D. L. Allara, J. M. Tour, and P. S. Weiss, "Are single molecular wires conducting?," *Science*, vol. 271, no. 5256, pp. 1705–1707, 1996.

[6] M. A. Reed, C. Zhou, C. Muller, T. Burgin, and J. Tour, "Conductance of a molecular junction," *Science*, vol. 278, no. 5336, pp. 252–254, 1997.

[7] J. M. Tour, W. A. Reinerth, L. Jones, T. P. Burgin, C.-W. Zhou, C. J. Muller, M. R. Deshpande, and M. A. Reed, "Recent Advances in Molecular Scale Electronics," *Ann. N.Y. Acad. Sci.*, vol. 852, no. 1, pp. 197–204, 1998.

[8] M. A. Reed, "Molecular-scale electronics," *Proc. IEEE*, vol. 87, no. 4, pp. 652–658, 1999.

[9] M. A. Reed and J. M. Tour, "Computing with molecules," *Sci. Amer.*, vol. 282, no. 6, pp. 86–93, 2000.

[10] M. A. Reed, J. Chen, A. Rawlett, D. Price, and J. Tour, "Molecular random access memory cell," *Appl. Phys. Lett.*, vol. 78, no. 23, pp. 3735–3737, 2001.

[11] H. Park, J. Park, A. Lim, E. Anderson, A. Alivisatos, and P. McEuen, "Nanomechanical oscillations in a single-C_{60} transistor," *Nature*, vol. 407, no. 6800, pp. 57–60, 2000.

[12] J. Park, A. N. Pasupathy, J. I. Goldsmith, C. Chang, Y. Yaish, J. R. Petta, M. Rinkoski, J. P. Sethna, H. D. Abruña, P. L. McEuen, *et al.*, "Coulomb blockade and the Kondo effect in single-atom transistors," *Nature*, vol. 417, no. 6890, pp. 722–725, 2002.

[13] K. Moth-Poulsen and T. Bjørnholm, "Molecular electronics with single molecules in solid-state devices," *Nat. Nanotechnol.*, vol. 4, no. 9, pp. 551–556, 2009.

[14] G. Cuniberti, G. Fagas, and K. Richter, *Introducing Molecular Electronics*. Springer New York, 2010.

[15] R. L. Carroll and C. B. Gorman, "The genesis of molecular electronics," *Angew. Chem. Int. Ed.*, vol. 41, no. 23, pp. 4378–4400, 2002.

[16] P. T. Mathew and F. Fang, "Advances in molecular electronics: a brief review," *Engineering*, vol. 4, no. 6, pp. 760–771, 2018.

[17] T. A. Su, M. Neupane, M. L. Steigerwald, L. Venkataraman, and C. Nuckolls, "Chemical principles of single-molecule electronics," *Nat. Rev. Mater.*, vol. 1, no. 3, p. 16002, 2016.

[18] P. Gehring, J. M. Thijssen, and H. S. van der Zant, "Single-molecule quantum-transport phenomena in break junctions," *Nat. Rev. Phys.*, vol. 1, no. 6, pp. 381–396, 2019.

[19] Y. Tanaka, M. Kiguchi, and M. Akita, "Inorganic and organometallic molecular wires for single-molecule devices," *Chem.–Eur. J.*, vol. 23, no. 20, pp. 4741–4749, 2017.

[20] F. Evers, R. Korytár, S. Tewari, and J. M. van Ruitenbeek, "Advances and challenges in single-molecule electron transport," *Rev. Mod. Phys.*, vol. 92, no. 3, p. 035001, 2020.

[21] G. Sedghi, V. M. García-Suárez, L. J. Esdaile, H. L. Anderson, C. J. Lambert, S. Martín, D. Bethell, S. J. Higgins, M. Elliott, N. Bennett, J. E. Macdonald, and R. J. Nichols, "Long-range electron tunnelling in oligo-porphyrin molecular wires.," *Nat. Nanotechnol.*, vol. 6, no. 8, pp. 517–523, 2011.

[22] R. Breslow and S. T. Schneebeli, "Structure-property relationships in molecular wires," *Tetrahedron*, vol. 67, no. 52, pp. 10171–10178, 2011.

[23] T. Woller, N. Ramos-Berdullas, M. Mandado, M. Alonso, F. de Proft, and J. Contreras-García, "Understanding conductivity in molecular switches: a real space approach in octaphyrins," *Phys. Chem. Chem. Phys.*, vol. 18, pp. 11829–11838, 2016.

[24] T. Stuyver, M. Perrin, P. Geerlings, F. De Proft, and M. Alonso, "Conductance Switching in Expanded Porphyrins through Aromaticity and Topology Changes," *J. Am. Chem. Soc.*, vol. 140, no. 4, pp. 1313–1326, 2018.

[25] S. V. Aradhya and L. Venkataraman, "Single-molecule junctions beyond electronic transport," *Nat. Nanotechnol.*, vol. 8, no. 6, p. 399, 2013.

[26] Q. Li, I. Duchemin, S. Xiong, G. C. Solomon, and D. Donadio, "Mechanical tuning of thermal transport in a molecular junction," *J. Phys. Chem. C*, vol. 119, no. 43, pp. 24636–24642, 2015.

[27] S. Ahn, S. V. Aradhya, R. S. Klausen, B. Capozzi, X. Roy, M. L. Steigerwald, C. Nuckolls, and L. Venkataraman, "Electronic transport and mechanical stability of carboxyl linked single-molecule junctions," *Phys. Chem. Chem. Phys.*, vol. 14, no. 40, pp. 13841–13845, 2012.

[28] B. Lounis and W. E. Moerner, "Single photons on demand from a single molecule at room temperature," *Nature*, vol. 407, no. 6803, pp. 491–493, 2000.

[29] J. C. Cuevas and E. Scheer, *Molecular Electronics*. WORLD SCIENTIFIC, 2010.

[30] S. Datta, *Quantum Transport: Atom to Transistor*. Cambridge University Press, 2005.

[31] J. Ulrich, D. Esrail, W. Pontius, L. Venkataraman, D. Millar, and L. H. Doerrer, "Variability of conductance in molecular junctions," *J. Phys. Chem. B*, vol. 110, no. 6, pp. 2462–2466, 2006.

[32] L. Venkataraman, J. E. Klare, C. Nuckolls, M. S. Hybertsen, and M. L. Steigerwald, "Dependence of single-molecule junction conductance on molecular conformation," *Nature*, vol. 442, no. 7105, pp. 904–907, 2006.

[33] V. M. Santhini, O. Stetsovych, M. Ondráček, J. I. Mendieta Moreno, P. Mutombo, B. de la Torre, M. Švec, J. Klívar, I. G. Stará, H. Vázquez, *et al.*, "On-surface synthesis of polyferrocenylene and its single-chain conformational and electrical transport properties," *Adv. Funct. Mater.*, vol. 31, no. 5, p. 2006391, 2021.

[34] C. Nacci, A. Viertel, S. Hecht, and L. Grill, "Covalent assembly and characterization of nonsymmetrical single-molecule nodes," *Angew. Chem. Int. Ed.*, vol. 55, no. 44, pp. 13724–13728, 2016.

[35] M. Koch, F. Ample, C. Joachim, and L. Grill, "Voltage-dependent conductance of a single graphene nanoribbon," *Nat. Nanotechnol.*, vol. 7, no. 11, pp. 713–717, 2012.

[36] L. Lafferentz, F. Ample, H. Yu, S. Hecht, C. Joachim, and L. Grill, "Conductance of a single conjugated polymer as a continuous function of its length," *Science*, vol. 323, no. 5918, pp. 1193–1197, 2009.

[37] F. Prins, T. Hayashi, B. De Vos van Steenwijk, B. Gao, E. Osorio, K. Muraki, and H. Van der Zant, "Room-temperature stability of Pt nanogaps formed by self-breaking," *Appl. Phys. Lett.*, vol. 94, no. 12, p. 123108, 2009.

[38] C. A. Martin, J. M. van Ruitenbeek, and H. S. van der Zant, "Sandwich-type gated mechanical break junctions," *Nanotechnology*, vol. 21, no. 26, p. 265201, 2010.

[39] W. Lee and P. Reddy, "Creation of stable molecular junctions with a custom-designed scanning tunneling microscope," *Nanotechnology*, vol. 22, no. 48, p. 485703, 2011.

[40] M. S. Inkpen, Z.-F. Liu, H. Li, L. M. Campos, J. B. Neaton, and L. Venkataraman, "Non-chemisorbed gold–sulfur binding prevails in self-assembled monolayers," *Nat. Chem.*, vol. 11, no. 4, pp. 351–358, 2019.

[41] B. Xu and N. J. Tao, "Measurement of single-molecule resistance by repeated formation of molecular junctions," *Science*, vol. 301, no. 5637, pp. 1221–1223, 2003.

[42] Y. Dedkov, E. Voloshina, and M. Fonin, "Scanning probe microscopy and spectroscopy of graphene on metals," *Phys. Status Solidi (B)*, vol. 252, no. 3, pp. 451–468, 2015.

[43] D. G. de Oteyza, P. Gorman, Y.-C. Chen, S. Wickenburg, A. Riss, D. J. Mowbray, G. Etkin, Z. Pedramrazi, H.-Z. Tsai, A. Rubio, *et al.*, "Direct imaging of covalent bond structure in single-molecule chemical reactions," *Science*, vol. 340, no. 6139, pp. 1434–1437, 2013.

[44] J. Su, M. Telychko, P. Hu, G. Macam, P. Mutombo, H. Zhang, Y. Bao, F. Cheng, Z.-Q. Huang, Z. Qiu, *et al.*, "Atomically precise bottom-up synthesis of π-extended [5] triangulene," *Sci. Adv.*, vol. 5, no. 7, p. eaav7717, 2019.

[45] M. Paulsson, "Non equilibrium green's functions for dummies: Introduction to the one particle negf equations," *arXiv preprint cond-mat/0210519*, 2002.

[46] J. M. Soler, E. Artacho, J. D. Gale, A. García, J. Junquera, P. Ordejón, and D. Sánchez-Portal, "The SIESTA method for ab initio order-N materials simulation," *J. Phys.: Condens. Matter*, vol. 14, no. 11, p. 2745, 2002.

[47] M. Brandbyge, J.-L. Mozos, P. Ordejón, J. Taylor, and K. Stokbro, "Density-functional method for nonequilibrium electron transport," *Phys. Rev. B*, vol. 65, no. 16, p. 165401, 2002.

[48] T. Markussen, R. Stadler, and K. S. Thygesen, "The relation between structure and quantum interference in single molecule junctions," *Nano Lett.*, vol. 10, no. 10, pp. 4260–4265, 2010.

[49] P. Fowler, B. Pickup, T. Todorova, and W. Myrvold, "A selection rule for molecular conduction," *J. Chem. Phys.*, vol. 131, no. 4, p. 044104, 2009.

[50] J. Xia, B. Capozzi, S. Wei, M. Strange, A. Batra, J. R. Moreno, R. J. Amir, E. Amir, G. C. Solomon, L. Venkataraman, and L. M. Campos, "Breakdown of interference rules in azulene, a nonalternant hydrocarbon," *Nano Lett.*, vol. 14, no. 5, pp. 2941–2945, 2014.

[51] R. Stadler, "Comment on" breakdown of interference rules in azulene, a nonalternant hydrocarbon"," *Nano Lett.*, vol. 15, no. 11, p. 7175–7176, 2016.

[52] M. Strange, G. C. Solomon, L. Venkataraman, and L. M. Campos, "Reply to "comment on 'breakdown of interference rules in azulene, a nonalternant hydrocarbon"'," *Nano Lett.*, vol. 15, no. 11, pp. 7177–7178, 2015.

[53] A. Borges and G. C. Solomon, "Effects of Aromaticity and Connectivity on the Conductance of Five-Membered Rings," *J. Phys. Chem. C*, vol. 121, no. 15, pp. 8272–8279, 2017.

[54] K. Yoshizawa, "An orbital rule for electron transport in molecules," *Acc. Chem. Res.*, vol. 45, no. 9, pp. 1612–1621, 2012.

[55] J. Koga, Y. Tsuji, and K. Yoshizawa, "Orbital control of single-molecule conductance perturbed by π-accepting anchor groups: Cyanide and isocyanide," *J. Phys. Chem. C*, vol. 116, no. 38, pp. 20607–20616, 2012.

[56] J. P. Perdew, K. Burke, and M. Ernzerhof, "Generalized gradient approximation made simple," *Phys. Rev. Lett.*, vol. 77, no. 18, p. 3865, 1996.

[57] Y. J. Chang and T. J. Chow, "Triaryl linked donor acceptor dyads for high-performance dye-sensitized solar cells," *Tetrahedron*, vol. 65, no. 46, pp. 9626–9632, 2009.

[58] P. Song, Y. Li, F. Ma, T. Pullerits, and M. Sun, "External electric field-dependent photoinduced charge transfer in a donor–acceptor system for an organic solar cell," *J. Phys. Chem. C*, vol. 117, no. 31, pp. 15879–15889, 2013.

[59] D. T. Chase, A. G. Fix, S. J. Kang, B. D. Rose, C. D. Weber, Y. Zhong, L. N. Zakharov, M. C. Lonergan, C. Nuckolls, and M. M. Haley, "6, 12-diarylindeno [1, 2-b] fluorenes: syntheses, photophysics, and ambipolar ofets," *J. Am. Chem. Soc.*, vol. 134, no. 25, pp. 10349–10352, 2012.

[60] V. Bandi, H. B. Gobeze, and F. D'Souza, "Ultrafast photoinduced electron transfer and charge stabilization in donor–acceptor dyads capable of harvesting near-infrared light," *Chem.–Eur. J.*, vol. 21, no. 32, pp. 11483–11494, 2015.

[61] A. N. Amin, M. E. El-Khouly, N. K. Subbaiyan, M. E. Zandler, M. Supur, S. Fukuzumi, and F. D'Souza, "Syntheses, electrochemistry, and photodynamics of ferrocene–azadipyrromethane donor–acceptor dyads and triads," *J. Phys. Chem. A*, vol. 115, no. 35, pp. 9810–9819, 2011.

[62] H. Kawauchi, S. Suzuki, M. Kozaki, K. Okada, D.-M. S. Islam, Y. Araki, O. Ito, and K.-i. Yamanaka, "Photoinduced charge-separation and charge-recombination processes of fullerene [60] dyads covalently connected with phenothiazine and its trimer," *J. Phys. Chem. A*, vol. 112, no. 26, pp. 5878–5884, 2008.

[63] O. S. Wenger, "Photoinduced electron and energy transfer in phenylene oligomers," *Chem. Soc. Rev.*, vol. 40, no. 7, pp. 3538–3550, 2011.

[64] C. Tao, J. Sun, X. Zhang, R. Yamachika, D. Wegner, Y. Bahri, G. Samsonidze, M. L. Cohen, S. G. Louie, T. D. Tilley, *et al.*, "Spatial resolution of a type II heterojunction in a single bipolar molecule," *Nano Lett.*, vol. 9, no. 12, pp. 3963–3967, 2009.

[65] B. Schuler, S.-X. Liu, Y. Geng, S. Decurtins, G. Meyer, and L. Gross, "Contrast formation in kelvin probe force microscopy of single π-conjugated molecules," *Nano Lett.*, vol. 14, no. 6, pp. 3342–3346, 2014.

[66] G. Novell-Leruth, A. Valcárcel, A. Clotet, J. M. Ricart, and J. Pérez-Ramírez, "DFT characterization of adsorbed NHx species on Pt(100) and Pt(111) surfaces," *J. Phys. Chem. B*, vol. 109, no. 38, pp. 18061–18069, 2005.

[67] P. Rivero, V. Manuel García-Suárez, D. Pereñiguez, K. Utt, Y. Yang, L. Bellaiche, K. Park, J. Ferrer, and S. Barraza-Lopez, "Systematic pseudopotentials from reference eigenvalue sets for DFT calculations: Pseudopotential files," *Data Br.*, vol. 3, pp. 21–23, 2015.

[68] M. Marder P, *Condensed matter physics*. New York: John Wiley, 2000.

[69] R. Haddon, R. Rayford, and A. Hirani, "2-Methyl-and 5-methyl-9-hydroxyphenalenone," *J. Org. Chem.*, vol. 46, no. 22, pp. 4587–4588, 1981.

[70] J. Tersoff and D. R. Hamann, "Theory of the scanning tunneling microscope," *Phys. Rev. B*, vol. 31, pp. 805–813, 1985.

[71] R. Ebeling, N. P. Arasu, L. Bensch, B. S. Lammers, B. Mayer, T. J. Müller, H. Vázquez, and S. Karthäuser, "Preservation of the donor–acceptor character of a carbazole–phenalenone dyad upon adsorption on Pt(111)," *Nanoscale Adv.*, vol. 3, no. 2, pp. 538–549, 2021.

[72] M. Dion, H. Rydberg, E. Schröder, D. C. Langreth, and B. I. Lundqvist, "Van der waals density functional for general geometries," *Phys. Rev. Lett.*, vol. 92, p. 246401, 2004.

[73] P. J. Stang, "Unsaturated carbenes," *Chem. Rev.*, vol. 78, no. 4, pp. 383–405, 1978.

[74] M. Schulz, "Hauptmann, S.: Organische Chemie. 893 S., 131 Abb., 65 Tab., Format 17 × 24 cm. Leipzig: VEB Deutscher Verlag f. Grundstoffindustrie 1985. Kunststoff, 60,– M," *J. prakt. Chem.*, vol. 329, no. 2, pp. 348–348, 1987.

[75] O. Kühl, "The chemistry of functionalised N-heterocyclic carbenes," *Chem. Soc. Rev.*, vol. 36, no. 4, pp. 592–607, 2007.

[76] A. J. Arduengo, R. L. Harlow, and M. Kline, "A stable crystalline carbene," *J. Am. Chem. Soc.*, vol. 113, no. 1, pp. 361–363, 1991.

[77] W. A. Herrmann, "N-heterocyclic carbenes: a new concept in organometallic catalysis," *Angew. Chem. Int. Ed.*, vol. 41, no. 8, pp. 1290–1309, 2002.

[78] L. Mercs and M. Albrecht, "Beyond catalysis: N-heterocyclic carbene complexes as components for medicinal, luminescent, and functional materials applications," *Chem. Soc. Rev.*, vol. 39, no. 6, pp. 1903–1912, 2010.

[79] L. Mercs, A. Neels, and M. Albrecht, "Probing the potential of N-heterocyclic carbenes in molecular electronics: redox-active metal centers interlinked by a rigid ditopic carbene ligand," *Dalton Trans.*, no. 41, pp. 5570–5576, 2008.

[80] E. A. Doud, M. S. Inkpen, G. Lovat, E. Montes, D. W. Paley, M. L. Steigerwald, H. Vázquezz, L. Venkataraman, and X. Roy, "In situ formation of N-heterocyclic carbene-bound single-molecule junctions," *J. Am. Chem. Soc.*, vol. 140, no. 28, pp. 8944–8949, 2018.

[81] G. S. Tulevski, M. B. Myers, M. S. Hybertsen, M. L. Steigerwald, and C. Nuckolls, "Formation of catalytic metal-molecule contacts," *Science*, vol. 309, no. 5734, pp. 591–594, 2005.

[82] C. M. Crudden, J. H. Horton, I. I. Ebralidze, O. V. Zenkina, A. B. McLean, B. Drevniok, Z. She, H.-B. Kraatz, N. J. Mosey, T. Seki, *et al.*, "Ultra stable self-assembled monolayers of N-heterocyclic carbenes on gold," *Nat. Chem.*, vol. 6, no. 5, pp. 409–414, 2014.

[83] V. Lavallo, Y. Canac, B. Donnadieu, W. W. Schoeller, and G. Bertrand, "Cyclopropenylidenes: From interstellar space to an isolated derivative in the laboratory," *Science*, vol. 312, no. 5774, pp. 722–724, 2006.

[84] J. D. Masuda, W. W. Schoeller, B. Donnadieu, and G. Bertrand, "NHC-mediated aggregation of P4: isolation of a P12 cluster," *J. Am. Chem. Soc.*, vol. 129, no. 46, pp. 14180–14181, 2007.

[85] O. Back, G. Kuchenbeiser, B. Donnadieu, and G. Bertrand, "Nonmetal-Mediated Fragmentation of P4: Isolation of P1 and P2 Bis (carbene) Adducts," *Angew. Chem. Int. Ed.*, vol. 121, no. 30, pp. 5638–5641, 2009.

[86] G. Kuchenbeiser, B. Donnadieu, and G. Bertrand, "Stable bis (diisopropylamino) cyclopropenylidene (BAC) as ligand for transition metal complexes," *Journal of Organomet. Chem.*, vol. 693, no. 5, pp. 899–904, 2008.

[87] E. A. Doud, R. L. Starr, G. Kladnik, A. Voevodin, E. Montes, N. P. Arasu, Y. Zang, P. Zahl, A. Morgante, L. Venkataraman, H. Vázquez, D. Cvetko, and X. Roy, "Cyclopropenylidenes as Strong Carbene Anchoring Groups on Au Surfaces," *J. Am. Chem. Soc.*, vol. 142, no. 47, pp. 19902–19906, 2020.

[88] G. Mills, M. S. Gordon, and H. Metiu, "Oxygen adsorption on Au clusters and a rough Au (111) surface: The role of surface flatness, electron confinement, excess electrons, and band gap," *J. Chem. Phys.*, vol. 118, no. 9, pp. 4198–4205, 2003.

[89] J. C. Love, L. A. Estroff, J. K. Kriebel, R. G. Nuzzo, and G. M. Whitesides, "Self-assembled monolayers of thiolates on metals as a form of nanotechnology," *Chem. Rev.*, vol. 105, no. 4, pp. 1103–1170, 2005.

[90] R. S. Klausen, J. R. Widawsky, T. A. Su, H. Li, Q. Chen, M. Steigerwald, L. Venkataraman, and C. Nuckolls, "Evaluating atomic components in fluorene wires," *Chem. Sci.*, vol. 5, no. 4, pp. 1561–1564, 2014.

[91] Y. S. Park, A. C. Whalley, M. Kamenetska, M. L. Steigerwald, M. S. Hybertsen, C. Nuckolls, and L. Venkataraman, "Contact chemistry and single-molecule conductance: a comparison of phosphines, methyl sulfides, and amines," *J. Am. Chem. Soc.*, vol. 129, no. 51, pp. 15768–15769, 2007.

[92] M. S. Hybertsen, L. Venkataraman, J. E. Klare, A. C. Whalley, M. L. Steigerwald, and C. Nuckolls, "Amine-linked single-molecule circuits: systematic trends across molecular families," *J. Phys. Condens. Matter*, vol. 20, no. 37, p. 374115, 2008.

[93] B. Xu, X. Xiao, and N. J. Tao, "Measurements of single-molecule electromechanical properties," *J. Am. Chem. Soc.*, vol. 125, no. 52, pp. 16164–16165, 2003.

[94] J. Hihath and N. Tao, "The role of molecule–electrode contact in single-molecule electronics," *Semicond. Sci. Technol.*, vol. 29, no. 5, p. 054007, 2014.

[95] W. Hong, H. Li, S. X. Liu, Y. Fu, J. Li, V. Kaliginedi, S. Decurtins, and T. Wandlowski, "Trimethylsilyl-terminated oligo(phenylene ethynylene)s: An approach to single-molecule junctions with covalent Au-C σ-bonds," *J. Am. Chem. Soc.*, vol. 134, no. 47, pp. 19425–19431, 2012.

[96] M. Kamenetska, M. Koentopp, A. Whalley, Y. Park, M. Steigerwald, C. Nuckolls, M. Hybertsen, and L. Venkataraman, "Formation and evolution of single-molecule junctions," *Phys. Rev. Lett.*, vol. 102, no. 12, p. 126803, 2009.

[97] D. R. Jones and A. Troisi, "Single molecule conductance of linear dithioalkanes in the liquid phase: apparently activated transport due to conformational flexibility," *J. Phys. Chem. C*, vol. 111, no. 39, pp. 14567–14573, 2007.

[98] M. Mayor, H. B. Weber, J. Reichert, M. Elbing, C. Von Hänisch, D. Beckmann, and M. Fischer, "Electric Current through a Molecular Rod - Relevance of the Position of the Anchor Groups," *Angew. Chem. Int. Ed.*, vol. 42, no. 47, pp. 5834–5838, 2003.

[99] A. Mishchenko, L. A. Zotti, D. Vonlanthen, M. Bürkle, F. Pauly, J. C. Cuevas, M. Mayor, and T. Wandlowski, "Single-molecule junctions based on nitrile-terminated biphenyls: A promising new anchoring group," *J. Am. Chem. Soc.*, vol. 133, no. 2, pp. 184–187, 2011.

[100] M. Kamenetska, S. Y. Quek, A. C. Whalley, M. L. Steigerwald, H. J. Choi, S. G. Louie, C. Nuckolls, M. S. Hybertsen, J. B. Neaton, and L. Venkataraman, "Conductance and geometry of pyridine-linked single-molecule junctions," *J. Am. Chem. Soc.*, vol. 132, no. 19, pp. 6817–6821, 2010.

[101] Z.-L. Cheng, R. Skouta, H. Vázquez, J. R. Widawsky, S. Schneebeli, W. Chen, M. S. Hybertsen, R. Breslow, and L. Venkataraman, "In situ formation of highly conducting covalent Au-C contacts for single-molecule junctions.," *Nat. Nanotechnol.*, vol. 6, no. 6, pp. 353–357, 2011.

[102] S. Fujii, S. Marqués-González, J.-Y. Shin, H. Shinokubo, T. Masuda, T. Nishino, N. P. Arasu, H. Vázquez, and M. Kiguchi, "Highly-conducting molecular circuits based on antiaromaticity," *Nat. Commun.*, vol. 8, no. 1, pp. 1–8, 2017.

[103] W. Chen, J. R. Widawsky, H. Vázquez, S. T. Schneebeli, M. S. Hybertsen, R. Breslow, and L. Venkataraman, "Highly conducting π-conjugated molecular junctions covalently bonded to gold electrodes," *J. Am. Chem. Soc.*, vol. 133, no. 43, pp. 17160–17163, 2011.

[104] I. J. Olavarria-Contreras, M. L. Perrin, Z. Chen, S. Klyatskaya, M. Ruben, and H. S. Van Der Zant, "C-Au covalently bonded molecular junctions using nonprotected alkynyl anchoring groups," *J. Am. Chem. Soc.*, vol. 138, no. 27, pp. 8465–8469, 2016.

[105] N. P. Arasu and H. Vázquez, "Direct Au–C contacts based on biphenylene for single molecule circuits," *Phys. Chem. Chem. Phys.*, vol. 20, pp. 10378–10383, 2018.

[106] Y. Ie, K. Tanaka, A. Tashiro, S. K. Lee, H. R. Testai, R. Yamada, H. Tada, and Y. Aso, "Thiophene-based Tripodal Anchor Units for Hole Transport in Single-Molecule Junctions with Gold Electrodes," *J. Phys. Chem. Lett.*, vol. 6, no. 18, pp. 3754–3759, 2015.

[107] M. Lukas, K. Dössel, A. Schramm, O. Fuhr, C. Stroh, M. Mayor, K. Fink, and H. V. Löhneysen, "A tripodal molecule on a gold surface: Orientation-dependent coupling and electronic properties of the molecular legs," *ACS Nano*, vol. 7, no. 7, pp. 6170–6180, 2013.

[108] R. Breslow, "Antiaromaticity," *Acc. Chem. Res.*, vol. 6, no. 12, pp. 393–398, 1973.

[109] R. Breslow and F. W. Foss Jr, "Charge transport in nanoscale aromatic and antiaromatic systems," *J. Phys.: Condens. Matter*, vol. 20, no. 37, p. 374104, 2008.

[110] S. Schneebeli, M. Kamenetska, F. Foss, H. Vázquez, R. Skouta, M. Hybertsen, L. Venkataraman, and R. Breslow, "The electrical properties of biphenylenes," *Org. Lett.*, vol. 12, no. 18, pp. 4114–4117, 2010.

[111] C. Perthuisot, B. L. Edelbach, D. L. Zubris, N. Simhai, C. N. Iverson, C. Müller, T. Satoh, and W. D. Jones, "Cleavage of the carbon–carbon bond in biphenylene using transition metals," *J. Mol. Catal. A: Chem.*, vol. 189, no. 1, pp. 157–168, 2002.

[112] H. Zhou, L. Yang, and W. You, "Rational design of high performance conjugated polymers for organic solar cells," *Macromolecules*, vol. 45, no. 2, pp. 607–632, 2012.

[113] S. Lamansky, P. Djurovich, D. Murphy, F. Abdel-Razzaq, H.-E. Lee, C. Adachi, P. E. Burrows, S. R. Forrest, and M. E. Thompson, "Highly phosphorescent bis-cyclometalated iridium complexes: synthesis, photophysical characterization, and use in organic light emitting diodes," *J. Am. Chem. Soc.*, vol. 123, no. 18, pp. 4304–4312, 2001.

[114] G. Horowitz, M. E. Hajlaoui, and R. Hajlaoui, "Temperature and gate voltage dependence of hole mobility in polycrystalline oligothiophene thin film transistors," *J. Appl. Phys.*, vol. 87, no. 9, pp. 4456–4463, 2000.

[115] M. B. Smith, *March's advanced organic chemistry: reactions, mechanisms, and structure*. John Wiley & Sons, 2020.

[116] I. Thanopulos, E. Paspalakis, and V. Yannopapas, "Optical switching of electric charge transfer pathways in porphyrin: a light-controlled nanoscale current router.," *Nanotechnology*, vol. 19, no. 44, p. 445202, 2008.

[117] T. Yelin, R. Korytar, N. Sukenik, R. Vardimon, B. Kumar, C. Nuckolls, F. Evers, O. Tal, R. Korytár, N. Sukenik, R. Vardimon, B. Kumar, C. Nuckolls, F. Evers, and O. Tal, "Conductance saturation in a series of highly transmitting molecular junctions," *Nat. Mater.*, vol. 15, no. 4, pp. 444–449, 2016.

[118] W. Chen, H. Li, J. R. Widawsky, C. Appayee, L. Venkataraman, and R. Breslow, "Aromaticity decreases single-molecule junction conductance.," *J. Am. Chem. Soc.*, vol. 136, no. 3, pp. 918–920, 2014.

[119] R. Breslow, J. Brown, and J. J. Gajewski, "Antiaromaticity of cyclopropenyl anions," *J. Am. Chem. Soc.*, vol. 89, no. 17, pp. 4383–4390, 1967.

[120] J. Pople and K. Untch, "Induced paramagnetic ring currents," *J. Am. Chem. Soc.*, vol. 88, no. 21, pp. 4811–4815, 1966.

[121] R. Breslow, R. Grubbs, and S. Murahashi, "Electrochemical evidence for the antiaromaticity of cyclobutadiene," *J. Am. Chem. Soc.*, vol. 92, no. 13, pp. 4139–4140, 1970.

[122] T. Ito, Y. Hayashi, S. Shimizu, J. Y. Shin, N. Kobayashi, and H. Shinokubo, "Gram-scale synthesis of nickel(II) norcorrole: The smallest antiaromatic porphyrinoid," *Angew. Chem. Int. Ed.*, vol. 51, no. 34, pp. 8542–8545, 2012.

[123] N. P. Arasu and H. Vázquez, "Origin of the electron transport properties of aromatic and antiaromatic single molecule circuits," *ChemPhysChem*, vol. 22, no. 9, pp. 864–869, 2021.

[124] A. Mahendran, P. Gopinath, and R. Breslow, "Single molecule conductance of aromatic, nonaromatic, and partially antiaromatic systems," *Tetrahedron Lett.*, vol. 56, no. 33, pp. 4833–4835, 2015.

List of Figures

1.1 Mechanical break junction experiment (taken from Ref. [38]). The inset shows the sourse (S) and drain (D) of the electronic device, molecule can be tunned by gate electrode (G) in the background. The nanometer gap is controlled by mechanical motion through piezoelectric material (pushing rod). 4

1.2 a) STM break junction experiment (taken from Ref. [39]) STM tip is pushed and pulled against a substrate containing molecules in solution while measuring current with respect to voltage. b) Graphics of a molecule filling the gap between electrodes during tip retraction c) chemical structure of a triphenyl molecule for which conductance histogram is shown in d). Histograms corresponds to change in chemical groups at metal-molecule interface. Figure c) and d) are adapted from Ref.[40] 4

1.3 a) Experimental setup of STM (figure is taken from Ref.[42]). b) STM images of molecules (above) and chemical structure (below) (figure adapted from Ref.[43]). 5

1.4 (a) STM images of a single triangulene on Au(111) surface. (b) dI/dV spectra measured over different sites of the triangulene molecule on the Au(111) substrate. dI/dV curves taken at the edge (blue) and at the center (black) of triangulene and measurment taken on the clean Au(111) surface (red) are shown. The figure is taken from [44]. c) A single molecule chain is lifted by a STM tip, the figure is taken from [36]. 6

1.5 a) Quantum particle in a 1D box with potential energy walls of infinite height. b) Wavefunctions (ψ) at energies corresponding to first three (n = 1,2 3) principal quantum numbers. c) Probability density ψ^2 of the wavefunctions shown in b). 7

1.6 Energies plotted using equation 1.18 for 2D symmetric (square) box and asymmetric (rectangular) box. We can see that the symmetry gives rise to degeneracy of states i.e., there are two states at the same energy ($E_{1,2}$ and $E_{2,1}$). 9

1.7 Wavefunction of the first four states of a particle in a symmetric 2D box plotted with equation 1.17. a) 3D plot with z axis showing the energy. x and y directions are the box dimension, b) projection of panel a) over x and y planes. We can see the increase in number of nodes with increasing n. States $\psi(1,2)$ and $\psi(2,1)$ are degenerate, rotated with respect to each other by 90°. 11

1.8 Illustration of an electron passing a rectangular potential barrier of height U and width a. A, B and C are the coefficients of the electron wave vector. + and - indicate incoming and outgoing waves respectively. 11

1.9 a) Transmission probability as a function of energy plotted using equations 1.26 and 1.25. When E < U (inset) transmission increases exponentially with with the energy of the particle. b) Transmission is plotted as a function of the length of the potential barrier showing exponential decay with length. The height of potential energy barrier U is fixed at 4 eV (i.e., E < U). 13
1.10 Illustration of an electron passing two symmetric potential barriers of height U and width a. The distance between the two barriers is L. 14
1.11 Transmission probability vs energy plotted using equations 1.29, showing enhanced tunneling coefficients at specific energies, the energy axis is in log scale. The corresponding states between the double potential barrier are also shown. 14
1.12 a) A prototypical single-molecule circuit. b) Illustration of molecular discrete energy state coupling to the metal Fermi level. . . . 19
1.13 a) Benzene molecule represented as a hexagon, each corner is a carbon site b) Molecular orbitals and energy level diagram of benzene obtained with onsite energy $\epsilon_0 = 0$ and hopping energy t = 1. The solid circles on the hexagon are positive, and the hollow circles are the negative amplitude of the wavefunction. Red dashed lines show nodal planes. 22
1.14 Transmission spectra plotted using equation 1.57. Hamiltonian of the molecule is from the tight-binding model show in equation 1.64. The molecule is connected to the electrodes via meta, para and ortho positions. 23
1.15 Molecular structures (top), graphical rules applied to the molecules (middle), and transmission plotted as a function of energy by tight-binding and DFT calculations (bottom)/ Color code of the transmission functions, CC1 (red), CC2 (dotted blue) and CC3 (dotted black). According to the graphical rule the green circle denotes the unpaired atom which results in DQI feature. The graphical rules correctly predicts DQI feature in CC1 CC2 and no DQI in CC3. The figure is taken from [48]. 24
1.16 a) Atomic structure of naphthalene molecule. b) Energies and wavefunctions of five occupied and three unoccupied π molecular orbitals. 30
1.17 a) Potential energy along the z-direction of a junction with naphthalene molecule (red) and without molecule i.e, a vacuum gap (black). The Fermi energy is set at the origin. b) Atomic structure of a naphthalene molecule pinned between Au electrodes, the geometry is aligned with the horizontal axis of a). The potential energy barrier created by the molecular region is similar to the potential barriers in section 1.4.3 30
1.18 Transmission spectra of the naphthalene molecule (inset) contacted by two electrodes on either side. The arrows point to peaks corresponding to relevant frontier molecular orbitals. This naphthalene junction shows LUMO derived conductance. 31

2.1 Top and side vies of carbazole donor (CB), a phenalenone (HP) acceptor, and an aliphatic methylene bridge of CBHP donor-acceptor molecule. Upon deposition to Pt(111) substrate the -OH group of the acceptor unit dissociates and the molecule forms an O-Pt bond with a Pt adatom. 34
2.2 Band structure (left) and projected density of states (right) plots of bulk Pt calculated using the SIESTA default pseudopotential (red) and the pseudopotential obtained from Rivero et al., [67] (black). Rivero et al., pseudopotential provides an improvement on the electronic dispersion. 35
2.3 CBHP molecule consisting of carbazole donor and phenalenone acceptor units seperated by a methylene unit. When deposited on a Pt(111) substrate the CBHP molecule forms two distinct configurations, ConA (top) and ConB (bottom). The figure was taken from the TOC figure from the article [71]. 36

3.1 Electronic structure of singlet and triplet carbenes. The figure is same as Fig. 1 of [75]. 59
3.2 Chemical structures of NHC and BAC molecules. R represents bulky side group attached to the molecule. Lone pairs are indicated by two dots. 60
3.3 Insets show the bis(dialkylamino)cyclopropenylidenes (BAC) molecules forming a uniform coverage on the Au (111) surface upon annealing. The tilted adsorption of BAC is shown as graphical illustration. The figure is taken from the TOC of the article [87]. . 61

4.1 Typical anchoring groups for single-molecule electronics. 83
4.2 Chemical structure of biphenylene molecule. Two benzene rings are connected together through two C=C bonds. 84
4.3 Biphenylene molecule forming two direct Au-C bonds on an Au(111) surface. The top side of the molecule shows the chemical functionalization of five different linker groups. The mechanical and transport properties of five linker groups were studied over the strong bipodal biphenylene platform. The figure is the same as the TOC figure of the article [105]. 85

5.1 Core structures of first stable antiaromatic molecule synthesized (Ni-norcorrole, right) and its aromatic counterpart (Ni-porphyrin, left). The difference comes from two pairs of C-H atoms missing in Ni-norcorrole, marked as red boxes in Ni-porphyrin. 104
5.2 Antiaromaticity is shown to be double p-doping of the electronic structure of the aromatic analogue, whereby the HOMO of the aromatic molecule is fully depleted. These general principles have wide consequences on electron transport, quantum interference, and molecular design rules. The figure is the same as the table of the content figure of article 2 [123]. 105
5.3 Aromatic, antiaromatic, and quinoidal molecular structures. Quinones are oxidized derivatives of aromatic molecules. The bond order of quinones is similar to antiaromatic molecules. 106

List of Abbreviations

STM Scanning Tunnelling Microscopy

STM-BJ Scanning Tunnelling Microscopy-Break Junction

DFT Density Functional Theory

NEGF Non Equilibrium Green's Functions

HOMO Highest Occupied Molecular Orbital

LUMO Lowest Unoccupied Molecular Orbital

GGA Generalized Gradient Approximation

vdW van der Waals

B3LYP Type of hybrid exchange-correlation functional (Becke,Lee,Yang,Parr)

DQI Destructive Quantum Interference

CBHP 5-[4-(9H-carbazol-9-yl)benzyl]-9-hydroxy-1H-phenalen-1-one

BAC bis(dialkylamino)cyclopropenylidenes

NHC N-heterocyclic carbene